UNIVERSITÉ D'AIX-MARSEILLE
CENTRE NATIONAL D'ÉTUDES SPATIALES

École Doctorale 352: Physique et Sciences de la Matière
UFR SCIENCES
LABORATOIRE D'ASTROPHYSIQUE DE MARSEILLE

Thèse présentée pour obtenir le grade universitaire de docteur

Discipline : Astrophysique

Samuel QUIRET

Circum Galactic Medium emission : from modeling to detection by a dedicated UV space mission

Soutenue le 18/11/2016 devant le jury :

Christopher MARTIN	Caltech (Pasadena, USA)	Rapporteur
Michele FUMAGALLI	Durham University (UK)	Rapporteur / Examinateur
Varsha KULKARNI	Univ. of South California (Colombia, USA)	Examinatrice
Jérémy BLAIZOT	CRAL (Lyon)	Examinateur
Phiippe AMRAM	LAM	Président du Jury
Céline PÉROUX	LAM	Co-Directrice de thèse
Bruno MILLIARD	LAM	Directeur de thèse

Résumé L'évolution des galaxies est un sujet relativement débattu en astronomie extra-galactique, étant donné que la plupart des mécanismes responsables des propriétés observées dans les galaxies (masse, taux de formation d'étoiles, contenu en métaux, moment angulaire) sont encore peu contraints et certains ne sont probablement même pas encore observés. Ma thèse porte sur une analyse de la région entourant les galaxies, connue sous le nom de Milieu Circum Galactique (MCG). Le MCG est à l'interface entre les galaxies et le Milieu Inter Galactique (MIG) et est considéré comme le lieu de prédilection pour les échanges gazeux et énergétiques entre les galaxies et le MIG, ce qui en fait la clé pour une meilleure compréhension de l'évolution des galaxies et du destin des baryons. Je présenterai dans un premier temps l'analyse d'un échantillon de systèmes à forte absorption issuent de la spectroscopie de quasars en absorption qui tracent les régions denses en hydrogène généralement associées au MCG des galaxies. Dans un deuxième temps, je présenterai ma contribution au développement d'une mission ballon embarquant un spectrographe UV, FIREBall-2, spécialement conçu pour observer l'émission faible et diffuse du MCG des galaxies à décalage vers le rouge inférieur à 1. D'un point de vue technique, je présenterai l'étude du composant optique clé de l'instrument: le réseau. D'un point de vue modélisation, je décrirai une simulation complète des observations, qui servira à la préparation du vol prévu pour l'Automne 2017 notamment en ce qui concerne la sélection des cibles, la stratégie observationelle et le traitement des données.

Abstract The evolution of galaxies is a rather hot topic in extra galactic astronomy, as many of the main mechanisms underlying the observed properties of galaxies (mass, star formation rate, metal content, angular momentum) are still poorly constraints and many of them are probably undiscovered yet. My thesis focuses on an analysis of the region surrounding galaxies, known as the Circum Galactic Medium (CGM). The CGM interfaces the galaxy with the Inter Galactic Medium (IGM) and is thought to be the most active location for gas and energy exchanges (in and out), which makes it a key ingredient towards a better understanding of galaxy evolution and the fate of all baryons. I will present in a first part, the analysis of a sample of strong absorption features based on quasar absorption spectroscopy, that probe the dense neutral hydrogen usually associated with galaxies' CGM. In a second part, I will present my contribution to the development of a balloon-borne UV spectrograph, FIREBall-2, specifically designed to observe the faint and diffuse emissions from the CGM of galaxies at redshifts below 1. On the technical side, I will present the characterization of the key optical component of the instrument: the grating. On the modeling side, I will focus on an end-to-end pixel simulation of the observations to prepare for the upcoming flight, planned for Autumn 2017, in terms of target selection, observational strategy and data analysis.

Résumé

L'évolution des galaxies est un sujet relativement débattu en astronomie extra-galactique, étant donné que la plupart des mécanismes responsables des propriétés observées dans les galaxies (masse, taux de formation d'étoiles, contenu en métaux, moment angulaire) sont encore peu contraints et certains ne sont probablement même pas encore observés. Ma thèse porte sur une analyse de la région entourant les galaxies, connue sous le nom de Milieu Circum Galactique (MCG). Le MCG est à l'interface entre les galaxies et le Milieu Inter Galactique (MIG) et est considéré comme le lieu de prédilection pour les échanges gazeux et énergétiques entre les galaxies et le MIG, ce qui en fait la clé pour une meilleure compréhension de l'évolution des galaxies et du destin des baryons.

Je présente dans un premier temps l'analyse d'un large échantillon de systèmes à forte absorption issuent de la spectroscopie de quasars en absorption qui tracent les régions denses en hydrogène généralement associées au MCG des galaxies. Je réalise une étude globale sur la métallicité de ces systèmes, indicateur direct de l'évolution des galaxies puisqu'elle nous renseigne sur le contenu en poussière de ces régions denses mais aussi sur l'évolution de leur enrichissement chimique. Dans un deuxième temps, je présente ma contribution au développement d'une mission ballon embarquant un spectrographe UV, FIREBall-2, spécialement conçu pour observer l'émission faible et diffuse de MCG des galaxies à décalage vers le rouge inférieur à 1. D'un point de vue technique, je travaille sur un composant optique clé de l'instrument: le réseau. Je réalise des mesures UV polarisées et une modélisation d'un réseau holographique à 2400 t/mm et je propose et évalue une solution utilisant un dépôt surfacique de $\mathrm{MgF_2}$ pour améliorer l'efficacité dans les conditions de vol. D'un point de vue modélisation, je prépare l'analyse des données de l'instrument grâce à une simulation complète des observations. À l'aide d'un modèle réaliste de la réponse du détecteur et d'une modélisation de l'émission du MCG pour trois raies significatives (Lyα, CIV et OVI) couplée à une simulation numérique hydrodynamique à haute résolution de l'Univers, je prédis l'observation des cibles potentielles pour FIREBall-2 et prépare le terrain pour la future analyse des données.

Mots clés : Évolution des Galaxies, MCG, UV, FIREBall, Spectroscopie, Spectroscopie de Quasars en Absorption, Metallicité, Réseau, Ballon

Abstract

The evolution of galaxies is a rather hot topic in extra galactic astronomy, as many of the main mechanisms underlying the observed properties of galaxies (mass, star formation rate, metal content, angular momentum) are still poorly constraints and many of them are probably still undiscovered. My thesis focuses on an analysis of the region surrounding galaxies, known as the Circum Galactic Medium (CGM). The CGM interfaces the galaxy with the Inter Galactic Medium (IGM) and is thought to be the most active location for gas and energy exchanges (in and out), which makes it a key ingredient towards a better understanding of galaxy evolution and the fate of all baryons.

I first present the analysis of a large sample of strong absorption features based on quasar absorption spectroscopy, that probes the dense neutral hydrogen usually associated with galaxies' CGM. I perform a broad analysis of the sample metallicity, which directly probes galaxy evolution as it brings insight in terms of dust content, but also in terms of chemical enrichment.

In a second part, I present my contribution to the development of a balloon-borne UV spectrograph, FIREBall-2, specifically designed to observe the faint and diffuse emissions from the CGM of galaxies at redshifts below 1. On the technical side, I work on the key optical component of the instrument: the grating. I perform UV polarized efficiency measurements and a characterization of a 2400 l/mm holographic grating and I propose and evaluate a solution using $\mathrm{MgF_2}$ coatings to improve the efficiency in flight conditions. On the modeling side, I prepare the data analysis of the instrument with an end-to-end pixel simulation of the observations. Using a realistic model for the detector output along with a model for the CGM emission in three lines of interest (Lyα, CIV and OVI) coupled with a high resolution numerical hydrodynamical simulation of the Universe, I predict the observations of potential targets for FIREBall-2 and prepare the tools for further data analysis.

Keywords : Galaxy Evolution, CGM, UV, FIREBall, Spectroscopy, Quasar Absorption Spectroscopy, Metallicity, Grating, Balloon

Remerciements

Je voudrais remercier Bruno Milliard et Céline Péroux pour m'avoir accompagné, soutenu, compris, et appris tant de choses sur ce sujet passionant qu'est l'étude de l'évolution des galaxies. Je réalise maintenant la chance que j'ai eu de les avoir eu comme directeurs de thèse. Sans leur écoute, et leur acharnement à me sortir la tête de l'eau, la qualité de mon travail n'aurait jamais été le même. J'espère que nos chemins un jour se recroiseront. MERCI!

Un grand merci aussi pour tous ces collègues qui font que travailler dans ce domaine est un plaisir que j'aimais partager avec eux. Merci à Didier, Robert, Pierre, Gérard, Jean-Charles, Hadi, Varsha, Mat, Debopam, Jérémy, Amandine, Mohamed, Vincent et Ramona.

Merci aussi pour tous mes co-doctorants, ce fut un plaisir de partager les moments de galère, essayer de trouver un peu de normalité dans ce monde de fous! Merci à mon beau Javier, Bastien, Francesca, Giovanni, Alice, Anna, Anna, Mario, Debora, Thibaud, Pol, Brian, Darko, Firas, Carlo, Giulia, Lucía, Raffaella, Janine, Ilane, Lauren, Sergei, Nicolas!

Merci à Alain pour toutes ces magnifiques photos du Canigou.

Et pour finir, un grand merci à tous les autres, ceux qui ont fait de ces trois années marseillaises des années qui resteront gravées dans mon être.

Et un gros Big Up à Will, qui n'a jamais rechigné à la relecture des diverses publications et pour l'élaboration de ce manuscript!

Contents

List of Figures

List of Tables

Introduction

In the course of my academic studies, I have developed an interest for galaxies. In particular, this PhD has allowed me to study the mechanisms that explain how these galaxies evolve, that is how they feed, how they grow, how they breath[a]. To study galaxy evolution, one has to understand first what the term *galaxy* refers to. Of course it is wrong to assume that these galaxies, whatever they might represent, are living systems. And yet, the temptation for living creature analogy is strong! Let's start with some general insights about galaxies.

An historical review of the Universe

In the early nineteenth century, two major events changed drastically the course of extra-galactic astrophysics. In 1915, Einstein published his theory of *General Relativity*, which proposed a new way to consider gravity to much larger scales than the well known Newtonian theory of gravity.

Soon after, in 1923, two astronomers, Harlow Shapley and Heber Curtis, led an international conference, known as *The Great Debate*, the goal of which was to come to an agreement in the astronomical community regarding the question of the size of the Universe. More precisely, the question was to know whether the Universe was limited to one system, the Milky Way (Shapley's point of view) or if the Universe was, in fact, much bigger and if the different observed nebulae, referred to as *Island Universes* (the original term used to refer to current galaxies) could be replicas of our own galaxy, but at greater distances (Curtis' point of view).

Edwin Hubble brought an end to the debate in 1924 with his observations of *standard candles*, the Cepheids. The Cepheids are variable stars, which have luminosity pulsating with a frequency proportional to their intrinsic luminosity (Leavitt et al., 1912). They can therefore be used as rulers: by measuring their frequency, we can derive their intrinsic luminosity $\mathrm{I}_{\mathrm{intrinsic}}$ and therefore their distance r to the observer; the flux scaling as $\mathrm{I}_{\mathrm{intrinsic}}/\mathrm{r}^2$. Hubble's observation

[a] I have been told once that I should really be careful with the analogy I am using when I want to explain my work to non specialist or non astronomers, but let's make an exception for a few lines.

of Cepheids in the Andromeda Galaxy made it clear that the Universe was not confined to a restricted volume, but that it was actually far more extended and that it could hold several *Island Universes*, or galaxies such as the Andromeda Galaxy.

In 1929, Hubble observed a correlation between the distance of an object and its recession velocity: it appears that the more distant an object, the faster it appears to move away from the observer. This is known as the Hubble law:

$$v = H_0 r$$

and was the first clue of the Universe expansion. Recent observations of type Ia supernovae, another type of standard candles, showed that this expansion was in fact accelerating (Riess et al., 1998; Perlmutter et al., 1999)! These decades of discoveries drastically changed the way astronomers considered the Universe. Then a rather compact system, it is now a huge expanding structure containing apparently countless galaxies. Cosmology, the study of the Universe, is therefore a crucial topic in the astronomical community. Indeed, now that we see the Universe as an evolving object, the well known questions of the origin of Man emerge: *Where Do We Come From? What Are We? Where Are We Going?*

The question of the origin of the Universe is crucial in Cosmology. Following the discovery of the Universe expansion, two models emerged: one with continuous creation of matter to keep matter density constant in time and space, and the other without. The former, referred to as the *Steady State theory* (Bondi et al., 1948; Hoyle, 1948), implies continuous creation of matter, and suggests that the Universe has no age, that it has always existed. The latter, referred to as the *Big Bang theory*, suggests that the Universe originally emerged from a Singularity in time and space (Lemaître, 1927). The latter model was adopted with the observation of the Cosmic Microwave Background (CMB) (Alpher, Bethe, et al., 1948; Alpher and Herman, 1948).

Figure 0.1.: Where Do We Come From? What Are We? Where Are We Going? (Painting from Paul Gaugin, 1897, Museum of Fine Arts, Boston.)

From the Big Bang to the Cosmic Microwave Background

According to the nucleosynthesis theory, the Universe post Big Bang was a hot ionized plasma, meaning that its temperature $kT > 13.6$ eV was sufficient to keep it fully ionized. The photons that were then emitted were tightly coupled to ions due to Thomson scattering:

$$e^- + \gamma \rightarrow e^- + \gamma$$

When it cooled sufficiently, due to the expansion, the Thomson scattering *froze out*, such that the reaction was no longer possible. Indeed, as the Universe expands, the mean free path of the interaction stays constant and there is a point where the expansion rate outpaces the interaction rates, *freezing out* the reaction. Photons are then decoupled from matter and can escape the plasma. We call these newly freed photons the Cosmic Microwave Background (CMB). At this time, around $z \sim 1100$ or 370000 years after the Big Bang, the *recombination* happened, when the neutral Hydrogen was first produced:

$$p^+ + e^- \rightarrow H^0 + \gamma$$

At this time, there were no such things as stars or galaxies, thus no light sources in all the Universe, which was just composed of neutral Hydrogen. This epoch is called the *Cosmic Dark Ages*.

The Cosmic Dark Ages and the Reionization Epoch

The Cosmic Dark Ages refer to a time when the Universe was transparent (no more Thomson scattering) and mostly composed of neutral hydrogen. Very few

photons are observed from that time, as no sources existed back then, and because the few photons ever emitted were immediately absorbed by the neutral hydrogen (and helium) present. Around $z \sim 15 - 30$ (100 to 270 million years after the Big Bang), the first stars started to appear, and around $z \sim 10 - 30$ (100 million to 500 million years after the Big Bang) the first galaxies[b]. With these started the *Reionization epoch*. Indeed, the ultraviolet (UV) radiations then produced were energetic enough to ionize the gas surrounding the sources: bubbles of ionized gas were forming.

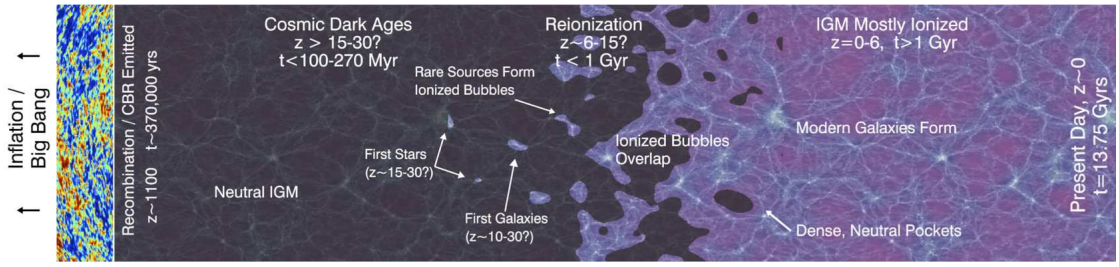

Figure 0.2.: Cosmic Reionization: from the cosmic dark ages to the mostly ionized present Universe. Credit: Robertson et al., 2010

Within these bubbles, the photons with energy $h\nu > 13.6$ eV produced by the stars were able to propagate freely (without being absorbed), until they reached the limit of the bubble. The size of these bubbles grew with the number of stars produced by these first galaxies, until the point when the bubbles overlapped, making the entire Universe ionized. This marked the end of the reionizing epoch, around $z \sim 6 - 20$ (180 million to 1 billion years after the Big Bang).

The current state of the Universe: the Cosmic Web

After the reionizing epoch, the Universe was mostly composed of ionized hydrogen, and it is now mostly transparent, meaning that we are able to observe objects that formed after this epoch. The galaxies and quasars currently in formation provide a powerful UV background that maintains the ionization of neutral hydrogen.

Recent simulations of the Universe nevertheless predict a coherent structure formed by the densest regions of Hydrogen, collimated into filamentous structures resulting from the action of gravity on the primordial matter fluctuations,

[b] A galaxy is a system of gas, stars, interstellar dust gravitationally bound together by a *Dark Matter* halo, and usually revolving around a huge black hole at its center. Dark Matter, in opposition to baryonic matter, is a theoretical tool used to explain complex physical processes observed within the Universe. The concept was first introduced to explain the flat end of the velocity curves of galaxies. It is something that has not been discovered yet, but is thought to be invisible-like matter interacting solely with gravity.

to form a web-like structure called the *Cosmic Web* (Fig. 0.3, left panel). These filaments are assumed to be mostly ionized, and to host most of the baryonic matter. The position of galaxies is highly correlated with the presence of gas, therefore it is possible to see the signature of the Cosmic Web via a slice through a SDSS 3-dimensional map showing the distribution of galaxies (Fig. 0.3, right panel).

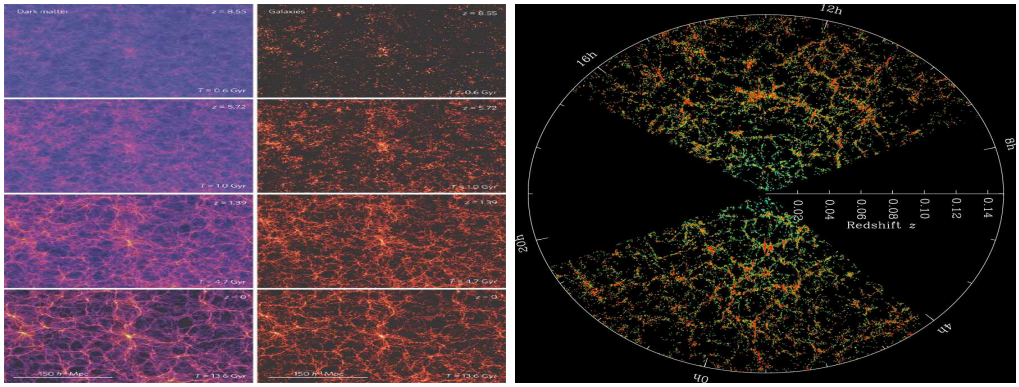

Figure 0.3.: Left: Evolution of the IGM from the Millenium N-body simulation. On the left is shown the projected dark matter distribution and on the right the galaxy distribution at four different redshifts. The color scale represents the velocity dispersion in the dark matter and the brightness of each pixel the logarithm of the projected density. The z=0 panels represent the present day simulated universe, with its web-like structure. Credit: Springel et al., 2006. Right: Slice through the SDSS 3-dimensional map of the distribution of galaxies. Our Galaxy is at the center, and each point represents a galaxy, color coded accordingly to the age of its stellar population. Credit: M. Blanton and the Sloan Digital Sky Survey. The similarity in both simulation and observation is striking.

The Circum Galactic Medium

The evolution of galaxies is closely related to the evolution of the cosmic web, more commonly referred to as the Inter Galactic Medium (IGM). Indeed, the IGM acts as a gas reservoir for galaxy formation, and is in turn greatly impacted by the galaxies that are born in it. One way to look at it is through the evolution of the baryonic content of the Universe. Indeed, if the IGM account for the overwhelming majority of baryons at high redshifts (Penton, Shull, et al., 2000; Dave et al., 2001), it only accounts for 24% at $z < 0.4$ (about 9.2 Gyr after the Big Bang, Tilton et al., 2012), while present galaxies themselves account for about 7% (Shull, Smith, et al., 2012) of the total baryonic budget. The rest of

the baryons are in fact thought to be found under a warm-hot phase of the IGM, where the gas is heated up to high temperatures ($10^5 - 10^7$ K) via gravitational collapse or interactions with powerful galactic winds (Cen and Fang, 2006; Shull, Danforth, et al., 2014). This phase is commonly referred to as the Warm-Hot Intergalactic Medium (WHIM, see Fig. 0.4).

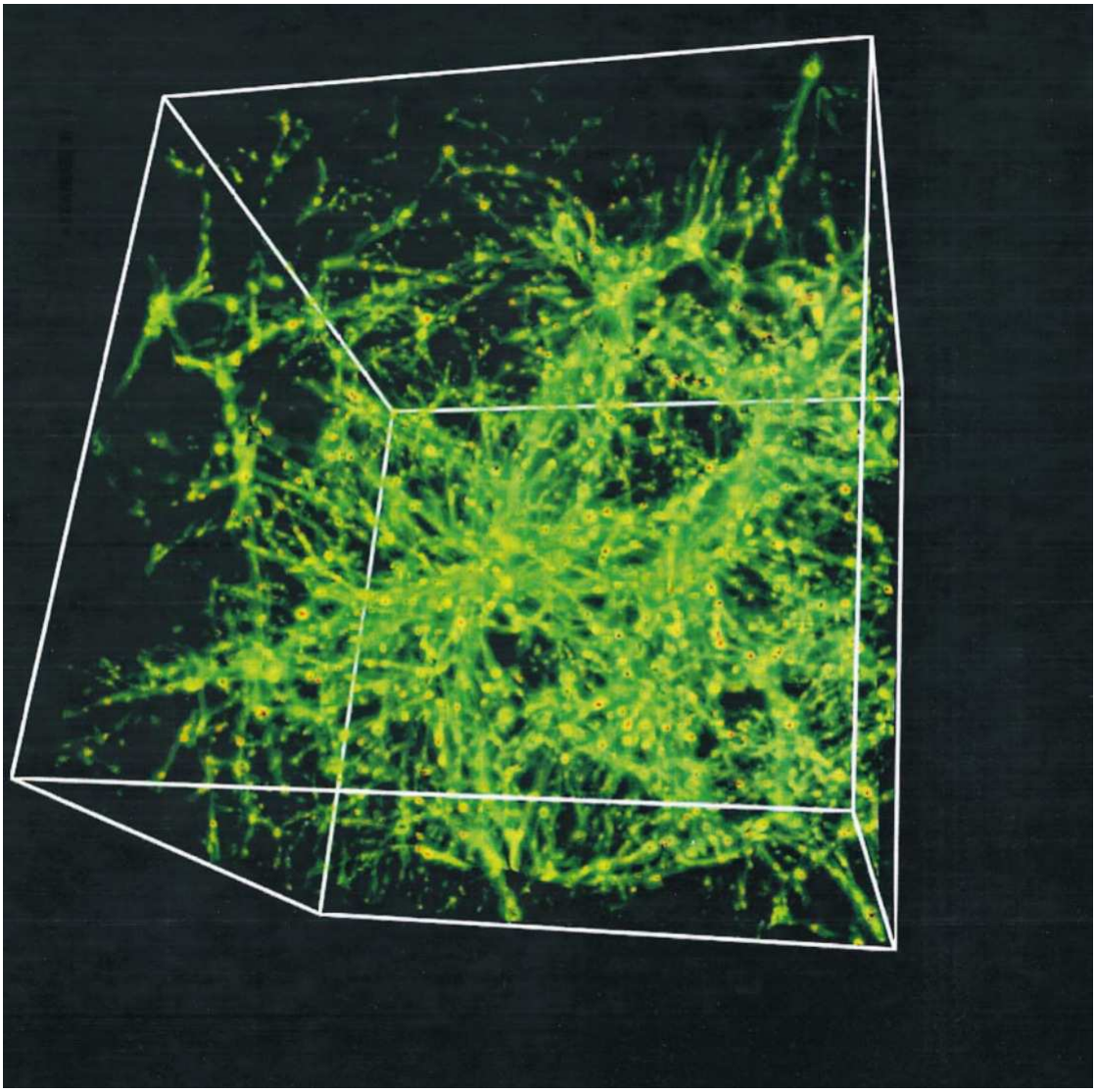

Figure 0.4.: Spatial distribution of the WHIM at z = 0 from a numerical simulation box of size $85\ \mathrm{Mpc/h}$. The filamentary structure taken by the hot gas is commonly referred to as the Cosmic Web. Credit: Cen and Ostriker, 2006

The multi-phase status of the IGM and its close interactions with galaxies indubitably call for a more thorough understanding of the physics regulating the

evolution of galaxies. Indeed, the processes behind matter accretion and the latter's link to star formation are still poorly constrained and understood nowadays. The same goes with the way galaxies expel their metal-enriched gas, and how these expulsions interact with the IGM and star formation.

The Circum Galactic Medium (CGM), interfacing galaxies with the IGM, is the choice candidate for answering such questions as it covers the area of these fundamental gaseous exchanges. If the first occurrence for such a multi-phase medium will soon celebrate its 50th anniversary (Bahcall et al., 1969), its exact spatial extent is still poorly constrained because of the very low surface brightness of the CGM gas (Steidel, Bogosavljević, et al., 2011; Feldmeier et al., 2013). However, based on the distribution of strong absorbers at redshifts $\mathrm{z} \sim 2 - 2.5$, Rudie et al., 2012 suggested a working definition of the CGM to be all locations within 300 physical kpc and $\pm 300\ \mathrm{km\ s^{-1}}$ of a galaxy. This definition is currently commonly accepted among the community on the basis of correlations between galaxies and the presence of strong absorbers within a few hundred physical kiloparsecs (Rakic et al., 2012).

The CGM is a multi-phase medium. A 'cold' phase ($< 10^5$ K), traced by the Lyα line[c] and other low-ionization ions such as FeII, is spatially distinct from a 'hot' phase ($\sim 10^{5-6}$ K), traced by high ionization gas such as OVI. These two phases are indicators for different mechanisms within the CGM. Indeed, the OVI is detected up to large radii and probably originates from collisional excitation of the gas from powerful outflows (Tumlinson et al., 2011). These phases are usually associated with the different mechanisms, the accretion of 'cold' gas and the ejection of 'hot' gas, taking place within the CGM.

The Gas Flows: In and Out

Outflows of metal-enriched gas from the galaxies are ubiquitous at all redshifts (Heckman et al., 1990; Weiner et al., 2009; Erb, Quider, et al., 2012; Newman et al., 2012; Rubin, Prochaska, Koo, Phillips, et al., 2014, and references therein). These outflows can reach important velocities (up to ~ 1000 km/s), and can eject masses two to three times the instantaneous Star Formation Rate (SFR) of galaxies (Bouché, Hohensee, et al., 2012). They are detected up to 70 kpc (Tripp, Meiring, et al., 2011) and contribute essentially to the chemical enrichment of the IGM and the regulation of the star formation in galaxies. Outflows can regulate star formation in both ways, as they can remove the gas from their host galaxy, thus quenching star formation, but they can trigger star formation via the induced pressure at the edge of the wind (Cresci et al., 2015).

[c] The Lyα line corresponds to the the first level of Hydrogen ionization (about 66% of the energy level transitions): 1216Å.

However, accretion mechanisms are still poorly constrained. The existence of such a mechanism is suggested via the quasi non-evolution of the neutral gas mass density (Hopkins et al., 2008; Zafar, Péroux, et al., 2013) despite the peak in the SFR density at $z \sim 2.1$ (Cucciati et al., 2012). Only a few examples of accretion have been detected today (Giavalisco, Vanzella, et al., 2011; Ribaudo et al., 2011; Barger et al., 2012; Voort, Schaye, et al., 2012; Rubin, Prochaska, Koo, and Phillips, 2012; Bouché et al., 2013a; Fraternali et al., 2014; Péroux, Quiret, et al., 2016). The difficulty in observing accretion can be explained by the fact that accretion of gas onto the galaxy might occur as collimated streams of cold gas with low covering fractions ('cold mode' accretion, Keres et al., 2005; Dekel et al., 2006; Ocvirk et al., 2008; Bordoloi et al., 2011; Stewart et al., 2011; Voort and Schaye, 2012). Moreover, recent work by Kacprzak, Churchill, et al., 2012 and Schroetter et al., 2015 suggests that the outflowing material is preferably ejected in the minor-axis of the galaxy, while the accretion occurs preferably along the major axis, which has a lower solid angle than the minor axis.

Fig. 0.5 shows the mass-weighted projections of gas density, temperature, entropy, and radial velocity for a halo at z=2, from a large volume, cosmological hydrodynamical simulation called Illustris (Nelson, Pillepich, et al., 2015). We can see clearly the collimated streams of cold gas entering the center of the galaxy and the ejection of hot high-entropy material.

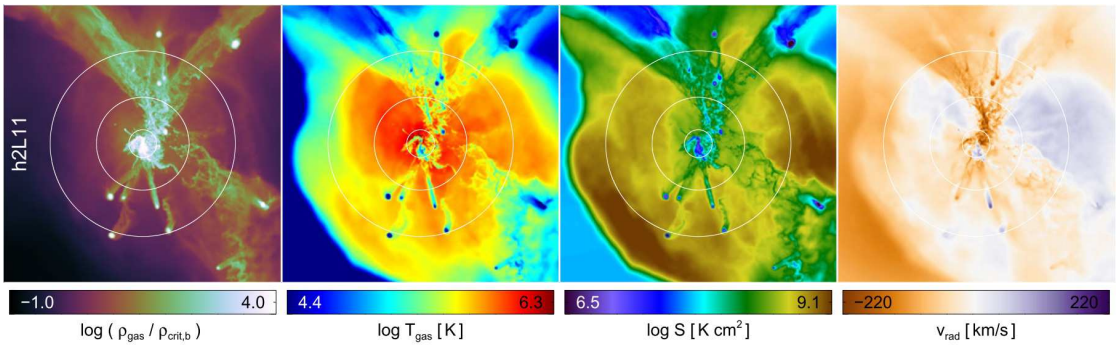

Figure 0.5.: Mass-weighted projections of gas density, temperature, entropy, and radial velocity for a simulated halo at z=2. The white circles denote $\{0.15, 0.5, 1.0\}\ r_{vir}$. Credit: Nelson, Genel, et al. (2016)

Observing the CGM

Absorption spectroscopy

The main source for CGM observational data comes from quasar absorption line spectroscopy. This technique refers to the concept of using distant bright light

sources, such as quasars or gamma ray bursts, as a support to study the spectroscopic absorption features caused by intervening absorbing systems. These systems are of diverse origin and diverse properties. Essentially, we observe the (very) small fraction of neutral hydrogen present in the Universe. This is a very powerful technique, as it can detect and measure neutral gas with column densities[d] as low as 10^{12} $\mathrm{at/cm^2}$[e], independently to redshift.

Quasars are extremely bright point source-like objects. Before reaching our telescopes, their photons go through a majority of ionized gas. When they encounter a region of neutral hydrogen, they are absorbed, mostly at the $Ly\alpha$ wavelength. Then, as the photons finish their journey toward our telescopes, the absorbed line gets *redshifted* as a consequence of the Universe's expansion:

$$\lambda_{obs} = (1 + z_{abs})\ \lambda_{rest}$$

where λ_{obs} is the observed wavelength of the absorption, λ_{rest} is the rest frame wavelength of the transition responsible for the absorption and z_{abs} is the redshift of the absorbing system.

[d] The column density of a system is the density of that system integrated along the line of sight to the observer.

[e] as a comparison, there is about 5×10^{16} $\mathrm{at/cm^2}$ at atmospheric pressure and temperature.

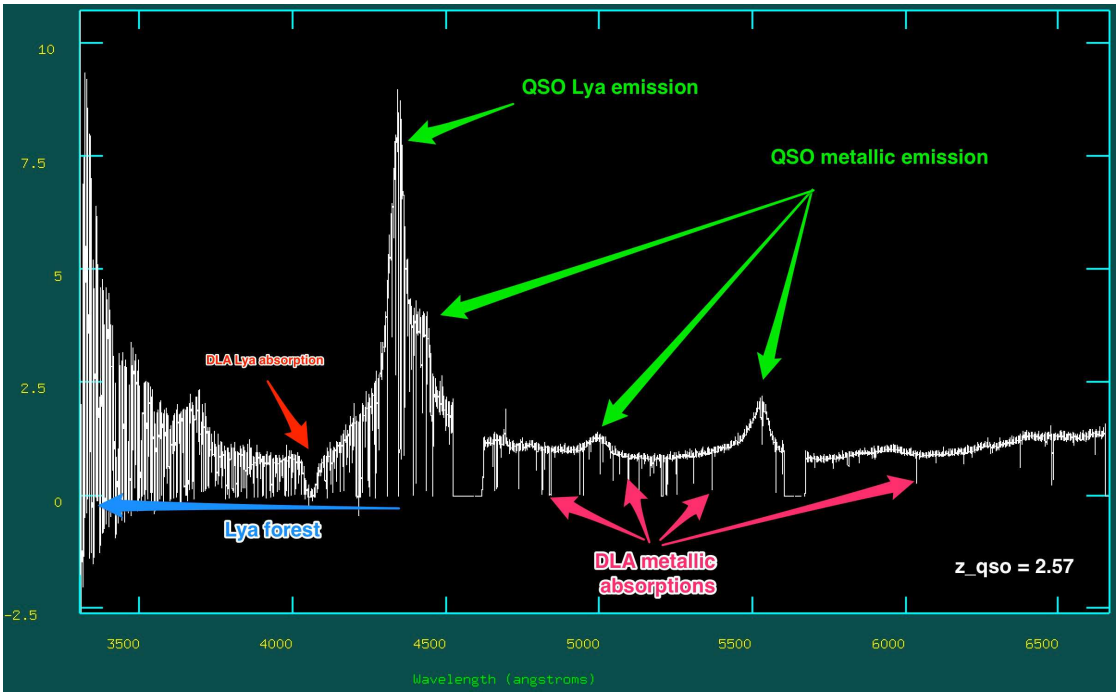

Figure 0.6.: UVES spectrum of LBQS 1232+0815, z=2.57. Shown on the spectrum the Lyα forest, bluewards of the quasar Lyα emission, the DLA Lyα absorption, with its metal absorption lines redwards of the Lyα emission. The ordinate is in arbitrary units, as the spectrum will be normalized so as to take out the quasar's signature from the absorption study.

It is thought that the CGM hosts dense regions of neutral hydrogen, as the increasing density in the accreting streams from the halo potential well causes the gas to protect itself from the surrounding ionizing radiation with a mechanism called *self-shielding*. Those regions present very high HI column density ($\mathrm{N(HI)} > 10^{19}$ cm^{-2}) and are called Damped Lyman α Absorbers (DLAs, $\mathrm{N(HI)} > 2 \times 10^{20}$ cm^{-2}) and sub-DLAs ($10^{19} < \mathrm{N(HI)} < 2 \times 10^{20}$ cm^{-2}). They are dubbed as 'Damped' because of the shape of their absorption profile, which happens to be saturated, with characteristic damping wings (see Fig. 0.7). The wings of the absorption profile give us all the information needed, as they are not Doppler parameter-dependent and very well constrained by the neutral hydrogen column density $\mathrm{N(HI)}$[f].

[f] An introduction on the physics of quasar absorbers is presented in Appendix A.2.

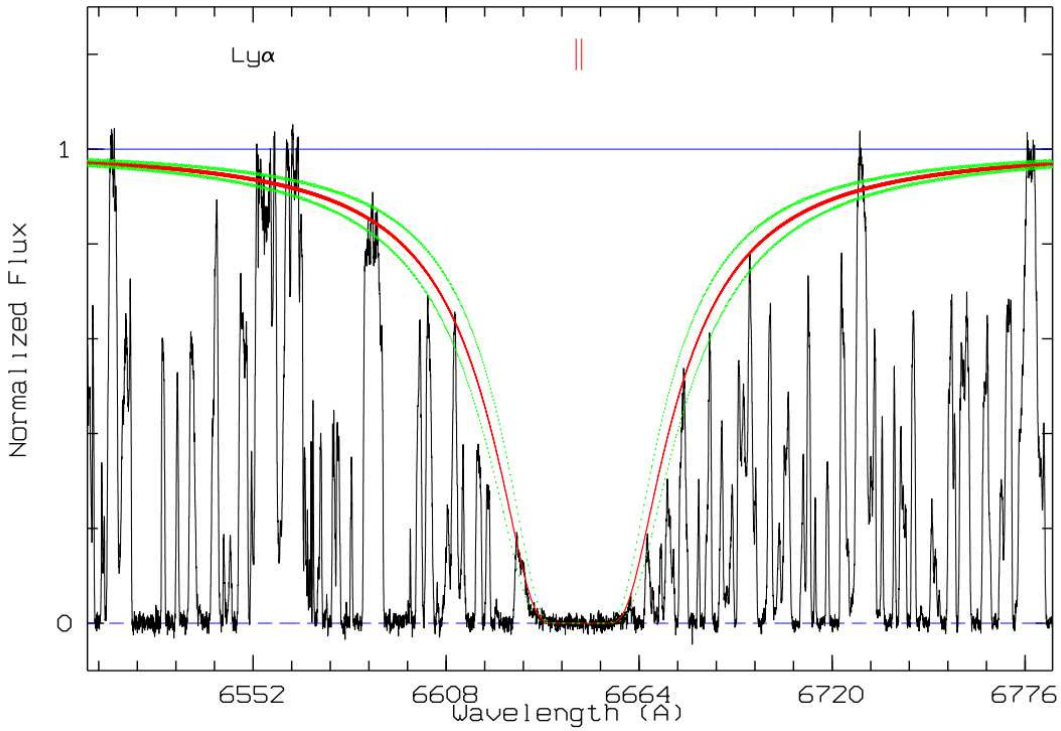

Figure 0.7.: Lyα absorption line for the BR J0307-4045 DLA. The spectrum (black) has been normalized to the continuum and the green and red lines constitute the Voigt profile fit to the data. Credit: Péroux (2001)

DLAs and sub-DLAs are probably tracing the faint end of the Luminosity Function that is otherwise little studied in galaxy formation and evolution (Rauch et al., 2008). Nevertheless, there seems to be a consensus on the fact that DLAs and sub-DLAs are closely related to the evolution galaxy. Rafelski, Wolfe, et al., 2012 propose that the DLAs are the progenitors of halo stars. Charlton et al., 2000 infer from the kinematic structures of neutral and low ionized ions that z=3 DLAs are progenitors of normal spiral galaxies. Wolfe, Prochaska, et al., 2008 observed a bimodality in the distribution of high-redshift DLAs (mainly in terms of different SFR, velocity widths, metallicities and dust-to-gas ratio).

The tremendous sensitivity of quasar absorption spectroscopy enables not only measurement of HI density, but that of metals[g] as well, independently of the redshift. It is for example possible to get a census on the evolution of the metallicity in galaxies, or chemical enrichment of the IGM. Metals are crucial in the question of galaxy evolution because they relate directly to the star forming activity of the galaxy. Indeed, they are the fossils of ancient star forming activity, and they trace

[g]Elements heavier than boron.

materials outflowing from galaxies. Moreover, they contribute to faster cooling of the accreting gas, and enhance star formation, explaining why we find more low-mass stars at lower redshifts. They are also a tracer of the stellar population in the galaxy.

The study of the metallicity of strong HI absorbers can yield valuable insight about the dynamics of the CGM, mainly what we call the baryon cycle. Indeed, Lehner, Howk, et al., 2013, followed by Wotta et al., 2016 and Lehner, O'Meara, Howk, et al., 2016 interpret the bimodality observed in the metallicity distribution of low redshift Lyman Limit Systems (LLS) as a hint that metallicity can trace metal-poor accreting gas from metal-rich feedbacks. However, such result is difficult to reproduce numerically as a recent FIRE simulation fails to reproduce the bimodality observed in the metallicity distribution of low redshift LLS (Hafen et al., 2016).

The CGM in emission

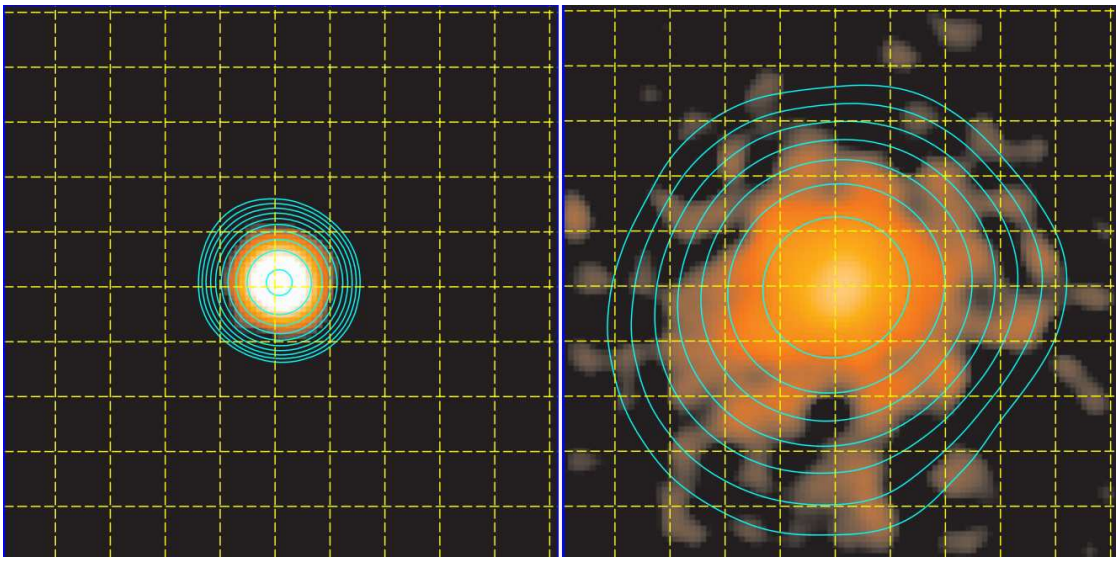

Figure 0.8.: Left panel: stacked UV continuum image of 92 continuum-selected Lyman Break Galaxies. Right panel: stacked continuum-subtracted NB Lyα image of the same objects. Both panels are 20 arcsec on a side, corresponding to 160 physical kpc at z = 2.65. The grid spacing is of 2 arcsec. Credit: Steidel, Bogosavljević, et al., 2011

Although it is very sensitive, absorption spectroscopy is limited to the presence of background sources and can only provide measurements of the CGM properties of a galaxy integrated along one line of sight, rarely two. The other way to consider CGM observations is to directly analyze the light the medium emits.

This, of course, has the advantage of mapping the location of the gas relatively to the galaxy, giving us insight into the different mechanisms involved in gaseous accretion or outflows, the quantity and the physical properties of the gas orbiting the galaxy. The main drawback of this technique is that the CGM has a low Surface Brightness (SB, $\sim 10^{-19}$ erg/s/cm^2/arcsec). This means that the sensitivity required to observe the CGM with a good signal to noise ratio must be high, or that the exposure time for one object must be long.

Using a long exposure (92h) on a long-slit search for Lyα fluorescence, Rauch et al., 2008 detected 27 faint emitters with line fluxes of a few 10^{-18} erg/s/cm^2/arcsec over a redshift range of $2.66 < z < 3.75$, about half of which show extended profiles. These Lyα emitters might be the counterparts of DLAs in emission. Another striking observation of the CGM in emission was performed by Steidel, Bogosavljević, et al., 2011, who stacked 92 both UV continuum and Lyα line images[h] to detect a flux down to the SB limit $\sim 10^{-19}$ erg/s/cm^2/arcsec at $z \sim 2.65$ and at projected radii of at least 80 physical kpc from the galaxy (Fig. 0.8). However, the detectability of such extended emission is highly debated, as Feldmeier et al., 2013 argue that Steidel, Bogosavljević, et al., 2011 observations are subject to low flux level surface brightness photometry errors and biased towards high luminosity halos. They find altogether lower fluxes within the central core, and a poorly extended emission. More recently, Wisotzki et al., 2016 observed 26 high redshift ($3 < z < 6$) extended emission from Lyα-emitting galaxies down to the surface brightness limit $\sim 10^{-19}$ erg/s/cm^2/arcsec using an ultra-deep exposure of 27 hours on a single 1x1 arcmin^2 field in the Hubble Deep Field South. This shows the evolution in the high-redshift observation of extended emission, as new generation spectrographs such as the Integral Field Units (IFU) MUSE at ESO-VLT give the possibility to reach sensitivities similar to what was previously achieved with the stacking hundreds of objects with lower observing time.

The origin of such emission is still poorly understood. It is thought from the observations that the observed Lyα extended emission is mainly driven by the resonant scattering of Lyα photons produced in HII regions in and around the galaxy (Faucher-Giguere, Keres, et al., 2010; Hayes et al., 2011; Steidel, Bogosavljević, et al., 2011; Matsuda et al., 2012; Wisotzki et al., 2016). This is also confirmed numerically by simulations using radiative transfer analysis (Laursen et al., 2007; Zheng et al., 2011; Verhamme, Dubois, et al., 2012). Cooling radiations from the gravitational collapse of CGM gas (i.e. an accreting stream) can have a significant impact on the total emission (Dijkstra and Kramer, 2012; Rosdahl and Blaizot, 2012), and would dominate the emission in the case of halos without on-going star formation (such as the so-called Lyα blobs, Fardal et al., 2001; Dijkstra and Loeb, 2009; Faucher-Giguere, Keres, et al., 2010). Finally, the present-day detection of fluorescent Lyα photons produced from hydrogen recombination is challenging, as the meta-galactic UV background at z~ 3 can

[h] This account for more than 200 hours integration time with a 10 m class telescope.

only photo-ionize the CGM to SB of a few $\sim 10^{-20}$ erg/s/cm^2/arcsec. However, there is hope to observe fluorescent emission produced by the presence of a bright source nearby of the galaxy (such as a quasar, see Fig. 0.9, Cantalupo, Porciani, et al., 2005; Kollmeier, Zheng, et al., 2010; Cantalupo, Arrigoni-Battaia, et al., 2014; Martin, Chang, Matuszewski, Morrissey, Rahman, Moore, and Steidel, 2014; Martin, Chang, Matuszewski, Morrissey, Rahman, Moore, Steidel, and Matsuda, 2014; Borisova et al., 2016).

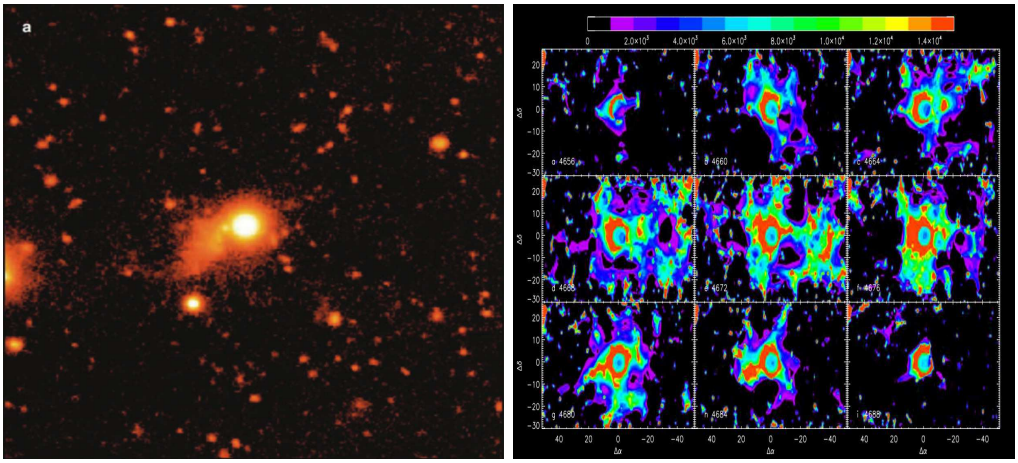

Figure 0.9.: Recent example of quasar-enhanced Lyα fluorescence. Left panel: the 'Slug nebula' observed by Cantalupo, Arrigoni-Battaia, et al., 2014 at z=2.3. The Lyα emission extends to approximately 460 physical kpc from the quasar. Right panel: Spectral slices of the quasar QSO HS1549+19 at z = 2.843 for several wavelengths. We see clearly some filamentary structures as long as 250–400 kpc at different wavelengths. One of these suggests the presence of cold accretion onto the quasar. Credit: Martin, Chang, Matuszewski, Morrissey, Rahman, Moore, and Steidel, 2014

Towards lower redshifts: the FIREBall project

The study of CGM emission is crucial for the understanding of the different mechanisms that regulate accretion and feedback processes, but the observations so far unanimously picture the high redshift Universe. Indeed, the large collecting areas required for such faint emission detection are only possible from the ground, inaccessible for UV photons due to the atmospheric absorption. The low-redshift Universe accounts for the major part of the Universe's age. It is therefore decisive to address the challenge that is low-redshift CGM emission observation.

So far, two satellites with UV telescopes have been feeding low-redshift data relevant to the CGM: the Galaxy Evolution Explorer (GALEX), an orbiting space telescope that produced a large archive of Lyα emitting galaxies, and the Hubble

Space Telescope (HST) providing a UV spectrograph, the Cosmic Origin Spectrograph (COS), that led to much of the data collection for low redshift absorbing systems. There has also been an attempt for such low-z CGM observation in 2009 with FIREBall-1, which did not reach low-enough sensitivity (Milliard et al., 2010).

Among the low-cost and interesting solutions available to UV astronomy, balloon borne telescopes benefit from a large experience from meteorological science and satellite observations. As a path-finder for a more ambitious UV satellite (the Imaging Spectroscopic Telescope for Origins Survey , ISTOS), FIREBall-2 (Faint Intergalactic Redshifted Emission Balloon-2), a UV Multi Object Spectrograph (MOS) is under development to observe the faint and diffuse emissions from the CGM of low-redshift galaxies.

An X-Ray observatory, Athena+, is also under preparation. The X-Ray wavelengths probe higher temperature emission lines, which can unveil the high energy physics at hand in the WHIM, such as violent feedbacks or gamma-ray bursts.

Organization of the thesis

Throughout this manuscript, I cover the different achievements in the range of fields of investigation I have come across.

The angle I address in the first part of the thesis is the analysis I have conducted using absorption spectroscopy (chapter 1). In this chapter, I present a sample of dense H I absorbers to which I have added a substantial contribution in terms of metallicity measurements. I present an innovative method to study dust depletion in those systems as well as hints for a bimodal distribution for the metallicity of their low-redshift counterpart, suggesting that sub-DLA metallicity might be a good tracer for gas dynamics within the CGM.

The second part of the manuscript is dedicated to the development of a balloon-borne experiment to observe the low-redshift CGM emission. After a general presentation of the FIREBall-2 project (chapter 2), I present my involvment on the measurements and characterization the grating, a key-component within the new FIREBall-2 optical design (chapter 3). I propose an experimental setup for UV polarized measurements of dense holographic gratings, and I propose and test a solution to improve the grating's efficiency by about 10%. In the last two chapters, I introduce the development of an end-to-end simulation of FIREBall-2 observations. In the one hand (chapter 4), I present the generation of mock cubes using a state-of-the-art hydrodynamical RAMSES simulation coupled with a model for CGM emission. On the other hand (chapter 5), I present an instrument model that reproduces the signal obtained on FIREBall's detector using an accurate optical model of FIREBall and I study the detectability of some example sources.

Part I.

Absorption

Chapter 1: The ESO UVES Advanced Data Products Quasar Sample

La jeunesse est l'âge où l'on passe à côté de tout.

Henry de Montherlant

I will now introduce my recently published work on damped Lyα absorbers (Quiret, Péroux, et al., 2016).

The ESO UVES Advanced Data Products Quasar Sample – VI. Sub-Damped Lyman-α Metallicity Measurements and the Circum-Galactic Medium

S. Quiret[a], C. Péroux[1], T. Zafar[2], V. P. Kulkarni[3], E. B. Jenkins[4], B. Milliard[1], H. Rahmani[1], A. Popping[5], S. M. Rao[6], D. A. Turnshek[6] and E. M. Monier[7]

[1]Aix Marseille Université, CNRS, LAM (Laboratoire d'Astrophysique de Marseille) UMR 7326, 13388, Marseille, France
[2]European Southern Observatory, Karl-Schwarschild-Strasse 2, 85748, Garching, Germany
[3]University of South Carolina, Dept. of Physics & Astronomy, Columbia, USA
[4]Princeton University Observatory, Princeton, NJ 08544-1001, USA
[5]International Centre for Radio Astronomy Research (ICRAR), The University of Western Australia, 35 Stirling Hwy, 6009 Crawley WA, Australia
[6]Department of Physics and Astronomy and PITTsburgh Particle physics, Astrophysics, and Cosmology Center (PITT PACC), University of Pittsburgh, Pittsburgh, PA 15260, USA
[7]Department of Physics, The College at Brockport, State University of New York, Brockport, NY 14420, USA

Accepted 2016 March 2. Received 2016 March 2; in original form 2015 June 26
MNRAS 458, 4074–4121 (2016) - Advance Access publication 2016 March 7
doi:10.1093/mnras/stw524

Abstract

The CGM can be probed through the analysis of absorbing systems in the line-of-sight to bright background quasars. We present measurements of the metallicity of a new sample of 15 sub-damped Lyman-α absorbers (sub-DLAs, defined as absorbers

with $19.0 < \log \mathrm{N(H\,I)} < 20.3$) with redshift $0.584 \leq \mathrm{z_{abs}} \leq 3.104$ from the ESO Ultra-Violet Echelle Spectrograph (UVES) Advanced Data Products Quasar Sample (EUADP). We combine these results with other measurements from the literature to produce a compilation of metallicity measurements for 92 sub-DLAs as well as a sample of 362 DLAs. We apply a multi-element analysis to quantify the amount of dust in these two classes of systems. We find that either the element depletion patterns in these systems differ from the Galactic depletion patterns or they have a different nucleosynthetic history than our own Galaxy. We propose a new method to derive the velocity width of absorption profiles, using the modeled Voigt profile features. The correlation between the velocity width $\Delta \mathrm{V_{90}}$ of the absorption profile and the metallicity is found to be tighter for DLAs than for sub-DLAs. We report hints of a bimodal distribution in the [Fe/H] metallicity of low redshift ($\mathrm{z} < 1.25$) sub-DLAs, which is unseen at higher redshifts. This feature can be interpreted as a signature from the metal-poor, accreting gas and the metal-rich, outflowing gas, both being traced by sub-DLAs at low redshifts.

1.1. Introduction

In depth studies of galaxy evolution require an understanding of the complex processes occurring at the interface of the galaxy and its nearby environment, the CGM.

On the one hand, the star formation process is believed to be fed in galaxies via accretion mechanisms (Rees et al., 1977; White et al., 1978; Prochaska and Wolfe, 2009; Bauermeister et al., 2010). For galaxies with masses typically below $\sim 10^{11-12}\mathrm{M_{\odot}}$, the accreting gas follows cold flows ($\mathrm{T} \sim 10^{4-5}\mathrm{K}$) while for more massive galaxies, a second mode of accretion appears, the "hot mode", where the gas is shock heated near the virial temperature ($\mathrm{T} \sim 10^{6}\mathrm{K}$) (Rees et al., 1977; Silk, 1977; White et al., 1978; Birnboim et al., 2003; Keres et al., 2005; Dekel et al., 2006; Ocvirk et al., 2008). Simulations show that about 40% of the accretion may be genuinely smooth (Genel et al., 2010). These modes also differ in metallicity (Fumagalli, Prochaska, et al., 2011; Shen et al., 2013). Indeed, Ocvirk et al., 2008 showed that the "cold mode" accreting gas can reach metallicities up to tenth solar, while the hot mode accreting gas metallicities are usually lower and are highly dependent on the distance to the center of the galaxy and on how well the gas is mixed. These accreting streams may also provide the galaxy with additional angular momentum (Fall et al., 1980). Observational evidences for accretion have been challenging to gather due to the low surface brightness and low filling factor of the infalling gas and its expected low metallicity. Nevertheless, cold accretion has been recently detected in a few objects (Steidel, Adelberger, et al., 2000; Martin, Shapley, et al., 2012; Rubin, Prochaska, Koo, and Phillips, 2012; Bouché et al., 2013b). Similarly, early evidences for cold accretion onto quasars have been recently reported by Cantalupo, Arrigoni-Battaia, et al., 2014 and Martin, Chang, Matuszewski, Morrissey, Rahman, Moore, and Steidel, 2014.

On the other hand, galaxies release energy and material in their environment (up to $\sim 125\mathrm{kpc}$) via supernovae (SNae), stellar winds or Active Galactic Nuclei (AGN) activity. These outflows tend to chemically enriched the IGM (Songaila et al., 1996; Simcoe

et al., 2004; Adelberger, Shapley, et al., 2005; Ryan-Weber et al., 2009; D'Odorico, Cupani, et al., 2013; Shull, Danforth, et al., 2014; Shull, Moloney, et al., 2015), and can regulate the star formation process of galaxies. Indeed, as the gas is released, it will starve the galaxy from fresh gas accreting along the galaxy major axis, quenching the star formation. It will also enhanced the star formation by cooling the gas via metal line emissions. Fountains can also be created if the gas does not leave the potential well of the galaxy. In this scenario, the fully metal enriched gas recycles and falls back onto the galactic disk and contribute directly to the star forming processes as it can cool efficiently. Simulations have shown that fountains dominate the global accretion mechanism for $\mathrm{z} \lesssim 1$ galaxies (Oppenheimer et al., 2010). Even though outflows are ubiquitous at all redshifts around star forming galaxies (Shapley et al., 2003; Martin, 2005; Rubin, Prochaska, Koo, Phillips, et al., 2014) and their existence is confirmed by signatures of OVI found within the CGM of low redshift star forming galaxies (Tumlinson et al., 2011), they remain poorly understood in the context of galaxy formation models.

In the context of emission line study, Bertone, Schaye, Booth, et al., 2010; Bertone, Schaye, Vecchia, et al., 2010 argued that the ionization state of elements provides valuable insight on the physical state of the CGM (mainly its temperature but also its ionizing process) and can be used to study the different feedback processes taking place, including metal pollution of accreting gas via galactic fountains. Fumagalli, Prochaska, et al., 2011 also argued that kinematic analysis of absorption lines can be used in addition to the metallicity analysis to distinguish metal-rich outflowing material from metal-poor ($\lesssim 0.01\mathrm{Z}_{\odot}$) accreting gas. Therefore, the study of metal lines (kinematics, line strengths, ionization states) might be the key diagnostic to observationally disentangle outflows from inflows and assess the level of metal enrichment of the CGM and thus galaxy evolution.

Absorbers observed in background quasar spectra are a tool to probe the low density gas and its metallicity. Indeed, simulations predict that cold accretion onto galaxies can be observed in absorption via dense H I absorbing systems with $\log \mathrm{N(H\,I)} > 15.5$ (Faucher-Giguere and Kereš, 2011; Voort, Schaye, et al., 2012; Shen et al., 2013). They predict that the cold streams could be traced with metal-poor H I absorption systems, mostly in the Lyman Limit System (LLS) range $17.2 \leq \log \mathrm{N(H\,I)} < 19.0$. Recently, Lehner, Howk, et al., 2013 showed observational evidence for low redshift LLS presenting a bimodal metallicity distribution, which they associated with infalls and outflows. However, the metallicities of LLS depend sensitively on model-dependent ionization corrections, since the LLS gas is highly ionized. This makes it harder to reliably detect the difference between inflows and outflows using the LLS. A more robust way of detecting the metallicity distribution of the gas around galaxies is by using the damped Lyman-α (DLA; $\log \mathrm{N(H\,I)} \geq 20.3$) and sub-damped Lyman-$\alpha$ (sub-DLA; $19.0 \leq \log \mathrm{N(H\,I)} < 20.3$) absorbers. These systems are the primary neutral gas reservoir at $0 < \mathrm{z} < 5$ (Storrie-Lombardi et al., 2000; Péroux et al., 2005; Prochaska, Herbert Fort, et al., 2005; Rao, Turnshek, and Nestor, 2006; Zafar, Péroux, et al., 2013) and offer the most precise element abundance measurements in distant galaxies. In particular, at $\mathrm{z} \leq 2$, Fumagalli, Prochaska, et al., 2011 anticipate that almost half of the cross-section in the sub-DLA H I column density range is due to streams, while at $\mathrm{z} \sim 3$, Voort, Schaye, et al., 2012 anticipate that it is more than 80%.

In an era of large quasar surveys, with samples of thousands of DLAs available (e.g.,

Noterdaeme, Petitjean, Carithers, et al., 2012), sub-DLAs remain little studied. Indeed, at low H I column densities, one requires a high spectral resolution and high signal to noise ratio (SNR) to derive element abundances. The large quasar samples observed with the high resolution spectrographs VLT/UVES (Zafar, Popping, et al., 2013) and Keck/HIRES (O'Meara et al., 2015) are therefore crucial tools for our understanding of sub-DLA properties. Here, we present a detailed study of the metallicity and kinematics of a large sample of DLAs and sub-DLAs observed at high resolution with UVES.

The paper is organised as follows. In §2 we present the data sample and in §3 we describe the abundance measurements. The results are discussed in §4 followed by conclusions in §5.

1.2. The Data

1.2.1. New absorbers

In order to put together a significant sample of sub-DLAs observed at high spectral resolution, we make use of the ESO UVES Advanced Data Products (EUADP) sample from Zafar, Popping, et al., 2013. This sample consists of 250 high-resolution ($\mathrm{R} \sim 42,000$) quasars spectra covering a total of 196 damped absorbers (with log $\mathrm{N(H\,I)} > 19.0$).

This dataset has motivated a number of studies including a report of new H I systems (Zafar, Popping, et al., 2013) and how they can be used to constrained the neutral gas mass density of sub-DLAs in particular (Zafar, Péroux, et al., 2013), the nucleosynthetic history of Nitrogen (Zafar, Centurion, et al., 2014) and the low Argon abundances observed in DLAs (Zafar, Vladilo, et al., 2014).

Most of the absorbers in the EUADP sample have their metallicity abundances published in the literature (Péroux, Kulkarni, Meiring, et al., 2006; Péroux, Meiring, Kulkarni, Ferlet, et al., 2006; Péroux, Meiring, Kulkarni, Khare, et al., 2008; Zafar, Péroux, et al., 2013, and reference therein). We present here the analysis of 14 new EUADP sub-DLAs covering a redshift range $0.584 \leq \mathrm{z_{abs}} \leq 3.104$. We also include 6 new DLAs for completeness. The measurements of HI column densities and redshifts of each system in the EUADP sample are reported in Zafar, Popping, et al., 2013 and references therein.

In addition to these 14 new sub-DLAs from the EUADP sample, we present the UVES spectra of two other systems: one sub-DLA at $\mathrm{z_{abs}} = 0.584$ and one DLA at $\mathrm{z_{abs}} = 0.647$. These two low-redshift absorbers have been observed with the HST ACS grism from which an estimate of their H I column densities has been derived (Turnshek, Monier, et al., 2015). The quasars were subsequently observed with UVES on VLT under the programme 91.A-0300 (PI: C. Péroux) in Service Mode in August and September 2013. Each object was observed using a combined 346+564 nm setting with two different observations with exposure times lasting 4500 + 3600 sec (QSO J0018−0913) and 2 x 4500 sec (QSO J0132−0823). The data were reduced using the most recent version of the UVES pipeline in MIDAS (uves/5.4.3). Master bias and flat images were constructed using calibration frames taken closest in time to the science frames. The science frames were extracted with the "optimal" option and corrected to the vacuum

heliocentric reference. To combine the resulting spectra, we choose to weight them by the signal-to-noise ratio, as for the remaining of the EUADP sample (Zafar, Popping, et al., 2013), in line with standard practice at this spectral resolution (O'Meara et al., 2015).

The absorption redshifts, which are based on the $\mathrm{N(H\,I)}$ or MgII features, are used to analyse the associated metal lines. Table 1.1 summarises the properties of the quasars and absorbers in the sample studied here. The two additional objects which were not originally published by Zafar, Popping, et al., 2013 are shown in bold.

1.2.2. Literature sample

In addition to these 15 new sub-DLA measurements (+7 DLAs), we gather metallicity estimates of sub-DLAs from the remaining part of the EUADP sample as well as other recently published samples (Meiring, Kulkarni, et al., 2006; Meiring, Lauroesch, Kulkarni, Péroux, Khare, and York, 2009; Dessauges-Zavadsky, Ellison, et al., 2009; Battisti et al., 2012; Som, Kulkarni, Meiring, York, Péroux, Lauroesch, et al., 2015). In order to compare the properties of sub-DLAs to that of DLAs, we add to the sample a collection of DLA metallicity measurements from the EUADP sample as well as from the literature (see earlier references and Berg, Ellison, Prochaska, et al. 2015). Altogether, this literature sample is the largest and most up-to-date sub-DLA sample published today.

The table in Appendix B.3 lists the metallicity estimates of the full sample of absorbers and associated references. Fig. 1.1 illustrates the distribution in redshift of the absorber sample studied for both DLAs and sub-DLAs (top and middle panels respectively). The bottom panel presents the N(H I) distribution of the sample. We stress that the additional systems are consistent with the parent sample as they are not selected on their metal content or redshift but solely on their H I column density (see also Fig. 1.5).

In conclusion, the final sample, referred to as the EUADP+ sample, contains 92 sub-DLAs (with 15 new measurements) and 362 DLAs (7 new measurements). Clearly, the data presented here contribute most in the sub-DLA H I column density range.

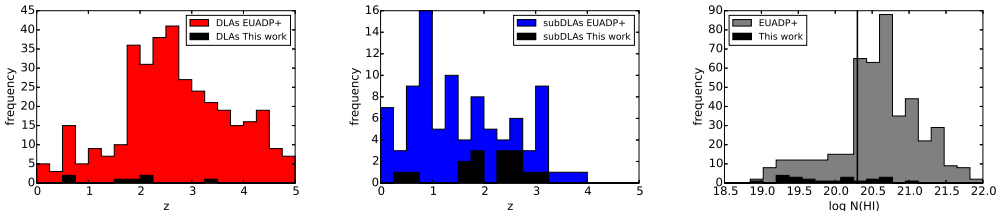

Figure 1.1.: Absorption redshifts and N(H I) distributions of the DLAs and sub-DLAs in our sample compared with the remaining absorbers covered by the EUADP survey and the literature (referred to as EUADP+ sample). The vertical line in the right panel indicates the canonical DLA definition. Clearly, the data presented here contribute most in the sub-DLA H I column density range at low redshift where few systems have been studied so far.

Table 1.1.: Properties of the 22 quasar absorbers (15 subDLAs and 7 DLAs) studied here. The majority of these absorbers are from the EUADP sample (Zafar, Popping, et al., 2013), but for the two systems shown in bold which have been observed recently with VLT/UVES by our group (see text for details).

QSO name	coordinates	z_{em}	z_{abs}	log(N(H I))	wavelength coverage (Å)
QSO J0008-2900	2.219-29.012	2.645	2.254	20.22 ± 0.10	3300-4970,5730-10420
QSO J0008-2901	2.24-29.024	2.607	2.491	19.94 ± 0.11	3300-4970,5730-10420
QSO J0018-0913	4.730-9.231	0.756	0.584	20.11 ± 0.10	3065-3875,4620-5602,5675-6650
QSO J0041-4936	10.381-49.603	3.24	2.248	20.46 ± 0.13	3290-4520,4620-5600,5675-6650
QSO B0128-2150	22.773-21.58	1.9	1.857	20.21 ± 0.09	3045-3868,4785-5755,5830-6810
QSO J0132-0823	23.041-8.397	1.121	0.647	20.60 ± 0.12	3065-3875,4620-5602,5675-6650
QSO B0307-195B	47.538-19.369	2.122	1.788	19.00 ± 0.10	3065-5758,5835-8520,8660-10420
QSO J0427-1302	66.78-13.048	2.166	1.562	19.35 ± 0.10	3285-4515,4780-5760,5835-6810
PKS 0454-220	74.037-21.986	0.534	0.474	19.45 ± 0.03	3050-3870,4170-5162,5230-6210
J060008.1-504036	90.033-50.677	3.13	2.149	20.40 ± 0.12	3300-4520,4620-5600,5675-6650
QSO B1036-2257	159.79-23.224	3.13	2.533	19.30 ± 0.10	3300-5758,5838-8525,8660-10420
J115538.6+053050	178.911+5.514	3.475	3.327	21.00 ± 0.10	3300-5600,5675-7500,7665-9460
LBQS 1232+0815	188.656+7.979	2.57	1.720	19.48 ± 0.13	3285-4520,4620-5600,5675-6650
QSO J1330-2522	202.717-25.372	3.91	2.654	19.56 ± 0.13	3300-4515,4780-5757,5835-6810
QSO J1356-1101	209.195-11.025	3.006	2.397	19.85 ± 0.08	3757-4985,6700-8520,8660-10420
QSO J1621-0042	245.32-0.714	3.7	3.104	19.70 ± 0.20	3300-4515,4780-5757,5835-6810
4C 12.59	247.938+11.934	1.792	0.531	20.70 ± 0.09	3060-3870,4780-5757,5835-6810
LBQS 2114-4347	319.331-43.573	2.04	1.912	19.50 ± 0.10	3050-10420
QSO B2126-15	322.3-15.645	3.268	2.638	19.25 ± 0.15	3300-5600,5675-6650,6695-8520,
...	...	...	2.769	19.20 ± 0.15	8650-10420
LBQS 2132-4321	324.025-43.138	2.42	1.916	20.74 ± 0.09	3290-4530,4620-5600,5675-6650
QSO B2318-1107	350.369-10.856	2.96	1.629	20.52 ± 0.14	3050-4515,4780-5760,5840-6810

1.3. Analysis

1.3.1. Method

The continua of the quasar spectra are fitted using a spline function connecting the regions of the spectrum free from absorption features as described in Zafar, Péroux, et al. (2013). The Voigt profile fits are performed with the FIT/LYMAN package within the MIDAS environment (Fontana et al., 1995). The routine calculates a χ^2 Hessian minimization and enables fits of up to 50 free parameters including the central wavelength, the column density and the Doppler parameter of each component of the fit. This allows fitting several ions simultaneously as well as several transitions of the same species, thus making maximum use of the information available from the velocity profiles. The low-ionization species (OI, FeII, SiII, ...) are fitted as a separate group from the high-ionization species (CIV, SiIV, ...) (e.g., Wolfe, Gawiser, et al., 2005; Fox, Petitjean, et al., 2007; Milutinovic et al., 2010; Crighton, Hennawi, and Prochaska, 2013). The intermediate-ionization species AlIII are fitted either on its own, or with the low-ionization or high-ionization species, depending on the similarity in the absorption velocity profiles.

This process allows us to identify possible blends of interloping absorbers at the positions of the features under study. In case of blending, the profiles are fitted using information on central wavelengths and Doppler parameters from other un-blended profiles, thus leading to upper limits in the column density determination. In addition, saturated transitions or components are avoided because the column density information cannot be recovered in that case. The quasar continuum solution is iteratively refined when necessary during the Voigt profile fitting process. The fits are performed minimizing the number of components. In cases where a transition is not detected, we derive a 3-σ upper limit from an estimate of the SNR of the spectra at the expected position of the line. The laboratory wavelengths and oscillator strengths used throughout the fits are taken from Morton, 2003[a].

We estimate the abundance for various elements of each absorbing system by summing the column densities of the different components found in the velocity profile described above. The metallicity $[\mathrm{X/H}]$ of an element X with respect to solar metallicity is derived from the following expression:

$$[\mathrm{X/H}] = \log\left(\frac{\mathrm{N(X)}}{\mathrm{N(H)}}\right) - \log(\mathrm{X/H})_{\odot} \tag{1.1}$$

where $(\mathrm{X/H})_{\odot}$ is the photospheric solar abundance from Asplund et al., 2009 and $\mathrm{N(X)}$ is the column density of element X. The column density of each element is taken to be that of the dominant ion, and ionization correction is ignored here (see section 1.3.2 for further discussion on this point). The error estimate on the total column density $\log \mathrm{N}$ is

[a] Recently, a new set of oscillator strengths for SII and ZnII lines has been derived for studies of the Inter-Stellar Medium (ISM), DLAs and sub-DLAs (Kisielius, Kulkarni, Ferland, Bogdanovich, and Lykins, 2014; Kisielius, Kulkarni, Ferland, Bogdanovich, Som, et al., 2015). A change from Morton, 2003 oscillator strengths to this new study would lower [Zn/H] by about 0.1 dex.

calculated from the error on individual column density $\log \mathrm{N}$ of each component through the error propagation formula:

$$\sigma_{\log(\mathrm{N(X)})} = \frac{\sqrt{\sum_{\mathrm{i}} (\mathrm{N(X)_i} \sigma_{\log(\mathrm{N(X)})_\mathrm{i}})^2}}{\mathrm{N(X)}} \tag{1.2}$$

The global uncertainty on the abundance determination is then calculated from a quadratic sum of $\sigma_{\log(\mathrm{N(X)})}$ and $\sigma_{\log(\mathrm{N(H)})}$ since the errors in the solar abundances would introduce systematic effects which can be neglected in studies of relative abundances.

The resulting Voigt profile parameters and corresponding velocity plots for the low-, intermediate- and high-ionization species as well as a detailed description of the 22 individual systems mentioned earlier are provided in Appendix B.2. The column densities and abundances derived for these systems are gathered in tables 1.2 (for total column densities) and 1.3 (for abundances).

For the different H I and metals column densities presented in this paper, the associated error on the abundances are based on χ^2 minimization. The continuum placement error is not taken into account to be consistent with other measurements from the literature.

1.3.2. The Ionized Fraction of sub-DLAs

Given that observationally we are sensitive to the neutral gas in quasar absorbers, it is important to quantify the fraction of gas ionized in these systems. In the DLA column density range, the ionization corrections are below the typical abundance measurement errors (Vladilo, Centurion, et al., 2001; Dessauges-Zavadsky, Péroux, et al., 2003).

The situation might differ in the sub-DLA H I column density range given that the lower N(H I) might prevent complete self-shielding from the surrounding UV background. To address this issue, Dessauges-Zavadsky, Péroux, et al., 2003; Meiring, Lauroesch, Kulkarni, Péroux, Khare, York, and Crotts, 2007; Meiring, Lauroesch, Kulkarni, Péroux, Khare, and York, 2009; Som, Kulkarni, Meiring, York, Péroux, Khare, et al., 2013; Som, Kulkarni, Meiring, York, Péroux, Lauroesch, et al., 2015 among others studied the ionized fraction of sub-DLAs based on photo-ionization CLOUDY modeling of individual systems. These studies show that the ionized fraction of hydrogen varies greatly within the sub-DLA H I column density range (see e.g. Fig 4 of Meiring, Lauroesch, Kulkarni, Péroux, Khare, and York 2009 and Fig. 10 of Lehner, O'Meara, Fox, et al. 2014). Nevertheless, while sub-DLAs might have an important fraction of their gas ionized in some cases, the ionization corrections to the measured abundances for sub-DLAs are often low. The large majority of elements require an ionization correction $\epsilon < 0.3$ dex, while it is negligible for FeII but important for ZnII (Dessauges-Zavadsky, Péroux, et al., 2003). Based on these past results and in order to be in line with abundance measurements from the literature reported here, we choose not to apply ionization correction to the new abundances presented. A more statistical approach is now required. To this end, Fumagalli, O'Meara, et al., 2016 have recently built CLOUDY model grids to establish posterior probability distribution functions for different states of the gas with a Bayesian formalism and Markov Chain Monte Carlo algorithm. While such an analysis is beyond the scope of the current paper, we plan to address these issues in further publications.

Table 1.2.: Total logarithmic column densities of the newly studied systems derived from the Voigt profile fits. In column N(X), (a) refers to ArI, (b) to OI, (c) to NI, (d) to TiII, (e) to CI, and (f) to CII. For PKS 0454-220, the abundances with the asterisk have been derived by Som et al. 2015.

QSO	z_{abs}	**N(HI)**	**N(SII)**	**N(AlII)**	**N(SiII)**	**N(CrII)**	**N(MgI)**	**N(MgII)**
QSO J0008-2900	2.254	20.22 ± 0.1	-	-	< 14.40	< 12.37	-	> 15.01
QSO J0008-2901	2.491	19.94 ± 0.11	13.68 ± 0.18	-	-	< 12.90	-	-
QSO J0018-0913	0.584	20.11 ± 0.1	-	-	-	< 12.97	< 13.04	-
QSO J0041-4936	2.248	20.46 ± 0.13	< 14.82	> 14.06	14.78 ± 0.03	13.12 ± 0.45	-	-
QSO B0128-2150	1.857	20.21 ± 0.09	14.33 ± 0.03	-	14.82 ± 0.02	-	< 13.21	-
QSO J0132-0823	0.647	20.60 ± 0.12	-	-	-	< 13.17	12.60 ± 0.04	-
QSO B0307-195B	1.788	19.00 ± 0.10	-	-	15.00 ± 0.01	< 12.77	12.54 ± 0.00	-
QSO J0427-1302	1.562	19.35 ± 0.10	-	11.78 ± 0.10	-	< 12.39	< 12.38	-
PKS 0454-220	0.474	19.45 ± 0.03	$15.06 \pm 0.04^{*}$	-	$> 14.33^{*}$	-	-	-
J060008.1-504036	2.149	20.40 ± 0.12	-	> 14.33	15.08 ± 0.01	13.10 ± 0.01	-	-
QSO B1036-2257	2.533	19.30 ± 0.1	-	12.52 ± 0.01	13.64 ± 0.01	< 12.54	-	13.57 ± 0.02
J115538.6+053050	3.327	21.00 ± 0.1	15.31 ± 0.01	-	15.93 ± 0.01	-	< 13.33	-
LBQS 1232+0815	1.720	19.48 ± 0.13	< 14.19	-	14.41 ± 0.01	< 12.38	< 12.21	-
QSO J1330-2522	2.654	19.56 ± 0.13	-	12.18 ± 0.02	-	-	-	-
QSO J1356-1101	2.397	19.85 ± 0.08	-	-	-	< 12.64	-	-
QSO J1621-0042	3.104	19.70 ± 0.2	-	-	13.78 ± 0.03	-	-	-
4C 12.59	0.531	20.70 ± 0.09	-	-	-	-	-	-
LBQS 2114-4347	1.912	19.50 ± 0.10	< 13.97	13.00 ± 0.01	14.39 ± 0.02	< 12.77	-	14.40 ± 0.01
QSO B2126-15	2.638	19.25 ± 0.15	-	-	14.67 ± 0.02	-	-	-
QSO B2126-15	2.769	19.20 ± 0.15	-	> 14.04	14.79 ± 0.01	< 12.40	-	-
LBQS 2132-4321	1.916	20.74 ± 0.09	> 14.90	-	15.55 ± 0.01	13.32 ± 0.02	-	-
QSO B2318-1107	1.629	20.52 ± 0.14	< 14.54	< 14.93	-	< 12.47	< 12.37	-

QSO	**N(FeII)**	**N(NiII)**	**N(ZnII)**	**N(AlIII)**	**N(SiIV)**	**N(CIV)**	**N(MnII)**	**N(X)**
QSO J0008-2900	13.78 ± 0.01	-	< 11.68	12.39 ± 0.04	13.72 ± 0.03	-	< 12.02	$< 13.07^{(a)}$
QSO J0008-2901	13.65 ± 0.02	< 13.29	< 12.12	< 12.20	-	-	-	$15.31 \pm 0.24^{(b)}$
QSO J0018-0913	13.87 ± 0.03	-	< 12.41	-	-	-	-	-
QSO J0041-4936	14.43 ± 0.04	13.07 ± 0.07	11.70 ± 0.10	12.90 ± 0.01	-	> 14.56	-	$14.03 \pm 0.03^{(c)}$
QSO B0128-2150	14.44 ± 0.01	13.26 ± 0.05	< 12.26	12.78 ± 0.01	-	-	-	-
QSO J0132-0823	14.96 ± 0.07	-	-	-	-	-	-	$12.39 \pm 0.11^{(d)}$
QSO B0307-195B	14.48 ± 0.00	< 13.22	< 12.18	-	> 14.55	> 15.13	< 12.13	-
QSO J0427-1302	12.23 ± 0.04	< 13.23	< 11.75	-	13.90 ± 0.07	-	< 11.84	-
PKS 0454-220	14.71 ± 0.01	$13.69 \pm 0.08^{*}$	-	-	-	-	12.58 ± 0.01	-
J060008.1-504036	14.84 ± 0.03	13.62 ± 0.02	12.11 ± 0.03	12.78 ± 0.01	-	-	-	$< 12.5^{(e)}$
QSO B1036-2257	12.93 ± 0.01	< 12.93	< 11.74	-	13.71 ± 0.01	> 17.42	-	-
J115538.6+053050	-	13.74 ± 0.01	-	13.12 ± 0.01	13.56 ± 0.01	13.71 ± 0.01	-	-
LBQS 1232+0815	13.50 ± 0.01	< 13.05	< 11.58	13.28 ± 0.01	> 14.67	-	-	-
QSO J1330-2522	-	< 13.22	-	12.62 ± 0.02	-	-	-	-
QSO J1356-1101	13.44 ± 0.01	< 12.76	< 12.38	-	-	-	< 12.07	-
QSO J1621-0042	13.30 ± 0.04	-	-	-	14.24 ± 0.03	14.71 ± 0.01	-	$< 14.41^{(f)}$
4C 12.59	14.26 ± 0.08	-	-	-	-	-	-	-
LBQS 2114-4347	14.02 ± 0.01	< 12.88	< 12.17	< 12.09	13.43 ± 0.01	14.39 ± 0.01	< 12.24	-
QSO B2126-15	14.05 ± 0.01	13.15 ± 0.01	< 11.58	13.24 ± 0.02	-	-	-	-
QSO B2126-15	14.17 ± 0.00	-	< 11.95	13.11 ± 0.01	13.84 ± 0.13	-	< 12.28	-
LBQS 2132-4321	15.03 ± 0.02	13.77 ± 0.02	12.66 ± 0.02	13.25 ± 0.01	14.20 ± 0.01	-	-	-
QSO B2318-1107	14.14 ± 0.02	-	< 11.74	12.17 ± 0.02	-	< 14.10	11.78 ± 0.04	-

Table 1.3.: Abundances with respect to solar for the 22 systems studied in this work. In column [X/H], (a) refers to Ar, (b) refers to O, (c) refers to N and (d) refers to C. For PKS 0454-220, the metallicities with the asterisk have been derived by Som, Kulkarni, Meiring, York, Péroux, Lauroesch, et al. 2015

QSO	z_{abs}	**log** N(H I)	**[S/H]**	**[Al/H]**	**[Si/H]**	**[Cr/H]**
QSO J0008-2900	2.254	20.22 ± 0.10	-	-	< -1.33	< -1.49
QSO J0008-2901	2.491	19.94 ± 0.11	-1.38 ± 0.21	-	-	< -0.68
QSO J0018-0913	0.584	20.11 ± 0.10	-	-	-	< -0.78
QSO J0041-4936	2.248	20.46 ± 0.13	< -0.75	> -0.85	-1.19 ± 0.16	-0.98 ± 0.58
QSO B0128-2150	1.857	20.21 ± 0.09	-1.00 ± 0.09	-	-0.90 ± 0.09	-
QSO J0132-0823	0.647	20.60 ± 0.12	-	-	-	< -1.07
QSO B0307-195B	1.788	19.00 ± 0.10	-	-	0.49 ± 0.10	< 0.13
QSO J0427-1302	1.562	19.35 ± 0.10	-	-2.02 ± 0.14	-	< -0.60
PKS 0454-220	0.474	19.45 ± 0.03	$0.49 \pm 0.04^{*}$	-	$> -0.78^{*}$	-
J060008.1-504036	2.149	20.40 ± 0.12	-	> -0.52	-0.83 ± 0.12	-0.94 ± 0.12
QSO B1036-2257	2.533	19.30 ± 0.10	-	-1.24 ± 0.10	-1.17 ± 0.10	< -0.40
J115538.6+053050	3.327	21.00 ± 0.10	-0.81 ± 0.10	-	-0.58 ± 0.10	-
LBQS 1232+0815	1.720	19.48 ± 0.13	< -0.41	-	-0.58 ± 0.13	< -0.74
QSO J1330-2522	2.654	19.56 ± 0.13	-	-1.83 ± 0.13	-	-
QSO J1356-1101	2.397	19.85 ± 0.08	-	-	-	< -0.85
QSO J1621-0042	3.104	19.70 ± 0.20	-	-	-1.43 ± 0.20	-
4C 12.59	0.531	20.70 ± 0.09	-	-	-	-
LBQS 2114-4347	1.912	19.50 ± 0.10	< -0.65	-0.95 ± 0.10	-0.62 ± 0.10	< -0.37
QSO B2126-15	2.638	19.25 ± 0.15	-	-	-0.09 ± 0.15	-
QSO B2126-15	2.769	19.20 ± 0.15	-	> 0.39	0.08 ± 0.15	< -0.44
LBQS 2132-4321	1.916	20.74 ± 0.09	> -0.96	-	-0.70 ± 0.10	-1.06 ± 0.11
QSO B2318-1107	1.629	20.52 ± 0.14	< -1.10	< -0.04	-	< -1.69

QSO	**[Fe/H]**	**[Ni/H]**	**[Zn/H]**	**[Mg/H]**	**[Mn/H]**	**[X/H]**
QSO J0008-2900	-1.94 ± 0.10	-	< -1.10	> -0.81	< -1.63	$< -1.55^{(a)}$
QSO J0008-2901	-1.79 ± 0.13	< -0.87	< -0.38	-	-	$-1.32 \pm 0.35^{(b)}$
QSO J0018-0913	-1.74 ± 0.10	-	< -0.26	-	-	-
QSO J0041-4936	-1.54 ± 0.14	-1.61 ± 0.20	-1.32 ± 0.16	-	-	$-2.36 \pm 0.13^{(c)}$
QSO B0128-2150	-1.27 ± 0.09	-1.17 ± 0.10	< -0.51	-	-	-
QSO J0132-0823	-1.06 ± 0.12	-1.00 ± 0.12	-0.85 ± 0.12	-	-	-
QSO B0307-195B	-0.02 ± 0.10	< 0.00	< 0.62	-	< -0.30	-
QSO J0427-1302	-2.62 ± 0.11	< -0.34	< -0.16	-	< -0.94	-
PKS 0454-220	-0.24 ± 0.03	$0.02 \pm 0.09^{*}$	-	-	-0.30 ± 0.03	$-1.34 \pm 0.09^{*(c)}$
J060008.1-504036	-1.14 ± 0.14	-	-	-	-	-
QSO B1036-2257	-1.87 ± 0.10	< -0.59	< -0.12	-1.33 ± 0.10	-	-
J115538.6+053050	-	-1.48 ± 0.10	-	-	-	-
LBQS 1232+0815	-1.48 ± 0.13	< -0.65	< -0.46	-	-	-
QSO J1330-2522	-	< -0.56	-	-	-	-
QSO J1356-1101	-1.91 ± 0.08	< -1.31	< -0.03	-	< -1.21	-
QSO J1621-0042	-1.90 ± 0.20	-	-	-	-	$< -1.72^{(d)}$
4C 12.59	-1.94 ± 0.12	-	-	-	-	$-5.77^{(d)}$
LBQS 2114-4347	-0.98 ± 0.10	< -0.84	< 0.11	-0.70 ± 0.10	< -0.69	-
QSO B2126-15	-0.70 ± 0.15	-0.32 ± 0.15	< -0.23	-	-	-
QSO B2126-15	-0.53 ± 0.15	-	< 0.19	-	< -0.35	-
LBQS 2132-4321	-1.21 ± 0.11	-1.19 ± 0.11	-0.64 ± 0.11	-	-	-
QSO B2318-1107	-1.88 ± 0.14	-	< -1.34	-	-2.17 ± 0.15	-

1.3.3. Assessing the Dust-Content of Quasar Absorbers: a Multi-Element Analysis

Refractory elements are easily incorporated onto dust (e.g. Fe, Cr, Ni), while volatile elements are less prone to locking up into dust grains (e.g. Zn, S). To estimate the level of depletion of a given line of sight, it is possible to compare the abundance of a volatile element with that of a refractive element. The quantity $[\mathrm{Zn/Fe}]$ is therefore an excellent tool to probe the quantity of Fe atoms locked into dust (Vladilo, 1998). Indeed, Zn is thought to behave like Fe in different stages of chemical evolution, excluding the effects of dust depletion. From studies of low metallicity stars in our Galaxy, (Saito et al., 2009; Barbuy et al., 2015), [Zn/Fe] stays steady at $[\mathrm{Zn/Fe}] \sim 0$ down to metallicities $[\mathrm{Fe/H}] = -3$ and then increases for lower values of [Fe/H]. Hence, $[\mathrm{Zn/H}]$ provides a robust metallicity indicator. Unfortunately, its low cosmic abundance and long rest-frame wavelengths make it challenging to measure in sub-DLAs, preventing from a robust dust-metallicity derivation.

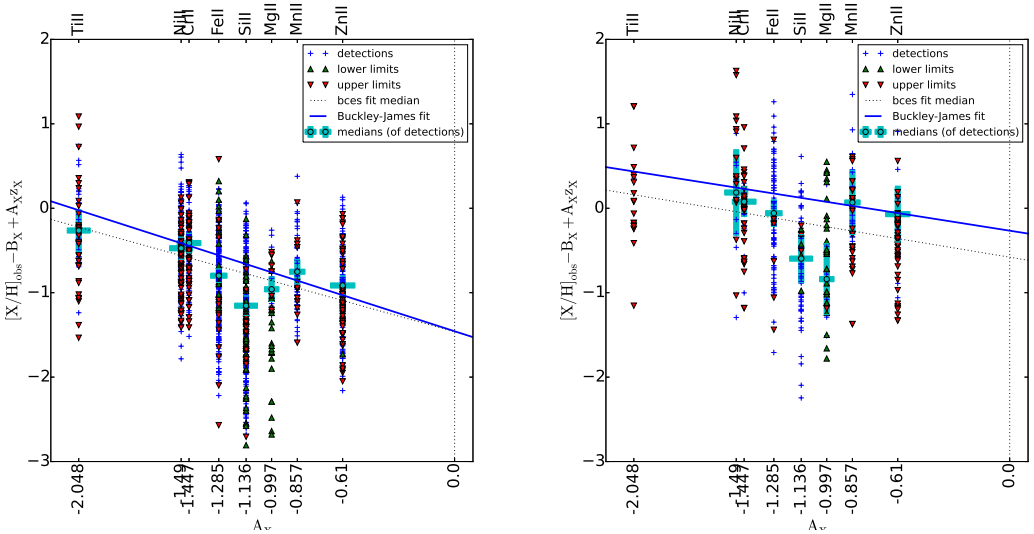

Figure 1.2.: Fits of F_* from equation B.5 for the DLAs (362 systems, left panel), and sub-DLAs (92 systems, right panel) in the EUADP+ sample. The blue crosses stand for the detections, the red triangles for the upper limits, the green triangles for lower lower limits, and the cyan points are the median of the detections for each element X. The fits are performed on the medians of the detections with a bisector fit (dashed line), and on the detections and the limits using a survival analysis technique, the Buckley-James method (solid line). We note that the α-elements (Mg and Si) are below the trend lines for both DLAs and sub-DLAs. We refer the reader to Appendix B.1.1 for a mathematical description of the fit.

Here, we propose a different approach for the study of dust depletion based on the

multi-element analysis proposed by Jenkins, 2009 to assess the level of dust in a given line of sight. Jenkins, 2009 proposed to use the abundances of different elements (namely C, N, O, Mg, Si, P, Cl, Ti, Cr, Mn, Fe, Ni, Cu, Zn, Ge, Kr and S) to compare the dust depletion of dense neutral hydrogen systems to that of the Interstellar Medium (ISM) of our Galaxy. Using a sample of 243 sight lines in our Galaxy, he established a connection between the line of sight depletion factor F_* and the different elements' abundances of each sight line. We refer the reader to Appendix B.1.1 for a mathematical description of the method.

Fig. 1.2 shows the fit for the line of sight depletion factor F_* (slope) for both populations of quasar absorbers from the EUADP+ sample. For each element, we plot in cyan the median of the detections if there is at least 4 systems measured. The vertical error bars represent the error on the median using a bootstrap technique with a confidence level of 95%.

We are confronted with a large number of non-detections, creating a bias in the sample towards metal-rich systems. A large fraction of these upper (resp. lower) limits falls below (resp. above) the associated median. To address this issue, a survival analysis is considered. A Buckley-James linear regression, from the stsdas.statistics package in IRAF, results in $\mathrm{F}_* = -0.34 \pm 0.19$ for sub-DLAs and $\mathrm{F}_* = -0.70 \pm 0.06$ for DLAs.

On the one hand, both populations show negative values for F_*, suggesting that sub-DLAs and DLAs arise in galaxies with a lower dust content than the Milky Way. On the other hand, the derived F_* values for both populations are different at the 1.8 σ level. The sub-DLA population is consistent with the Halo like ISM from our Galaxy[b] while the DLAs are described by an F_* value well below the ones measured in the Milky Way. This is counter intuitive as we expect DLAs to be self-shielded from the UV background towards the center of the galaxy. Indeed, numerous cosmological simulations predict DLAs to be closer to the center of the galaxy than sub-DLAs (Fumagalli, Prochaska, et al., 2011; Faucher-Giguere, Hopkins, et al., 2015). They should therefore exhibit an F_* value corresponding to regions within the halo.

But DLAs and sub-DLAs might not be systematically associated with spiral galaxies. They might arise from a mixture of galaxy types, hence the non-physical values of F_*. In addition, the method described here is based on measurements in our Galaxy at log $\mathrm{N(H\,I)} > 19.5$ to limit photo-ionization effects, while our quasar absorber sample goes down to $\log \mathrm{N(H\,I)} = 19.0$. Furthermore, the ionization levels of the sub-DLAs and DLAs in our EUADP+ sample are higher than in the Milky Way ISM, as F_* is quite different between ionized and neutral gas ($\mathrm{F}_* = -0.1$ for the warm ionized medium and $\mathrm{F}_* = 0.1$ for the warm neutral medium, e.g. Draine, 2011). We derive F_* for log $\mathrm{N(H\,I)} > 19.5$ sub-DLAs, and find similar results, suggesting that ionization effects do not affect the results much. Moreover, the quasar absorbers trace gas at high redshifts, which may differ from the Milky Way properties as a local galaxy. Overall, these results suggest that quasar absorbers differ from the Galactic depletion patterns or alternatively have a different nucleosynthetic history.

Also, the current QSO sample may suffer from dust selection bias. Indeed, it is

[b] $\mathrm{F}_* = -0.28$ for *Halo* like ISM, $\mathrm{F}_* = -0.08$ for *Disk+Halo* like ISM, $\mathrm{F}_* = 0.12$ for *Warm Disk* like ISM and $\mathrm{F}_* = 0.90$ for *Cool Disk* like ISM

possible that quasars in the background of dusty absorbers are not being accounted for in current selection techniques (Boissé et al., 1998). Programs to observe reddened quasars might bring valuable insights to the dust content of quasar absorbers (Maddox et al., 2012; Krogager, Geier, et al., 2015; Krogager, Fynbo, Noterdaeme, et al., 2016). Using the analysis from Vladilo, Centurión, et al., 2006[c], we recover estimates for the average extinction in our quasar absorber samples to be below 0.01, in line with results from Frank and Péroux, 2010 or Khare, Vanden Berk, et al., 2012. This suggests that the dust reddening is not observed in the current quasar selection.

Given these limitations, we do not apply dust corrections to the measured abundances. There is work underway (Tchernyshyov et al., 2015) to derive the parameters $\mathrm{A_X}$, $\mathrm{B_X}$ and $\mathrm{z_X}$ for the Small Magellanic Cloud, which is more in line with the expected morphological type or $\mathrm{H_2}$ fraction of DLAs.

1.3.4. α-elements

The production of α-elements (O, N, Mg, Si, S, Ti, Ca...) and Fe-peak elements (V, Cr, Mn, Fe, Co, Ni...) has different origins in the history of star formation. α-elements are mainly created during core-collapse Type II supernovae (SNe), whereas Fe-peak elements originate mainly from thermonuclear Type Ia SNe. These two processes have different time scales, as they originate from distinct stellar populations: the Type II SNe occur from short-lived massive stars while Type Ia SNe are thought to involve binary pairs containing a white dwarf exchanging material over longer periods of time. Observations of different objects suggest an excess of α-elements with respect to Fe-peak elements (from Wallerstein, 1962 for G-dwarf stars, to Timmes et al., 1995 for QSO absorption line systems and Rafelski, Wolfe, et al., 2012 for DLAs).

In Fig. 1.3, we plot $[\alpha/\mathrm{Fe}]$ versus metallicity using α = OI, SII, MgII and SiII for the sub-DLA (blue) and DLA (red) populations.

We observe a correlation between $[\alpha/\mathrm{Fe}]$ and $[\alpha/\mathrm{H}]$ for sub-DLAs. A Spearman test gives $\rho_{\mathrm{sub-DLA}} = 0.69$ with a probability of no correlation $\mathrm{P}(\rho_{\mathrm{sub-DLA}}) < 10^{-7}$. This correlation spans from low- to high-metallicity systems. The total number of DLA detections adds up to 227 systems. We do not see a flattening for DLAs with $[\alpha/\mathrm{H}] < -1$ as in Rafelski, Wolfe, et al., 2012, who attributed this flattening to the fact that the offsets in $[\alpha/\mathrm{Fe}]$ values for $[\alpha/\mathrm{H}] < -1$ are the effect of α-enhancement only. To avoid any dust extinction effects, we consider the 80 DLAs with $[\alpha/\mathrm{H}] < -1.5$ to derive a correction for α-enhancement for the EUADP+ DLAs (De Cia et al., 2013). We note that these systems might still be affected by dust depletion, as a trend is still visible between $[\alpha/\mathrm{Fe}]$ and $[\alpha/\mathrm{H}]$, even for $[\alpha/\mathrm{H}]$ down to -3 dex. We derive a mean value of $[\alpha/\mathrm{Fe}] = 0.32 \pm 0.18$ using 80 DLAs with $[\alpha/\mathrm{H}] < -1.5$, which is consistent with the value found by Rafelski, Wolfe, et al., 2012.

[c] see Appendix B.1.2 for details of the calculation

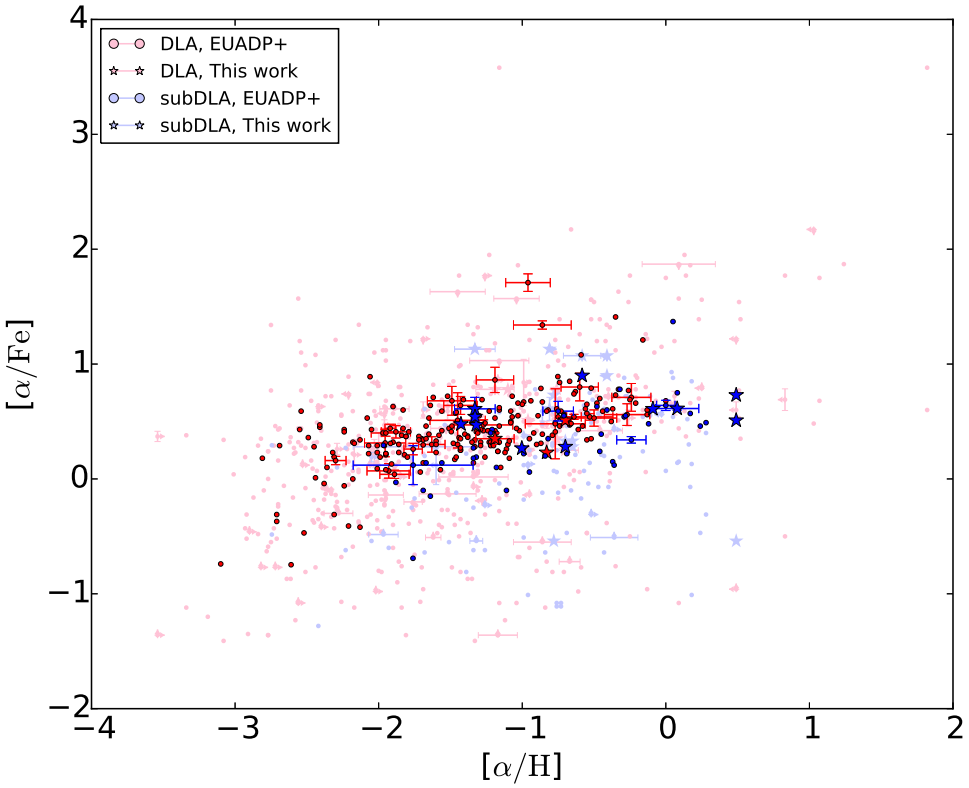

Figure 1.3.: The α-enhancement of DLAs (red) and sub-DLAs (blue) versus metallicity, $[\alpha/\mathrm{Fe}]$ versus $[\alpha/\mathrm{H}]$, with $\alpha =$ OI, SII or SiII. For clarity, only one in ten data point displays error bars and the limits have faint colors.

DLAs and sub-DLAs may have different nucleosynthetic histories, as they may originate from galaxies of different masses (Khare, Kulkarni, et al., 2007; Kulkarni, Khare, Som, et al., 2010) and hence experience different star formation rates. Indeed, different [Mn/Fe] vs. [Zn/H] trends for DLAs and sub-DLAs suggest different nucleosynthetic histories for the two populations (Meiring, Lauroesch, Kulkarni, Péroux, Khare, York, and Crotts, 2007; Som, Kulkarni, Meiring, York, Péroux, Lauroesch, et al., 2015). Therefore, one expects their α-enhancement to be statistically different and probably higher for sub-DLAs, which may experience higher star formation rates. In Fig. 1.3, there is no apparent plateau for sub-DLAs, probably due to the small number of detections at low metallicities. More observations of sub-DLAs are needed to obtain more definitive conclusions in this H I column density regime. Nevertheless, to address the question of α-enhancement for sub-DLAs at least partly, we make use of the value derived for DLAs. These corrections add 0.32 ± 0.18 dex to every metallicity derived using element Fe. This doesn't include a correction for dust extinction.

We emphasize that such a trend of $[\alpha/\mathrm{Fe}]$ versus $[\alpha/\mathrm{H}]$ in DLAs/sub-DLAs does not

necessarily imply nucleosynthetic α-enhancement. This is because of the increasing dust depletion of Fe with increasing metallicity, a trend that is seen to hold even at metallicities below -1 dex. $[\alpha/\mathrm{Zn}]$ is indeed less prone to depletion than $[\alpha/\mathrm{Fe}]$, but our current sub-DLA sample has only a limited number of Zn detections (19/92). Additional Zn observations in the future will help address this question better.

1.4. Results

1.4.1. Evolution of metals with redshift

Together, DLA and sub-DLA populations contain the majority of the neutral gas mass in the Universe (Zafar, Péroux, et al., 2013). Therefore, they present a valuable tool to estimate the cosmic metallicity throughout the ages. Models of cosmic chemical evolution claim that the global interstellar metallicity would rise with decreasing redshift, to reach near solar metallicity values at present day (Lanzetta et al., 1995; Pei and Fall, 1995; Malaney et al., 1996; Pei, Fall, and Hauser, 1999; Tissera et al., 2001). Sub-DLAs in particular contribute substantially to the cosmic metal budget. Indeed, Kulkarni, Khare, Péroux, et al., 2007 show that the contribution of sub-DLAs to the metal budget increases with decreasing redshift considering a constant relative H I gas in DLAs and sub-DLAs at low and high redshifts. Bouché, Murphy, Péroux, et al., 2007 anticipate that $\lesssim 17$ per cent of the metals are in sub-DLAs at $\mathrm{z} \sim 2.5$ but this estimate is highly dependent on the ionized fraction of the gas. It is therefore highly important to compare sub-DLA metallicities with those of DLAs. Our study adds 15 new measurements of sub-DLA metallicity. We chose to use ZnII as our main metallicity indicator (Pettini, Smith, Hunstead, et al., 1994) as it is nearly undepleted onto interstellar dust. Moreover, ZnII lines are usually unsaturated, and since ZnII is the dominant ionization state in neutral regions, it does not require strong ionization correction. However, Zn has an overall low cosmic abundance and the stronger lines $\lambda\lambda$ 2026 and 2062 can be blended with MgI λ 2026 and CrII λ 2062. When these ZnII lines are undetected, we use the dominant ions of other elements in the following order: OI, SII, SiII, MgII, FeII (corrected for the α analysis) and NiII.

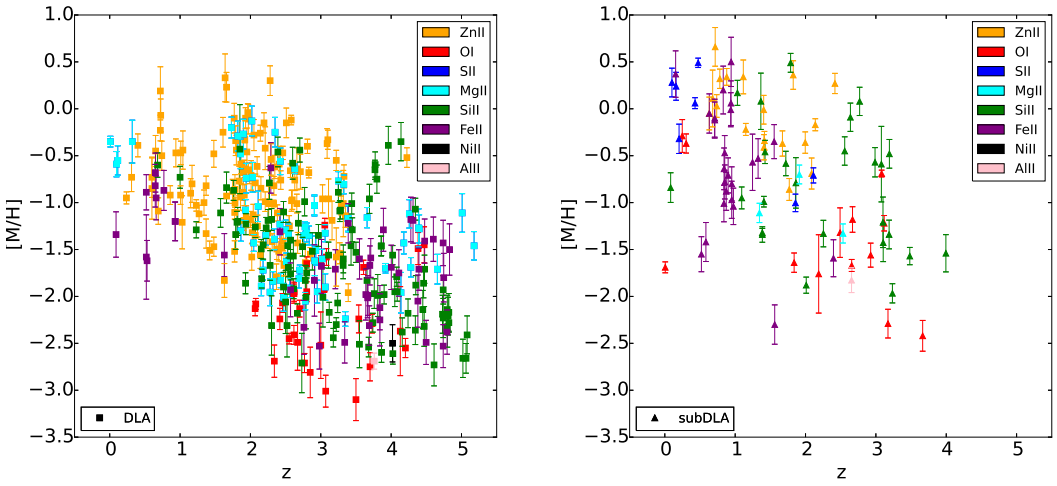

Figure 1.4.: Evolution of [M/H] with redshift, color-coded with respect to the element used to derive the metallicity for DLAs (left panel) and sub-DLAs (right panel) from the EUADP+ sample.

Fig. 1.4 shows the evolution of the metallicity [M/H] with redshift of the systems for the 92 sub-DLAs (bottom panel) and the 362 DLAs (top panel) from the EUADP+ sample, color-coded with respect to the element used to derive the metallicity. We note that Zn is only detected up to $\mathrm{z} = 3$ (but for one DLA measured at $\mathrm{z} \sim 4$), and O is only derived for metal-poor systems ($[\mathrm{M/H}] < -1$) because OI λ 1302, the only OI line usually accessible to ground-based telescopes, is saturated otherwise.

Lanzetta et al., 1995 estimated the cosmic metallicity from the gas mass density Ω_g and metal mass density Ω_m via the H I-weighted mean metallicity $\langle \mathrm{Z} \rangle$:

$$< \mathrm{Z(z)} >= \Omega_\mathrm{m}(\mathrm{z})/\Omega_\mathrm{g}(\mathrm{z}) = \frac{\sum_\mathrm{i} \mathrm{Z_i N(H\,I)_i}}{\sum_\mathrm{i} \mathrm{N(H\,I)_i}} \tag{1.3}$$

Fig. 1.5 shows the metallicity derived in our sample, as well as the H I-weighted mean metallicity $\langle \mathrm{Z} \rangle$ for both populations (sub-DLAs in blue and DLAs in red). The bins for $\langle \mathrm{Z} \rangle$ are chosen such that there is an almost constant number of systems in each bin, that is 16 for the sub-DLAs and 26 for the DLAs. The vertical error bars are derived from the consideration on sampling and measurements errors. The sampling errors are calculated from a bootstrap technique as described in Rafelski, Wolfe, et al., 2012 and the measurement errors from the propagation formula. The total errors are the quadratic sums of these two quantities for each bin. We note a large scatter for a third of the newly derived sub-DLA metallicities (blue dots). This points out to the need for a larger sample of sub-DLA measurements at all redshifts.

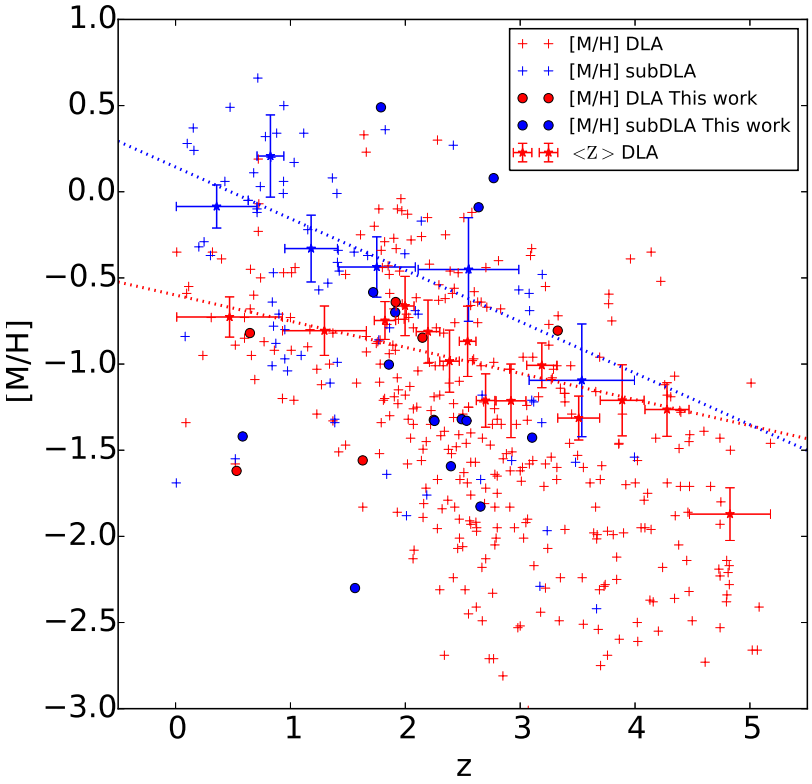

Figure 1.5.: Evolution of the N(HI)-weighted mean metallicity $\langle Z \rangle$ with redshift. Clearly, both DLA and sub-DLA populations show an increase of $\langle Z \rangle$ with decreasing redshift, but sub-DLAs have a steeper evolution of $\langle Z \rangle$ with redshift than DLAs. We also note a floor at $[X/H] = -3$ below which no metals are detected.

We measure an anti-correlation between redshift and metallicity for both populations. The Spearman coefficient for sub-DLAs is $\rho = -0.49$ and $\rho = -0.55$ for DLAs, with probabilities of no correlation $P(\rho) < 10^{-6}$ for both populations. The Kendall's τ is -0.34 for sub-DLAs and -0.38 for DLAs, with a probability of no-correlation of below 10^{-5} for both populations. The dotted lines in Fig. 1.5 show the best bisector fits for the metallicity evolution with redshift of both populations. We measure

$$< Z >_{\rm DLAs} = (-0.15 \pm 0.03)\, z - (0.6 \pm 0.13) \tag{1.4}$$

$$< Z >_{\rm sub-DLAs} = (-0.30 \pm 0.07)\, z + (0.15 \pm 0.31) \tag{1.5}$$

The fit has been performed shifting the y-axis to $z = 3$ to minimize the error on the intercept and ignoring the last DLA bin which presents a rapid decline in metallicity

(Rafelski, Neeleman, et al., 2014). The evolution with redshift is steeper for sub-DLAs than for DLAs. Previous authors (Khare, Kulkarni, et al., 2007; Kulkarni, Khare, Som, et al., 2010) argued that this effect might arise from the fact that sub-DLAs are more massive than DLAs.

Our results are in agreement with previous work (Kulkarni, Khare, Péroux, et al., 2007; Kulkarni, Khare, Som, et al., 2010; Som, Kulkarni, Meiring, York, Péroux, Lauroesch, et al., 2015), with a more significant result in the sub-DLA regime thanks to the larger sample presented here. The slope remains unchanged with respect to earlier studies. However, the significance of the result increases indicating a convergence towards a realistic value of the slope.

1.4.2. Kinematics

In addition to the different abundances derived from Voigt profile fitting, information on the kinematics of the absorbers can be derived from the UVES high resolution spectra.

1.4.2.1. Voigt Profile Optical Depth Method

We use the definition of the velocity interval $\Delta \mathrm{V}_{90}$ as defined by Prochaska and Wolfe, 1997b, based on the integrated optical depth $\tau_{tot} = \int \tau(v) dv$ and considering the velocity interval from 5% to 95% of this quantity.

In this paper, we do not consider the apparent optical depth (AOD) $\tau_{app} = -\log(I/I_c)$ to derive the velocity interval, as is usually done, but we use instead the optical depth derived from the Voigt profile fits (see appendix B.2 for a description of the fits for every system individually).

This method, which we refer to as Voigt profile optical depth (VPOD) method, makes use of the information gathered from the fits. The saturation and contamination issues are then considered when deriving $\Delta \mathrm{V}_{90}$. This is the main difference with the AOD method, which might provide $\Delta \mathrm{V}_{90}$ measurements affected by blends. In the VPOD method, we use simultaneously the information on several transitions to derive the velocity interval for any ion. Indeed, the only quantity that differs between transitions of the same ion is the oscillator strength, which has no impact on the velocity axis. Fig. 1.6 shows an example of the derivation of the velocity interval for an FeII line. Table 1.4 summarizes the $\Delta \mathrm{V}_{90}$ measurements for the 22 systems studied here. For 20 of them, we use the information from the FeII lines as it is the ion most detected in our sample.

One of the sub-DLA in our sample, towards PKS 0454-220, has already been studied by Som, Kulkarni, Meiring, York, Péroux, Lauroesch, et al., 2015. They use SII λ 1250 from an HST/COS spectrum and derive $\Delta \mathrm{V}_{90}$=155 km/s based on the AOD method. However, we find with the VPOD method described above a value almost twice smaller. We use the AOD method on the UVES spectrum with FeII λ 2374 and derive $\Delta \mathrm{V}_{90}\sim$85.0 km/s, consistent with the result from the VPOD method. We note that the Line Spread Function (LSF) derived from the COS consortium is responsible for the reported large value. To overcome this problem, we exclude COS measurements from our analysis.

In conclusion, the VPOD $\Delta \mathrm{V}_{90}$ values are not sensitive to blending and saturation effects, to the shape of the instrument's LSF, its resolution and to the SNR of the derived

spectrum. We note that depletion of refractory elements contributes to the error in the ΔV_{90} because the different components can be affected differently by dust depletion. In the present study, FeII has been used because it is uniformly detected among the 22 new systems presented here. In the remaining of the sample there is no object in common between the EUADP and the already derived ΔV_{90} found in the literature.

1.4.2.2. ΔV_{90} versus Metallicity Relation

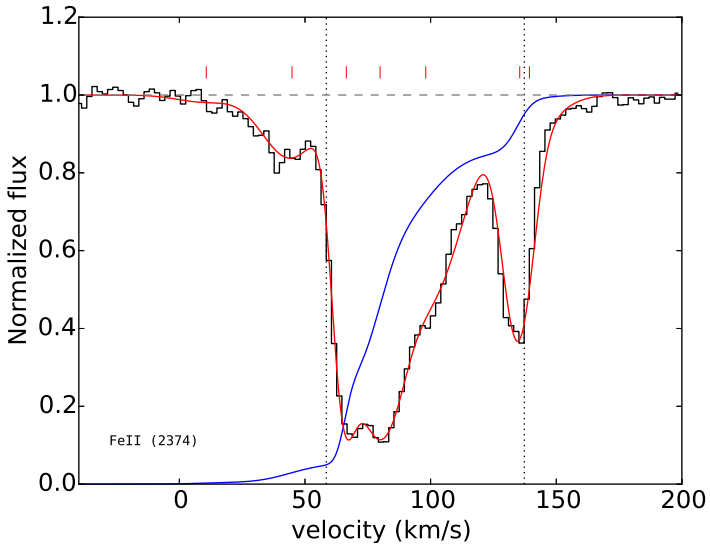

Figure 1.6.: An example illustrating the computation of the velocity interval ΔV_{90}. The black curve is the normalized spectrum of PKS 0454-220 centered on the FeII λ 2374 line, the red curve is the Voigt profile fit of the absorption and the blue curve is the integrated optical depth derived from the Voigt profile. The vertical dotted lines indicates the 5% and 95% thresholds for the integrated optical depth, defining the velocity width ΔV_{90}.

Recently, Som, Kulkarni, Meiring, York, Péroux, Lauroesch, et al., 2015 compared for the first time the sub-DLA metallicity versus velocity width trend over a statistically significant sample of 31 sub-DLAs at $0.1 \leq z_{abs} \leq 3.1$. We propose here to extend their analysis to a wider sub-DLA sample using our new 15 sub-DLAs. We consider a different sample than the one used in the remaining of the paper (EUADP+) as the velocity widths are not provided by all authors. We consider the data from Ledoux, Petitjean, Fynbo, et al., 2006 (52 DLAs and 14 sub-DLAs at redshifts $1.7 \leq z_{abs} \leq 4.3$, corrected for Asplund et al., 2009 photospheric solar abundances), observations from Meiring, Lauroesch, Kulkarni, Péroux, Khare, and York, 2009 (29 sub-DLAs at redshifts $z_{abs} < 1.5$, corrected for Asplund et al., 2009 photospheric solar abundances), observations from Neeleman et al., 2013 (98 DLAs at redshifts $1.6613 \leq z_{abs} \leq 5.0647$),

observations from Moller et al., 2013 (4 DLAs at redshifts $1.9 \leq z_{abs} \leq 3.1$), as well as results from this study (see Table 1.4). We only consider the systems with detected $[\alpha/H]$ (11/15 sub-DLAs and 4/7 DLAs). The resulting sample gathers 54 sub-DLAs and 162 DLAs.

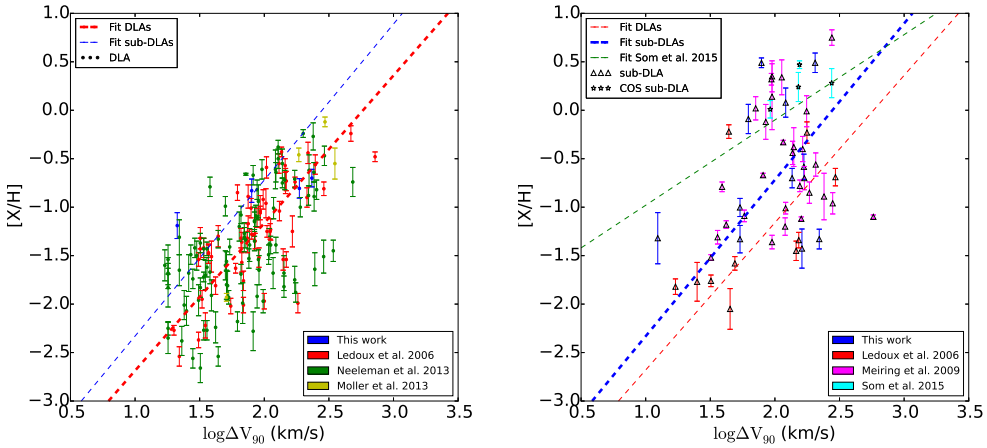

Figure 1.7.: [X/H] versus ΔV_{90} for the newly derived systems, the systems from Ledoux, Petitjean, Fynbo, et al., 2006, Neeleman et al., 2013, Som, Kulkarni, Meiring, York, Péroux, Lauroesch, et al., 2015, Meiring, Lauroesch, Kulkarni, Péroux, Khare, and York, 2009, and Moller et al., 2013 in blue, red, green, cyan, magenta and yellow, respectively. The upper panel shows the DLAs and the bottom panel the sub-DLAs. The data points measured with COS (stars) are not considered for the fit due to the discussion in section 1.4.2.1. The open triangles represent the sub-DLAs and the dots the DLAs. The dashed blue line reproduces the bisector fit of the sub-DLAs, the dashed red line is the bisector fit for all the DLAs and the green dashed line in the lower panel represents the Som, Kulkarni, Meiring, York, Péroux, Lauroesch, et al., 2015 sub-DLA fit.

Fig. 1.7 shows the trend between the metallicity and the velocity width ΔV_{90} for sub-DLAs (bottom panel) and DLAs (top panel) from this ΔV_{90} sample.

$$[X/H]_{DLA} = (1.52 \pm 0.08)\ \log \Delta V_{90} - (4.20 \pm 0.16) \tag{1.6}$$

$$[X/H]_{sub-DLA} = (1.61 \pm 0.22)\ \log \Delta V_{90} - (3.94 \pm 0.45) \tag{1.7}$$

The fits are performed shifting the y-axis to $\log \Delta V_{90} = 2$ to minimize the error on the intercept.

Som, Kulkarni, Meiring, York, Péroux, Lauroesch, et al., 2015 find a higher intercept and a shallower slope for the sub-DLA population, using only Zn and S with ionization

Table 1.4.: Measures of ΔV_{90} in our sample derived from Voigt profile fits to the FeII lines (except for two systems with no Fe coverage, for which we used SiII (a) and AlII (b)).

QSO	z_{abs}	log N(H I) [cm^{-2}]	Δv_{90} [km/s]
QSO J0008-2900	2.254	20.22	53.7
QSO J0008-2901	2.491	19.94	12.4
QSO J0018-0913	0.584	20.11	192.6
QSO J0041-4936	2.248	20.46	21.2
QSO B0128-2150	1.857	20.21	53.7
QSO J0132-0823	0.647	20.60	76.5
QSO B0307-195B	1.788	19.00	204.8
QSO J0427-1302	1.562	19.35	7.8
PKS 0454-220	0.474	19.45	78.7
J060008.1-504036	2.149	20.40	79.9
QSO B1036-2257	2.533	19.30	220.4
J115538.6+053050	3.327	21.00	186.8^a
LBQS 1232+0815	1.72	19.48	167.6
QSO J1330-2522	2.654	19.56	21.0^b
QSO J1356-1101	2.397	19.85	337.7
QSO J1621-0042	3.104	19.70	161.9
4C 12.59	0.531	20.70	62.4
LBQS 2114-4347	1.912	19.50	135.9
QSO B2126-15	2.638	19.25	62.3
QSO B2126-15	2.769	19.20	121.2
LBQS 2132-4321	1.916	20.74	233.4
QSO B2318-1107	1.629	20.52	13.8

corrections. Although this result is free from dust depletion effect on the metallicity estimation, it might be biased towards higher metallicity sub-DLAs, where Zn or S can be measured. A larger Zn-based metallicity sub-DLAs samples is required to recover the metallicity-ΔV_{90} relation free from the effects of dust bias. A larger Zn-based metallicity sub-DLAs samples is required to recover the metallicity-Delta v relation free from the effects of dust bias.

As in previous studies, the DLA sample is well correlated. The Spearman coefficient is $\rho = 0.63$, with a probability of no correlation $< 10^{-6}$. The Kendall's τ is 0.46 with a probability of no correlation $< 10^{-6}$. The sub-DLA sample is less correlated than the DLA sample, in agreement with Som, Kulkarni, Meiring, York, Péroux, Lauroesch, et al., 2015. The Spearman coefficient is $\rho = 0.39$, with a probability of no correlation of 0.004. The Kendall's τ is 0.25 with a probability of no correlation of 0.007. Adding more sub-DLAs to the ΔV_{90}-metallicity relation does not improve the correlation. Som, Kulkarni,

Meiring, York, Péroux, Lauroesch, et al., 2015 showed that the ionization correction also does not improve this correlation. This indicates a larger spread for the sub-DLAs, which may originate from more complex kinematic behaviors in sub-DLA clouds. However, the determination of ΔV_{90} appears to be sensitive to the resolution, the LSF and the SNR of the data. This might contribute to the observed scatter, although an intrinsic scatter is expected from CGM regions.

1.4.2.3. Is ΔV_{90} a Reliable Tracer of Mass?

A mass-metallicity relation (hereafter MZR) has been reported at low redshifts (Lequeux et al., 1979; Tremonti et al., 2004), intermediate redshifts (Savaglio et al., 2005) and high redshifts (Erb, Shapley, et al., 2006). It relates the stellar mass of galaxies to the metallicity of their ISM. This relation is crucial in our understanding of galaxy evolution as it supports the theory of metal ejection from galactic outflows in low-mass (and hence low potential well) galaxies and their enrichment with accreting metal-poor IGM gas, diluting the galactic metallicity.

For quasar absorbers, some simulations indicate that the origin of the velocity width, ΔV_{90}, could be strongly related to the gravitational potential well of the absorption system's host galaxy (e.g. Prochaska and Wolfe, 1997b; Haehnelt et al., 1998; Pontzen et al., 2008). Similarly, assuming a scaling of the galaxies luminosity with dark matter haloes, Ledoux, Petitjean, Fynbo, et al., 2006 and later Moller et al., 2013 proposed to interpret the ΔV_{90} versus metallicity relation of quasar absorbers as a MZR. Such a picture does not take into account the complex gas processes at play now known to take place in CGM regions. In other words, the ΔV_{90} may reflect bulk motions of the absorbing gas rather than motions governed by the gravitational potential well.

Observationally, a measurement of mass and ΔV_{90} has been possible in few individual systems. Infra-red IFU SINFONI observations of the galaxy hosts of 3 DLAs and 2 sub-DLAs in Péroux, Bouché, et al., 2011 and Péroux, Kulkarni, and York, 2014 allow one to determine the mass of the systems from a detailed kinematic study. In addition, Christensen et al., 2014 has used photometric information of the galaxy hosts and Spectral Energy Distribution (SED) fits to estimate the stellar mass of 13 DLAs. Combined together, these findings suggest that, individually, the absorption systems align well with the MZR reported at these redshifts.

In addition to these measurements in a few specific systems, several authors have put constraints on the mass estimates of quasar absorbers in a statistical manner. Interestingly, the local analogues to DLAs, the 21cm $z = 0$ emitting galaxies studied with HIPASS by Zwaan et al., 2008 show that the quantity ΔV_{90} correlates little with mass. Similarly, Bouché, Murphy, Péroux, et al., 2007 (and later Lundgren et al., 2009; Gauthier et al., 2014) have used the ratio of MgII systems auto-correlation with a correlation with Luminous Red Galaxies (LRG) at the same redshifts to derive an estimate of the overall mass of quasar absorbers. Their findings show an anti-correlation between equivalent width, a proxy for ΔV_{90}, and metallicity. Admittedly, the populations of absorbers do not completely overlap, the Ledoux, Petitjean, Fynbo, et al., 2006 sample contains mostly DLAs, while the MgII sample of Bouché, Murphy, Péroux, et al., 2007 might have at most 25% of DLAs (according to the criterion of Rao, Turnshek, and Nestor, 2006: 50% meet the FeII/MgII criteria and 35-50% of these are DLAs). In

fact, Bouché, Murphy, Péroux, et al., 2007 and Schroetter et al., 2015 argue that MgII absorbers can be used to trace superwinds as they are not virialized in the gaseous halo of the host-galaxies. Bouché, Hohensee, et al., 2012 also show that the inclination of the galaxy has a direct impact on the absorption profile and therefore on the velocity width. Put together, these many lines of evidence question the interpretation of the velocity width as a proxy for the mass of the host galaxy and the interpretation of the ΔV_{90}/metallicity correlation as a MZR for quasar absorbers.

1.4.3. Tracing the Circum-Galactic Medium with sub-DLAs

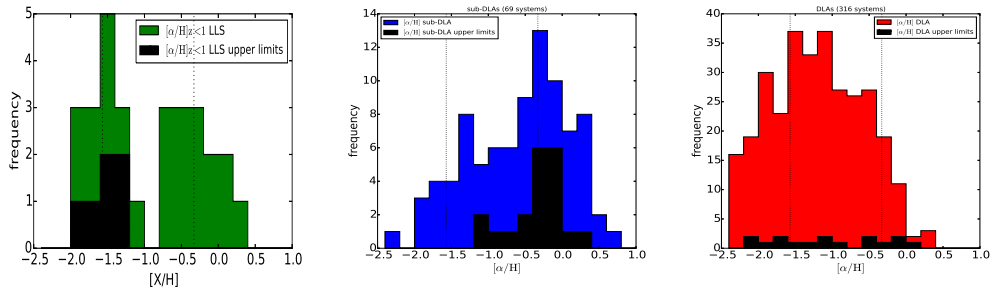

Figure 1.8.: Metallicity [α/H] distribution of LLSs (left panel), sub-DLAs (middle panel) and DLAs (right panel). The histogram for LLSs has been taken from Lehner, Howk, et al., 2013 and indicates a bimodality in the metallicity distribution for LLS at $z < 1$. The black vertical dashed lines represent the mean values derived from the $z_{abs} < 1$ LLS subgroups by Lehner, Howk, et al., 2013.

Our understanding of galaxy formation and evolution is tightly linked with the study of two opposite processes that take place within the CGM. Indeed, to create stars, the galaxy requires a continuous input of cold gas, that is believed to accrete along the filamentary structures from the cosmic web. In addition, cosmological simulations fail to reproduce the observed SFR without invoking feedback processes from star formation itself or AGN activity. These outflowing processes and their large scale impact have been confirmed observationnally (Steidel, Erb, et al., 2010; Bouché, Hohensee, et al., 2012; Kacprzak, Martin, et al., 2014), but there is still little observational evidence for accretion of cool material (Bouché et al., 2013b; Cantalupo, Arrigoni-Battaia, et al., 2014; Martin, Chang, Matuszewski, Morrissey, Rahman, Moore, and Steidel, 2014).

Quasar absorbers with H I column densities in the range of LLS and sub-DLAs are believed to be good probes of this CGM (Fumagalli, Prochaska, et al., 2011; Voort and Schaye, 2012). Lehner, Howk, et al., 2013; Lehner, O'Meara, Fox, et al., 2014 report a bimodality in the metallicity distribution of 29 $z < 1$ LLS, which they interpret as the signatures of outflows (metal-rich) and infalls (metal-poor).

Lehner, Howk, et al., 2013 extended their analysis on 29 sub-DLAs and 26 DLAs, but do not report a bimodality distribution in the metallicity of these systems based on

α-elements. Clearly, larger samples of quasar absorbers are required to perform such studies. Here, we perform similar analysis on a larger sample of sub-DLAs and DLAs with a broad redshift range.

Fig. 1.8 shows the bimodal metallicity distribution in $z < 1$ LLS by Lehner, Howk, et al., 2013 and the α-element metallicity distribution for DLAs (316 systems) and sub-DLAs (68 systems) derived from our EUADP+ sample at all redshifts. The sub-DLA $[\alpha/\mathrm{H}]$ distribution in the middle panel of Fig. 1.8 also suggests bimodality.

In Fig. 1.9, we plot the distribution of the α abundances (left panels) and Fe abundances (right panels) for the EUADP+ sub-DLAs in 3 redshift bins ($\mathrm{z_{abs}} > 2.4$ for the upper panels, $1.25 \leq \mathrm{z_{abs}} \leq 2.4$ for the middle panels and $\mathrm{z_{abs}} < 1.25$ for the bottom panels). We consider the metallicity traced by FeII as we have more detections with this ion and it is little affected by photo-ionization effect, even though Fe has an inclination to lock up onto dust grains. These histograms reveal the strong metallicity evolution with redshift for sub-DLAs. The sub-DLAs in the high redshift bin, $\mathrm{z_{abs}} > 2.4$, present an unimodal distribution centered around [M/H]~ -1.6, similar to the metal-poor LLS population derived by Lehner, Howk, et al., 2013. At intermediate redshifts, $1.25 \leq \mathrm{z_{abs}} \leq 2.4$, a transition from low to higher metallicities appears. At low redshifts, $\mathrm{z_{abs}} < 1.25$, however, the distribution presents hints of a bimodal distribution. This trend is more pronounced for the [Fe/H] distribution. A DIP test rejects the unimodal distribution at a significance level of 83%, taking the upper limit as a detection. The peaks of the distribution are located at $[\mathrm{Fe/H}] =$ -1.12 and $[\mathrm{Fe/H}] =$ -0.29, from a Gaussian Mixture Modeling. These values are compared with what is expected from simulations in terms of metallicity of accreting or outflowing gas. The prediction for the cold-mode accretion metallicity is above a hundredth solar, which is in line with the metal poor population in our distribution (Ocvirk et al., 2008; Shen et al., 2013). Therefore, the metal rich population should trace either outflowing gas or gas directly associated with the galaxy's ISM. However, this is not seen in the $[\alpha/\mathrm{H}]$ distribution, where the DIP test rejects the unimodal distribution at a significance level of 31%, still taking upper limits as detections. But these limits are located at the high metallicity end of the distribution, and therefore do not contradict the possible bimodal distribution seen in $[\mathrm{Fe/H}]$.

These results indicate a similar behavior for low redshift sub-DLAs as for low redshift LLS. However, we expect the position of the peaks to be higher than those derived for the $\mathrm{z} < 1$ LLS, as the $[\mathrm{Fe/H}]$ metallicity is underestimated due to depletion of Fe onto dust grains. Lehner et al. (in prep.) show that the bimodal distribution for LLS disappears at higher redshifts, similarly to what we find with sub-DLAs at higher redshifts. We note however that the bimodality in LLS could perhaps be incorrect, given that there are larger uncertainties in the metallicity determination of LLS (due to ionization corrections).

We note that the effect of redshift plays an essential role in such an analysis, as illustrated in Fig. 1.9.

Altogether, larger samples of both LLS and sub-DLAs at low-redshifts are required to distinguish between metal-poor gas accreting onto the galaxy and metal-rich gas being expelled.

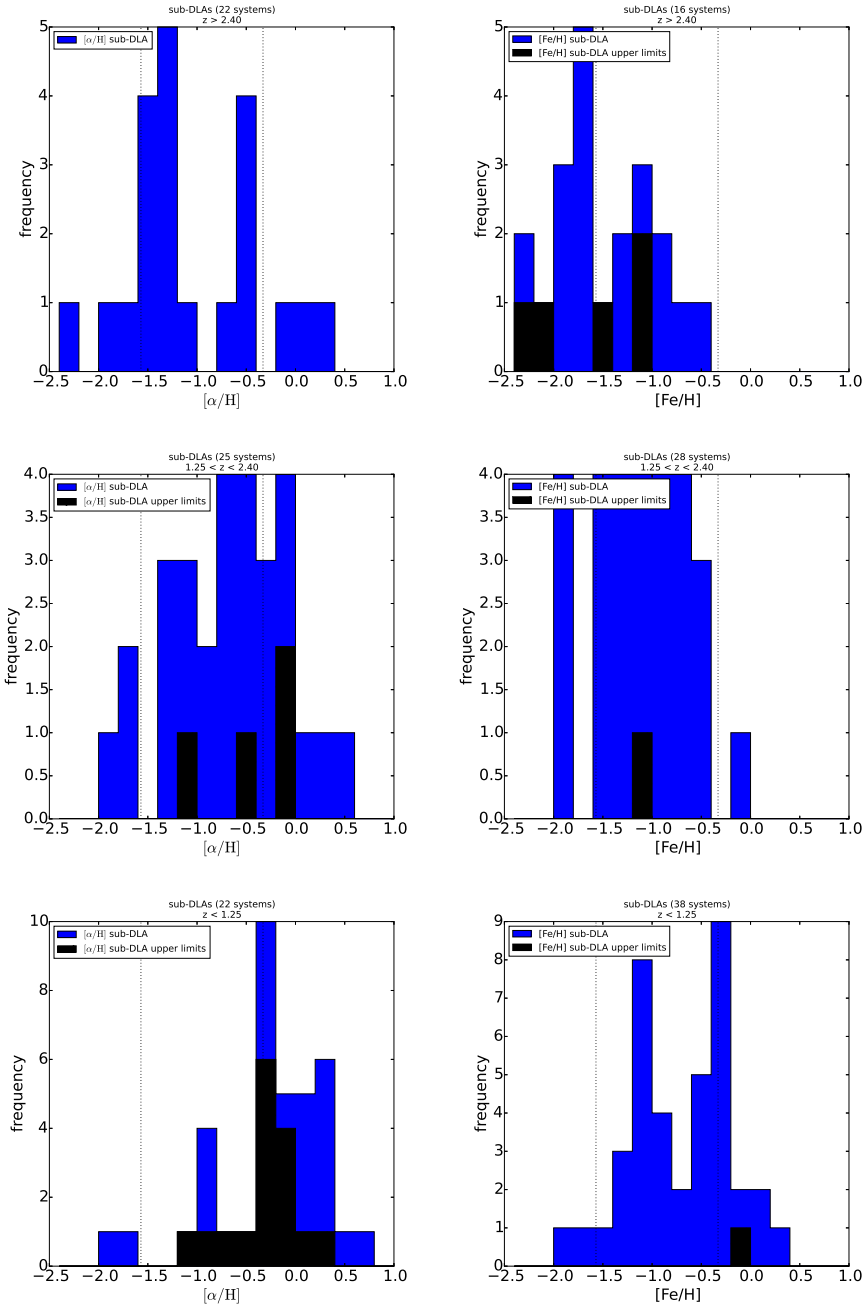

Figure 1.9.: Metallicity (left panels: $[\alpha/\mathrm{H}]$, right panels: [Fe/H]) distribution of sub-DLAs for different redshift bins: $\mathrm{z} > 2.4$ (top panels), $1.25 < \mathrm{z} < 2.4$ (middle panels) and $\mathrm{z} < 1.25$ (bottom panels). The black vertical dashed lines represent the mean values derived from the $\mathrm{z_{abs}} < 1$ LLS sub-groups by Lehner, Howk, et al., 2013. The black areas represent upper limits. The metallicity distribution is a strong function of redshift and only the lowest redshift range presents hints of a bimodal distribution for the [Fe/H] metallicity.

1.5. Conclusion

We present in this paper physical properties of 15 new sub-damped Lyman-α absorbers seen in absorption in background quasar's high resolution UVES spectra. These systems cover a wide redshift range ($0.584 \leq \mathrm{z_{abs}} \leq 3.104$). The metallicity measurements were performed using Voigt profile fitting of the normalized high resolution UVES quasar spectra. Our sub-DLA measurements add significantly to previous studies since high resolution spectroscopy is required to study these systems.

We apply a multi-element based method to assess the level of dust depletion in the line of sight to the quasar. This study appears to be promising as it uses the combined information from several ions, and is relative to measurements of our Galaxy's ISM. With a survival analysis, we derive the best fit of the depletion factor $\mathrm{F_*}$ for the DLAs and sub-DLAs and find negative values, statistically different, for both groups: $\mathrm{F_*^{sub-DLA}} = -0.34 \pm 0.19$ and $\mathrm{F_*^{DLA}} = -0.70 \pm 0.06$. In comparison with values derived in our Galaxy, DLAs lie outside the halo and the sub-DLAs are associated with Halo like stars, in terms of depletion patterns. This is counter-intuitive as we expect DLAs to be more self-shielded to the UV background than sub-DLAs. We conclude that quasar absorbers differ from the Galactic depletion patterns or alternatively have a different nucleosynthetic history. Future analysis with the Small Magellanic Cloud will enable comparisons to a galaxy more in line with the morphology or the $\mathrm{H_2}$ fraction of DLAs. Moreover, we derive the averaged rest frame extinction $\mathrm{A_V}$ for both populations to be below 0.01, suggesting that dust reddening is not observed in the current quasar selection.

We then examine the relative abundances of Fe and α-elements. We derived an offset in $[\alpha/\mathrm{Fe}]$ for the DLAs in our sample of 0.32 ± 0.18, excluding systems with $[\alpha/\mathrm{H}] > -1.5$ to be less sensitive to dust depletion. This value is similar to that derived by Rafelski, Wolfe, et al., 2012. However, we cannot derive a similar parameter for the sub-DLA population as we can not disentangle dust depletion effects from the α-enhancement. We therefore apply the DLA corrections to the sub-DLAs.

We study the evolution of the cosmic metallicity Ω_m, also described by the mean H I-weighted metallicity $\langle \mathrm{Z} \rangle$. We confirm the steeper evolution of sub-DLAs than DLAs eventually reaching a solar metallicity at low redshifts as expected from chemical evolution models. We note that a third of the newly derived sub-DLA abundances appear as outliers from the previous data.

We measure the velocity width of the absorption systems in our new sample, $\Delta \mathrm{V_{90}}$, with a new method using the information from the Voigt profile fits. We confirm that there is a correlation between $\Delta \mathrm{V_{90}}$ and metallicity for sub-DLAs. Indeed, sub-DLAs are potentially probing a different mass range than DLAs. Sub-DLAs could have a more important feedback mechanism than DLAs, thus increasing the scatter and weakening the possible velocity width/metallicity correlation.

Finally, we look at the metallicity distribution of sub-DLAs. At low redshifts, $\mathrm{z_{abs}} < 1.25$, we see a hint of a bimodal distribution which peaks at ~ -1.1 and ~ -0.3. This indicates that low-redshift sub-DLAs are tracing different mechanisms at play within the CGM, such as cold-mode accretion and outflows. Larger samples of sub-DLAs and LLS abundances at low redshifts are required to better identify their connection to gas

inflow/outflow processes.

ACKNOWLEDGMENTS

We thank N. Lehner, C. Howk, M. Fumagalli, M. Rafelski, M. Pieri, R. Bordoloi, J. O'Meara, D. Som and P. Møller for useful discussions. This work has been funded within the BINGO! ('history of Baryons: INtergalactic medium/Galaxies cO-evolution') project by the Agence Nationale de la Recherche (ANR) under the allocation ANR-08-BLAN-0316-01 as well as within the REGAL ('what REgulates the growth of GALaxies? ') project by the Labex (Laboratoire d'Excellence) OCEVU ('Origines, Constituants et Evolution de l'Univers'). This work has been carried out thanks to the support of the OCEVU Labex (ANR-11-LABX-0060) and the A*MIDEX project (ANR-11-IDEX-0001-02) funded by the "Investissements d'Avenir" French government program managed by the ANR. We thanks Pierre Mege for contributing in the development of the VPOD method. SQ acknowledges CNRS and CNES support for the funding of his PhD. CP thanks the ESO science visitor program for support. VPK acknowledges partial support from the NSF grant AST/1108830, with additional support from NASA grant NNX14AG74G and NASA/STScI grant for program GO 12536. EJ thanks Aix-Marseille University and Cécile Gry for a visit where part of this work was undertaken.

Part II.

Emission

Chapter 2: The FIREBall-2 project

Pour être, une fois, au monde, il faut à jamais ne plus être.

Albert Camus

Figure 2.1.: FIREBall launch, 2007, Palestine (Texas, USA)

While the majority of actual CGM observations comes from quasar absorption spectroscopy, a recent endeavor is aiming at mapping the CGM in emission. In particular, the high redshift Universe provides a window in which the UV photons get redshifted enough so that they can reach the Earth without being absorbed by the gas therein.

Low-z observations are crucial to the understanding of galaxy evolution, as they account for most of the age of the Universe and they can bring constraints on the relation between galaxies and the filamentary IGM. Indeed, Shull, Smith, et al., 2012 argue that one third of the gas at z=0 is seen in Lyα absorption, while the Lyα forest becomes progressively more transmissive as the Universe is further diluted by cosmological expansion (Meiksin, 2006). However, the main diagnosis lines (HI λ 1216Å, OVI λ 1031Åand CIV λ 1548Å) lie in the ultraviolet space and are not observable with ground-based instruments below z=2.2 because of the atmospheric UV absorption. The only solution to overcome this issue is to consider observations from above the atmosphere, which is of course far more limiting (technically and financially) than ground based astronomy. In addition, such a space mission must have a low sensitivity threshold and a good spatial resolution.

I present in this chapter the FIREBall-2 project, a balloon-borne UV spectroscopic mission (PI C. Martin, Caltech) which aims at observing and mapping the faint and diffuse emission from the CGM of low-z galaxies ($z < 1$). It is a joint collaboration between France and the United States, as the optics and the integration are based at LAM[a] (Marseille), the expertise on the balloon are provided the CNES[b] (Toulouse), the development of the detector is taken care of by Columbia University (New York City) and the thermal design is done at Caltech (Pasadena).

I will briefly present the scientific motivations for such a mission, then I will detail the optical design of the instrument.

2.1. Scientific Motivation

The FIREBall-2 UV spectrograph has been specifically designed to work on a narrow wavelength range: 200-208nm. This choice is mainly due to the atmospheric absorption of UV photons. Indeed, even if the balloon rises to an altitude of 40km, the band pass is limited by several molecular bands found in the lower atmosphere (which can go up to 100km high). The selected wavelength range actually benefits from a 'sweet spot' in the atmospheric transmission, in between the absorption by ozone O_3 at larger wavelengths and the absorption by dioxygen O_2 at shorter wavelengths (Fig. 2.2). In addition, the sky brightness is very

[a] Laboratoire d'Astrophysique de Marseille
[b] Centre National d'Étude Spatiales

low at these wavelengths (typically 1000 Continuum Units[c] in the UV window near 200nm), and there is a 'sweet spot' between NOδ emission bands where it is much lower, probably limited by extra-atmospheric emission.

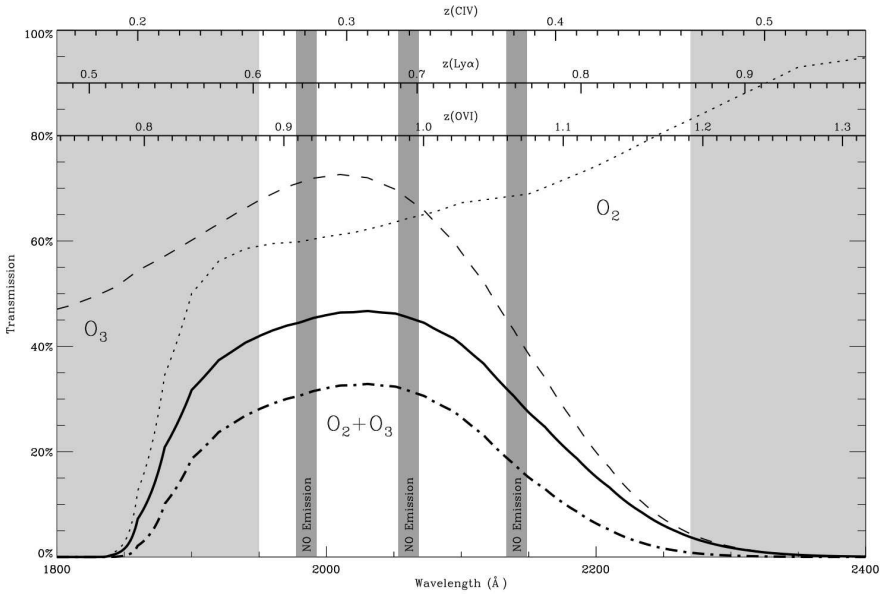

Figure 2.2.: Atmospheric transmission and NOδ band emission, revealing the atmospheric 'sweet spot' selected for FIREBall-2 window. Credit: Matuszewski, 2012

FIREBall-2 will aim at three lines of interest (see Fig. 2.3): Lyα, CIV and OVI. The Lyα line is the most dominant radiation in the Universe, as it is a resonant and scattering line from the most abundant element. The other two metal ionised gas lines bring additional physical information, as we expect powerful outflows from star forming galaxies to enrich their CGM. Absorption studies revealed presence of OVI at large distances from the center of high-redshift galaxies (Crighton, Hennawi, Simcoe, et al., 2014) and low-redshift galaxies (Tripp, Sembach, et al., 2008; Tumlinson et al., 2011; Werk et al., 2014). The COS data compilation by Danforth et al., 2016 shows that OVI are ubiquitously observed in absorption at low-redshifts and that CIV and NV are also commonly present[d]. Strong CIV absorbers happen to be strongly correlated with galaxies (Adelberger, Steidel, et al., 2003) and D'Odorico, Calura, et al., 2010 anticipate an increase of the cosmological mass density of CIV, Ω_{CIV}, towards lower redshifts. Moreover, Turner et al., 2014 found strong enhancements at z $\approx$ 2.4 of OVI, CIV and HI

[c] 1 Continuum Unit, or 1 CU, is 1 photon/s/cm^2/sr/Å. For Lyα, 1 CU$\approx$ 3.84 $\times$ 10^{-22} erg/s/cm^2/arcsec^2/Å.

[d] We detect quasi systematically CIV absorption in the absorption study performed in chapter 1).

within 180 physical kpc and 240 km/s of star-forming galaxies that are thought to be hosted by halos with masses $\sim 10^{12} M_{\odot}$. A recent observation of a z=2.304 sub-DLA also suggests that CIV could be associated with outflowing processes (Fox and Richter, 2016).

Furthermore, sub-DLAs are metal-richer than their denser counterparts, the DLAs, at low redshifts (see chapter 1). Their lower HI column density can be associated with the fact that they are likely located in the outskirts of galaxies (Faucher-Giguere, Keres, et al., 2010; Fumagalli, Prochaska, et al., 2011) where the metagalactic UV background is more efficient in photo-ionizing the clouds. Finally, it is interesting to note, once more, that the metallicity of sub-DLAs evolves steeply with decreasing redshift (see Fig. 1.5), which is in line with our motivation to find these lines at low redshifts.

Given the restframe wavelengths of these emission lines, FIREBall will be able to explore the low redshift Universe:

- With Lyα, $\lambda_{\rm em} = 1215.67$Å, the redshift probed is $z \sim 0.67$ corresponding to an age for the Universe of ∼7.6 Gyr
- With OVI, $\lambda_{\rm em} = 1031.93$Å, the redshift probed is $z \sim 1.0$ corresponding to an age for the Universe of ∼6.0 Gyr
- With CIV, $\lambda_{\rm em} = 1548.19$Å, the redshift probed is $z \sim 0.3$ corresponding to an age for the Universe of ∼10.8 Gyr

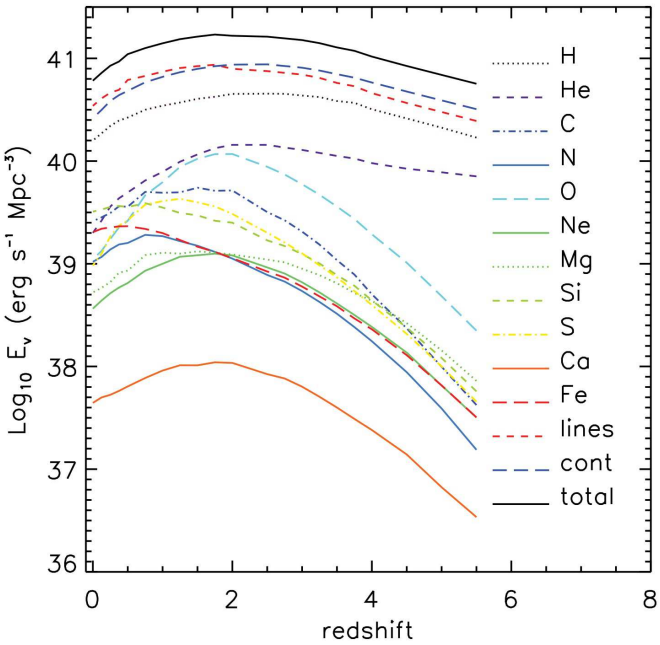

Figure 2.3.: Evolution of the specific emission lines (emission per unit volume) from individual elements and from the continuum, averaged over all the diffuse gas. Oxygen and Carbon are the most dominant metals in terms of emission at $z \sim 1$. Credit: Bertone, Aguirre, et al., 2013

In addition, the balloon experiment offers many advantages over satellite missions. Indeed, despite the short exposure time (one night of ∼7 hours) and the single narrow wavelength band available, it is a low cost solution to test in-flight cutting edge developments of new technological designs (such as the detector, the grating or the coatings). Moreover, the short project time line is best suited for the education of young scientists.

2.2. Presentation of the instrument

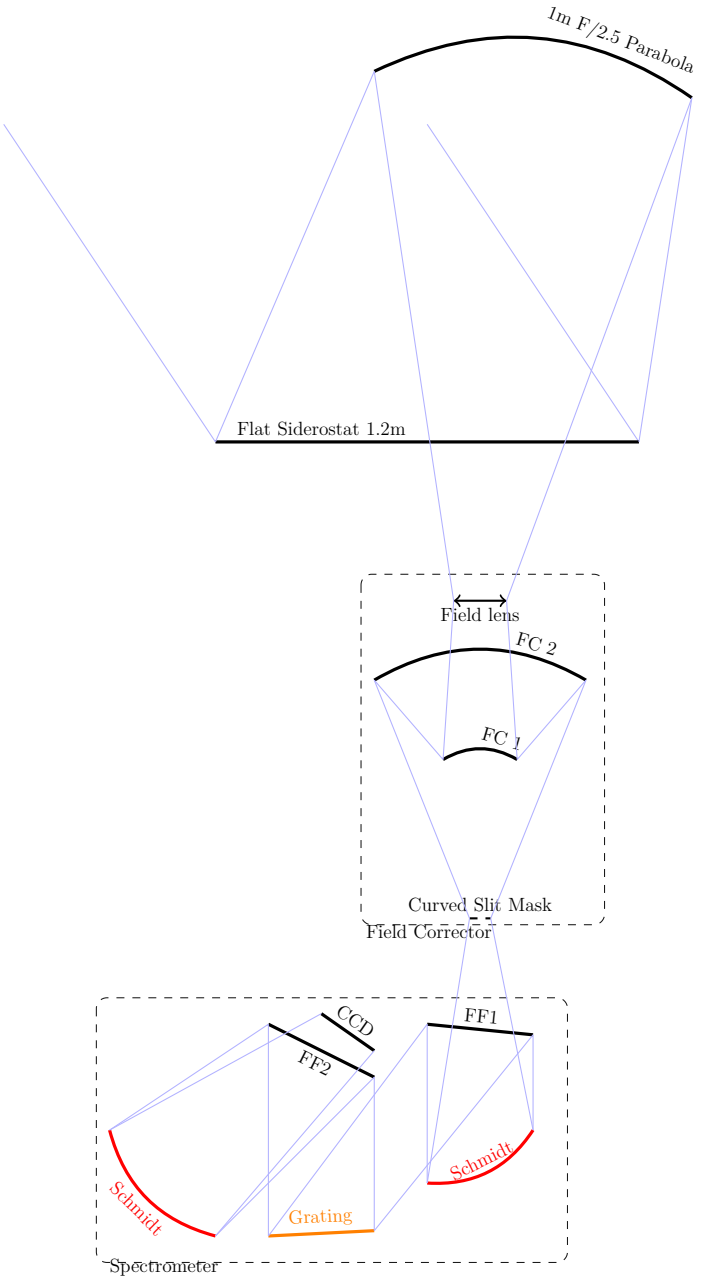

Figure 2.4.: FIREBall-2 optical design (indicative layout). It was made by Robert Grange in Marseille.

Since the first stages of the project, FIREBall has undergone some evolution. The balloon flew twice, in 2007[e] in Palestine, Texas (Fig. 2.1) and in 2009 in Fort Summer, New Mexico. At this time, the optical design of the spectrograph was different from the current one. It was originally equipped with a GALEX flight spare NUV micro-channel plate (MCP) and a fiber bundle Integral Field Units (IFU) with a 4x4 arcsec^2 field of view (FOV) (Grange, Milliard, McLean, et al., 2005; Milliard et al., 2010), but the sensitivity turned out to not be sufficient to detect the CGM emission.

The architecture chosen for new FIREBall-2 spectrometer is a Multi-Object Spectrograph (MOS). The short observing time allowed by the balloon (1 night, or 7 hours) will be compensated by the large number of targets to be observed simultaneously. Indeed, FIREBall-2 has a large FOV of 11x35 arcmin^2, a fast f-number of f/2.5, a spectral resolution R=$\frac{\lambda}{d\lambda} \sim 2200$ and a spatial Full Width Half Maximum (FWHM) of about 4 arcsec.

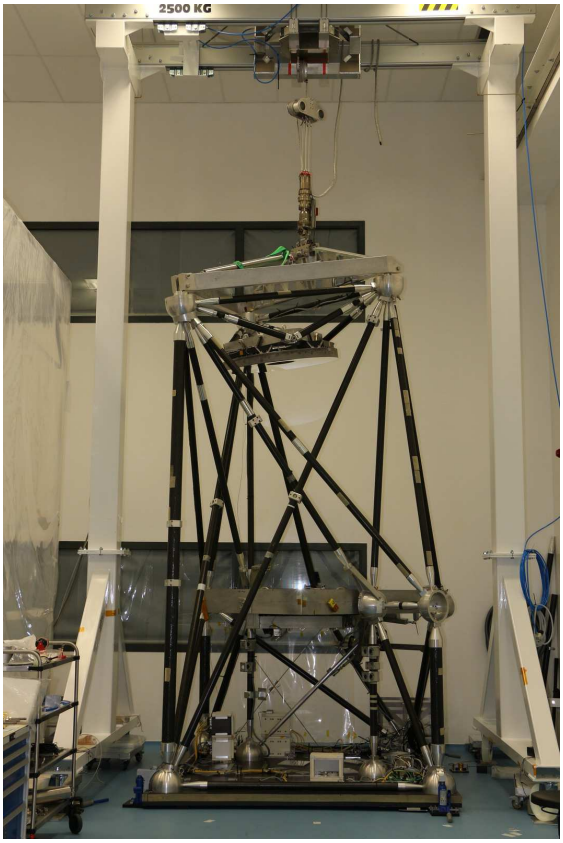

Figure 2.5.: Carbon-fiber gondola suspended on the testing rotation set. The integration is taking place in the Laboratory of Astrophysics of Marseille.

The telescope is mounted in a carbon-fiber gondola for the flight (Fig. 2.5).

[e]This launch resulted in a technical failure of the guidance following an abnormal violent launch.

This gondola provides a three axis guidance. The specification is 1 arcsec per axis, but the hanging ground tests have reached 0.1 arcsec in the X and Y guidance (Montel et al., 2016).

The light from the sky is first reflected on a 1x1.3m steerable holed plane mirror allowing field acquisition and tip-tilt slewing control during exposure. A 1m upside down concave parabolic mirror provides an f /2.5 focal surface – requiring coma correction – through the hole of the steerable mirror.

The collected f/2.5 beam then enters a vacuum tank (Fig. 2.6) through a field lens that hermetically closes the tank. The use of lenses is avoided for the conception of UV spectrographs because of the Cherenkov emission caused by UV photons going through the lens material. Thus FIREBall-2 is designed as an all-reflective system, except for that one lens. This vacuum tank contains the field corrector, the spectrograph and the detector, working at 140K owing to a Sun Power cryo-cooler that also cools a charcoal getter to 110K in order to perform the required cryo-pumping.

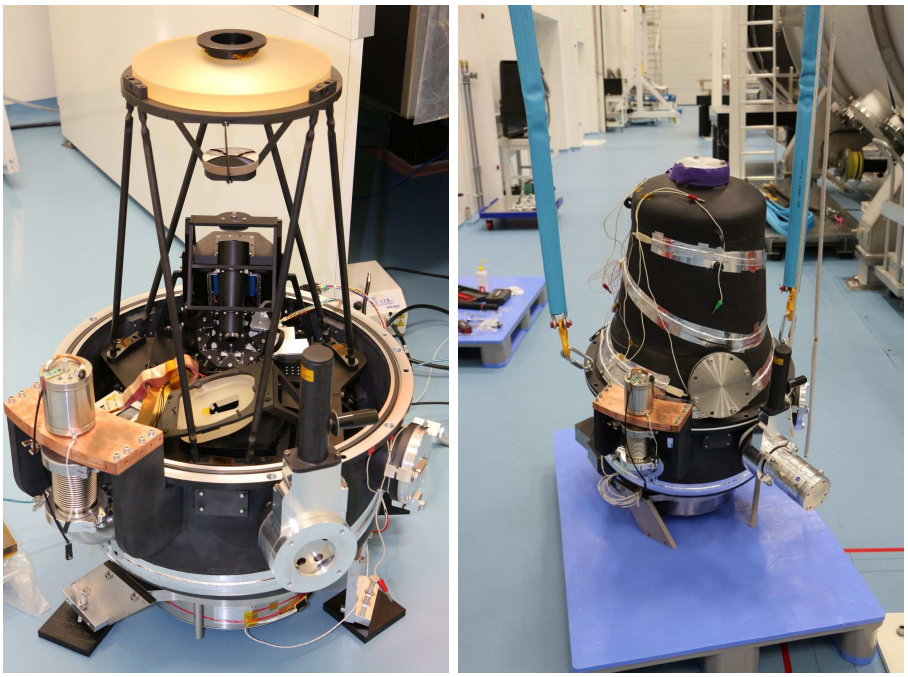

Figure 2.6.: Left panel: Opened vacuum tank with optics in place. Right panel: Closed vacuum tank, ready for cryo cooling and pumping. The tank is about 1 meter high.

For the new version of the FIREBall-2 optical design, a field corrector has been placed before the slit mask. This field corrector consists in a M=1 magnification two-mirror anastigmat system, leading to a curve focal plane (the slit mask). It corrects the coma aberration caused by the wide field of view of the new design

(400 arcmin^2 against 16 arcmin^2 previously) and provides a flat-field at the MOS output.

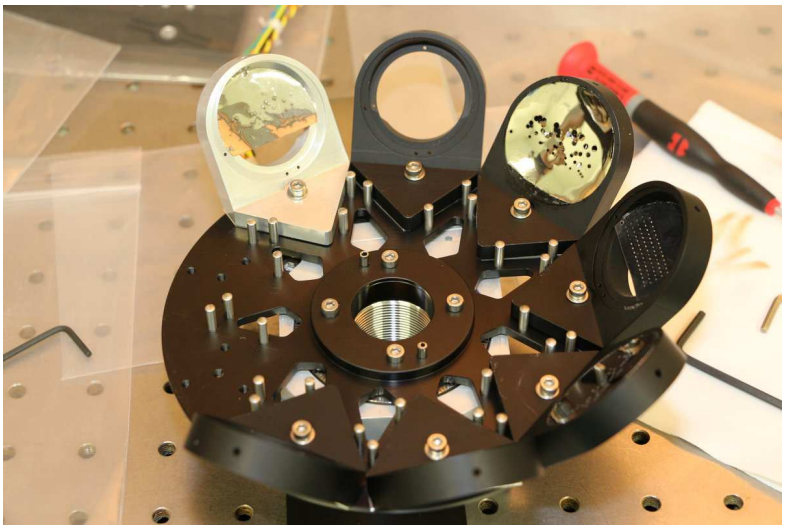

Figure 2.7.: Mask holder and some test masks

The different slits of the new MOS design of FIREBall-2 are organized as a set of different spherical multi-holed reflective masks, placed in a rotating holder at the focal plane of the field corrector (Fig. 2.7). The masks are manufactured from a reflective material in order to use the light that does not enter the slit for acquisition control and guiding. The slits are cut using laser beams. The curvature of the mask enables a flat focal plane at the detector's position[f], which is easier and cheaper than the manufacture of a curved detector. The disposition of the slits within each mask is yet to be defined, as it is closely linked to the observing strategy and science target choice. For example, for a blind search of bright objects along the entire field of view, a long-slit mask can be manufactured. We can put up to 50 slits per mask. These slits are typically $50\mu\mathrm{m}$ in width (4 arcsec) for a height of $300\mu\mathrm{m}$ (25 arcsec). Different observing strategies will be combined, with part of the field covered with large slits to perform blind detection.

The spectrograph is composed of a two identical f/2.5 Schmidt mirrors with an aspherical (with low curvature) diffraction grating close to the common pupil in the parallel beam. The Schmidt mirrors are simple spherical mirrors with a curvature of 500mm. On each Schmidt mirror, the access to the focal plane requires an extra folding flat mirror which also helps to improve the packaging.

[f]The Field corrector also produce as curved field so as to correct for the double curvature induced by the Schmidt mirrors.

Figure 2.8.: Left: Flat folding mirror with 'notch' filter coating. Right: Schmidt mirror with 'notch' filter coating. Credit: Grange, Milliard, Lemaitre, et al., 2016

Fig. 2.8 shows the first Schmidt mirror of the spectrograph and its corresponding flat folding mirror. An interesting feature of these mirrors is that they are coated with an UV notched filter associated with a cutoff at the frequency of visible light (Grange, Milliard, Lemaitre, et al., 2016). This cut off prevents visible light from being diffused off by the grating downstream into the spectrograph housing and possibly to the detector.

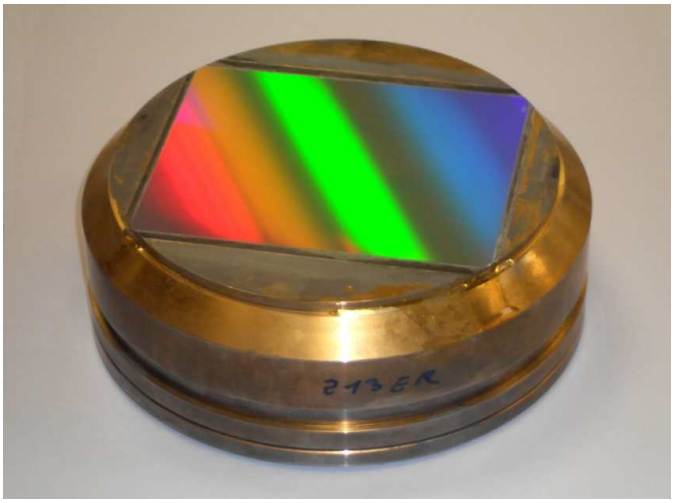

Figure 2.9.: Grating replica on its deformable matrix. Credit: Lemaitre et al., 2014

The dispersing element, located between the two Schmidt mirrors, is a reflective 2400 g/mm holographic aspherical grating manufactured by the company Jobin-Yvon. It is aspherized using the double replication technique of a metal deformable matrix, described by Lemaitre et al., 2014, in order to compensate the double spherical aberration induced by the Schmidt mirrors associated with the large field of view. This technique is commonly used for reflective axisymmetric

Schmidt grating spectrographs. First, a replica of a master grating is performed on the plane surface of an unstressed deformable matrix (Fig. 2.9). Then, this matrix is aspherized via injection of air at the correct pressure (typically 7 bar). The final aspherized grating is then obtained via a second replication on the final slightly concave Zerodur substrate.

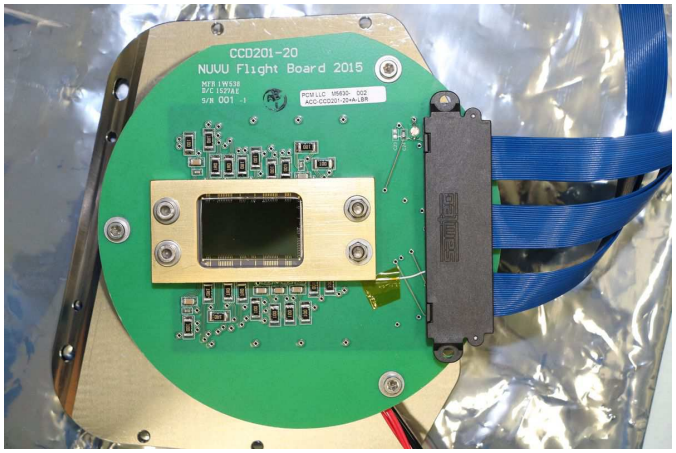

Figure 2.10.: FIREBall-2's detector

One of the new features of the FIREBall-2 design is the use of a low noise, 2K*1K, 13.5μm pixels, flat UV δ-doped electron multiplying charge coupled device used in counting mode[g] (EM-CCD, Fig. 2.10).

This EM-CCD uses multi-layer coating to improve the penetration of photons into the CCD. The δ-dopping prevents the acquired photons from being absorbed before their conversion into electrons. The Quantum Efficiency (the ratio between the number of electrons to the number of photons) is presently 0.4 but the goal is to push it up to 0.6 (Jewell et al., 2015).

2.3. Conclusion

The observational challenge that FIREBall-2 proposes to overcome is an interesting way to address the rich and complex physics of extra-galactic emission but also the multifaceted world of UV spatial instrumentation. Indeed, throughout this PhD, I have witnessed many milestones in the development of the instrument, as my host institute is the integration site of FIREBall-2 and I have participated in some of them. The following chapter stands for my participation on the characterization of the key component of the instrument's optical design: the grating.

[g]providing a negligible read-out noise.

Chapter 3: Characterisation and efficiency improvement of FIREBall-2 Gratings

Tout ce qui n'est ni une couleur, ni un parfum, ni une musique, c'est de l'enfantillage.

Boris Vian

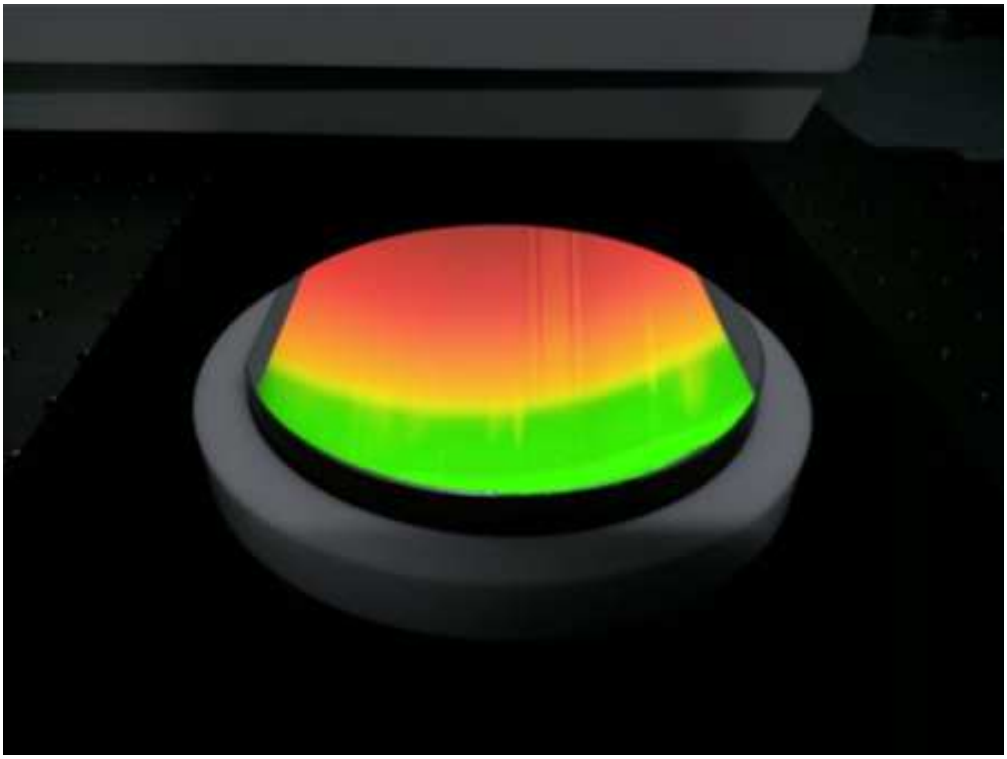

Figure 3.1.: FIREBall-2 flight grating

Here we describe our study on the grating, a critical component of the instrument. This component is causing most of the light losses during its travel towards the detector, it is therefore crucial to understand and improve the grating's efficiency to improve the performance of the instrument.

The technology of UV holographic gratings is of prime interest in many research fields, going from the observation of molecular structures to the observation of infinitely larger objects in the Universe such as the CGM of galaxies. They exhibit interesting properties, such as high sensitivity to resonant excitation of surface waves (commonly referred to as Wood anomalies, Loewen and Nevière, 1977; Caruso et al., 1981; Maystre, 2012). The search for higher UV efficiency, led by the development of UV spectrographs such as the Cosmic Origins Spectrograph (COS), triggered numerous discoveries in terms of coating and polarized behavior (Kuznetsov et al., 2004; Goray et al., 2006), but also in terms of numerical modeling (Goray, 2002). Based on this solid background, FIREBall-2 considered high density groove holographic gratings for the main diffractive element of its new optical design. This analysis is also a preliminary study for further UV gratings to be used for space-based missions, such as the satellite version of FIREBall-2: the Imaging Spectroscopic Telescope for Origins Survey (ISTOS), under proposal to NASA.

After a short presentation of the project time-line, I will introduce part of the work on the gratings within the FIREBall-2 collaboration. This has been published as a SPIE proceeding paper in 2014 (Quiret, Milliard, et al., 2014), and provides the basis of the UV polarized measurements done on a grating sample. I will then present the final experimental setup and modeling technique and apply it to determine FIREBall-2's flight grating's UV efficiency in polarized light within [200; 400]nm. Finally, I will explore a solution proposed in Quiret, Milliard, et al., 2014 to improve the overall efficiency in FIREBall-2's wavelength range using MgF_2 coatings.

Chronology of the projects – gratings

Throughout the project, a number of gratings have been studied and characterized. The first section of this chapter focuses on the characterization of the grating sample (first grating of Table 3.1) available at the beginning of this PhD. This was published as a proceeding paper in the SPIE conference of July 2014 (Montreal), where I present the UV polarized measurements in the range [240-350]nm and propose a solution to improve the efficiency using MgF_2 coatings under FIREBall-2 flight conditions. After the publication of this paper, we improved our UV measurements down to shorter wavelengths (200nm). We received two sample gratings with different MgF_2 coatings (30nm and 70nm, third and fourth gratings of Table 3.1) to validate the solution from the paper down to shorter wavelengths. Meanwhile, the flight grating was produced and measured

Table 3.1.: Summary of the different gratings analyzed in this chapter

Grating name	Size	Coating	section
53013330	50x50mm	bare aluminum	3.1
Flight	110x130mm	bare aluminum	3.2.2
T11	50x50mm	30nm MgF_2	3.3.1.1
T12	50x50mm	70nm MgF_2	3.3.1.2
Spare	110x130mm	70nm MgF_2	3.3.2

(second grating of Table 3.1). Once the MgF_2 samples were measured and the solution validated down to shorter wavelengths, a spare MgF_2 grating was manufactured and characterized (last grating of Table 3.1). These 4 new gratings are the object of the study of the second and third sections of this chapter.

3.1. The FIREBall-2 UV sample grating efficiency at 200-208nm

In this chapter, we present the measurements of a sample of the FIREBall-2 flight grating and an analysis for possible efficiency enhancement via a specific MgF_2 coating. These results are directly extracted from the published paper (Quiret, Milliard, et al., 2014) written in the first year of the PhD (July 2014). At the time of writing, we were only able to measure polarized efficiencies down to 240nm. Of course, several adjustments and improvements were developed throughout the thesis in terms of general knowledge on the subject and in terms of actual measurements and analysis. To this effect, I take the freedom to make some general comments in italic font within the paper and I will present the improvements on the experimental setup and analysis in the following sections.

The FIREBall-2 UV sample grating efficiency at 200-208nm

S. Quiret[a], B. Milliard[a], R. Grange[a], G. R. Lemaitre[a], A. Caillat[a], M. Belhadi[a], A. Cotel[b]

[a]Aix Marseille Université, CNRS, LAM (Laboratoire d'Astrophysique de Marseille) UMR 7326, 13388, Marseille, France
[b]HORIBA Jobin Yvon S.A.S., Avenue de la Vauve - Passage Jobin Yvon, CS 45002 - 91120 Palaiseau - France

Space Telescopes and Instrumentation 2014: Ultraviolet to Gamma Ray, edited by Tadayuki Takahashi, Jan-Willem A. den Herder, Mark Bautz, Proc. of SPIE Vol. 9144, 914432 · © 2014 SPIE
CCC code: 0277-786X/14/$18 · doi: 10.1117/12.2056972
Proc. of SPIE Vol. 9144 914432-1

Abstract

The FIREBall-2 (Faint Intergalactic Redshifted Emission Balloon-2) is a balloon-borne ultraviolet spectro-imaging mission optimized for the study of faint diffuse emission

around galaxies. A key optical component of the new spectrograph design is the high throughput cost-effective holographic $2400\ell/mm$, 110x$130mm$ aspherized reflective grating used in the range $200-208nm$, near $28°$ deviation angle. In order to anticipate the efficiency in flight conditions, we have developed a PCGrate model for the FIREBall grating calibrated on linearly polarized measurements at $12°$ deviation angle in the range $240-350nm$ of a 50x$50mm$ replica of the same master selected for the flight grating. This model predicts an efficiency within $[64.7; 64.9] \pm 0.7\%$ (S polarization) and $[38.3; 45] \pm 2.2\%$ (P-polarization) for the baseline aluminum coated grating with an Al_2O_3 natural oxidation layer and within $[63.5; 65] \pm 1\%$ (S-polarization) and $[51.3; 54.8] \pm 2.8\%$ (P-polarization) for an aluminum plus a $70nm$ MgF_2 coating, in the range $200-208nm$ and for a $28°$ deviation angle. The model also shows there is room for significant improvements at shorter wavelengths, of interest for future deep UV spectroscopic missions.

Resting on a large modeling and observational endeavor in the last decade, a coherent picture has emerged where galaxies evolution develops through a complex and poorly understood balance between accretion of inflowing gas from the intergalactic medium, and expulsion of energy and processed material through powerful winds. To get a grasp on those processes, mapping the ultraviolet (UV) emission lines from matter in the critical $300kpc$ radius region surrounding galaxies is a tantalizing approach, whose main difficulty is the extremely low surface brightness at play.

As a matter of consequence, dedicated high throughput instruments are being developed, such as the spectro-imager Palomar Cosmic Web Imager (PCWI, Martin, Chang, Matuszewski, Morrissey, Rahman, Moore, and Steidel, 2014) which recently provided evidence for a filament of gas inflow on a quasar in the distant Universe where the intrinsic UV light is redshifted at visible wavelengths. At smaller distances, one needs to rely on UV observations from satellite or stratospheric flights.

FIREBall is a NASA-CNES balloon-borne ultraviolet mission (PI C.Martin, Caltech), optimized for the study of the faint diffuse gas surrounding galaxies from emission lines in the range $200-208nm$, being prepared for a flight in the fall of 2015. Its optical design has evolved since FIREBall-1(Milliard et al., 2010) flown in 2009, with the $1m$ diameter parabola now feeding a brand-new field corrected f/2.5 Multi Object Spectrograph in place of the former integral field one. The new resolution is $R \approx 2200$, with a FWHM of 4 arcsec over an instrumented field of view of 400 arcmin^2 (against 16 arcmin^2 for FIREBall-1, Grange, Lemaitre, et al., 2014). It includes after the $1m$ f/2.5 parabola, a unit magnification f/2.5 field corrector re-imaging the focal plane onto a curved slit mask at the entrance of the spectrograph, to ensure a flat field at the detector level. The spectrograph itself is composed of 2 identical spherical mirrors used in Schmidt mount for the collimator and the chamber, with a 110x$130mm^2$, $2400\ell/mm$ reflective aspheric Schmidt grating in between, that both corrects for the combined spherical aberration

of the system, and disperses the light onto a low noise, high UV efficiency 1024x2048 UV EMCCD $13.5\mu m$ pixel developed at Caltech (Hamden et al., 2014), through the chamber. The grating is aspherized using a double replication technique via a metal deformable matrix (Lemaitre, 2009; Lemaitre et al., 2014; Grange, Lemaitre, et al., 2014). The collimated light arrives on the pseudo-plane aspheric grating – bisymmetric freeform – with angles of deviation (AD) in the range $26°$ and $30°$.

Developing high line density gratings with good efficiencies in the UV below $250nm$ is notoriously difficult (Loewen, Nevière, and Maystre, 1977; Maystre, 2012; Kuznetsov et al., 2004; Goray et al., 2006), largely because complex surface phenomena dominate the efficiency in this domain, that require sophisticated algorithms to be accurately predicted. The first FIREBall grating, a highly convex holographic $4800\ell/mm$ grating coated with bare aluminum made by Horiba Jobin-Yvon (HJY) in 2005, achieved only 17.0% efficiency near $200nm$. Following studies of the efficiency of the COS spectrograph whose several gratings fell well below predictions (Kuznetsov et al., 2004; Goray et al., 2006), we made a second grating coated with aluminum and a $54nm$ thick layer of MgF_2, which was measured at 34.4% efficiency near $200nm$. To improve the instrument throughput, the FIREBall-2 spectrograph relevant to this paper was designed with the grating efficiency as one of the main drivers. The short development timescale and limited funding of the balloon programs led us to design an instrument using a quasi plane grating, replicated from the 110x$130mm^2$, holographic plane master 530 13 available at HJY. With a groove depth to step ratio of ~ 0.25 ($\sim 100nm$ depth, $\sim 416nm$ step), the grating lies at the high end of the medium blaze region (Loewen and Nevière, 1977) where strong polarization effects are expected. It is used near lambda/step ~ 0.5 where resonance effects are important and the scalar theory does not apply, below the blaze region in a domain where the efficiency is globally decreasing towards shorter wavelengths, but it turned out to be very efficient in our range. Because of the holographic master, we expect a low scattering level, a key point for a diffuse emission spectrograph. Near $200nm$, there is no impervious need to protect aluminum from oxidation, so the baseline is uncoated aluminum.

We propose in this paper to establish a model for the FIREBall-2 flight grating through polarized measurements in the range $240-350nm$ of a 50x$50mm$ sample replica of the same master used for the flight grating. We present in section 2 the measurements of the sample performed with the LAM Perkin Elmer *Lambda 900* in polarized light, then in section 3 a model using the diffraction efficiency modeling software PCGrate SX 6.4, calibrated to measures performed in the range $240-350nm$ at $12°$AD. In the fourth and last section, we present possible improvements of the grating efficiency via a magnesium fluoride (MgF_2) coating in our range of interest $200-208nm$ at $28°$AD, as well as ways to improve efficiencies at shorter wavelengths in the context of future deeper UV spectroscopic missions.

This is an ongoing work that will soon be improved from new UV measurements at shorter wavelengths and from an optimal extraction of the measured AFM groove profile.

3.1.1. Measurements

In this paper we have been working on a 50x$50mm$ sample replica aluminum (Al) coated ($> 50nm$) on a Pyrex substrate of the $2400\ell/mm$, highly modulated ($h/d \approx 0.25$) holographic master (referenced as 53013 at HJY). This grating has been chosen for its expected low scattering, especially at UV wavelengths, its good blaze and for the clean groove profile. No protective coating was applied on the sample, which was the baseline choice for the next flight of FIREBall because the thin spontaneous oxidation only brings a small efficiency loss in our wavelength range. The incoming beam's field sets a range of $\pm 2^\circ$ incidence in the diffraction direction and in the orthogonal one. Conical diffraction effects have not been accounted for.

As the grating is the element that loses most of the light throughout the spectrometer, it is important to understand its behavior to be able to maximally improve its efficiency. We have built a model to explore different possibilities to optimize its efficiency in our range of interest. This model will be calibrated on efficiency measurements in polarized[a] light. As this paper shows, we anticipate a good in-flight efficiency near $200nm$, despite the fact that we are using the grating significantly away of the blaze wavelength ($250nm$).

3.1.1.1. Instrument and settings

We used the Perkin Elmer *Lambda 900* spectrometer to measure the efficiency of our grating. It consists of a double monochromator ($1440\ell/mm$ holographic gratings), with slit widths (spectral resolution) from $0.05nm$ to $5nm$ and height of $12mm$ maximum, a $60mm$Ø Spectralon integrating sphere and a photomultiplier detector. We use a Perkin Elmer polarizer, whose efficiency drops at $\lambda \approx 240nm$ and has been measured to have a contrast better than $100:1$, which is sufficient for the following considerations.

The measurement of an absolute efficiency is done via the VW accessory of the *Lambda 900*. This setup is not originally designed for grating measurements but for highly reflective mirrors efficiency measurements.

There are two steps to consider with the VW accessory: the first step is the baseline, in the V-mode (figure 3.2). This baseline corresponds to the dark R_0 and the light spectral reference R_{100}. The second step is done in the W-mode, with the sample placed in the dedicated compartment, the beam bouncing twice on its surface. The software associated with the *Lambda 900* evaluates the resulting efficiency via the formula:

$$R_{actual} = \sqrt{\frac{R_{measured} - R_0}{R_{100} - R_0}} \tag{3.1}$$

which only applies when the grating is illuminated in pure S- or P- polarization, a con-

[a] We use the usual convention to describe the different orientations of the electric field: let's call the component of the field which is parallel to the plane of incidence the P-polarized light, also known as *TM* light, and the component of the field which is normal to the plane of incidence the S-polarized light, or *TE* light. In this paper, we use a configuration where the grating is placed so that its grooves are vertical, and the light propagates horizontally, meaning that the P polarization is perpendicular to the groove and the S polarization is parallel to the groove, which differs from usual literature about gratings.

dition which we have checked is fulfilled with enough accuracy in our setup. Measuring in mixed polarization in this setup requires a more complex computation since the illumination at the second bounce has a different (generally higher) degree of polarization than the first one. For this reason, we have placed the sample and the polarizer so that they share a common incidence plane between M1 and M2, defining the base used for the definition of P and S polarizations. Note that all measurement are normalized to a control beam following the exact same optical path as the sample flux (except that it does not enter the VW mounting) and measured on the same detector as the sample beam via a high frequency switching to cancel any changes in the lamp flux level. As the polarizer has a low efficiency in the measurement range, we have set a 90% attenuation to the control beam for the normalization, in order to prevent the detector from swapping between very different intensity during the integration time, as it measures the sample flux and the control flux alternatively.

R_{actual} is the absolute efficiency, as the same optics and mirrors (except the grating) are used and as the beam follows the same optical path in both configurations.

In the W-mode, the grating is placed with the blaze toward the source[b] (configuration of figure 3.2) with an angle x[c] corresponding to a $12°$AD in the -1 order at the wavelength to be measured.

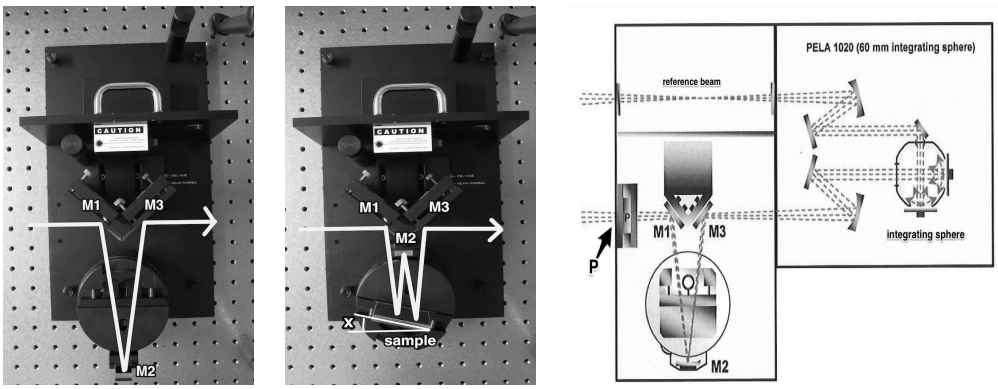

Figure 3.2.: Left: VW geometry. V-mode: the mirror M2 is facing M1 and M3. W-mode: the mirror M2 is rotated $180°$ and the sample placed in between the two M2 positions, with an offset angle corresponding to $12°$AD at the wavelength being measured. Right: Complete set up of polarizer + VW + integrating sphere detector. The reference beam enters the sphere without going through the polarizer (P) and the VW.

The $60mm$ Ø Spectralon integrating sphere accessory is commonly used along with samples that scatter the incoming light, as it spatially smooths out the beam entering the

[b] We have checked that for this high density grating, reversing the light path has little effect as expected from the reciprocity theorem in our regime.

[c] The angle x is defined as the angle between the grating diffracting surface and the external bisector of the V mount beams, see figure 3.2

sphere. Unfortunately, the UV detector stopped working before receiving a more UV polarizer, we therefore are not able to present polarized measurements below $\lambda = 240nm$ in this paper[d]. As the measurements were performed with an angular deviation of $12°$, which does not correspond to the FIREBall flight illumination condition, we have calibrated our model with this angle and extrapolate the solution to $28°$AD. The positive side of it is that we calibrate the model in a region where intrinsic uncertainties in particular on the refractive indices are smaller than at $200nm$ and the measurements are better. A similar approach has been followed by Goray et al., 2006 at shorter wavelengths.

3.1.1.2. Results

We measured the efficiency of the grating using the *Lambda 900* in the VW configuration described above, using a $1nm$ slit width, a wavelength step of $0.5nm$ and an integrating time of $0.32s$. We have checked that the effect of dispersion does not introduce significant systematics with the $1nm$ slit width used. To cover the range, we used 9 offset angles going from $17°$ and $25°$.

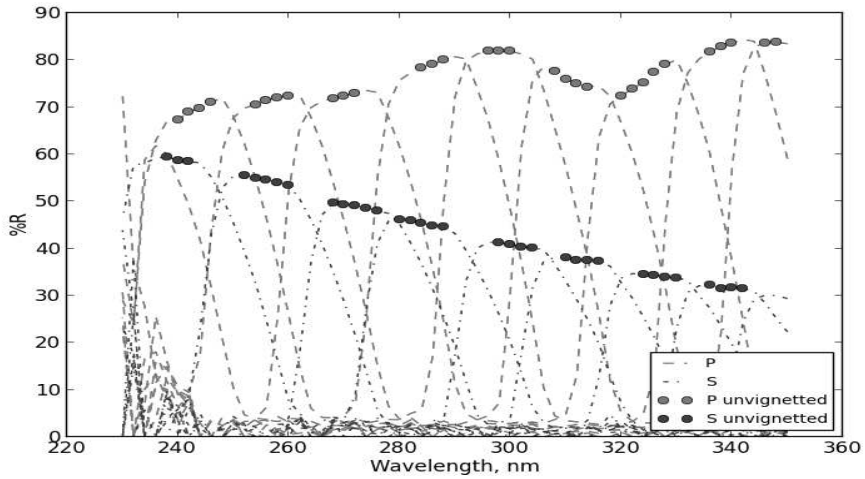

Figure 3.3.: $240 - 350nm$ polarized measurements at $12°$AD done with the integrating sphere. In dark grey the S-light measurements and in light grey the P-light measurements. We observe the presence of sharp slope variations for each curve, corresponding to the detection of the unvignetted beam. The dots correspond to the estimated efficiencies measured from the unvignetted beams.

Figure 3.3 shows the efficiencies measured for both polarizations. For each offset angle, we have been able to measure the grating efficiency in a range of about $10nm$

[d] *In the following sections, the new experimental set up no longer uses the* $60mm$ *Ø Spectralon integrating sphere, as the UV detector was latter fixed by the company.*

without vignetting of the beam. Indeed, if we place the grating at an angle x_0, corresponding to a wavelength λ_0 via the grating formula with a $12°$AD, then for $\lambda << \lambda_0$, the grating diffracts the first order outside of the sphere entrance, we therefore get no flux measured. Then, as λ increases, the beam starts to enter the sphere, and the efficiency goes up until the entire beam gets in, at $\lambda \approx \lambda_0$. As we then detect all the flux diffused by the grating, the measured reflectance corresponds to the effective reflectance (squared) of the grating. Finally, when $\lambda > \lambda_0$, the beam is no longer entirely detected by the sphere and the measured reflectance decreases, until the beam is entirely out of the sphere and the reflectance reaches zero.

The exit beam broadening resulting by the finite $1.0nm$ bandwidth has no significant effect on the measures as it is small with respect to the beam width at the sphere entrance and as the sphere spatially smooths it out.

We notice the presence of an anomaly (Hutley, 1982) around $\lambda = 315nm$ for the P polarization, which will provide a sensitive test for the adequacy of our model.

Note also that the AD perceived by the grating changes from the first to the second bounce and as the wavelength increases.

3.1.1.3. Uncertainties estimation

The measures can be affected by the shot noise, which is negligible given the small dispersion in the measurements along the non vignetted wavelength range at each angular position of the sample.

We used an estimation of the baseline statistical error to compute a total statistical absolute error σ_{stat} of 2% for $\lambda > 250nm$. For $240 < \lambda < 250nm$, the throughput of the polarizer drops sharply, rising the absolute statistical error to about 6%.

We think the systematics are low and dominated by:

- the imperfection of the alignment of the polarizer with the grating sample, on one hand, and with the rest of the detection chain, on the other hand. The constraint is loose, though: we have computed that these two contributions to the systematics are below 0.5% (absolute) if the alignments are better than $5°$, which was reached easily.
- unwanted changes in the angular deviation angle within an angular position of the sample of about $2.5°$ (figure 3.3). This is observed as slight discontinuities in the efficiency curve between the successive non vignetted ranges for each angle of the sample, calling for a systematic error of about 2% (absolute).

The systematic in the wavelengths are negligible as we have $\sigma^{\lambda}_{syst} = 0.08nm$ (Perkin Elmer, 2001).

3.1.2. Grating modeling

Our goal is to develop a model for our grating to predict the efficiency in the flight illumination conditions. The first step consists in establishing a realistic model of the groove profile, that will be processed with the diffraction efficiency modeling software, PCGrate (International Intellectual Group, 1996). The model is then calibrated using

our $12°$AD measurements (see section 3.1.1) and extrapolated at $28°$AD to predict the efficiency under flight illumination conditions in the current state of the grating, and with a suitable MgF_2 coating (test sample currently being processed at HJY).

3.1.2.1. Software

PCGrate runs on various types of relief and phase grating. It is a tool that calculates grating efficiency by an accurate boundary integral equation method. It can work either with models of grating (blazed, sinusoidal, ...) or with an user provided profile, and can be used with many coating layers with customizable refractive indices (RI). We used the 'Penetrating Solver' for our calculations (as we plan to model a thin-oxidized grating), with a finite low border conductivity.

The choice of the RI library for materials in thin layers in the UV is still being debated, so we have chosen to first create our model based on the Palik's handbook (Palik, 1991), and then compare the results with the AIP's handbook (Gray, 1972).

In this work, we have ensured the 3 following convergence criteria are always checked:

- each step must have a positive absorption
- the final energy balance must be close to 1 by 1% (knowing that a possible loss in the total balance may be expected from anomalies, Hutley, 1982)
- the critical angles parameter must be null

We also used for almost all our calculations a number of collocation points of 300, which corresponds to the number of quadrature nodes used in the profile. This number was sufficient to reach the criteria evoked above while keeping a workable computing time. For layers below $3nm$ thick, a number of collocation points of 500 has been used.

In order to validate our handling of PCGrate in similar conditions, we have checked that we can reproduce a result from Loewen, Nevière, and Maystre, 1977: we simulated a $1200\ell/mm$ trapezoidal grating (blaze angle of $10°$) with an angle of deviation of $8°$ and computed the efficiency in the non-polarized and polarized lights and in the finite conductivity configuration. We obtain very similar results, both in terms of curve behavior for both the polarized lights S and P, with even more details in the anomalies with our model (due to a high number of collocation points) as in terms of efficiency values. This therefore comforts us with the following modeling and calculations characterizing our sample.

3.1.2.2. Model

3.1.2.2.1. Profile determination A real boundary profile of the Al coated sample, measured by Atomic Force Microscopy (AFM)[e], has been provided by HJY for our grating, overlapping a little more than 4 periods.

In order to use the maximal information from the AFM measurement, we have entered in PCGrate the 4 available steps as a whole, instead of averaging them to build a single

[e] on a 2.0 x $0.3\mu m^2$ area and average over the width, with no correction from the tip radius effect

step, which should be more representative of the grating than a single step profile. Note that in this approach one has to use the computed 4th order to predict the first observed one, and a period 4 times larger for the density spacing. In addition, following Goray (private communication), the PCGrate computation had to be performed with the blaze oriented toward negative X values.

The main problem we met was the use of an uncalibrated AFM[f]. We have extracted a $1778nm$ length profile corresponding to our estimation of four complete steps, corresponding to a groove density of about $2249\ell/mm$. We have checked with a goniometric measurement, using the first order diffraction of a $632.8nm$ laser, that the grating was indeed a $2400\ell/mm$. We therefore adjusted the period of our profile to $1/2400\ell/mm = 416.67nm$. As a first guess, we assume that the default in calibration was the same for both axis, and we therefore chose a groove height h that would respect the original h/d ratio given by the raw AFM (d being the period). We then start with $h = 96.3nm$ (min to max over the 4 steps), a value that will be adjusted later from the efficiency measurements of the sample (see section 3.1.2.4).

This paper has been based on the groove profile described in the above paragraph. Nevertheless, in the process of testing the sensitivity of the results to the length of the extracted profile, we have discovered that a slightly shorter value ($1738.5nm$ for 4 steps, or $434.6nm$ for a single step and a groove density of $2301\ell/mm$) provides a better periodicity of the profile, with higher values of the autocorrelation function near multiples of one step. This came too late to be used thoroughly in the present paper, but we have checked the differences are small, and we discuss how this affects our uncertainties in section 3.1.3.1.1 and in the conclusion.

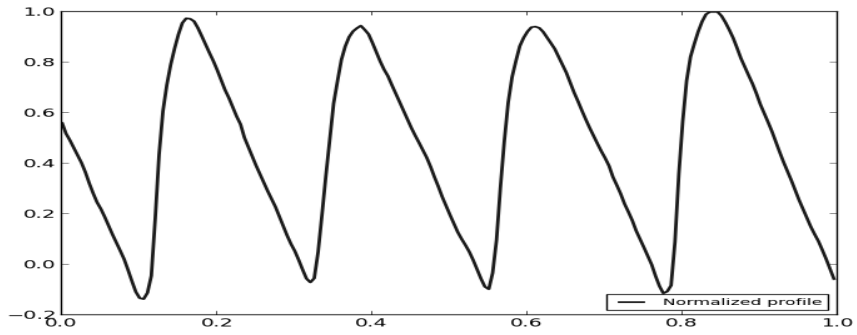

Figure 3.4.: Full AFM profile, normalized in the x- and y- axis, of the Al coated sample provided by HJY.

3.1.2.2.2. PCGrate's first model There are many parameters that may impact the model output, but the most important by far is the groove profile, as described in

[f] *This issue has been solved following the publication of the paper. Indeed, we measured with the same AFM calibration nano-chips, and it appears that the AFM was well calibrated at the time of writing.*

section 3.1.2.2.1. However, the small and unique area covered by the AFM limits its representativity of the complete sample.

We have explored the effect of two free parameters to fine tune the model: the unknown oxidation layer thickness (strongly dependent on the environment and surface conditions) and the unknown groove depth (assuming the default in the AFM calibration to be different for the x- and y-axis). As mentioned above, we start with a groove depth of $96.3nm$ for the estimation of the Al_2O_3 thickness (a refinement will be performed below) and we explored the efficiency for a range of groove depths from $80nm$ to $110nm$. As for the Al_2O_3 layer thickness, the natural oxidation process usually results in a layer of a few nanometers, and we decided to calculate the efficiency for a range of Al_2O_3 thickness from $2nm$ to $15nm$. We based the fine tuning of the model on the Palik's RI library.

As for the layer modeling, we must consider 2 different setups: the grating sample, which has a Pyrex substratum, and the flight grating which will have a Zerodur substratum. As there are no UV RI libraries available for Pyrex and Zerodur in the literature, we decided to use a model based on a silicon dioxide (SiO_2) substratum. We compared the results of a semi infinite Al layer against a semi infinite SiO_2 layer with a $50nm$ Al layer, and the difference is just about a few percents from $140nm$ up to $350nm$. One possible cause for this lies in the fact that Al has a rather small light penetration (it has a skin depth of about $2.18nm$ at $200nm$, meaning that at this depth about 63% of the current density has been absorbed) so that the choice of the substratum has very little optical impact.

We will thereafter use a semi infinite SiO_2 substratum with a $50nm$ Al coating.

We assume the layers to be conformal, which means that the profile of each layer is obtained simply by vertical translation of the profile of the layer below.

Note that the $\lambda > 200nm$ range is a regime where the RIs are reliable, allowing for a good determination of the boundary profile as in Goray et al., 2006, in our case essentially a rescaling of the profile height.

3.1.2.3. Efficiency as a function of Al_2O_3 thickness

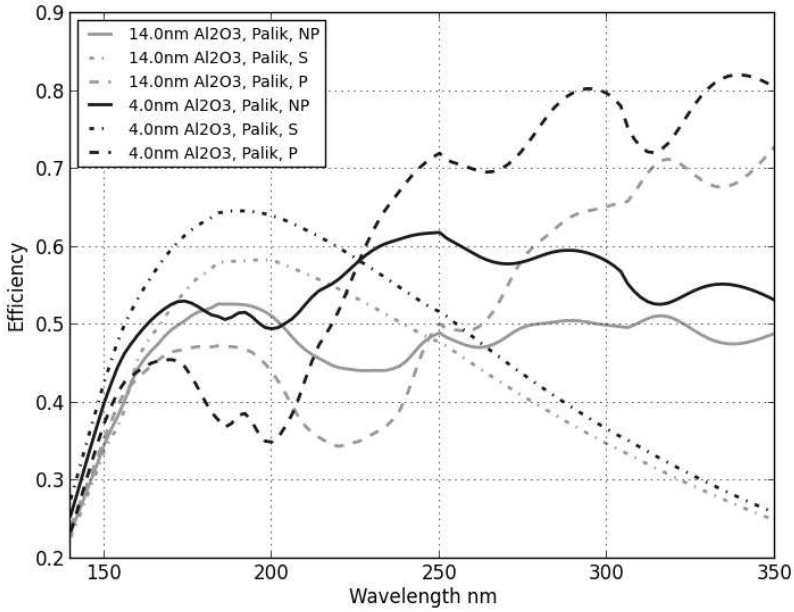

Figure 3.5.: Efficiency curves (12°AD) of the model with $4nm$ (dark grey) and $14nm$ (light grey) of Al_2O_3: non-polarized efficiency (solid line), P-light efficiency (dashed line) and S-light efficiency (dot-dashed line). The RI used are from Palik's handbook.

The efficiency is strongly dependent on the Al_2O_3 thickness. Figure 3.5 shows polarized and non-polarized efficiencies of the model with the characteristic thicknesses of $4nm$ and $14nm$. We notice that while the S-light curve keeps the same shape with essentially a multiplicative change from 4 to $14nm$, the P-light curve presents significant differences. Indeed, the anomaly around $\lambda = 325nm$ gets shifted towards longer wavelengths with higher Al_2O_3 thickness, and the crossing point between S-light and P-light shifts from $\approx 220nm$ at $4nm$ Al_2O_3 to $\approx 250nm$ at $14nm$ Al_2O_3.

3.1.2.4. Confrontation to the measures

The best match to measures is reached for an Al_2O_3 thickness of $3.7nm$ and a groove height of $102nm$: figure 3.6 shows the efficiency curves in both polarizations given by PCGrate with Palik and AIP's librairies along with the measurements. The S-light curve has been fitted to the measures by adjusting the height of the profile, and is not strongly dependent on the choice of RI's library. The P-light curve is more sensitive to the Al_2O_3 thickness, and is more dependent on the RI's library used for the calculations (probably due to higher sensitivity to surface plasmon resonance). We are able to

predict the anomaly around $\lambda = 320nm$, but the measured anomaly is slightly weaker than the calculated one. We are also able to predict the crossing-point of the S and P polarizations at $\lambda \approx 240nm$.

We point out that, as the correction for the AFM tip radius effect has not been accounted for, the comparison between the model and the measurements maybe slightly biased, an effect presently under investigation.

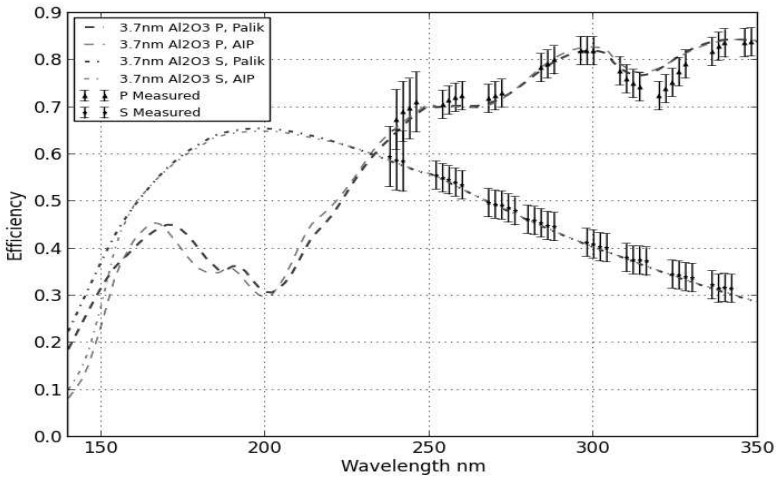

Figure 3.6.: Comparison between efficiency measurements ($12°$AD) with the Perkin Elmer polarizer (stars and triangles) and the adjusted model with a groove height of $102nm$ and a $3.7nm$ Al_2O_3 thickness, with two RI librarys: Palik (black thick line) and AIP (grey thin line), non-polarized efficiencies (solid lines), P-light efficiencies (dashed lines) and S-light efficiencies (dot-dashed lines). The error bars correspond to the statistical errors determined from a verification of the baseline, and the identified systematics.

3.1.3. Prediction for flight conditions and improvements

In this section, we will use our model calibrated at $12°$AD to study the efficiency expected with our current baseline grating (Al_2O_3 layer) at $28°$AD (flight illumination conditions) and ways to optimize the efficiency in the FIREBall wavelength range using a MgF_2 coating. We will also study how the groove density or the groove depth impact the efficiency, in the perspective of future UV spectrographs working at shorter wavelengths.

3.1.3.1. MgF2 coating

MgF_2 coatings are usually used for UV gratings because they prevent natural oxidation which degrade efficiency at UV wavelengths below $220nm$, while not having much

optical influence when used in thin ($\approx 10nm$) coatings (Loewen and Neviere, 1978). Conversely, very thick coatings (above 100nm) can have disastrous effects on gratings efficiency. Moreover, particular care must be taken when dealing with dielectric coatings because they act as wave guides, causing absorption (Wood anomalies), or simply shifting the anomalies to other wavelengths. However, such coating can be used to improve the efficiency (via shifts of anomalies for example) as it had been measured for the previous FIREBall configuration[g].

We study here the effects of MgF_2 conformal coating on the grating efficiency. Such a coating is applied directly after the Al coating, so that no oxygen enters the installation between the two coatings, and no Al_2O_3 can form between the Al and the MgF_2 layers.

As for Al_2O_3 above, we assume conformal coatings and apply a simple vertical translation of the profile determined from the AFM measurement of the aluminum-coated sample to the two other layer interfaces. This assumption has weak implications for the underlying substrate, because of the near opacity of the aluminum coating, but needs be checked for the MgF_2 layer whose shape has significant effects on the efficiency, in particular for coating thicknesses reaching the groove depth (about $100nm$), where significant non conformal effect are known to occur (Goray et al., 2006).

At the time of the writing, we have not received the $40nm$ and $70nm$ MgF_2 coated samples yet, therefore we are not able to study the non conformality of the coating layer.

As FIREBall-2 grating works with a range of ADs from $26°$ to $30°$, we apply the $12°$AD calibrated model to the $28°$AD flight illumination conditions for all the following simulations.

3.1.3.1.1. Efficiency diagrams Figure 3.7 shows the efficiency diagram of the grating at $28°$AD, as a function of wavelength (x-axis) and MgF_2 conformal coating thickness (y-axis), using the Palik's handbook for the RIs of SiO_2 (semi infinite layer), Al ($50nm$ layer) and MgF_2. The two vertical lines represent the FIREBall-2 wavelength range of interest ($200 - 208nm$).

[g] A $54nm$ MgF_2 coating rose the efficiency of the grating from 17% to 34.4% in the band of interest.

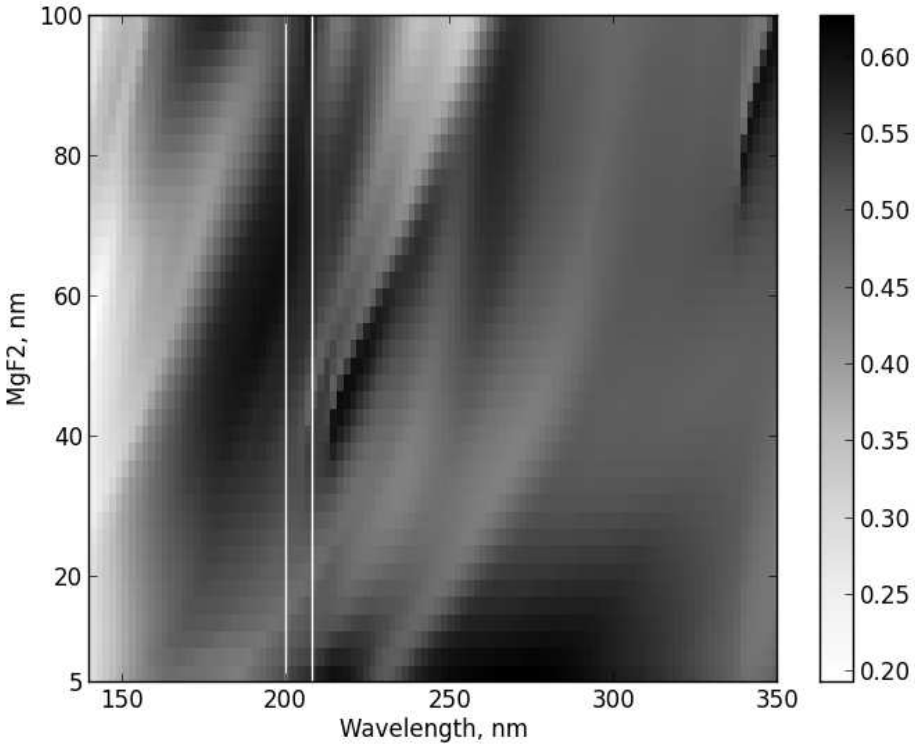

Figure 3.7.: Non-polarized efficiency diagram for the grating at $28°$AD with a groove height of $102nm$, $50nm$ of Al and a semi-infinite layer of SiO_2, as a function of MgF_2 thickness (y-axis) and wavelength (x-axis). The RI used are from Palik's handbook.

We can clearly see from this diagram the behavior of the anomalies: as the MgF_2 thickness rises, the anomalies get shifted to longer wavelengths. We also note that the efficiency rises strongly with thinner MgF_2 coating thickness, at $220nm$ and $275nm$[h]. This efficiency decreases as the coating thickness increases for all wavelengths (e.g. for $\approx 20nm$ MgF_2 in our range) then rises again for thicker coatings (e.g. from $\approx 40nm$ MgF_2 in our band of interest and above $100nm$ thickness). Figure 3.8 shows the non-polarized and polarized efficiency curves of the modeled grating at $28°$AD:

- with a natural oxidation layer of $3.7nm$ of Al_2O_3 (grey curves) representative of the current state the grating
- with a $70nm$ thick MgF_2 layer (black curves). This thickness has been selected as optimal for FIREBall-2 range of interest from the efficiency diagram (figure 3.7).

[h]In a separate computation, we have also noted that the high efficiency of bare Al is well preserved with thin (few nanometers) MgF_2 layer.

All calculations were done using the Palik's RI library (thick lines) and the AIP's RI library (thin lines).

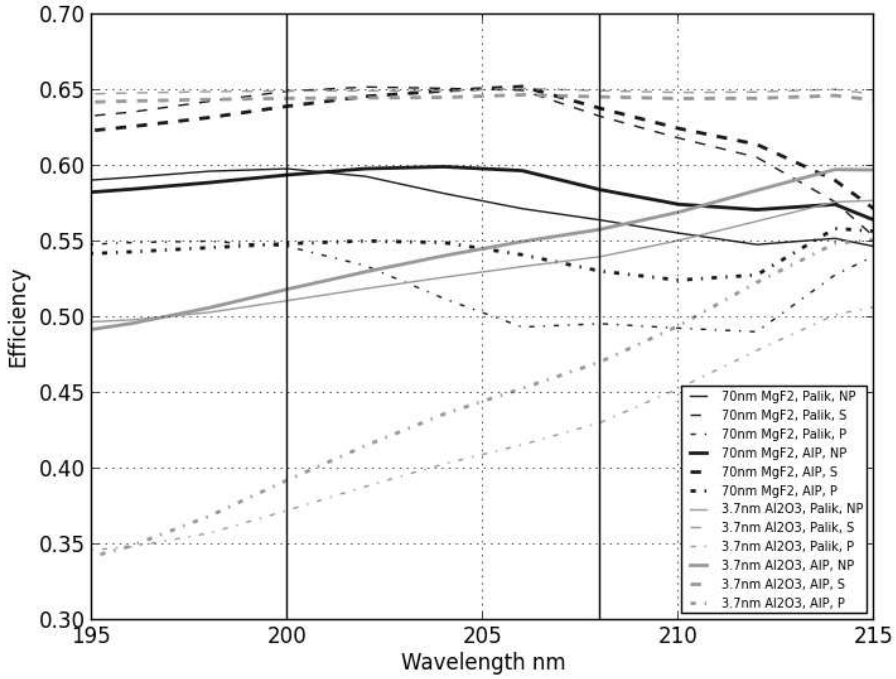

Figure 3.8.: Comparison between the baseline efficiency at 28°AD with $3.7nm$ of Al_2O_3 (grey) and a $70nm$ MgF_2 coating (black): non-polarized efficiencies (solid lines), P-light efficiencies (dashed lines) S-light efficiencies (dot-dashed lines). The thick lines correspond to the Palik library and the thin lines to the AIP library.

The baseline non-polarized efficiency that we expect to reach in the bandpass $204 - 208nm$ with the current Al coated grating at 28°AD is within $[51.4; 55] \pm 0.9\%$[i]. We also notice a strong polarization, with $\sim 64.75\%$ at $204nm$ for the S-light efficiency against $\sim 42\%$ at $204nm$ for P-light efficiency, or a ratio about 1.5 between the two. The P-light efficiency is more sensitive to the library used as it is the polarization that is more prone to plasmon resonance absorption (Wood's anomalies).

The diagram also shows that a $70nm$ conformal MgF_2 layer could improve the P-light efficiency, rising the non-polarized efficiency in our band above the 55%, with $[63.5; 65] \pm 1\%$ for the S-light efficiency against $[51.3; 54.8] \pm 2.9\%$ for P-light efficiency. This coating's main effect is to improve the P-light efficiency, the S-light efficiency being totally unaffected in this range.

[i]The uncertainties are evaluated considering the differences resulting from the choice of the RI library and considering the effect of the AFM extraction for the groove profile.

The two RI libraries show a good agreement down to $\lambda = 160nm$ (about 4% absolute difference in our band for the P-light and 1% for the S-light), but for shorter wavelengths the two polarizations show different behavior on the model.

A model based on an AFM groove profile derived from an optimal length extract of the AFM profile as described section 3.1.2.2.1 has been calibrated on measurements for the groove height, with an optimal value of $96nm$ for the groove height. In the allocated time it has not been possible to also adjust the Al_2O_3 thickness. This improved AFM-based model shows efficiencies in non-polarized light that differ from those calculated above by 2% (resp. 1%) for the Al_2O_3 layer and 3% (resp 2%) for the MgF_2 $70nm$ thick coating at wavelength above $250nm$ (resp. in the FIREBall bandpass near $204nm$), for both AIP and Palik's RIs. This provides confidence on the data derived near $204nm$ in this paper with our sub-optimally extracted AFM groove profile.

3.1.3.1.2. Robustness of the model prediction While waiting for the $40nm$ and $70nm$ MgF_2 coated samples from HJY, along with the post coating AFMs, we wanted to challenge the conformity of the coating and see how slight modifications would impact the efficiency. One way to proceed is to assume a sinusoidal default: $L_2(X) = L_1(X) + 70 - A\cos\left(\frac{2(X-X_0)}{d}\pi\right)$, where L_1 and L_2 are the layers' profiles in nanometers, A is the amplitude of the default (we took $A = 10nm$ and $A = 20nm$ in our simulations), X_0 is the position of the first maximum and d is the period (figure 3.9). This default tends to reproduce a non homogeneous MgF_2 deposit by increasing the thickness in the flat part of the profile and decreasing it at the peaks, reproducing some kind of erosion on the profile. It is clearly an arbitrary default illustrative of the robustness of the profile.

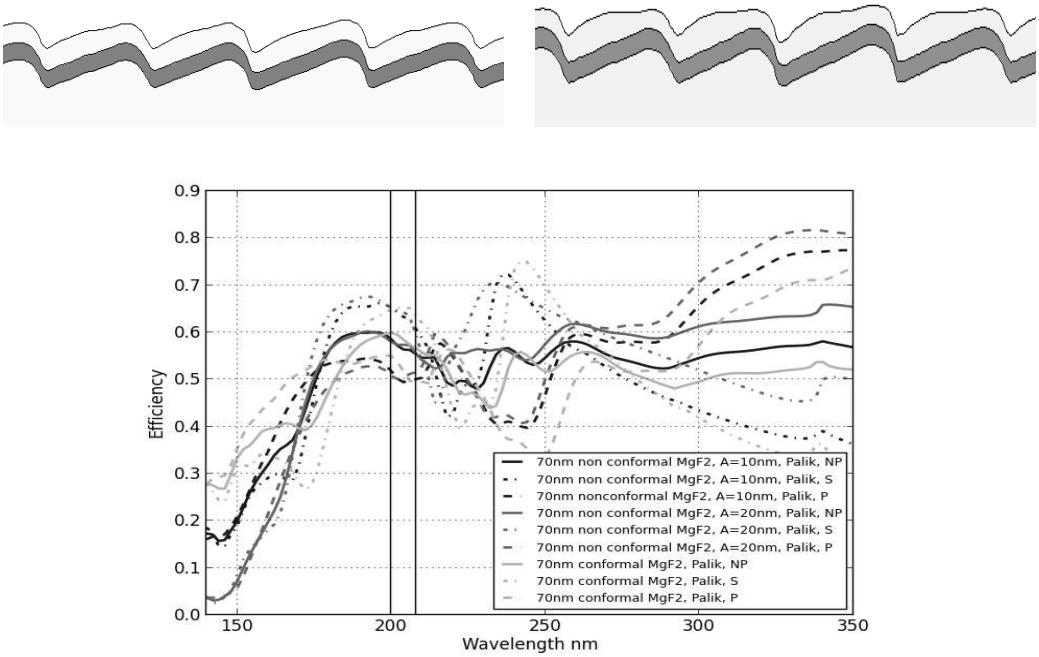

Figure 3.9.: Top left: $70nm$ MgF_2 groove profile with $A = 10nm$ deformation. Top right: $70nm$ MgF_2 groove profile with $A = 20nm$ deformation. Bottom: Comparison of the efficiencies (28°AD) between the $70nm$ MgF_2 conformal layer (light grey), $A = 10nm$ non conformal layer (black) and $A = 20nm$ non conformal layer (dark grey) in non-polarized light (solid lines), P-light (dashed lines) and S-light (dot-dashed lines).

Figure 3.9 shows that the efficiency predicted at $200nm$ is robust against such non conformality even though it is strongly dependent for longer wavelengths.

3.1.3.2. Application to shorter wavelengths

In order to evaluate the performance of this type of gratings at shorter wavelengths, and even though we don't have at hand other samples for measurements, we have studied the effects of slight modifications in the grating's characteristics, namely the groove density and the groove height, on the efficiency. Figure 3.10 shows the non-polarized efficiency for our model with a $70nm$ thick conformal MgF_2 layer (using Palik's RI library) for different grating characteristics:

- Left: we varied the groove density of the grating ($2200\ell/mm$ in dark grey, $2400\ell/mm$ in grey and $2700\ell/mm$ in light grey), keeping the same profile height of $96.3nm$. We notice that the efficiency curve shifts toward shorter wavelength as the density increases.
- Right: we varied the height of the profile ($105nm$ in light grey, $96nm$ in grey and $85nm$ in dark grey), keeping the same groove density of $2400\ell/mm$. There is also

a shift in the efficiency behavior toward shorter wavelengths as the groove height decreases.

Both parameters provide ample room for efficiency optimization at shorter wavelengths. On top of that, in the same wavelength range, an additional efficiency gain can be provided for each case through the optimization of MgF_2 thickness. For instance, in the current baseline grating, a coating between 50 and $90nm$ of MgF_2 would provide significant improvements on the efficiency (figure 3.7).

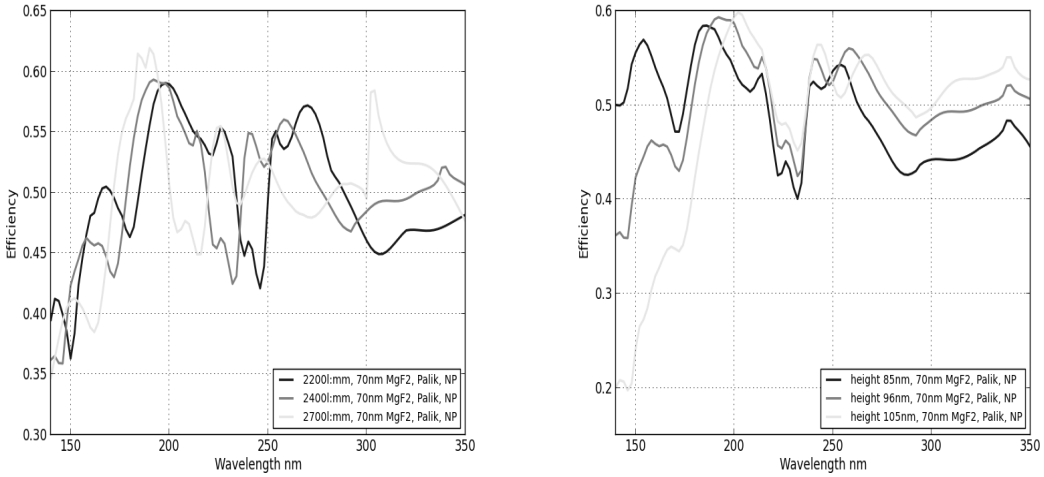

Figure 3.10.: Left: Comparison of non-polarized efficiency ($28°$AD) with varying groove densities (left) and varying groove heights (right), using a $70nm$ conformal MgF_2. The RI used are from Palik's handbook.

3.1.4. Conclusion

3.1.4.1. Model and possible improvement

Based on our model calibrated against polarized measurements of a sample grating replica in the range $240 - 350nm$ at an angular deviation of $12°$, we anticipate a well in-specs performance for the FIREBall-2 flight grating in the range $200 - 208nm$ at $28°$ angular deviation. With the baseline option of an aluminum coating with natural oxidation we anticipate an efficiency within $[38.3; 45] \pm 2.2\%$ (P-light) and $[64.7; 64.9] \pm 0.7\%$ (S-light) in the range $200 - 208nm$, i.e. $[51.4; 55] \pm 0.9\%$ in non-polarized light, with only a small dependency of the choice of the refractive index library. This efficiency can be improved, according to this model, with the deposition of a $70nm$ layer of MgF_2. This layer would push the non-polarized efficiency up to $[57.3; 59.5] \pm 1.5\%$, assuming a conformal layer.

An additional benefit of a $70nm$ thick MgF_2 coating is the relative stability of the efficiency versus MgF_2 coating thickness near this value, making it tolerant to the deposit

thickness. Two samples repectively coated with $40nm$[j] and $70nm$ thick MgF_2 layers are being fabricated at HJY to check those predictions from measurements in the range $200 - 208nm$, and the conformal layer assumption with post-coating AFM profiles. A quick study of the non conformality of the layer points to a robust prediction of the model for flight conditions. We also plan on improving the current model with polarized measurements down to $\lambda = 175nm$ (with a N_2 purge of the Perkin Elmer spectrometer) using a more UV Glan-Laser polarizer from Thorlabs which has a contrast ratio of $100,000:1$ this fall, and by considering a better extraction from the AFM optimizing the periodicity of the groove profile, although we have checked that the differences in efficiency between the profile used in this paper and the periodicity-optimized one are small and don't affect the conclusions of the paper.

3.1.4.2. Polarization

Another interesting feature of the FIREBall spectrograph is the polarization induced by the grating. In the baseline configuration, we expect to reach a ratio of about 1.5 at $204nm$, between S and P-light efficiencies. This can be used to study the polarization of the medium surrounding the galaxies by observing the same target with two different orientations of the spectrograph. The degree of polarization is lower with the MgF_2 layer deposit, as it improves the P-light efficiency by about 10% (absolute).

3.1.4.3. Perspectives

In the perspective of deeper UV spectroscopic missions, we have studied possible factors that may improve the efficiency, compared to the current baseline grating. We therefore expect that a higher groove density or a lower groove height may shift the interesting peak in non-polarized efficiency towards shorter wavelengths, that could provide non-polarized efficiencies above 50% down to $140nm$. For each of these factors, the same MgF_2 thickness optimization is still an option for an additional efficiency gain.

ACKNOWLEDGMENTS

SQ acknowledges CNES support for the CNRS-CNES funding of this PhD. We acknowledge Leonid Goray's support during the modeling. We acknowledge pertinent comments from Kjetil Dohlen and the efficient support in measurements by Sandrine Pascal and Gabriel Moreau. The FIREBall project, a NASA/CNES mission, is funded by CNES for the French part.

[j] *A 30nm coated sample was in fact manufactured.*

3.2. Flight Grating

The previous section introduced an innovative method to measure the efficiency of a grating sample in polarized light. However, these measurements could only reach wavelengths down to 240nm, which is not enough to estimate the FIREBall's grating performances in the working conditions of the instrument. Here we propose an extension of these measurements to shorter wavelengths, using a new experimental set-up, along with a method to accurately model the grating's efficiency in any configuration.

3.2.1. Characterization improvements

3.2.1.1. Experimental improvements

New Polarizer - GLB10 In section 3.1, no measuremetns below $\lambda = 240\text{nm}$ were possible, mainly because the polarizer available at that time was not designed for UV measurements and because the $60mm$ Ø Spectralon integrating sphere was used instead of the regular UV detector. We acquired 2 UV polarizers (*GLB10* from Thorlab) which enable polarized measurements down to 200nm. These are Glan-Laser α-BBO Polarizers, with a single-layer MgF_2 anti-reflection coating (SLAR-MgF_2) offering good UV performances in the range 210nm - 450nm (Thorlabs, n.d.).

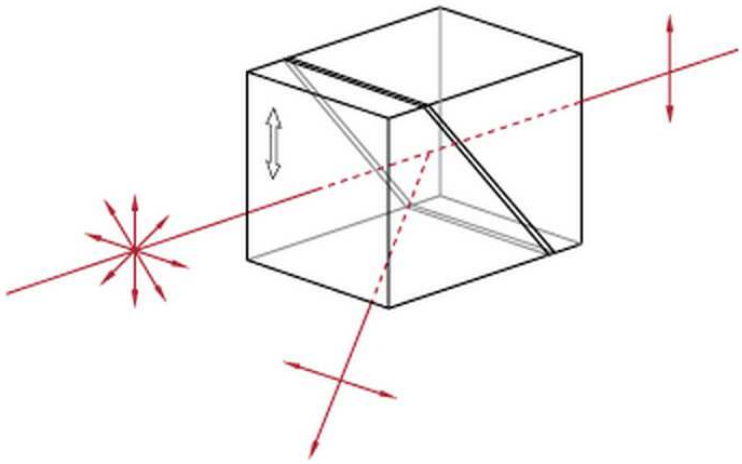

Figure 3.11.: Sketch of the GLB10 polarizer. Here, a non-polarized beam enters the front face of the polarizer. The beam splitter then reflects the S-polarization and only the P-polarization gets through the device in the same direction as the incoming beam. Credit: Thorlabs, n.d.

The Glan-Taylor Design (Air-Spaced Birefringent Crystal Prisms) of the GLB10

enables total reflexion of one of the polarizations, while the other gets transmitted. Fig. 3.12 shows the range of angles available for the opening window with respect to wavelength. Between FOV1 and FOV2, only the polarization of interest gets through. Above FOV1, there is direct transmission of both polarizations, and below FOV2, there is direct reflection of both polarizations. Special care has been taken to ensure that the outcoming beam is purely polarized:

- For $\lambda > 250\text{nm}$: we used a wedge of $\sim .45\text{mm}$ to produce a $1.5°$ shift for the polarizer, in order to recenter the field on FOV2 and get away from the FOV1 limit.
- For $\lambda < 250\text{nm}$: no wedge is used. Indeed, there is total reflection of both polarizations below FOV2.

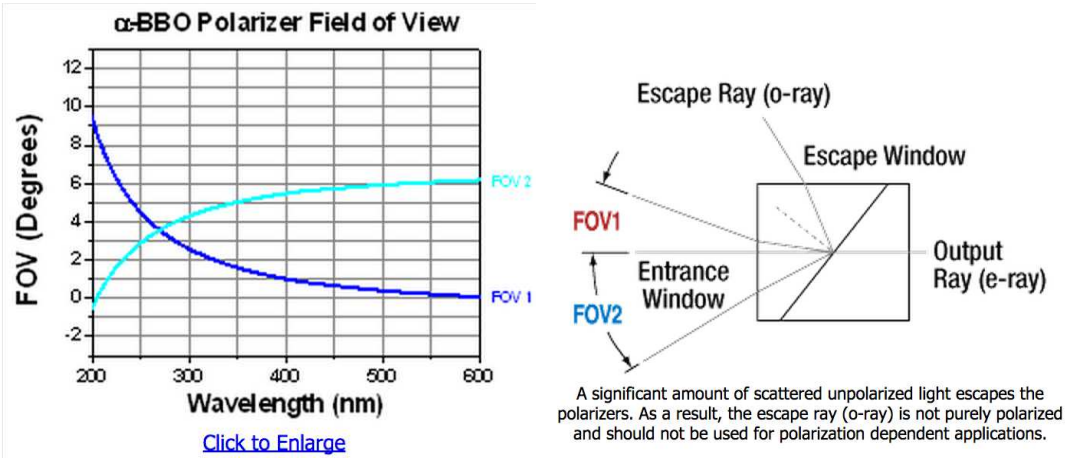

Figure 3.12.: Left: α-BBO Polarizer Field of View. Right: Sketch of the different angular configurations of the GLB10. Credit: Thorlabs, n.d.

New Detector The UV detector from Perkin Elmer has been revised following the publication, allowing UVer measurements. We made sure regularly that the measure and reference beam occupy the same spot centered onto the detector area.

New experimental setup I designed an experimental setup to reproduce and compare the measurements of the 4 new gratings. Little has changed with respect to the method described in section 3.1, apart from the nomenclature and the care used in ensuring the creation of a purely polarized beam.

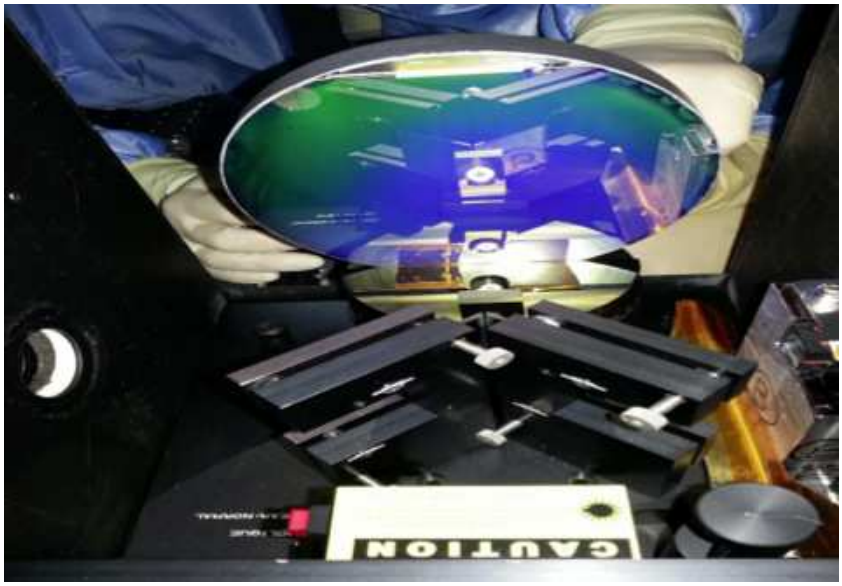

Figure 3.13.: Flight grating being mounted on the Perkin Elmer in its W-mode. Manipulator: R. Grange.

To ensure a reproducible set up from one measure to the other, we manufactured two polarizer holders. Their purpose is to hold the polarizers at beam height. They are positioned at a fixed distance from the edge of the VW device to center the beam in the entrance face of the polarizer. Also, to account for the narrow angular window of the new polarizer (Fig. 3.12), we have added a mask on a pupil of the Perkin Elmer optical path to ensure an acceptable and similar angular range of the incoming beam in the horizontal and in the vertical direction.

Once the polarizer is in place, we perform a baseline in the V mode (one at 0% and one at 100%) in order to normalize the flux for the measurement. To verify that the lamp is in the stationary regime, we then perform a blank measure, to make sure we retrieve a 100% signal at all wavelengths (top panel of Fig. 3.14). This is done before and after each measure to ensure that the polarizer holder has not moved during the grating's manipulations within the Perkin Elmer. This measurement also gives us a systematic error coming from the lamp illumination. We then place the second polarizer in the opposite polarization state as the first one, to make sure the beam coming out of the first polarizer is polarized before measuring the grating. This measurement gives us the contrast reached by the polarizer for each measurement (bottom panel of Fig. 3.14).

This special care in making a purely polarized beam is systematically taken for each change of polarization during the experimental sessions. This guarantees that the measurements are purely polarized.

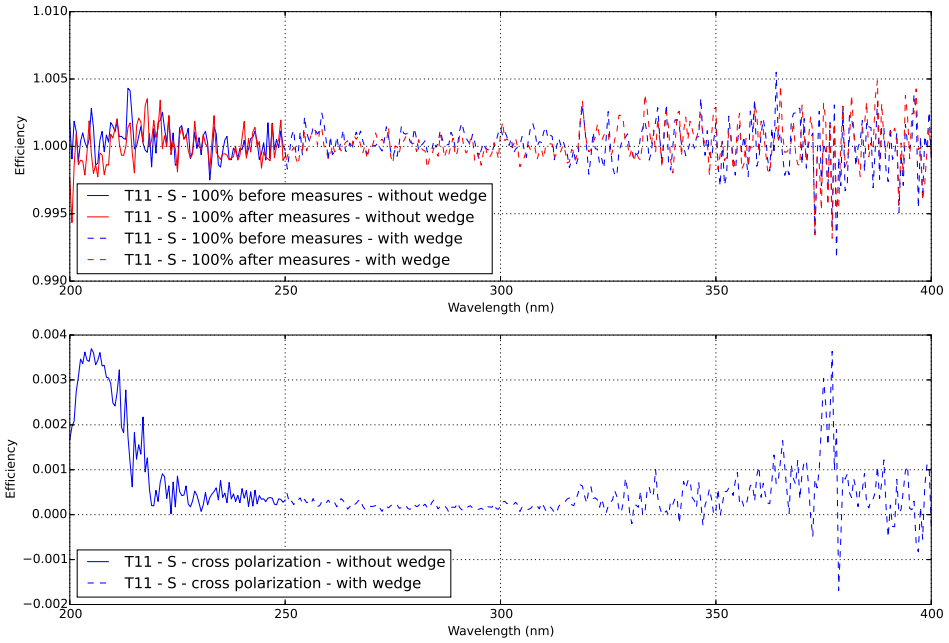

Figure 3.14.: Top: verification of the baseline before and after the measurements on the sample 53013330 T11. Bottom: Verification of the purity of the S polarization by cross polarization on the sample 53013330 T11. Between these two panels, the only difference is the addition of the second polarizer in the P mode.

The errors were determined by multiplying the slope of the plateau at the middle point of each measure (Fig. 3.15) by the range of uncertainty in the wavelength determination (fixed at 2nm around the middle point). We quadratically add an error of 0.5% from the 100% calibration and polarizer contrast, and an error of 0.5% from misalignment of the grating with respect to the mirrors.

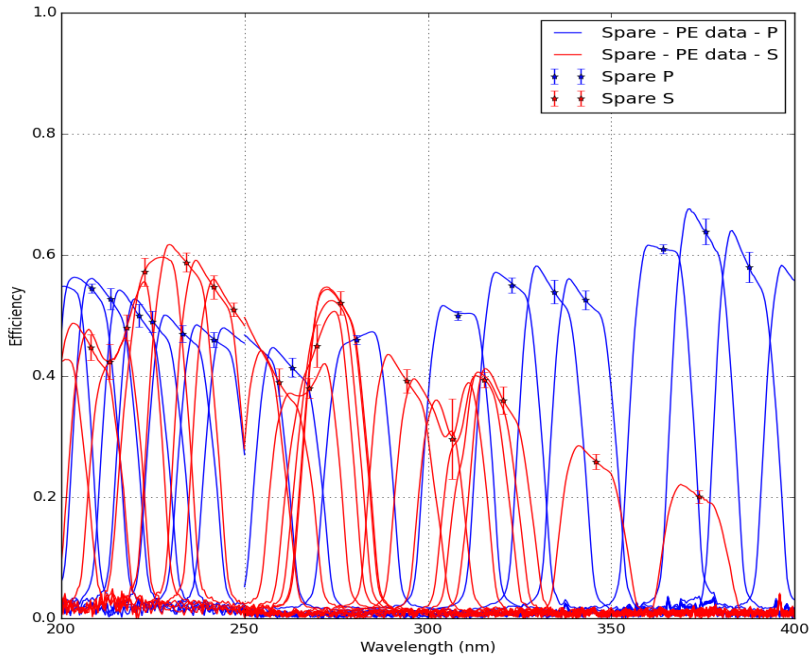

Figure 3.15.: Perkin Elmer output on the Spare measurement, with the chosen data points and error bars.

Validation of the new experimental set-up Fig. 3.16 compares the measurements of the 53013330 sample in both polarizations from the paper with the new experimental setup presented above. In addition to the extension of the range of wavelengths probed to [200; 400]nm, the measurements in both polarizations are in very good agreement in the previous wavelength range [240; 350]nm. Indeed, the shapes and level of both polarizations agree, and the anomaly for the P-polarization at 320nm is still present.

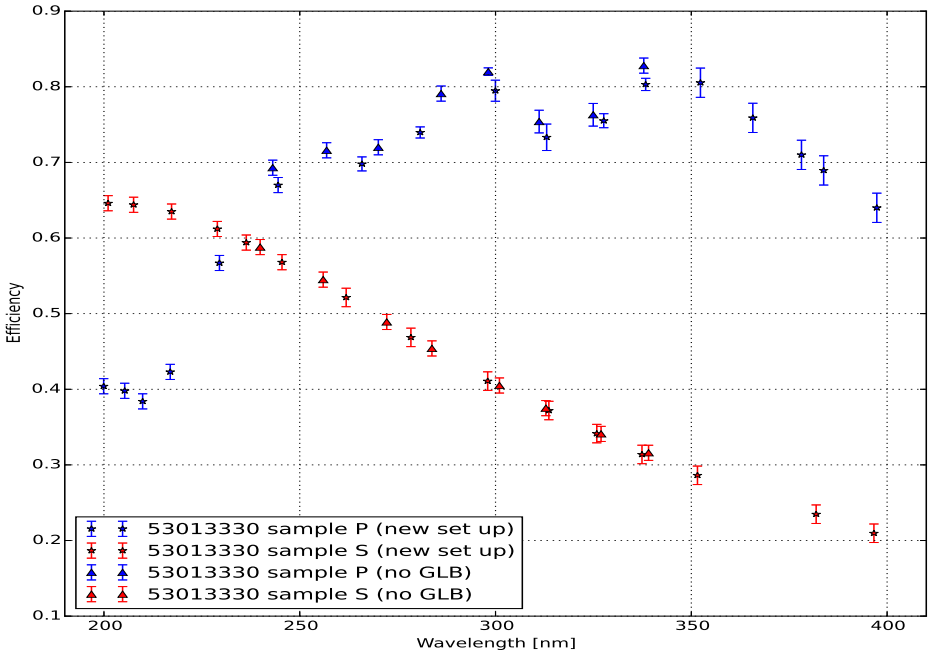

Figure 3.16.: Measurements of the 53013330 sample with the new polarizer (200-400nm) and comparison with previous data.

3.2.1.2. Modeling Improvements

In the paper presented in section 3.1, the only unknowns to the fit of the 53013330 were the Al_2O_3 thickness and the groove height, these having been determined manually. We now consider a more systematic way of fitting the different unknowns to the data, using a python least-square minimization algorithm.

In addition to the thickness of the different coatings applied to the gratings, we have the possibility to modify other parameters that will impact the shape of the grooves, or the composition of the coating used.

AFM measurements have been performed on the different gratings to model the groove shape of the different layers. In the case of the flight grating, the expected thin alumine layer ($< 10nm$) is a strong argument for conformal layers, meaning that the groove profile of the Al/Al_2O_3 layer should be identical to that of the Al_2O_3/air layer. We then used the Al_2O_3/air AFM to model the Al/Al_2O_3 layer. In the the following section (3.3), the use of thick MgF_2 coatings changes this configuration, and other parameters will be considered to properly model the non-conformality.

Moreover, the material's refractive indices have significant impact on the model. Two libraries are available within the software PCGrate (Palik and AIP). We de-

cide to choose, for each material, an RI library defined as a linear interpolation of the two libraries given by the formula:

$$RI_{Re\ or\ Im}^{Al\ or\ MgF2} = Palik_{Re\ or\ Im} + x^{Al\ or\ MgF2}(AIP_{Re\ or\ Im} - Palik_{Re\ or\ Im}) \quad (3.2)$$

The fitting parameter is $x^{Al\ or\ MgF2}$. In some cases, we will consider different interpolation wavelengths to best fit the data.

3.2.2. Analysis of the Flight grating

I will now introduce the measurements and modeling of the 'Flight' grating, i.e. the 110x130mm grating with bare aluminum coating, planned to be embarked within the instrument for the flight.

This analysis is the first step towards the characterization of the next generation UV spectrograph ISTOS.

3.2.2.1. Experimental care

This grating is significantly bigger than the samples, and therefore the experimental set-up had to be adjusted accordingly. We use the flat side of the grating as a support, which we keep in place using a custom support in the VW mounting. We used screws instead of springs (as used for the samples) to hold the grating in place during the measurements, in order to apply as little pressure on the grated surface as possible. Consequently, the measurements are not performed on the center of the grating, due to the impossibility to regulate the height of the beam or the support. However, this is not an issue for the present analysis as this very central area will not effectively be used during the flight due to the many obscurations within the FIREBall-2's optical chain.

3.2.2.2. Measurement and comparison with the sample

We present in Fig. 3.17 the polarized measurement of two gratings' efficiencies: the 53013330, which is the sample of the flight grating design (cf section 3.1) and the flight grating itself. We stress that these two gratings are manufactured from the same master replica.

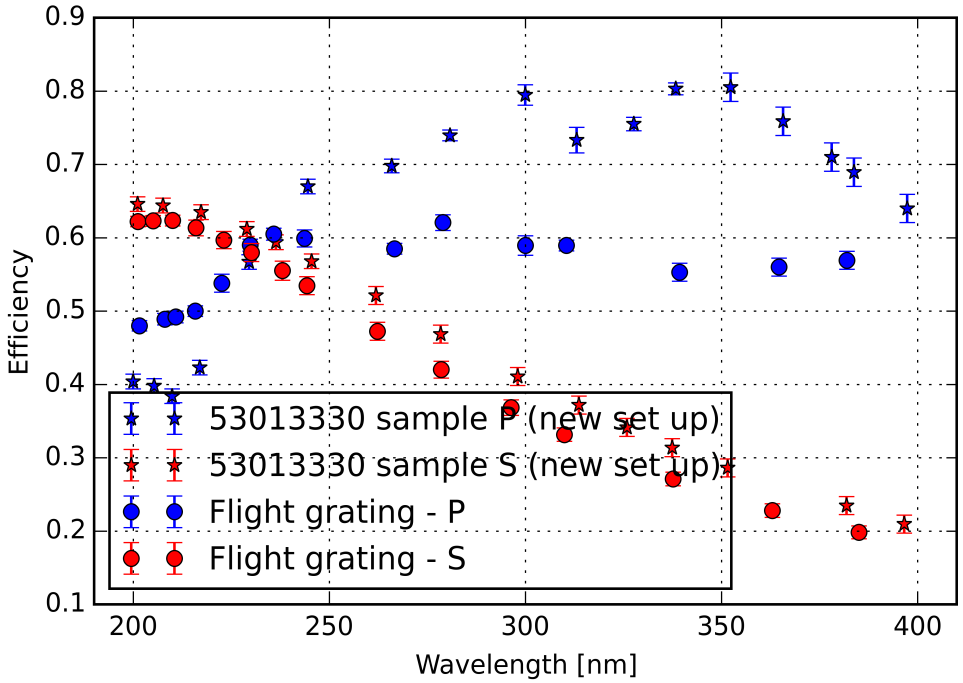

Figure 3.17.: Comparison between Flight grating and sample efficiency measurements

Surprisingly, the polarized efficiency measured on the flight grating differs greatly from the polarized efficiency measured on the 53013330 sample. We note that there is a slight offset of a few percent (absolute) in the S polarization, and a much more pronounced change in the P polarization. It seems also that the P-light profile is flatter at larger wavelengths.

We have verified that this was not a local effect by measuring the flight grating at a different spot (still near the edge, but in the opposite direction).

This shows the difficulty to produce such large size grating. What could be responsible for such P-light absorption? The suggested explanation is that this polarization is more prone to Wood's anomalies (caused by absorption from resonance of surface plasmons) than the S-light. Thus the surface quality of the grating is responsible for the behavior of the P-light.

3.2.2.3. Modeling under experimental conditions

We ran several fits with special care given to the RIs, but none of them were able to reach such low P-efficiencies at larger wavelengths. It was only when setting the aluminum thickness as a free parameter that we were able to reach a viable solution. Fig. 3.18 shows the result of the best fit, with aluminum thickness set

Table 3.2.: Results from the fit of the Flight grating

groove height	93.84 nm
Al thickness	23.15 nm
Al2O3 thickness	9.32 nm
RI Re Al	-8.5
RI Im Al	-0.53
RI Re Al2O3	2.43
RI Im Al2O3	0.5

as a free parameter. Table 3.2 gathers the different parameters from this best fit. This solution was reached for different initial conditions.

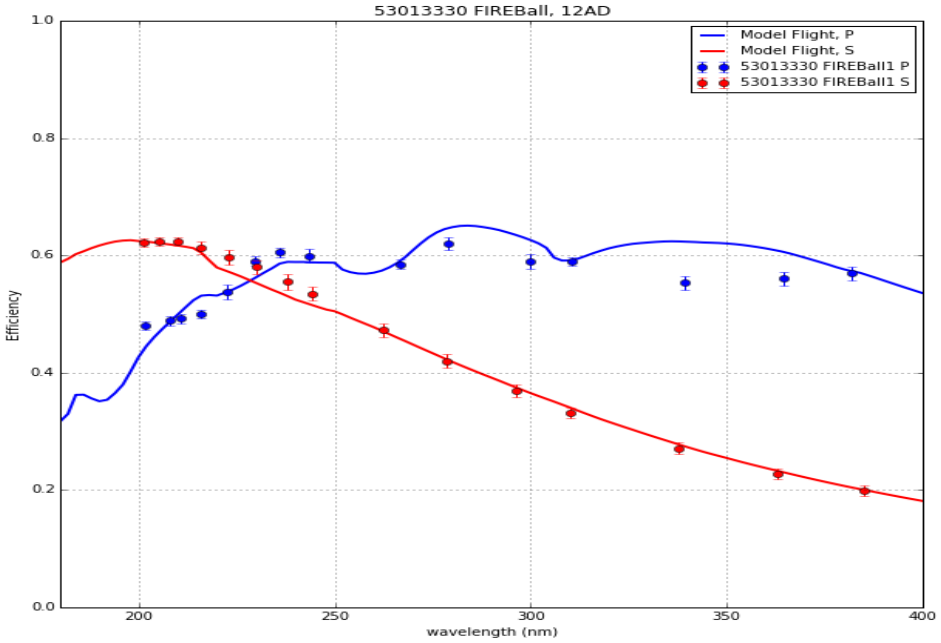

Figure 3.18.: Fit of the Flight grating under measurement conditions (at 12°AD), with an Al thickness of 23nm

To recover the P polarization, it seems that a viable solution would be a total Al thickness of about 23nm instead of minimum 50nm. This value is given in JY specifications, and a previous study, non published, showed that above this thickness, the behavior of the efficiency remains unchanged.

3.2.2.4. Extrapolation of the model towards flight conditions

As described in section 3.1.1, the experimental set-up can not reproduce the flight working conditions regarding the angular deviation (AD) produced by the grating. Indeed, the spectrometer *Lambda 900* can produce measurements for 12°AD, while during the flight the grating will be used at ~ 28°AD. This difficulty is overcome using the model derived from the 12°AD measurements interpolated to 28°AD.

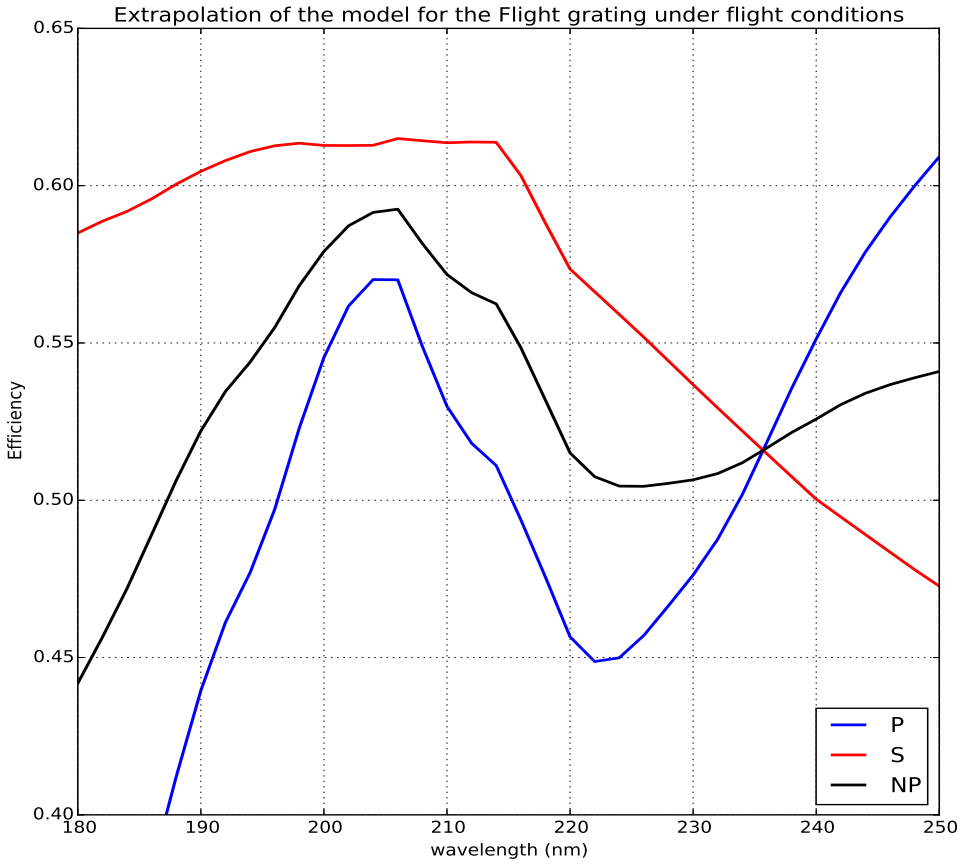

Figure 3.19.: Extrapolation of the model for the Flight grating's efficiency under flight conditions (at 28°AD.)

Fig. 3.19 shows the modeled efficiency of the Flight grating under observing conditions (28°AD). The non-polarized efficiency reaches values above 57% within the entire FIREBall-2 wavelength range, which is actually better than predicted from the sample measurements (section 3.1.3.1.1). This is probably due to the thin Al layer predicted from the model. However, the P-polarization

presents a sharp peak around 205nm, which makes the robustness of the present high efficiency questionable.

In conclusion, the low-cost aspherized holographic 2400nm grating turns out to be quite promising for an UV spectroscopic mission such as FIREBall-2.

3.3. Test of the proposed new design: MgF_2 coating

The Flight grating, as measured in the last section, shows a rather good non-polarized efficiency between 200 and 208nm under FIREBall-2 flight conditions, more than what was anticipated from the sample (section 3.1). We infer this difference to come from a different Aluminum thickness used for the sample ($> 50nm$) and the Flight grating ($\sim 23nm$).

We now investigate the proposed solution discussed in section 3.1, which consists in using MgF_2 coating to enhance the grating's performances in flight conditions.

3.3.1. Validation of the design at shorter wavelengths

The proposed MgF_2 design relies on the manual modeling of the Flight grating's sample, the 53013330, measured only between 240 and 350nm. It anticipated a rise of the non-polarized efficiency, compared to the sample, by about 10% absolute using a 70nm MgF_2 thickness. In order to validate this solution at shorter wavelengths, two MgF_2 coated samples were manufactured at Jobin Yvon:

- A 30nm MgF_2 coated sample, referred to as the **53013330 T11**
- A 70nm MgF_2 coated sample, referred to as the **53013330 T12**

These samples are similar to the Flight grating sample 53013330 in terms of dimension but also in terms of production: they are replicated from the same master.

3.3.1.1. The 30nm MgF_2 coated sample - 53013330 T11

For the MgF_2 coated gratings, the coating thicknesses at hand are much thicker than a few nanometers, and we cannot consider the two boundaries to be conformal anymore. As we only have access to the AFM of the air/MgF_2 border, we assume that the MgF_2/Al border is similar to that of the 53013330 air/Al_2O_3 border, as the same matrix has been used in the making of the 53013330 gratings. But the conditions of the realization being unknown, we decide to add a degree of freedom to the profile of the MgF_2/Al layer, by starting with the 53013330 AFM, and considering a scaling in the **groove height**. We verified that a scaling in the groove depth of the air/MgF_2 profile had no impact on the model. We do not have any precise measurement of the actual amount of deposited MgF_2,

thus the **vertical offset** between the air/MgF_2 border and the MgF_2/Al border has to remain free. Likewise, the **horizontal offset** between those two layers is unknown, and therefore has to be set free. Fig. 3.20 shows the organization of the different layers used for the MgF_2 coated samples.

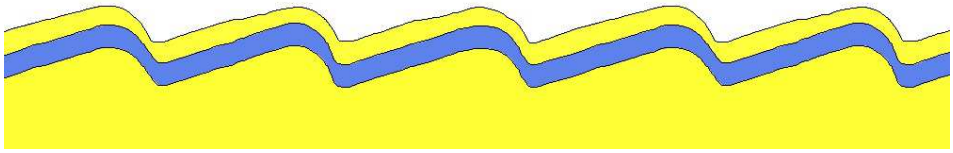

Figure 3.20.: Model used for the modeling of the unconformal layer for the 30nm MgF_2 coated sample 53013 T11. The bottom layer (yellow) is the silicate substrat, the blue layer is the aluminum layer ($\sim 50\text{nm}$ thick) and the upper layer (yellow) is the MgF_2 coating.

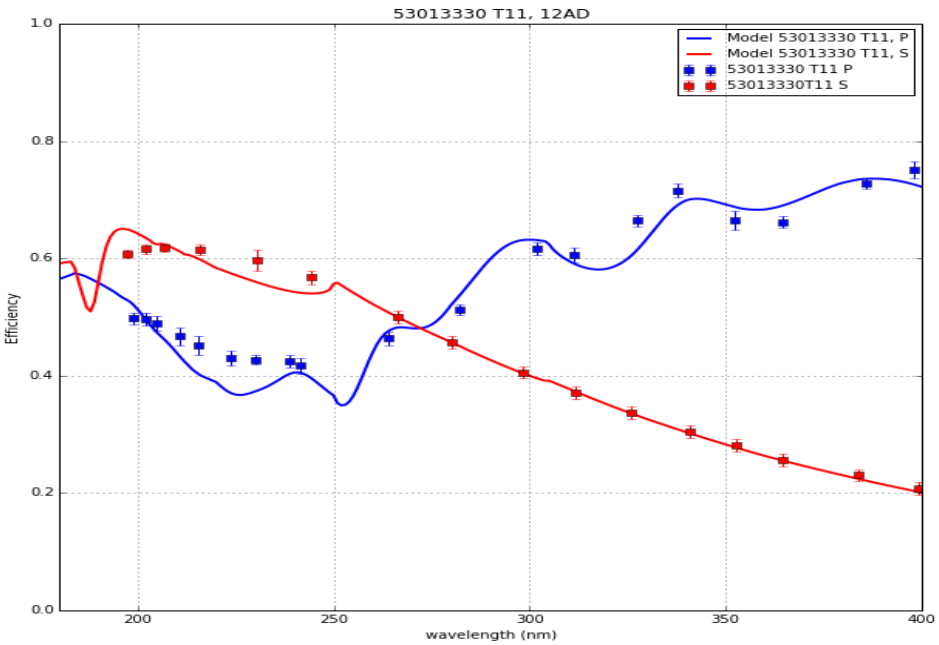

Figure 3.21.: Fits of the 53013330 T11 sample under measurement conditions (at 12°AD)

Fig. 3.21 shows the measurements of the 53013330 T11 in both polarizations

Table 3.3.: Results from the fit of the 53013330 T11 sample grating

vertical offset	53.61 nm
horizontal offset	1057.57 nm
groove height	91.24 nm
RI Re Al	0.038
RI Im Al	1.98
RI Re MgF2	-3.06

and the best fit to the data. We stress that the measurements were performed under purely polarized light. Table 3.3 gathers the different fitted parameters. We see that the best fit gives quite surprising results. Indeed, the $\mathrm{MgF_2}$ thickness, expected to be around 30nm is evaluated at $53.61\mathrm{nm}$ (vertical offset in the table). The fit in itself is quite satisfactory for the S-polarization, because for $\lambda > 250\ \mathrm{nm}$, the model is able to recover all of the data points. However, the P-polarization suffers from underestimation of the efficiency for $\lambda < 250\ \mathrm{nm}$. Above 250nm, it seems that the fit is able to reproduce possible anomalies.

3.3.1.2. The 70nm $\mathrm{MgF_2}$ coated sample - 53013330 T12

The second sample is the $70\mathrm{nm}\ \mathrm{MgF_2}$ coated sample, 53013330 T12, designed from the analysis made in section 3.1.3.1. This grating is thought to bring an improvement to the existing design under FIREBall-2 flight conditions.

A slightly different set of parameters than for the other grating modeling is considered here. Instead of considering one single scaling parameter for the whole wavelength range of the refractive indices, we divide the range into 5 zones, delimited by $\lambda = 200, 225, 250, 325, 400\mathrm{nm}$. We are reaching here the limitations of our model as we are distancing more and more from Palik and AIP's RI's measurements. Nevertheless, the different conditions of coating deposition have unknown effects on the actual RI and the surface might not be homogeneous, that is why we took the liberty of adjusting it more freely. An actual characterization of these RIs could help bringing more insights in the modeling of the gratings, but this is beyond the scope of the present manuscript. This results in an 18 free-parameter fit, the best-fit of which is presented in table 3.4. The polarized measurements of the 53013330 T12 and the best fits to the data are presented in Fig. 3.22.

Table 3.4.: Results from the fit of the 5301330 T12 sample grating

vertical offset	82.18 nm
horizontal offset	41.65 nm
groove height	91.58 nm
RI Re Al 200	2.78
RI Im Al 200	2.97
RI Re Al 225	2.96
RI Im Al 225	2.93
RI Re Al 250	2.97
RI Im Al 250	2.93
RI Re Al 325	-0.39
RI Im Al 325	2.94
RI Re Al 400	-2.94
RI Im Al 400	-0.28
RI Re MgF2 200	0.13
RI Re MgF2 225	2.81
RI Re MgF2 250	2.93
RI Re MgF2 325	-0.43
RI Re MgF2 400	-2.9

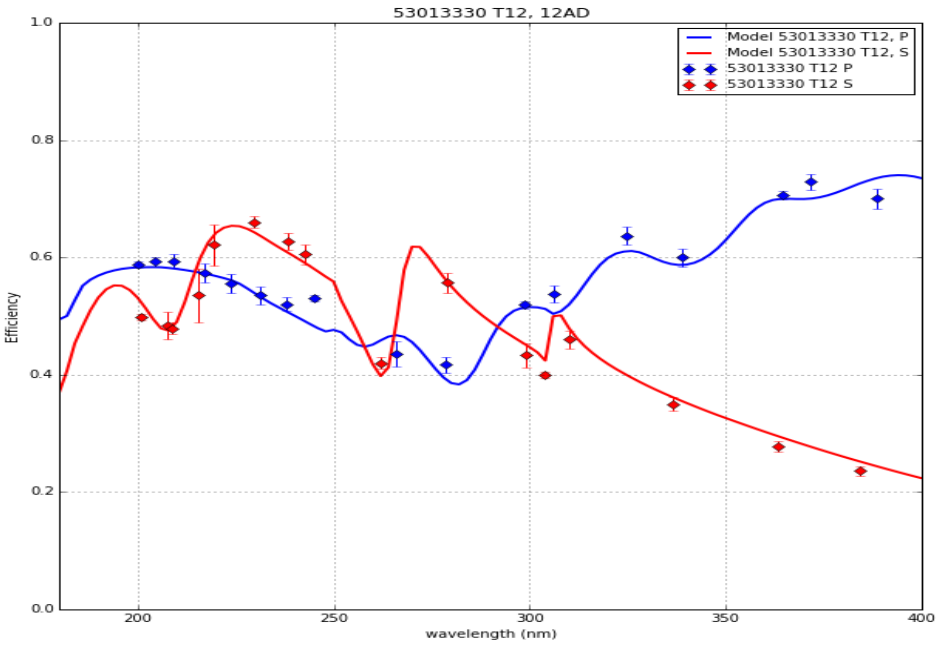

Figure 3.22.: Fits of the 53013330 T12 sample under measurement conditions (at 12°AD)

The best fit fits the data quite well, for both polarizations and at different wavelengths. We recover some anomalies for the S-polarization at $\sim 210\text{nm}$, $\sim 260\text{nm}$, $\sim 310\text{nm}$ (these are similar to the anomalies found in the S-polarization of the sample with 30nm MgF_2 coating, the 53013330 T11, see section 3.3.1.1). The estimated MgF_2 thickness is of 82.2nm, which is coherent with the specifications (70nm).

3.3.1.3. Extrapolation of the models toward flight conditions

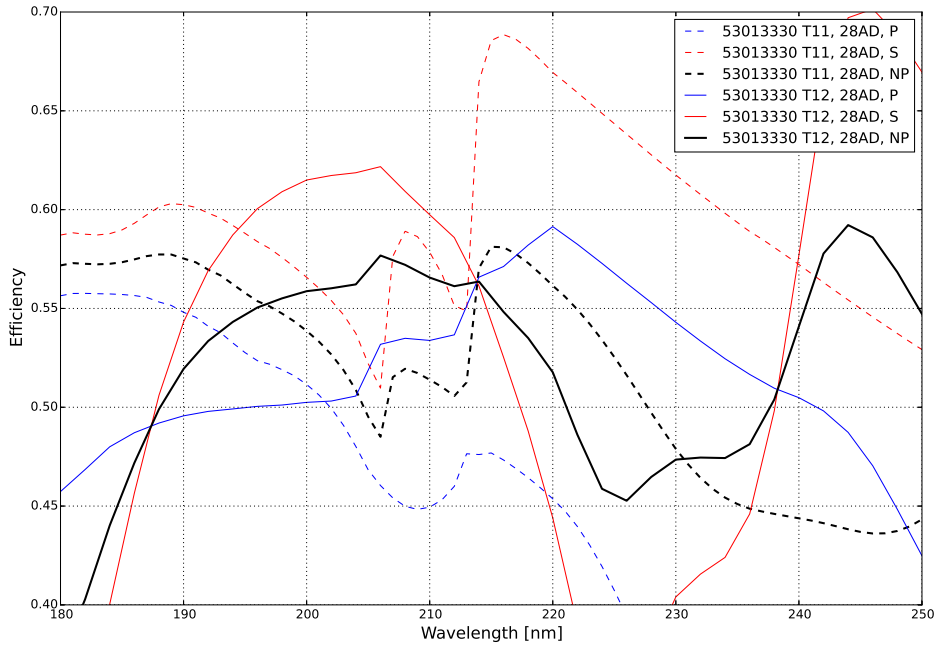

Figure 3.23.: Comparison between the 30nm (T11) and 70nm (T12) MgF_2 coated samples efficiencies under flight conditions (at 28°AD)

Fig. 3.23 shows the 53013330 T11 and T12 efficiencies interpolated under FIREBall-2 flight conditions (28°AD).

From Fig. 3.7, we expect a non-polarized efficiency under flight conditions (at 28°AD) of

- $\sim 60\%$ at 204nm for 80nm MgF_2 coating.
- $\sim 50\%$ at 204nm for 50nm MgF_2 coating.

The non-polarized efficiencies derived from the model are in good agreement with these values. The MgF_2 coated samples 53013330 T11 and T12 confirm

that a 70nm MgF_2 coating does increase the efficiency at 28°AD in the wavelength range 200-208nm by a few percent absolute.

3.3.2. Spare grating

Once the design has been validated down to shorter wavelengths by the analysis described above, a 110x130mm grating with 70nm MgF_2 coating can be produced. This new grating is referred to as the 'Spare' grating, mainly because it will be the second grating available for the flight, in case of an incident affecting the flight grating (see section 3.2.2).

Although we are now able to improve the MgF_2 design from broader wavelength range measurements on the MgF_2 coatings, we chose to maintain the 'optimal' coating thickness at 70nm so as to maintain the experimental setup unchanged for the manufacturer Jobin Yvon. Moreover, our solution represent a local maximum for the efficiency, so there would certainly be little improvements of the final efficiency if the optimal thickness were to be used.

3.3.2.1. Measurement and modeling

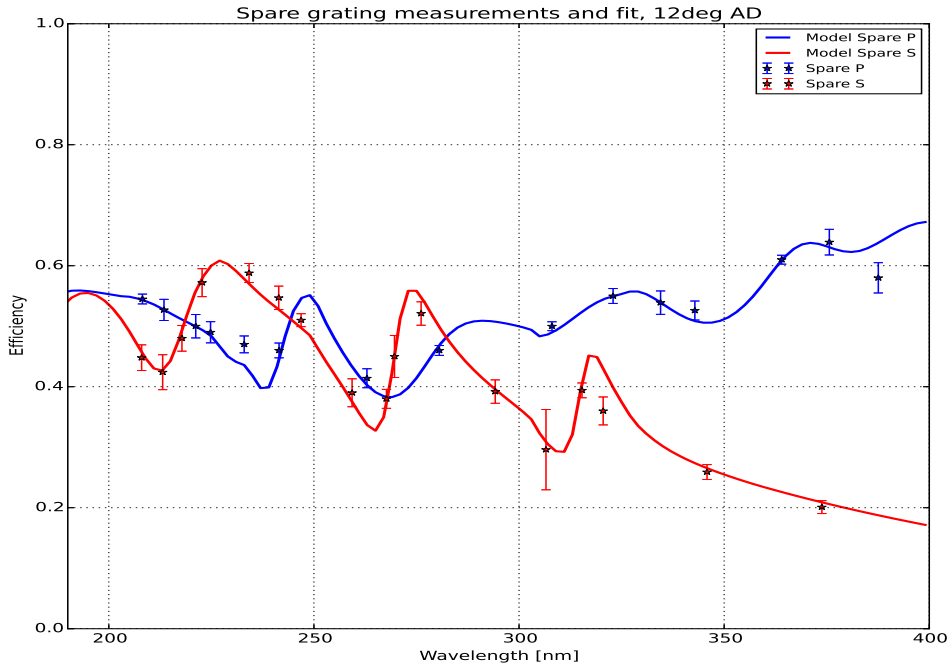

Figure 3.24.: Fits of the Spare under measurement conditions (at 12°AD)

Table 3.5.: Results from the fit of Spare grating

vertical offset	90.51 nm
horizontal offset	40.11 nm
groove height	82.47 nm
RI Re Al 200nm	2.84
RI Im Al 200nm	2.72
RI Re Al 225nm	2.93
RI Im Al 225nm	1.85
RI Re Al 250nm	2.27
RI Im Al 250nm	1.19
RI Re Al 325nm	-2.81
RI Im Al 325nm	2.53
RI Re Al 400nm	-0.57
RI Im Al 400nm	2.23
RI Re MgF_2 200nm	-2.35
RI Re MgF_2 225nm	2.80
RI Re MgF_2 250nm	0.03
RI Re MgF_2 325nm	2.20
RI Re MgF_2 400nm	-2.80

The same grating holder as for the Flight grating is used to measure the Spare. Fig. 3.24 shows the efficiency measurements, in purely polarized light, performed on the Spare grating, along with the best fit to the data.

Similarly to the fit of the 53013330 T12 sample grating, we run an 18 free-parameters fit to the data, with a 5-point linear interpolation of the refractive indices for Al and MgF_2. The best fit parameters are gathered in table 3.5.

The fit recovers the different anomalies ($\lambda = 215, 260, 310\text{nm}$) for S-light. For the P-light, the fit recovers most of the measurements, except for $\lambda \sim 240\text{nm}$ and $\lambda \sim 370\text{nm}$. We note that the expected MgF_2 thickness of this grating is 90.51nm. This is above the specified MgF_2 thickness (70nm) and above the measured thickness of the sample 53013330 T12 (80nm).

3.3.2.2. Comparision between Spare and sample

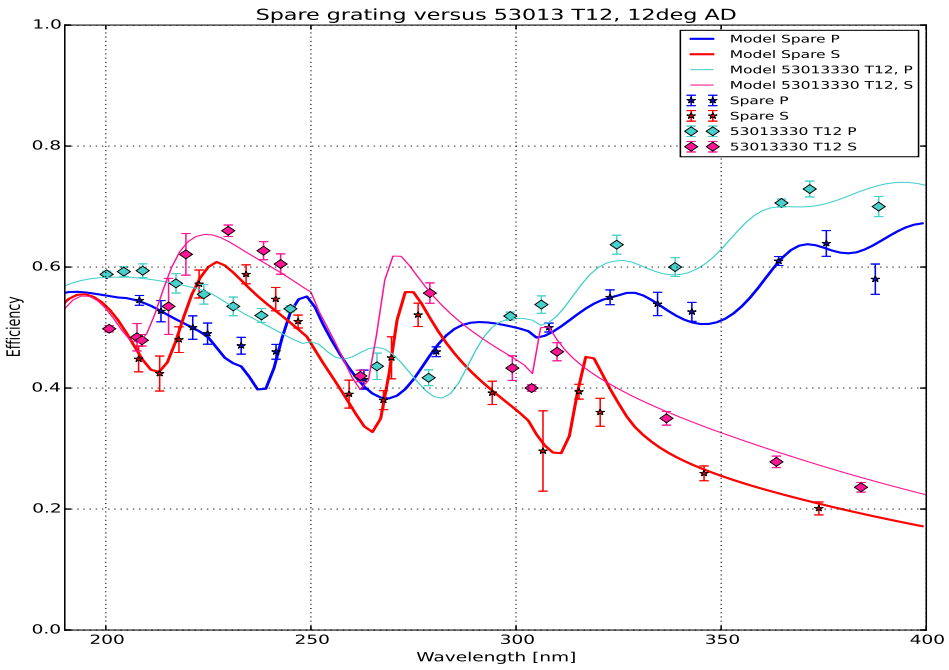

Figure 3.25.: Comparison between the Spare grating and the T12 sample under measurement conditions (at 12°AD)

Fig. 3.25 shows the data and the fit of the 70nm-MgF_2 coated sample (53013330 T12) and Spare gratings. The Spare grating is less efficient overall (under measurement conditions, that is 12° AD) than the sample. This is possibly due to a higher MgF_2 thickness (92nm) of the Spare than that of the sample (80nm).

For the S-light, the Spare is within 5% absolute below the sample across the entire wavelength range, and the main anomalies are recovered ($\lambda \sim 210$nm, $\lambda \sim 260$nm, $\lambda \sim 300$nm). For the P-light, the analysis is the same, except that the absolute difference between the two measurements is overall slightly higher than for the S-light.

3.3.2.3. Extrapolation under flight conditions and comparison with Flight grating

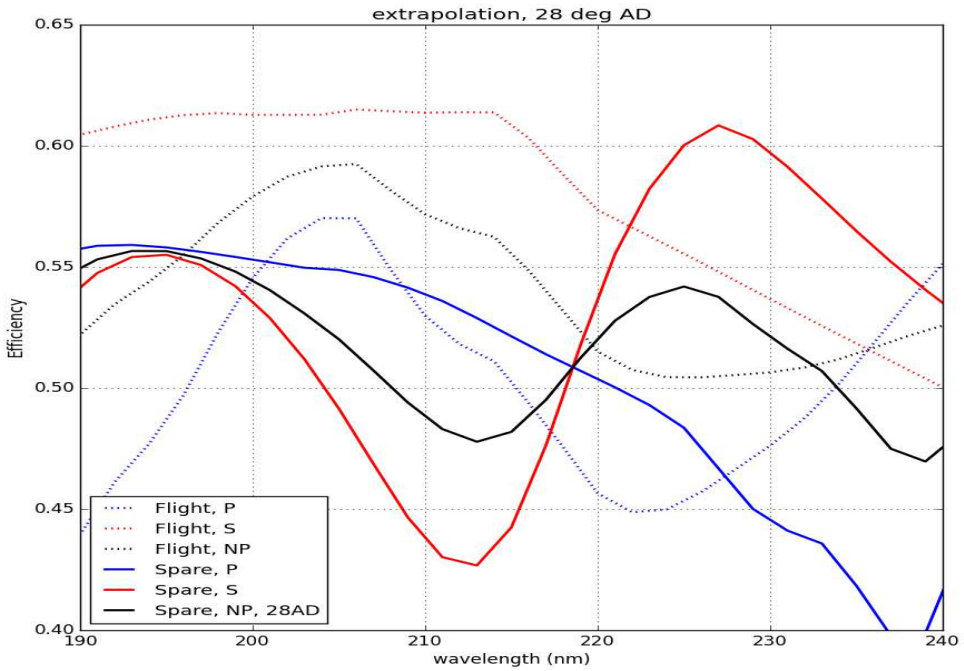

Figure 3.26.: Comparison between the Flight grating and the Spare grating efficiency measurements under flight conditions (at 28°AD)

Fig. 3.26 shows the extrapolation of the models to flight conditions for the Spare and the Flight gratings. We notice that the Spare is, overall and looking at the NP polarization, less efficient than the Flight. This result does not reach the values expected from the 70nm MgF_2 coating sample. Although the sample shows relatively promising results, the Spare proves that it is extremely difficult, technically, to reproduce such a coating on a larger scale. We note that the total MgF_2 thickness has a great importance in the final efficiency, and that we may not be able to accurately control the amount of MgF_2 coated onto the grating. It may be that, in the case of deposition by pulverization[k], the actual thickness of coating is dependent on the size of the grating but also other external factors that may not be known accurately (humidity, temperature...). Indeed, the thickness deposited on the Spare was measured at $\sim 90\text{nm}$ MgF_2 instead of the 70nm as specified in the paper. Also, the Flight grating is believed to bear a very thin

[k] the coating process has been kept secret from JY, so we can not firmly conclude on the possible explanation for such differences in coating thicknesses.

layer of Al ($\sim 25\text{nm}$ instead of $> 50\text{nm}$) and, fortunately, we have shown that this tends to increase the efficiency in flight conditions and in the wavelength range of interest. Nevertheless, the effect of the thin Al layer for the flight seems to produce a peak in the Flight P-polarized efficiency, which is extremely sensitive to the model, and might turn out to be a pure artifact.

3.4. Conclusion

I have conducted in this chapter a rather complete study of FIREBall-2's grating, one of the key components in the optical design of the instrument.

For 5 different gratings (3 samples and 2 flights), I have been able to produce clean efficiency measurements in pure polarized light from 200nm to 400nm. The baseline grating (Flight) shows good efficiencies within FIREBall-2's wavelength range (above 50%). Moreover, I have produced accurate models of these grating to predict the efficiency at different angular deviations. These models enable an indirect probe of the different physical parameters of the gratings such as the groove shape (groove height, layer conformality), the coating thickness or the refractive indices. I was able, for example, to pinpoint a manufacturing defect in the realization of the Flight grating. Indeed, my model predicts an abnormally thin layer of aluminum coating (23nm instead of 50nm), fortunately resulting in an enhanced efficiency under FIREBall-2 flights conditions.

I have also proposed a solution that would increase the throughput of the grating quite significantly. This solution was tested and the produced grating also shows interesting characteristics, although lesser than the original one due to the difficulty in accurately controlling the thickness of the $\mathrm{MgF_2}$ layer during production.

Overall, the low-cost aspherized holographic 2400 l/mm grating seems therefore to be one of the best performing UV gratings produced for UV spectrometers, and could be a good candidate for a more ambitious project like ISTOS. However, because the main factor for the efficiency difference between the samples and the flights is the coating thickness, further investigation into grating manufacture and coating deposition should be made for such a project.

Chapter 4: A model for the CGM emission

> It is often safer to be in chains than to be free.
>
> Franz Kafka

The observation of CGM emission lines is a challenge in the current range of observational capabilities. At high redshifts, large ground based telescopes such as the Very Large Telescope (VLT), Subaru or Keck offer the first hints of Lyα emission CGM mapping, but this is only achievable through the stacking of a large number of systems (Momose et al., 2014), long exposures (Rauch et al., 2008; Wisotzki et al., 2016) or by selecting objects whose Lyα luminosity is boosted by the presence of a bright quasar nearby (Cantalupo, Arrigoni-Battaia, et al., 2014; Martin, Chang, Matuszewski, Morrissey, Rahman, Moore, and Steidel, 2014; Martin, Chang, Matuszewski, Morrissey, Rahman, Moore, Steidel, and Matsuda, 2014; Borisova et al., 2016). The next generation of UV telescopes (ISTOS) or X-Ray telescopes (Athena) will bring tremendous insights into the mapping of these regions at low redshifts and to the general understanding of the different emission mechanisms and the different scenarios for gas flows in and out of the galaxies. The path-finder experiment to ISTOS, FIREBall-2, relies on a single night observation to acquire decisive insight into both the physical properties of the CGM in emission and the instrument capabilities, and therefore a reliable model of such emissions is crucial to the preparation of the flight for target selection purposes, design of observational strategies and data analyses.

In the next two chapters, I will present an end-to-end pixel analysis of the observational capabilities of the Multi-Object UV-Spectrograph FIREBall-2 to characterize the low-redshift ($z < 1$) CGM of galaxies. The present chapter starts from the first end of the analysis, the modeling of low-redshift CGM emissions using a high resolution hydrodynamical cosmological simulation, while the next chapter covers the modeling of the observations of such modeled emission.

4.1. The Zoom Simulation

4.1.1. Motivations

Frank, Rasera, et al., 2012 studied the emission flux from different lines (Lya, CIV and OVI) within the CGM at low redshift using a grid-based hydrodynamical solver with adaptive mesh refinement (AMR), dubbed RAMSES (Teyssier, 2002). Bertone and Schaye, 2012 performed a similar analysis for the high redshift IGM ($2 < \mathrm{z} < 5$). These analyses are preliminary expectations in observational campaigns of the CGM. With the goal to map for the first time the CGM of low-redshift galaxies using a UV MOS, FIREBall-2, a high resolution simulation of the IGM has been developed with the AMR RAMSES code (Rasera, private communication). This simulation builds on that of Frank, Rasera, et al., 2012 with new developments as detailed below. The spatial resolution in the highest refinement levels of the Frank, Rasera, et al., 2012 simulation reaches 1.53 physical kpc h^{-1}. Given the various processes regulating the gas dynamics within the CGM, such as accretion of gas, outflows, Y. Rasera and J. Blaizot have computed a '*zoom*' on one of the brightest halos of the Frank, Rasera, et al., 2012 RAMSES simulation, in order to better constrain the physical conditions within the CGM and reach smaller physical scales. The selected halo has a Dark Matter (DM) mass of about $1.5\ 10^{13}\ \mathrm{h^{-1}M_\odot}$ (at $\mathrm{z} = 0.7$) and is located close to the edge of the box. This should not cause errors as the boundary conditions as periodic.

This new high-resolution simulation has initial conditions downgraded in a 128^3 grid over a size of 100 comoving Mpc/h centered on the halo. We used the MUlti-Scale Initial Conditions code (MUSIC, Hahn et al., 2013) to zoom on a cubic region of 13.92 comoving Mpc/h size. The simulation was performed using non-thermal SuperNovae (SNae) feedback (Teyssier et al., 2013) with the '*on-the-fly*' self-shielding option (see section 4.1.3). The maximum refinement level is set to 18, giving a spatial resolution in the densest region of the simulation of about a few hundred parsecs ($\sim 380\ \mathrm{h^{-1}}$ comoving pc). The mass resolution, in the central region, is of $\sim 8.7\ 10^5\ h^{-1}\ M_\odot$ for the Dark Matter particles, $\sim 1.8\ 10^5\ h^{-1}\ M_\odot$ for the gas cells, and $\sim 1.95\ 10^5\ h^{-1}\ M_\odot$ for stellar particles. The final number of particles is about 205 million for Dark Matter, 51 million for stars and 592 million gas cells, and at $\mathrm{z} = 0$, the central zoomed halo mass is about $3\ 10^{13}\ \mathrm{h^{-1}\ M_\odot}$, with about 30 million particles. Our analysis follows that of Bertone, Schaye, Booth, et al., 2010 and Frank, Rasera, et al., 2012, but with an increased resolution enabling us to probe colder and denser gas in a full cosmological context. We assume a ΛCDM flat Universe with $\Omega_\Lambda = 0.742$, $\Omega_m = 0.258$, $\Omega_b = 0.045$ and $\mathrm{h} = 0.719$.

Fig. 4.1 shows a projection of the Lyα emission prediction (in arbitrary units) over a large volume of the simulation (about 10 Mpc on a side). The web-like structure of the IGM clearly emerges in this snapshot, where we see faint filaments connecting overdense regions. We also see the presence of some isolated

halos within each filament.

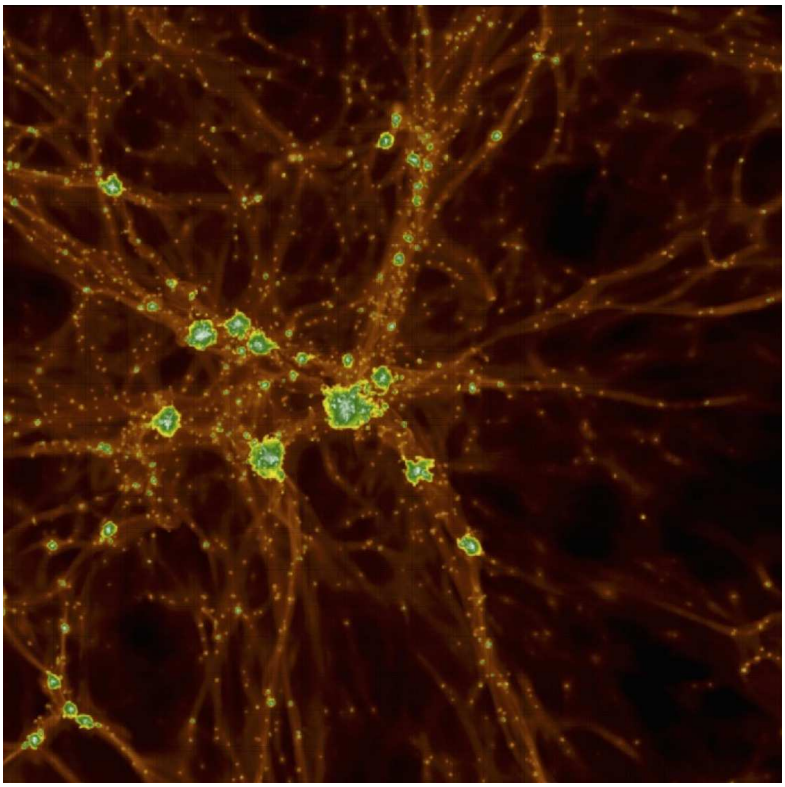

Figure 4.1.: Projected Lyα emission (arbitrary units) from the new high-resolution simulation at z=0.67. The image is about 10 comoving Mpc/h on a side.

4.1.2. Main halo evolution

The narrow wavelength range of FIREBall-2[a] encompasses three lines of interest: Lyα at $z \sim 0.7$ tracing cold gas at $T \sim 10^4$K, CIV at $z \sim 0.3$ tracing warm gas at $T \sim 10^{5-5.5}$K and OVI at $z \sim 1.0$ tracing warm-hot gas at $T \sim 10^{5.5-6}$K. For each line, we use the corresponding snapshot of the simulation. Thus, similarly to what will be the case for the instrument, we do not get emission predictions from different lines in a same region. This limitation will be overcome with the orbital version of FIREBall-2, ISTOS.

[a] $200 - 208$ nm, i.e. at the position of the atmospheric transmission 'sweet spot', see chapter 2.

Table 4.1.: Main halo characteristics for the three redshifts of interest.

Line	z	$t_{Universe}$ [Gyr]	M_{DM} [$M_\odot$]	M_* [$M_\odot$]	M_{gas} [$M_\odot$]	R_{vir} [pkpc]	R_{vir} [ckpc]	SFR [$M_\odot$/yr]
OVI	1.0	~ 6.0	$9.61\ 10^{12}$	$5.64\ 10^{12}$	$1.56\ 10^{12}$	327	655	622
Lyα	0.67	~ 7.6	$1.36\ 10^{13}$	$7.44\ 10^{12}$	$1.69\ 10^{12}$	391	652	246
CIV	0.25	~ 10.8	$2.83\ 10^{13}$	$9.80\ 10^{12}$	$4.15\ 10^{12}$	679	848	333

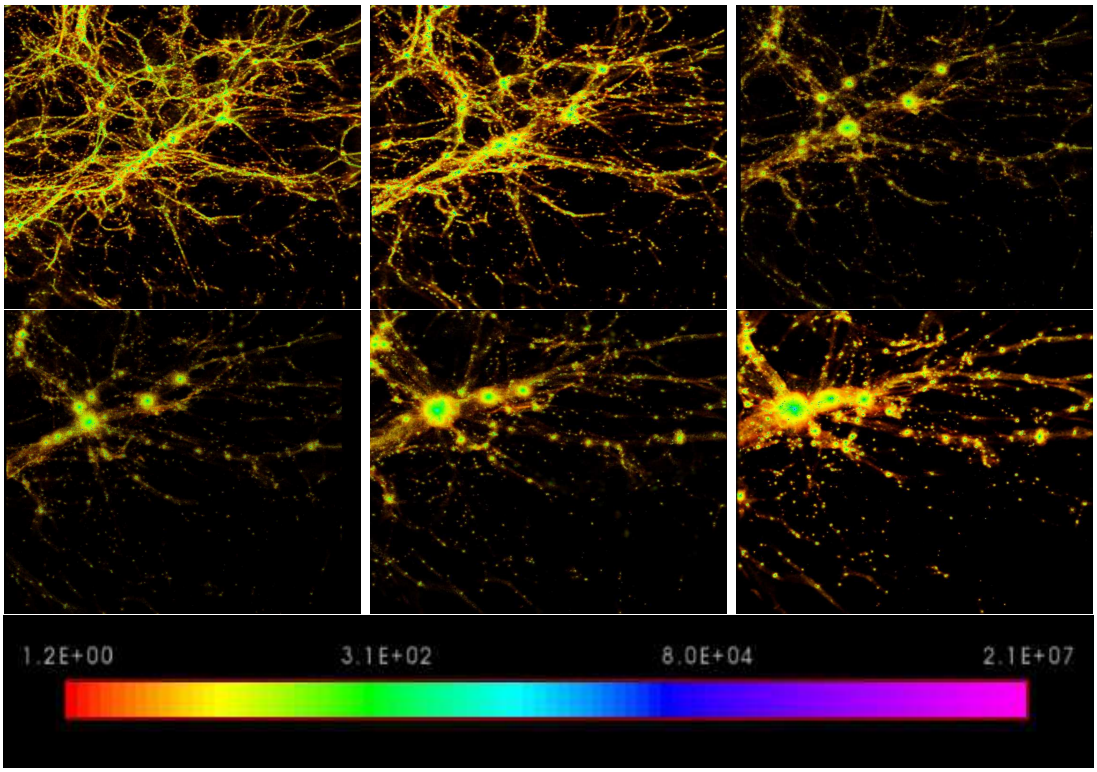

Figure 4.2.: Evolution of the gas distribution in the high-resolution simulation for 6 different redshifts: z=2.3, 1.5, 1.0, 0.67, 0.25, 0 (from top left to bottom right). Each panel corresponds to the 'zoomed' region of the high-resolution simulation, which is about 13.5 comoving Mpc/h. We can see the filamentary structure of the IGM, and the formation of the massive halo chosen for the zoom. The same color scale has been used, in arbitrary units from the 3D visualization tool GLNemo2 (Lambert et al. private communication)

Fig. 4.2 shows the high-resolution part of the simulation for 6 different redshifts $z = 2.33,\ 1.0,\ 1.5,\ 0.67,\ 0.25,\ 0.0$ respectively. We can see the progressive

formation of the main halo from $z = 1.0$. The properties at different redshifts of this halo are gathered in table 4.1. These quantities are derived within the virial radius of the main halo which is measured from the structure finder HaloFinder (Aubert et al., 2004; Tweed et al., 2009, see section 4.3.2). It is worth noticing that over the 4.8 Gyr covered, the DM and the gas mass nearly triple, while the SFR shrinks by a factor of $\sim$2, a seemingly paradoxical situation that illustrates that all the gas is not available for star formation.

4.1.3. Contributions of the high-resolution simulation

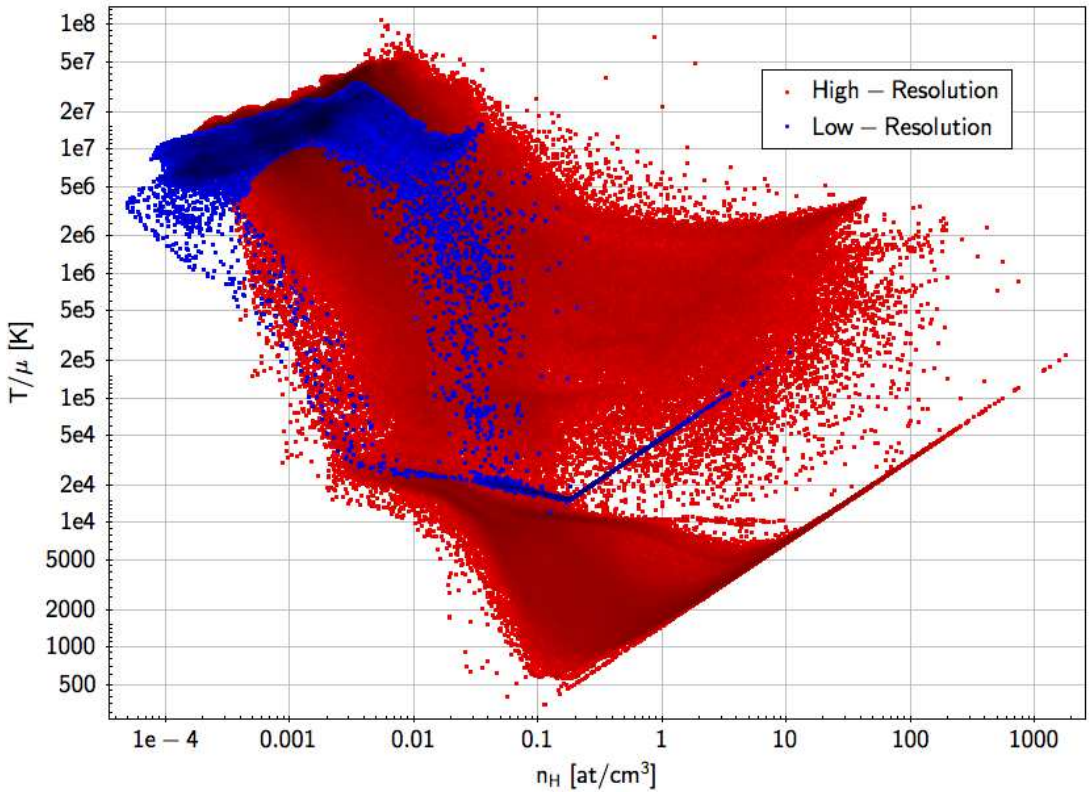

Figure 4.3.: Density-temperature phase diagram of the selected halo for the low-resolution (blue) and high-resolution simulation (red).

Fig. 4.3 represents the density-temperature diagram for the zoomed halo in the low-resolution (blue points) and high resolution (red points) simulations at redshift $z = 0.67$ (correponding to Lyα observation). As expected, the high-resolution simulation extends to a larger parameter space. Two striking differences between these two simulations lie at the high density end of Fig. 4.3. First, as the resolution increases, the gas can reach higher densities as it reaches the

center of the gravitational well. Consequently, the density threshold for star formation has been increased from $\mathrm{n_H} = 0.1\ \mathrm{at/cm^3}$ to $\mathrm{n_H} = 3\ \mathrm{at/cm^3}$ (Rasera et al., private communication). The cells showing a power law in both simulation is an artifact from the simulation code to artificially stabilize the gas versus the Jeans stability at the resolution limit.

Another feature, called '*on-the-fly*' self-shielding, is used with the high-resolution simulation. This option will disable the ionizing background for cells with a neutral hydrogen density $\mathrm{n_{HI}} > 0.01\ \mathrm{at/cm^3}$. This reproduces the self-shielding of gas cells in dense regions from the background ionizing flux. This threshold value is based on radiative transfer studies which have derived an estimate on the density at which the fraction of neutral hydrogen becomes dominant (Faucher-Giguere, Keres, et al., 2010; Rosdahl and Blaizot, 2012). This results in further gas cooling in the high-resolution simulation. Indeed, the '*gutter*' ($\mathrm{n_H} \sim 0.1\ \mathrm{at/cm^3}$ and $\mathrm{T} \sim 10^4\ \mathrm{K}$), where cooling processes are in equilibrium with heating from external sources, occurs at a lower temperature for the high-resolution. The coupling of this '*on-the-fly*' self-shielding option with the significantly higher resolution results in the emergence of an ISM gas phase, for which gas cells reach temperatures below $10^4\ \mathrm{K}$, with densities higher than $0.1\ \mathrm{at/cm^3}$. Such low temperatures could not be reach in the previous simulation set (**Frank12**). These ISM cells are clearly identified in the visual inspection of the simulation through the presence of disks (Fig. 4.4). However, the simulation reaches here its limits as the spatial resolution in the high density zones is of $381\ \mathrm{pc/h}$ (comoving), which is not enough to properly resolve the ISM.

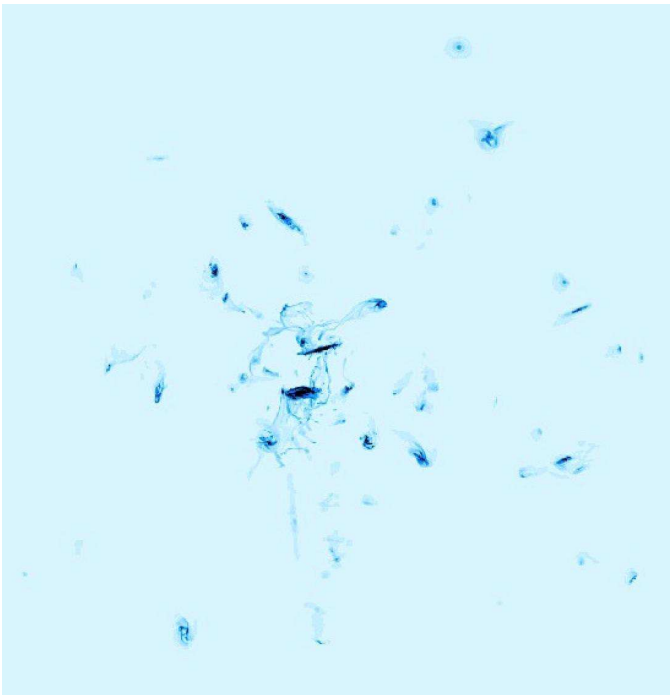

Figure 4.4.: Density map (in arbitrary units) showing some disk like structures at z=1.22. The image is about 400 physical kpc on a side.

Another addition to the high-resolution simulation is the implementation of non-thermal SNae feedback from Teyssier et al., 2013. In hydrodynamical cosmological simulations, there are typically two ways to simulate the feedback from supernovae or AGN activity: the momentum-driven feedback and the energy-driven feedback (Costa et al., 2014). The former injects pressure to the neighboring gas cells of a star particle undergoing supernova, acting a bit like a 'velocity kick', while the latter directly injects thermal energy and pushes the gas via adiabatic expansion of the hot shocked wind bubble. The energy-driven solution is chosen here, given that the efficiency of momentum-driven outflows is lower in cosmological simulations than in isolated halo simulations (Costa et al., 2014). However, a major drawback of the energy-driven solution is that the injected energy is instantly radiated away by strong cooling, which appears to be a numerical effect of the simulation (Ceverino et al., 2009). While other mechanisms with longer dissipative time scales are thought to sustain the pressure of the blast from this instant cooling[b] (Cox, 2005; Salem et al., 2016, such as cosmic rays or magnetic fields,), we choose to momentarily stop the cooling of the gas after the energy injection. This feature, called 'delayed cooling', has been used in other works (Stinson et al., 2006; Governato et al., 2010; Agertz et al., 2011), and results in a temporary over-estimate of the temperature of the affected cells (this

[b]hence the term 'non-thermal'

has unwanted effects in the emission prediction, see section 4.2.1.3).

4.2. Flux emission prediction

The main objective of this chapter is to put together a realistic model for faint diffuse emission from the CGM of low-redshift galaxies in order to prepare for FIREBall-2 data analysis and its target selection. We emphasize here that it is beyond the scope of the present analysis to propose any improvement of the very complex emission predictions from the CGM. Nevertheless, the high resolution reached on such a large scale simulation box brings innovative insight towards CGM gas phase emission line physics.

There are different physical processes responsible for the expected extended CGM emission. The first one, referred to as *gravitational cooling*, is due to the collisional ionization of accreting gas, radiating away part of the energy acquired by compression and shock heating. This is thought to be the main source for spatially extended Lyα sources (about 50% of this cooling radiation emerges as Lyα photons), commonly referred to as Lyα blobs, as the photons thus created would be emitted in the dust-poor outskirts of the disk, protecting these photons from further dust absorption (Fardal et al., 2001; Dijkstra and Loeb, 2009; Faucher-Giguere, Keres, et al., 2010).

The second process is the photo-ionization by external UV sources, which causes the emission of photons via recombination processes (*fluorescence*). Among these UV sources, there is the metagalactic UV background (UVB), which consists of the UV photons emitted from distant objects, such as stars or quasars (Haardt et al., 2001; Haardt et al., 2012; Kollmeier, Weinberg, et al., 2014). The computation of the UV backgrounds is a complex task, as many parameters come into play, such as the ionizing photon escape fraction, the dust content and opacity, the density distribution of neutral hydrogen absorbers (Haardt et al., 2001; Kollmeier, Weinberg, et al., 2014)... In addition to this metagalactic background, one can expect the presence of a photo-ionizing bright source nearby (such as a quasar, Cantalupo, Porciani, et al., 2005; Kollmeier, Zheng, et al., 2010; Cantalupo, Arrigoni-Battaia, et al., 2014; Martin, Chang, Matuszewski, Morrissey, Rahman, Moore, and Steidel, 2014) enhancing the illumination of the gas which then re-radiates through fluorescence.

The final contribution comes from the production of ionizing photons from star forming galaxies or a quasar inside the halo. Indeed, $h\nu > 1\ Ryd$ photons can ionize the ISM gas, producing photons (mainly Lyα) scattering out of the star forming regions. This last contribution is not taken into account in the model from Frank, Rasera, et al., 2012.

The relative contribution of these different sources to the total luminosity, an actively debated topic within the community, is analyzed in what follows on the basis of our high-resolution simulation.

4.2.1. Photo-ionization and collisional excitation in the CGM

The exact determination of the contributions from these different sources would require on-the-fly calculation within the hydrodynamical simulation itself. This has been done for the UV ionizing continuum which impacts the ionization, the temperature and the dynamic of the gas, and consequently changes its emissivity (Rosdahl, Blaizot, et al., 2013). A good approximation of this on-the-fly UV ionizing photons transfer has been developed by Rosdahl, Blaizot, et al., 2013, namely the 'on-the-fly' self-shielding, used in this simulation (see section 4.2.1.4).

Nevertheless, the post-processing of the transfer of the resonant Lya photons gives rather good estimates of the total flux emitted (Verhamme, Schaerer, et al., 2006; Kollmeier, Zheng, et al., 2010; Faucher-Giguere, Keres, et al., 2010; Trebitsch et al., 2016).

4.2.1.1. Emissivity tables

Similarly to Bertone, Schaye, Booth, et al., 2010; Frank, Rasera, et al., 2012, we generate emissivity tables for our lines of interest at the corresponding redshifts to attribute a luminosity to each gas cell. These tables will account for the flux produced by the gravitational cooling of the gas, and the recombinations from the UVB photo-ionization.

We use the photo-ionization code CLOUDY, version 10.01[c], last described by Ferland et al., 1998. This code predicts the thermal, ionization, and chemical structure of a cloud illuminated in a variety of physical conditions.

We consider a 1cm slab of optically thin gas at solar metallicity[d], with no molecules and using the element abundances in the solar photosphere as described by Grevesse et al., 2010. In our model, we use the background derived by Haardt et al., 2001 (HM01 in the following) with contributions from both quasars and galaxies.

We derive the hydrogen density $\mathrm{n_H} = \frac{\mathrm{X_\odot}}{\mathrm{m_H}}\rho$, with $\mathrm{X_\odot} = 0.7380$, $\mathrm{Y_\odot} = 0.2484$, $\mathrm{Z_\odot} = 0.0134$, and the weighted temperature $\mathrm{T}/\mu = \frac{\mathrm{m_H}}{\mathrm{k_B}}\frac{\mathrm{P}}{\rho}$ from the simulation using Grevesse et al., 2010 abundances (also used in the Cloudy models for consistency).

[c] We are using this version of Cloudy as it includes the option to compile with double floats, which is not computed in the c13 Cloudy version. This feature is important in our case, as we are deriving the emissivity from very low density regions. These regions can have emissivities below -32 dex.

[d] The emissivity ϵ scales linearly with metallicity in the first order.

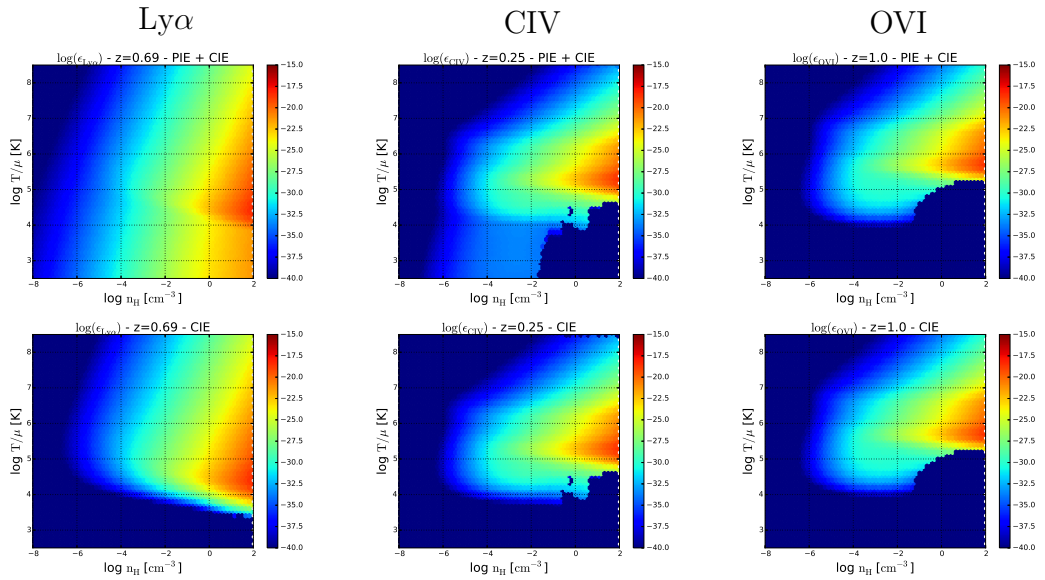

Figure 4.5.: Emissivity tables $(\log(\mathrm{n})/\log(\mathrm{T}/\mu))$ for Lyα at z=0.69 (left panels), CIV at z=0.25 (middle panels) and OVI at z=1.0 (right panels). The top panels show the dual contribution of photo-ionization equilibrium (PIE) and collisional ionisation equilibrium (CIE), while the bottom panels show the sole contribution of the CIE, used for the self-shielded gas. There are some patches in the CIV and OVI emissivity tables that are unresolved by the Cloudy calculation (see text).

The tabulation of $\log \mathrm{T}/\mu$ goes in two steps. First, we generate emissivity tables as well as electronic density tables in (n,T). We use $\log \mathrm{n_{min}} = -8$, $\log \mathrm{n_{max}} = 4$, $\mathrm{d}\log \mathrm{n} = 0.1$, $\log \mathrm{T_{min}} = 2$ and $\log \mathrm{T_{max}} = 8$, $\mathrm{d}\log \mathrm{T} = 0.1$. For each point (n,T) in the emissivity tables, we generate a new coordinate (log n,$\log \mathrm{T}/\mu$) using $\mu = \frac{\mathrm{n_H A_H + n_{He} A_{He}}}{\mathrm{n_H + n_{He} + n_e}}$ where $A_H = 1.0074$ is the mass number of hydrogen, $\mathrm{A_{He}} = 4.002602$ the mass number of helium, and $\mathrm{n_H}$, $\mathrm{n_{He}}$ and $\mathrm{n_e}$ are the hydrogen, helium and electronic densities respectively, tabulated along the emissivity tables. This gives a non-uniformly distributed (log n, $\log \mathrm{T}/\mu$) emissivity table which we interpolate back onto a regular grid with the python package scipy.interpolate.LinearNDInterpolator using $\log(\mathrm{T}/\mu)_{\mathrm{min}} = \min(\log \mathrm{T}/\mu)$ and $\log \mathrm{T_{max}} = \max(\log \mathrm{T}/\mu)$ and $\mathrm{d}\log \mathrm{T}/\mu = \frac{1}{3}\mathrm{d}\log \mathrm{T}$.

We then interpolate the different emissivity tables available to the corresponding expansion factor of the considered snapshot.

Fig. 4.5 shows the emissivities tables for the 3 differents lines of interest: Lyα, OVI and CIV. The top panels shows the joint contribution of Photo-ionization (PIE) and collisional ionization (CIE), while the bottom panels show the sole contribution of CIE, used for the self-shielded gas. In all the lines, the emission above $\mathrm{T} = 10^4$ K is dominated by collisions. Photo-ionization emerges from densities $\mathrm{n_H} \sim 10^{-4}$ at/cc. The emission reaches a maximum around $\mathrm{T} \sim 10^{4.5}$ K

for Lyα, T $\sim 10^5$ K for CIV and T $\sim 10^{5.5}$ K for OVI. The Lyα recombinations predominantly affect low temperature gas.

There are unresolved emissivities for the metal line emissions, but this poorly affects the model as they occur in dense regions where the cells are usually found with lower temperatures (in the ISM region, below 10^4 K).

4.2.1.2. Induced processes (photon pumping)

Another significant number of Lyα photons are produced by the reprocessing of absorbed continuum photons doppler shifted down to the broad Lyα line, which is commonly referred to as pumping of Lyα photons. Only the metagalactic background continuum enters our definition of pumping, as the stellar continuum contribution is accounted for by the successive scattering and cascading of ionizing photons and higher order Lyman lines. The question of pumping of $\mathrm{Ly}\alpha$ continuum photons by the gas is a crucial in the issue of total emission budget. Indeed, absorption of isotropic continuum photons near the $\mathrm{Ly}\alpha$ line by the gas via Doppler effect mechanisms does not contribute to the net emission of the gas as it is simply isotropic scattering of an isotropic source. In other words, optically thin gas can be considered as transparent to the pumping of an isotropic source such as the sky background. This is not the case if we consider a non isotropic source (such as a nearby quasar). However, the cascading of higher order isotropic Lyman photons (except $\mathrm{Ly}\beta$) to $\mathrm{Ly}\alpha$ does contribute to the net budget, but this represents only a few percent of the total emission (Furlanetto et al., 2004).

In different works (Furlanetto et al., 2005; Frank, Rasera, et al., 2012), the Cloudy models have been ran with the option 'no induced processes', which turns off the 'cascading' of Lyman photons to Lya photon. This prevents unphysical treatment of $\mathrm{Ly}\beta \rightarrow \mathrm{Ly}\alpha$ cascading, which does not apply in our density regime. The contribution is limited for optically thin gas to Lyγ (Fig. 1 of Furlanetto et al., 2005), but it might become important when the gas gets optically thick and would require full radiative transfer treatments. On the other hand, turning off these 'induced processes' might turn out to be unphysical as well, as described in Cloudy User's Manual since it turns off all fluorescent excitation processes.

We compared the emissivity from a Cloudy model with the 'induced processes' on, from which we removed the 'pumped' contribution of the line, to a Cloudy model without induced processes. Fig. 4.6 shows the logarithmic difference between the model with induced processes free from Pumping ($\log(\epsilon^{\mathrm{induced}}_{\mathrm{Ly}\alpha} - \epsilon^{\mathrm{Pump}}_{\mathrm{Lya}})$ and the model without induced processes ($\log \epsilon^{\mathrm{noinduced}}_{\mathrm{Ly}\alpha}$).

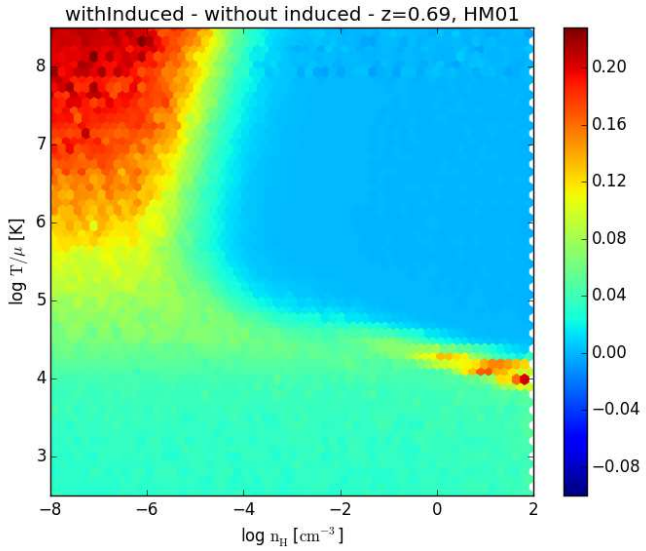

Figure 4.6.: Comparison between the 'no induced' option and the pumping removal from the total emissivity: $\log(\epsilon_{\rm total}^{\rm induced} - \epsilon_{\rm pump}^{\rm induced}) - \log(\epsilon_{\rm total}^{\rm no\ induced})$. Table for Ly$\alpha$ at z=0.69 with UV background HM01.

In the Lyα cooling region[e] and ISM region[f], the logarithmic difference between the two models is rather low and homogeneous: $\log(\epsilon_{\rm total}^{\rm induced} - \epsilon_{\rm pump}^{\rm induced}) - \log(\epsilon_{\rm total}^{\rm no\ induced}) \sim 0.05$. For regions where collisions prevail[g], these two models are equivalent. Finally, it increases up to $\log(\epsilon_{\rm total}^{\rm induced} - \epsilon_{\rm pump}^{\rm induced}) - \log(\epsilon_{\rm total}^{\rm no\ induced}) \sim 0.2$ for low density and high temperature gas (top left region in Fig. 4.6).

We choose to remain conservative by using the 'non-induced' model, thus preventing an over-estimate of the emission, especially in the star forming area. Moreover, this choice is consistent with previous work on the subject (Furlanetto et al., 2005; Frank, Rasera, et al., 2012).

4.2.1.3. Non-thermal feedback

For many star forming halos in our high-resolution simulation, we find a small percentage ($< 1\%$) of gas cells with active delayed cooling (from the non thermal feedback, see section 4.1.3). These cells reach temperatures of 10^{5-6}K, with densities consistent with ISM gas cells ($\rm n_H > 0.1\ at/cm^3$). They have emissivities about ten orders of magnitudes above their regular value, and contribute to more than 99% of the total luminosity of the halo, despite their small numbers.

We choose not to consider these particular cells in the total luminosity budget,

[e] $\rm n_H \sim 0.1$ at/cc and $\rm T \sim 10^4$ K
[f] $\rm n_H > 0.1$ at/cc and $\rm T < 10^4$ K
[g] $\rm n_H > 10^{-4}$ at/cc and $\rm T > 10^{4.5}$ K

as they would in reality not reach these high temperatures but in fact higher pressure, and for a shorter time scale duration, more as a flash. This consideration brings no particular bias in the total luminosity budget (we remain conservative by not taking them into account), as we checked that these cells, originally associated with ISM gas, should not contribute predominantly.

4.2.1.4. Post-processing self-shielding

Asserting the fraction of gas self-shielded from ionizing radiations is a rather delicate topic. Indeed, modeling the optical depth of a cloud is challenging for some lines such as Lyα and specialized radiative transfer models can be set up to establish trends. In the Frank, Rasera, et al., 2012 analysis, the most optimistic self-shielding model uses Popping et al., 2009 results, using the equilibrium between sound speed in the gas and radiative recombination along with a model for molecular hydrogen formation. The first condition is rather conservative as we find the same behavior in our tables for the ionized fraction of hydrogen, but the second condition is limited to the resolution of their simulation. With our increased resolution, this condition does not hold any longer, as much of the gas with a temperature lower than $\mathrm{T} = 10^4$ K, and thus in the ISM regime, will be considered in the PIE state, and will contribute significantly more to the total emission budget.

We adopt the model proposed by Furlanetto et al., 2004 that simply puts a condition on the temperature (the gas at $\mathrm{T} > 10^{4.5}$ K is collisionally ionized and therefore can not be self-shielded) and on the density. The density threshold is $\mathrm{n_{HI}} \sim 10^{-2}\,\mathrm{at/cm^3}$, in line with Rosdahl and Blaizot, 2012 (at z=3) and Faucher-Giguere, Keres, et al., 2010 prescription based on radiative transfer analysis.

4.2.2. Nearby stellar contribution to the Lyα luminosity

In addition to those from distant stars accounted for in HM, ionizing photons ($\nu \geq 1$ Ryd) emitted by nearby young stars, in particular these belonging to the considered halo, contribute substantially to the total Lyα emission for star forming galaxies. However, intergalactic dust, as well as gas kinematic properties within the gas cloud have a major impact on the actual number of ionizing and Lyα photons escaping the disk (Kunth et al., 2003; Verhamme, Dubois, et al., 2012). These ionizing photons may be absorbed by the dust in the ISM, which produce important extinction at short wavelengths. In contrast, the Lyα photons produced by recombination will scatter a number of times before they escape the ISM due to the high resonance of the Lyα line and the high neutral gas density of the ISM which increase the probability of absorption by dust grains. These dust attenuations are poorly constrained at low redshift, so we will consider a empirical approach. We use the prescription from Furlanetto et al., 2005 to estimate the intrinsic Lyα luminosity from ionizing photons in the absence of

dust: $L_{Ly\alpha}^{stars}$ [erg/s] $= 10^{42}$ SFR [$M_\odot yr^{-1}$]. We compute the SFR of each halo from the mass of young stars, using the "continuous star formation" approximation (Kennicutt, 1998):

$$\text{SFR } [M_\odot/\text{yr}] = \frac{M_{\text{stars}<10^8 \text{ yrs}} \ [M_\odot]}{10^8 \ [\text{yr}]} \tag{4.1}$$

Using COS data of low redshift ($z \sim 0.03$) star forming galaxies, Wofford et al., 2013 measured a Lyα escape fraction[h] ranging from 1 to 10%. They estimate that this fraction is very sensitive to the presence of dust and to the HI column density as well as to their geometry, the Lyα photons escaping more easily through holes of low HI and dust column densities, resulting in a large scatter.

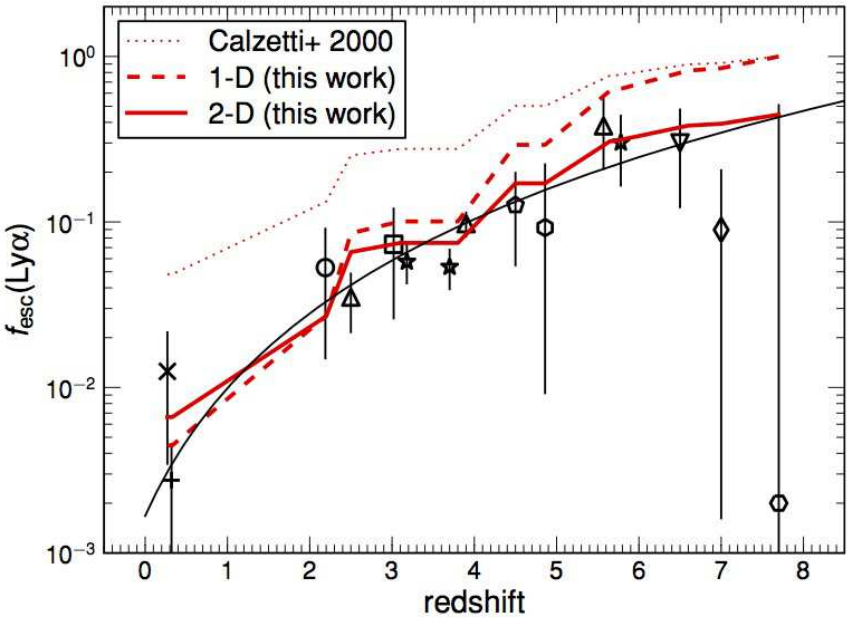

Figure 4.7.: Evolution of the Lyα escape fraction, $f_{esc}(Ly\alpha)$. Credit: Hayes et al., 2011

Given the large uncertainty in the models for either the dust or radiative transfer, we will consider two cases for the Lyα luminosity from the stellar contribution: one with a Lyα escape fraction of 1%, and another with a Lyα escape fraction of 0.1%. These values bracket most of the observed data, though some values can be lower at low redshift (Fig. 4.7).

Predicting the spatial and spectral profiles of such emission requires the full calculation from radiative transfer techniques (Verhamme, Schaerer, et al., 2006; Verhamme, Dubois, et al., 2012; Rosdahl, Blaizot, et al., 2013; Lake et al., 2015;

[h]The Lyα escape fraction is the ratio between the observed and the intrinsic Lyα luminosity.

Trebitsch et al., 2016), but this is beyond the scope of this thesis. However, as our goal is to study the detectability of such emission via FIREBall-2, we chose to make the simple assumption that all the photons only go through one aborption/re-emission process before leaving the cloud. Also, we assume that all of the ionizing photons are emitted from the center of the galaxy. We then weight the profile proportionally to the hydrogen density of the gas cell and by its inversed squared distance to the center. This gives us, for each cell j the luminosity L^*_j:

$$L^*_j[\mathrm{erg/s}] = f_{esc}(Ly\alpha)\ \frac{\frac{n^j_H}{R^2_j}}{\int_{R_{vir}} \frac{n_H}{R^2}}\ 10^{42}\ SFR_j\ [M_\odot/yr] \tag{4.2}$$

This approximation has a moderate impact on the radial profile of the emission as seen in Fig. 3 of Trebitsch et al., 2016.

4.2.2.1. Total Lyα Luminosity

From the previous sections, we study here the two major origins to the emission of Lyα photons: $Ly\alpha^{\text{grav. cooling + UVB fluo.}}$ and $Ly\alpha^{\text{stars}}$. To simplify the calculation, we consider that the total luminosity for the Lyα line is the sum of these two quantities:

$$L^{\text{total}}_{Ly\alpha} = L^{\text{grav. cooling + UVB fluo.}}_{Ly\alpha} + L^{\text{stars}}_{Ly\alpha} \tag{4.3}$$

This formulation is not fully accurate, as we should strictly take into account the ionizing flux from the young stars directly in the Cloudy model used and during the simulation computation to reproduce the density/temperature state of the gas in these conditions. So far, the RAMSES simulation only reproduces the gravitational effects and the heating from the UVB. Regarding the purpose of the present work, this assumption gives valuable insights on the level of radiation from the CGM and the relative contribution of both emission mechanisms.

4.2.3. UV continuum near the lines

To properly reproduce mock observations for FIREBall-2, we now need to model the UV continuum of each halo. We first compute the SFR of each halo from the mass of young stars, from which we infer the flux derived by Kennicutt, 1998 , $L_{\lambda,1500\ \text{Å}}(\lambda)\ [\mathrm{erg/s/Å}] = \frac{SFR\ [M_\odot/yr]}{1.4}\frac{c}{\lambda^2}\ 10^{28}$. To derive the spatial extent of this continuum, we assume that the UV continuum is mainly produced by these young stars, so we use them to derive a 'stellar density field' that we scale with $L_{\lambda,1500\ \text{Å}}(\lambda)$. To account for the dust attenuation of these continuum photons, we use the model from Zahid et al., 2012 to get the color excess E(B-V) from each stellar particle (not just the young stars) using their stellar mass M_* and

metallicity Z:

$$E(B-V) = 0.44\ (p_0 + p_1 Z^{p_2})\ M^{p_3} \tag{4.4}$$

where $Z = 10^{(12+\log(O/H)-8)}$, $M = M_*/10^{10}$, $p_0 = 0.12 \pm 0.01$, $p_1 = 0.041 \pm 0.006$, $p_2 = 0.77 \pm 0.06$, and $p_3 = 0.240 \pm 0.002$. We consider the stellar mass weighted metallicity to derive Z from the simulation. We derive the extinction $k'(\lambda)$ following Calzetti et al., 2000:

$$k'(\lambda) = 2.659(-2.156 + 1.509/\lambda - 0.198/\lambda^2 + 0.011/\lambda^3) + R'_V \tag{4.5}$$

for $0.12\mu m \leq \lambda \leq 0.63\mu m$. We choose to use $R'_V = 3.1$ to account for a dusty environment such as the Galactic diffuse ISM. The attenuation of the continuum then scales as $10^{-0.4\ k'\ E(B-V)}$. We make the assumption that the attenuation is constant within the ISM. Finally, the total continuum level is estimated as follows:

$$L_{\lambda,1500\ Å}(\lambda)\ [erg/s/Å] = 10^{-0.4\ k'\ E(B-V)}\ \frac{SFR\ [M_\odot/yr]}{1.4}\frac{c}{\lambda^2}\ 10^{28} \tag{4.6}$$

4.3. Results

4.3.1. Comparison to higher redshift observations

In the absence of low-redshift observations of CGM emission, we consider recent observations of Lyα emission from high redshift Lyα halos from the Subaru telescope (z=2.3, Momose et al., 2014) and the VLT/MUSE (z=4.0, Wisotzki et al., 2016) to check our model. Although the description of the model in the previous sections is optimized for FIREBall-2 low-redshift objects, we transpose the model down to redshifts z=2.3 and z=4.0. This transposition does not bring major changes in the post-processing self-shielding treatment, as the density cut is already calibrated following high redshift simulated galaxies and the temperature cut is purely empirical. We use the same model for the dust attenuation factor, for the continuum, assuming the properties of dust grains do not evolve much with redshift. However, the Lyα escape fraction $f_{esc}^{Ly\alpha}$ increases with redshift, and can be of the order of 10% at redshift 4 (Hayes et al., 2011). For this PhD work, we limit ourselves to the comparison of these observations with one selected halo from our Zoom Simulation.

4.3.1.1. Surface Brightness Profiles at z=4

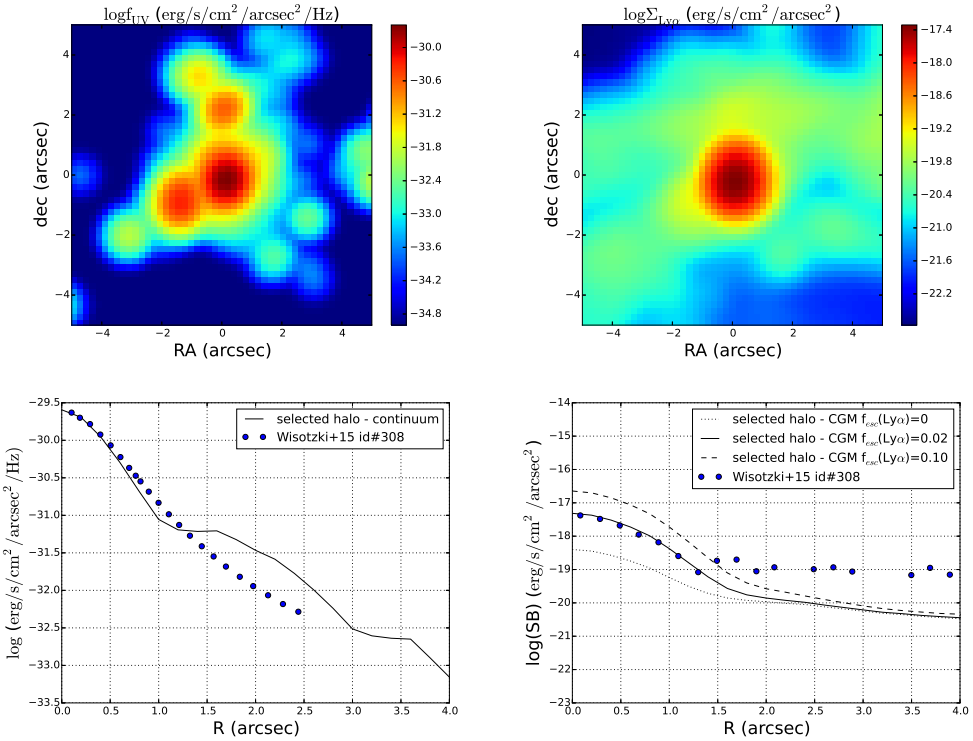

Figure 4.8.: Top left panel: Surface Brightness (SB) map of the continuum of the halo selected for the comparison with object #308 from Wisotzki et al., 2016 at z=4.018. Bottom left panel: SB radial profile of the continuum for the selected halo and object #308. Top right panel: SB map of the Lyα line emission, using $\mathrm{f_{esc}(Ly\alpha)} = 2\%$ for the selected halo. Bottom right panel: SB radial profiles of the Lyα line emission for the selected halo with Lyα escape fractions of {0, 2, 10}% and for object #308.

We chose object #308 from Wisotzki et al., 2016 for the comparison, as it lies at a redshift matching our high-resolution simulation set. We tentatively compare this object to one of the halo from our Zoom Simulation which has a similar Surface Brightness (SB) radial profile in the UV continuum. The selected halo has a stellar mass $\mathrm{M_*} = 7.0\ 10^9\ \mathrm{M_\odot}$ and a SFR of $50.9\ \mathrm{M_\odot/yr}$, the latter being larger than the observed one ($\mathrm{M_*} = 10^{8-9}\ \mathrm{M_\odot}$ and $\mathrm{SFR} = 0.3 - 16\ \mathrm{M_\odot/yr}$).

The top left panel of Fig. 4.8 shows the SB map of the continnum of the selected halo. We convolved the image with a 0.66 arcsec FWHM PSF to account for the seeing and with a 0.71 arcsec FWHM PSF to reproduce the instrument's resolution (Bacon et al., 2014). The bottom left panel shows the SB radial profile

for the selected halo and object #308. The top right panel shows the SB map of the Lyα line for the selected halo, with the same convolutions than the continuum. The bottom right panel shows the SB radial profile for the simulated object using Lyα escape fractions of {0, 2, 10}% and that of object #308. We recover a similar Lyα luminosity than the one measured by Wisotzki et al., 2016 for object #308 ($L_{Ly\alpha} = 1.6\ 10^{42}$ erg/s) with $f_{esc}(Ly\alpha) = 2\%$: $L_{Ly\alpha} = 2.0\ 10^{42}$ erg/s. This Lyα escape fraction is 5 times lower than what Hayes et al., 2011 fit at this redshift. This can be considered as a reasonable agreement given the large scatter in the Lyα emission.

4.3.1.2. Surface Brightness Profiles at z=2.2

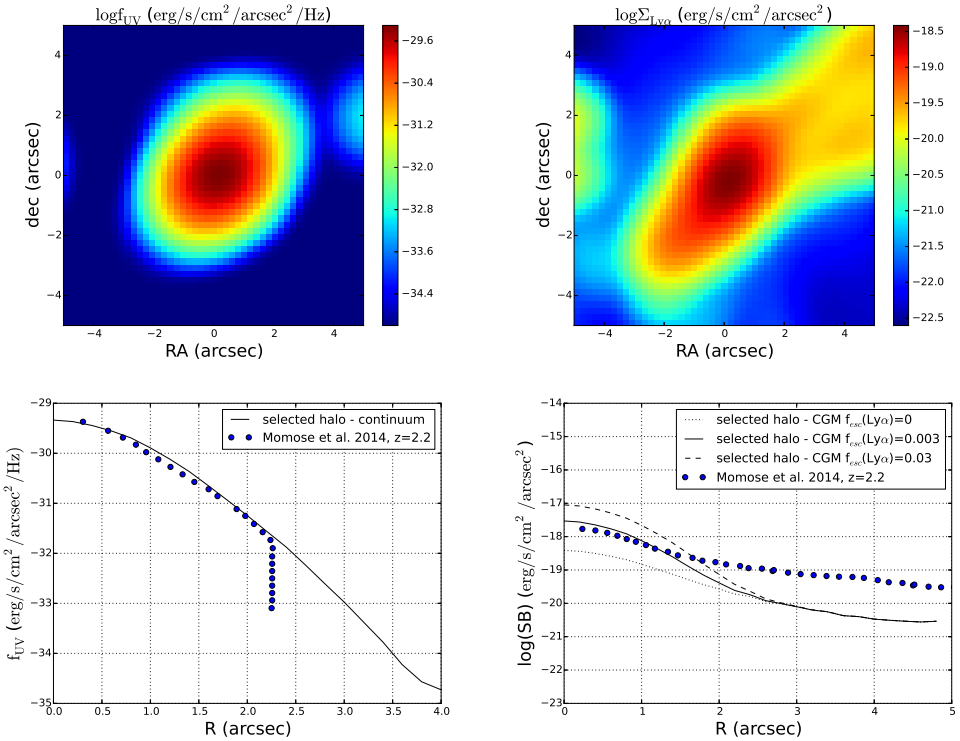

Figure 4.9.: Top left panel: SB map of the continnum of the halo selected for the comparison with the stack of 3556 LAEs from Momose et al., 2014 at z=2.2. Bottom left panel: SB radial profile of the continuum for the selected halo and the stack. Top right panel: SB map of the Lyα line emission, using $f_{esc}(Ly\alpha) = 0.003$, for the selected halo. Bottom right panel: SB radial profile of the Lyα line emission for the selected halo with Lyα escape fractions of {0, 0.3, 3}% and for the stack.

The SB profile at z=2.2 performed by Momose et al., 2014 results from the stacking of 3556 LAEs. The comparison to one of our objects is therefore illustrative but biased. However, I selected a halo with $M_* = 4.8\ 10^{10}\ M_\odot$ and $SFR = 91.9\ M_\odot/yr$ which has a SB radial profile of the UV continuum similar to that of the stack.

The top left panel of Fig. 4.9 show the SB map of the continuum of the selected object, while the bottom left panel shows its SB radial profile with a comparison the the stack. As in the analysis by Momose et al., 2014, we convolved the image with a PSF of 1.32 arcsec FWHM to reproduce the largest seeing size of the stacked images.

The top right panels shows the SB map of the selected object Lyα line, with the same convolution than the continuum. The bottom right panel shows the SB radial profile for the simulated object using Lyα escape fractions of {0, 0.3, 3}% and that of the stack. We are able to reproduce the Lyα line level with a Lyα escape fraction of 0.3% (which is ten times below the measurements from Hayes et al., 2011, at this redshift), which corresponds to a Lyα luminosity of $L_{Ly\alpha} = 3.46\ 10^{41}\ erg/s$. This low value for the escape fraction is in agreement with Matthee et al., 2016 for $SFR \approx 90\ M_\odot/yr$ (Fig. 4.10), as they show that the escape fraction is anti-correlated with the SFR at z=2.23.

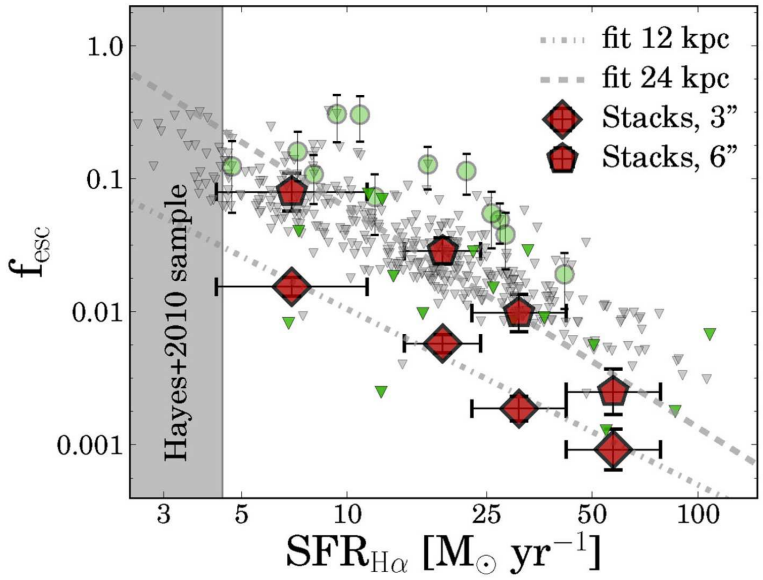

Figure 4.10.: Evolution of $f_{esc}(Ly\alpha)$ with SFR and effect of stacking. Credit: Matthee et al., 2016

4.3.1.3. Conclusion

Overall, we are able to reproduce the continuum level of high redshift observation with halos selected from our high-resolution simulation.

However, the measurements from Hayes et al., 2011 for the Lyα escape fraction yields higher fluxes (by a factor 5 at z=4.0 and by a factor 10 at z=2.2) for the CGM with comparable UV fluxes. We attribute this difference to the large SFR of our chosen halo at z=2.2, as the escape fraction is expected to be anti-correlated with SFR at this redshift (Matthee et al., 2016). At z=4, the comparison holds given the dispersion inherent to the observations.

We note that accounting for a complete transfer could affect the distribution of scattered Lyα photons, which could be redistributed out to larger radii (**Trebisch2016**; Rosdahl and Blaizot, 2012). Also, in this thesis work, we assume a spatially uniform escape fraction, while observations show that it is not the case (see the different values for the escape fraction from stacks at 3" and 6" on Fig. 4.10). This supports the need to better constrain the distribution of scattered photons from radiative transfer analyses.

In the following, which is focused on low redshifts ($z < 1$), we will use two different Lyα escape fractions: the one prescribed by Hayes et al., 2011 at redshift z=0.67, $f_{esc}(Ly\alpha) = 1\%$, and one lowered by a factor of 10, typically 0.1%. This should provide a secure range for the coming investigation concerning the detection of Lyα emitting sources with FIREBall-2 at z=0.67. This range is conservative, since high SFR galaxies can show high Lyα escape fractions due to the presence of holes of low HI column density or dust content (Giavalisco, Koratkar, et al., 1996; Atek et al., 2009), which may be created by the violent galactic feedback that is predominant in star forming galaxies.

4.3.2. Lyα luminosity of the different halos and sub-halos near $z \sim 0.67$

In order to prepare the FIREBall-2 target selection, we look at the properties of individual halos found within the zoomed region of the high-resolution simulation (defined as the cube centered on the simulation's center and of $13.5\ h^{-1}\ cMpc$ on a side) to infer the different correlations with the halos' luminosities. A classification of halos and sub-halos is performed with HaloMaker, a structure finder using AdaptaHOP[i] (Aubert et al., 2004; Tweed et al., 2009).

In order to remain conservative, we consider the different contributions (in terms of luminosity, masses, SFR, attenuation) from each halo and sub-halo individually, meaning that we extract the contribution of higher order sub-halos from their host halo/sub-halo. Moreover, we only consider the sub-halos whose

[i] We use a minimum of 20 particles per halo, the Most massive Sub maxima Method (MSM), and the following parameters for adaptahop: b=0.2, nvoisin=32, nhop = 16, rhot = 80, fudge = 4, fudgepsilon = 0, slphap = 4 (Blaizot et al., private communication).

gas is in the cooling phase ($T \sim 10^4$ K). Indeed, as the HaloFinder uses the Dark Matter distribution to derive the halo tree, a large part of the halos are in fact DM halos which do not contain cool gas yet. They are all low mass DM halos, with $M_{DM} < 10^{10}$ $M_\odot$. Keres et al., 2005 have argued that the low mass DM halos ($M_{DM} < 10^{11.4}$ $M_\odot$) are the preferred candidates for the 'cold-mode' accretion (in opposition with the 'hot-mode' accretion) at high redshifts. In the 'cold-mode' model, the gas enters the galaxy via collimated streams that prevent part of the gas (around 50%) to shock-heat close to typical virial temperatures ($T \sim 10^6$ K for Milky Way-like galaxies), leaving the gas cool by radiating out the acquired gravitational energy down to lower temperatures ($T < 10^5$ K). In our case, the halos removed from the present analysis can not be associated with such cold-mode accretion as they are only witnessing the premises of such accretion. This is obvious when looking to their density/temperature diagram. These low mass DM halos have very low luminosities (there is a 2 dex drop off in cooling luminosity between halos within cooling gas and these halos, located approximately at $M_{gas} = 10^8$ $M_\odot$) and therefore do not contribute substantially to the present study.

4.3.2.1. Cooling and UVB Luminosity near $z \sim 0.67$

The top (resp. bottom) panel of Fig. 4.11 shows the evolution of the cooling emission and UVB luminosity of each halo/sub-halo of the zoomed region of the high-resolution simulation at $z = 0.67$ as a function of gas mass (resp. virial radius) and color-coded according to their SFR. The luminosity seems to evolve sharply with the virial radius up to a critical radius of about a few hundred parsecs where it increases less steeply. This is however subject to poor statistics above 200kpc.

We detect an inflection in the slope of the relation between luminosity and gas mass, located between star forming sub-halos and non star forming sub-halos, above $M_{gas} = 10^9$ $M_\odot$. The evolution of the luminosity is less steep for star forming halos than non star forming halos because the cells shock-heated by the blast produced during the SNae feedback (whose number correlates with the SFR) have been ignored in the model described in section 4.2.1.3. We can therefore expect a higher contribution from the cooling + UVB luminosity in SF halos than computed here. This inflection can also be associated with the removal of the sub-halo's contribution to the host halo luminosity. Indeed, the volume removed for each sub-halo was computed from the HaloFinder-based virial Radius. This removal is purely theoretical, and does not intend to reproduce the observational conditions in such a clustered regions, leaving only the contribution from the luminosity deprived of the sub-halos.

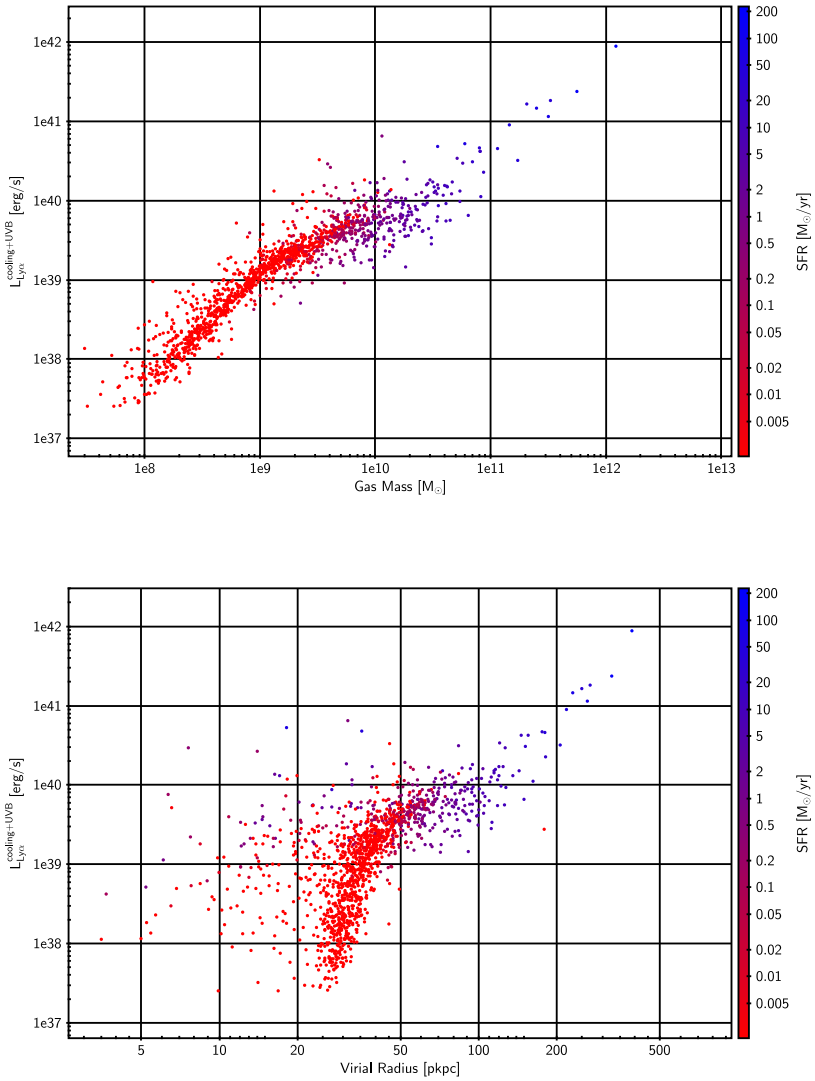

Figure 4.11.: Lyα luminosity from cooling radiations and UVB fluorescence $L_{Ly\alpha}^{cooling+UVB}$ as a function of gas mass (top panel) and virial radius (bottom panel) for the selected halos and sub-halos at z=0.67.

4.3.2.2. Total Lyα Luminosity near z ~ 0.67

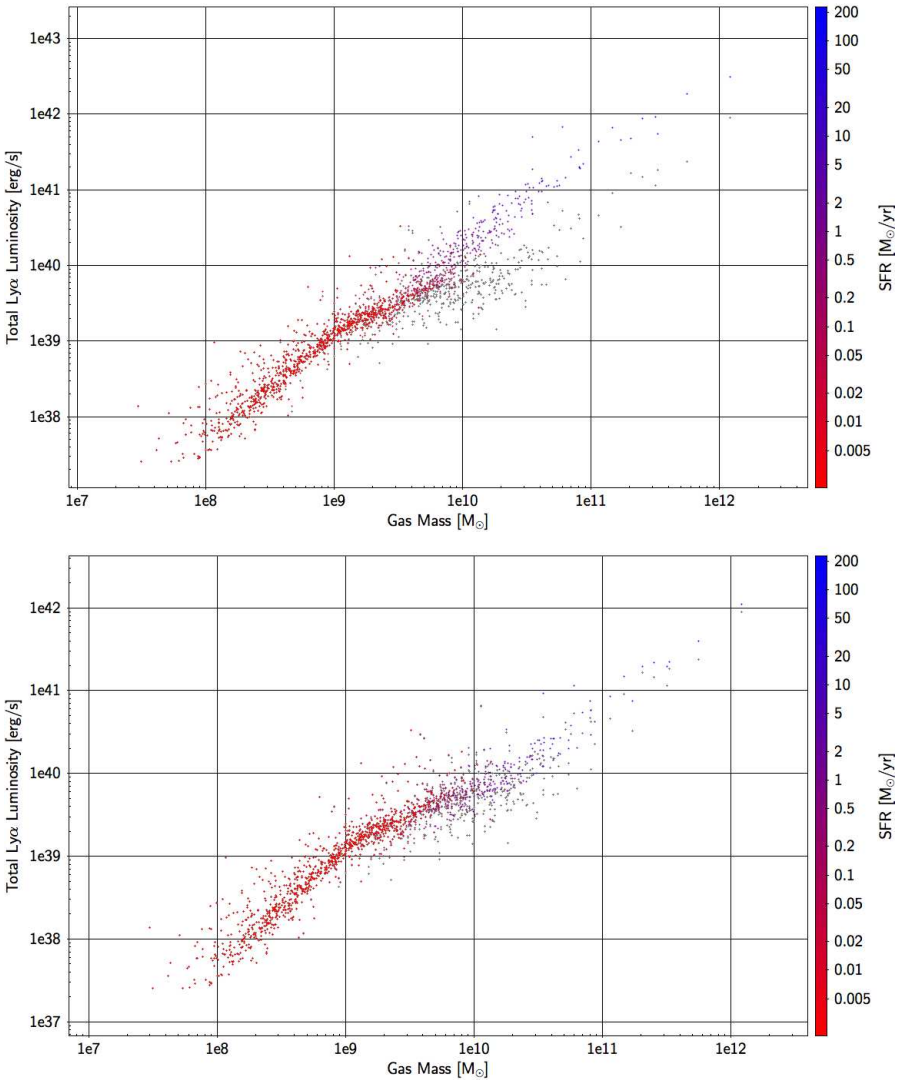

Figure 4.12.: Total Lyα luminosity versus gas mass at z=0.67 with $f_{esc} = 1\%$ (top panel) and $f_{esc} = 0.1\%$ (bottom panel). In both panels, the grey dots represent the cooling+UVB luminosity level.

The top (resp. bottom) panel of Fig. 4.12 shows the total luminosity with respect to gas mass, using an escape fraction for the ionizing photons contributing to the stellar Lyα scattering of 1% (resp. 0.1%). In both panels, the grey dots represent the gravitational cooling and UVB photo-ionization Lyα only (non stellar contributions). In the $f_{esc}(Ly\alpha) = 1\%$ case, the inflection present in Fig. 4.11 disappears. We reach a maximum Lyα luminosity of a few 10^{42} erg/s, which is lower than what Wold et al., 2014 observed at low-redshift with GALEX.

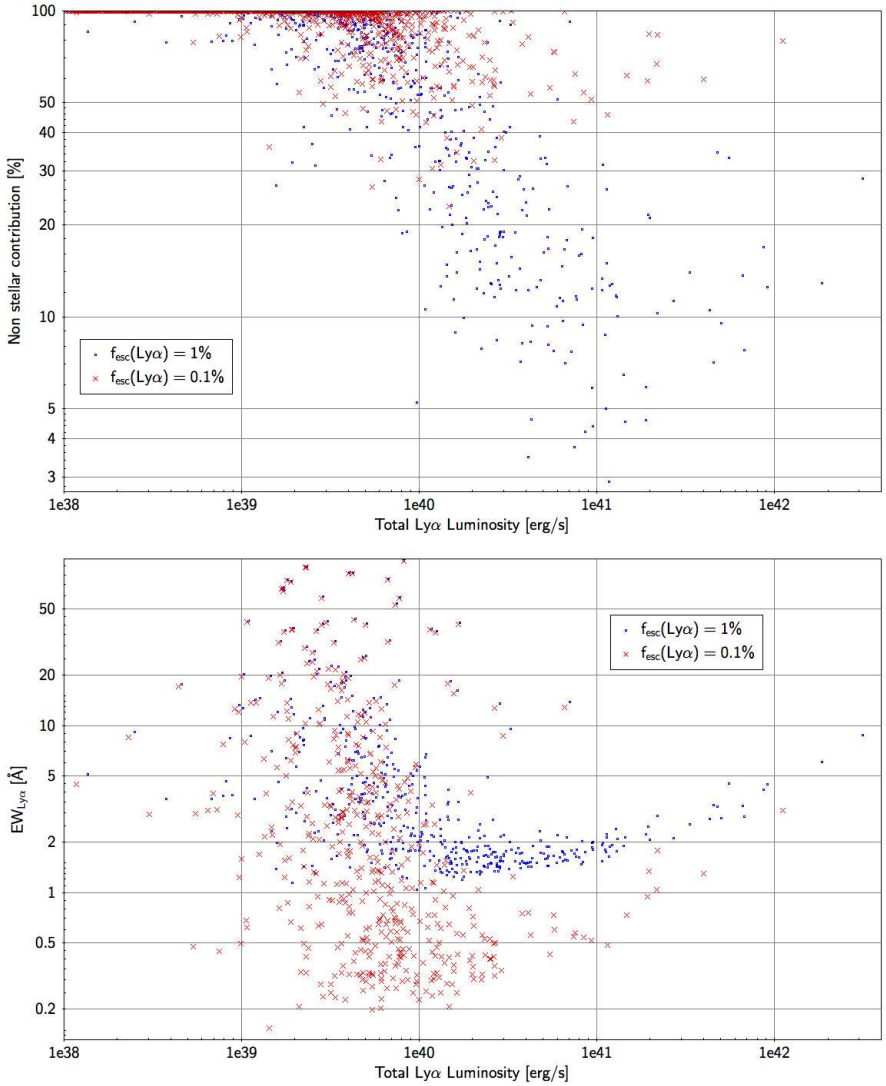

Figure 4.13.: Top panel: Non stellar contribution to the total Lyα luminosity versus total Lyα luminosity at z=0.67 with $f_{esc} = 1\%$ (blue squares) and $f_{esc} = 0.1\%$ (red crosses). Bottom panel: Lyα rest-frame equivalent width versus total Lyα luminosity at z=0.67 with $f_{esc} = 1\%$ (blue squares) and $f_{esc} = 0.1\%$ (red crosses).

The top panel of Fig. 4.13 shows the non stellar contribution to the total Lyα luminosity versus the total Lyα luminosity ($L_{Ly\alpha}^{cooling+UVB} + L_{Ly\alpha}^{stars}$) for $f_{esc}(Ly\alpha) = 1\%$ (blue squares) and $f_{esc}(Ly\alpha) = 0.1\%$ (red crosses). The non stellar contribution decreases with increasing total Lyα luminosity, reaching a minimum of about 5% at $\sim 10^{41}$ erg/s, then increases up to $\sim 40\%$. Our model predicts a non negligible impact of non stellar luminosity up to high luminosities. The halos and sub-halos with a SFR larger than $1\ M_\odot/yr$ have a predominant ($> 50\%$)

stellar contribution to the total Lyα luminosity. The gravitational cooling and UVB contributions account for a minimum of a few percent. This suggests that the extended Lyα emission around high redshift galaxies should be associated with SFR. Also, Lake et al., 2015 suggest from radiative transfer analysis at $z = 3$ that the stellar origin scattered in the outer region of the halo is dominating the emission, but that the radiation from gravitational cooling and UVB fluorescence still accounts for a substantial fraction of the emission (about 30% up to 70 kpc). In the $f_{esc}(Ly\alpha) = 0.1\%$ case, we divide the stellar contribution by a decade, thus resulting in an enhanced non stellar contribution to the total luminosity. This goes up to 80% for the most luminous objects and is never below 30%. With these values, the non stellar luminosity is equivalent to the stellar Lyα luminosity and should picture the behavior of galaxies with high dust content. Indeed, as the CGM has a much lower dust content than the ISM of galaxies[j], the Lyα produced into dense dusty regions should have more difficulty in escaping the galaxy than photons created in the dust free regions.

The bottom panel of Fig. 4.13 shows the rest-frame Lyα equivalent width with respect to the total Lyα luminosity for $f_{esc}(Ly\alpha) = 1\%$ (blue squares) and $f_{esc}(Ly\alpha) = 0.1\%$ (red crosses). For these two Lyα escape fractions, the predicted equivalent widths do not go beyond 10Å, which is the minimum value measured in the GALEX observations at low-redshift (Wold et al., 2014). A possible explanation for this difference is that the galaxies can show higher escape fractions than we have assumed, leading to higher Lyα luminosities and larger equivalent widths, such as is observed with the UV satellite.

4.3.3. Comparison of the main halo luminosity to the low-resolution simulation near $z \sim 0.67$

We note that the maximum Lyα luminosity does not exceed a few 10^{42} erg/s, while our high-resolution simulation is based on one of the brightest halos from the analysis performed by Frank, Rasera, et al., 2012. In their analysis, they predict Lyα luminosities to go up to 10^{44} erg/s, without even accounting for the SFR induced Lyα luminosity. This two dex difference with our present analysis finds its origin in the recipe used for the high-resolution simulation. Indeed, while we used '*on-the-fly*' self-shielding (see section 4.1.3) in our simulation, preventing $n_H > 10^{-2}$ at/cc gas cell to be heated by the metagalactic UVB, the gas cells in Frank, Rasera, et al., 2012 show larger temperature in the cooling 'gutter' of Lyα emission (see Fig. 4.3). This increase of the equilibrium temperature, although rather limited, has dramatic effects on the effective emission rate, as there is a steep dependency of the Lyα cooling emissivity on temperatures of a few 10^4 K ($\epsilon(10^4\ \mathrm{K}) \approx 10^2\ \epsilon(2\ 10^4\ \mathrm{K})$), Fig. 4.14). Because of that correction and the improved resolution, we argue that the emission level predicted in our

[j] We assume no dust extinction for the emissions from the cooling+UVB.

model is more realistic, despite being less optimistic than those derived in the original study as the crucial question of cooling temperature has been improved since the last implementation of the code.

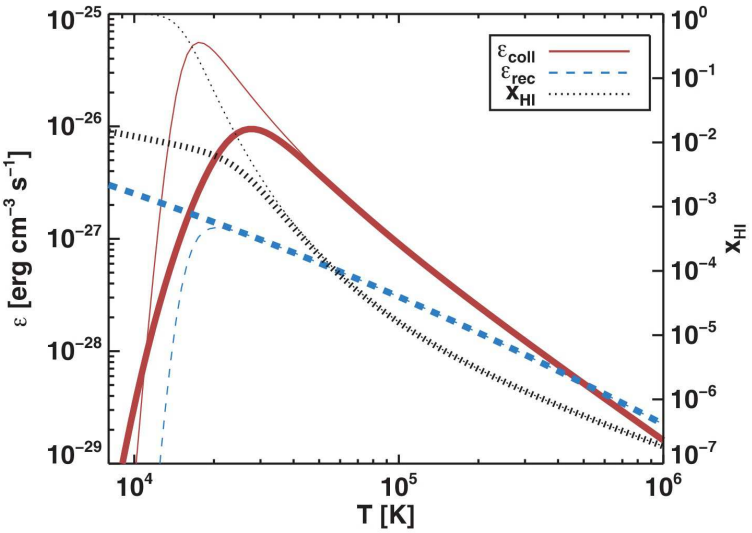

Figure 4.14.: Cooling Lyα emissivity versus temperature. This shows the strong $\epsilon - \mathrm{T}$ dependency at $\mathrm{T} \sim 10^4$ K. Credit: Rosdahl and Blaizot, 2012.

4.4. Conclusion

In this chapter, I have dealt with the extremely complex question of CGM faint emission modeling and the possibilities of its observation through a dedicated UV multi-slit spectrograph, FIREBall-2.

I have used a state-of-the-art high resolution hydrodynamical cosmological RAMSES simulation to extract different massive halos ($\gtrsim 10^{13}$ $\mathrm{M}_\odot$). Using a photo-ionization code, I modeled three different line emissivities (Lyα, CIV and OVI) produced by the UVB fluorescence and the gravitational cooling of the gas. I also computed the stellar contribution to the gas fluorescence in the case of Lyα photons and I derived the level of the UV continuum in those wavelengths accounting for the attenuation from the dust in the ISM.

The validation of the model is rather difficult considering the scarcity of low-redshift observations to compare to. Moving to higher redshifts (z=4.0 and z=2.33), our CGM Lyα emission model agrees well with the observational data provided we use a lower Lyα escape fraction than is usually inferred from observations. This effect might originate from the limitations due to the stacking of a large number of object in the z=2.33 case. Considering this discrepancy, we consider a range of possible Lyα escape fractions for our analysis at z=0.67. In

addition to the predicted value of $f_{esc}(Ly\alpha) = 1\%$ for this redshift, we also look at the conservative case of using a ten times lower escape fraction.

We analyzed the contribution of the different origins for Lyα luminosity, cooling radiations + photo-ionization by the UV background and photo-ionization by ionizing photons from star formation. It appears that the non stellar origin of the Lyα photons accounts for a substantial fraction of the total luminosity, even in the case of high Lyα escape fraction, which is in line with an analysis at higher redshift using radiative transfer (Lake et al., 2015). However, the Lyα equivalent widths we recover from our model appear to be rather low compared to what is seen from low-redshift GALEX observations (Wold et al., 2014), strengthening the argument for the need of further observations of the CGM in emission, such as the ones planned for FIREBall-2, to put better constraints on the modeling of the physical processes at play within the CGM of galaxies. However, we need to be cautious in this comparison because the radius covered by the Lyα GALEX measurements is not clearly defined.

Chapter 5: The end-to-end simulation of FIREBall-2 observations

Noooorrr... Nnnnnooorrrr... Nnnnnooooorrrrr...
NORS-KA !

Golgoth the 8th

I will now address the end-to-end analysis of the observational capabilities of the UV spectrograph FIREBall-2. From a high-resolution hydrodynamical simulation coupled to a model for the CGM emission at low redshifts (chapter 4), I produce detector outputs showing a realistic estimate for the observation of a simulated halo. The instrument model (IMO), interfacing the simulation and these outputs, is presented in the first section of this chapter. The last section focuses on a detailed signal to noise analysis of the observation of different halos from the simulation.

5.1. The Instrument Model

In order to prepare for the upcoming data analysis of FIREBall-2, Mège et al., 2015 developed a code that simulates the end-to-end image formation process along the optical path of the instrument. This code firstly generates a set of Point Spread Functions (PSFs) from an optical model at uniformly distributed field positions and wavelengths. These PSFs can then be interpolated at any point (in the field and wavelength), giving access to fundamental optical properties (magnification matrix, optical throughput, optical distortion, spectral dispersion) derived from the optical mappings existing between the sky plane and the instrument's mask or detector plane. Secondly, it produces 2D images of the electronic map of a detector patch corresponding to the observation of a simulated emission line from a simulated galaxy (chapter 4). In this section, I will briefly introduce the main characteristics of the FIREBall Instrument Model (hereafter IMO), and I

will present some improvements that Didier Vibert and I have implemented in the code since its publication.

5.1.1. Generating PSFs and detector images

The main work presented here is from Mège et al., 2015.

5.1.1.1. Generating PSFs

The simulation of FIREBall-2 and many UV instruments relies on the knowledge of the different optical components throughput and the estimation of total instrument's PSF at any point (field or wavelength). The determination of the PSFs is done on a uniformly distributed grid. For each position in the field and for each wavelength, the code generates a number of rays (typically 256^2) which will propagate through the instrument down to the mask, realistically modeled by an optical and illumination design software, Zemax. An example of their final distribution onto the mask is shown in Fig. 5.1.

These distributions are the PSFs of the instrument up to the mask, called the sky-to-slit PSFs. An image density hypercube is then created for these PSFs (Fig. 5.2). Then, the code generates a mapping between the centroid of these PSFs and their original sky position. At this point, the slit is introduced. Centered on the position of the centroids, the slit is added to the Zemax model and another group of rays are generated, this time down to the detector and through the slit. Another dimension is considered for the sky-to-detector PSF hypercube: the spatial decentering of a point-source photocentroid with respect to the slit center in FIREBall-2's mask plane. This produces a 4-dimensional hypercube of sky-to-detector PSFs, for each angular position on the sky, wavelength and spatial decentering of the slit center relatively to the photocentroid.

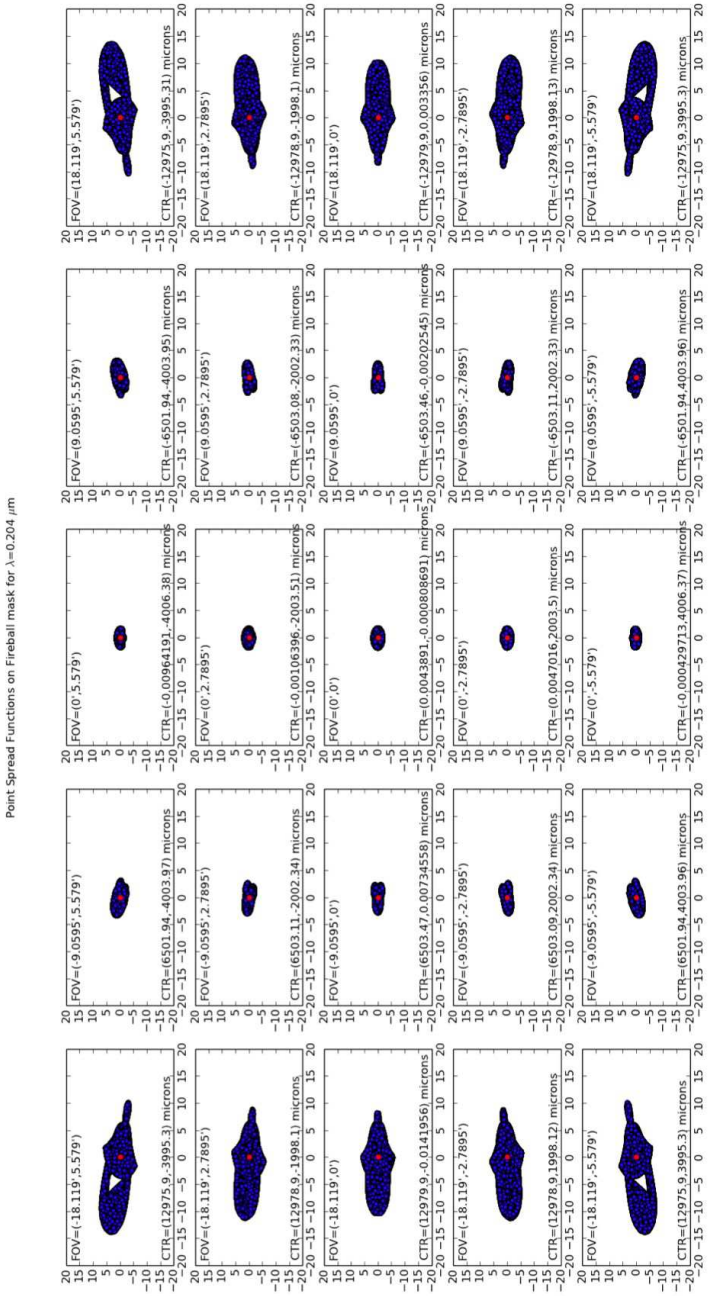

Figure 5.1.: PSF Rays of the sky-to-slit mapping at 204nm, sampled on 5x5 positions on the field: {-18.12, -9.06, 0, 9.06, 18.12}x{-5.58, -2.79, 0, 2.79, 5.58} arcmin. The red dot in each panel represent the PSF centroid used for following analysis. The apparent asymmetry in the image quality regarding the horizontal to vertical axis is an effect of the larger angular range probed in the horizontal direction of this figure. Warning: the scale is not the same in the horizontal and vertical directions. Credit: Mège et al., 2015

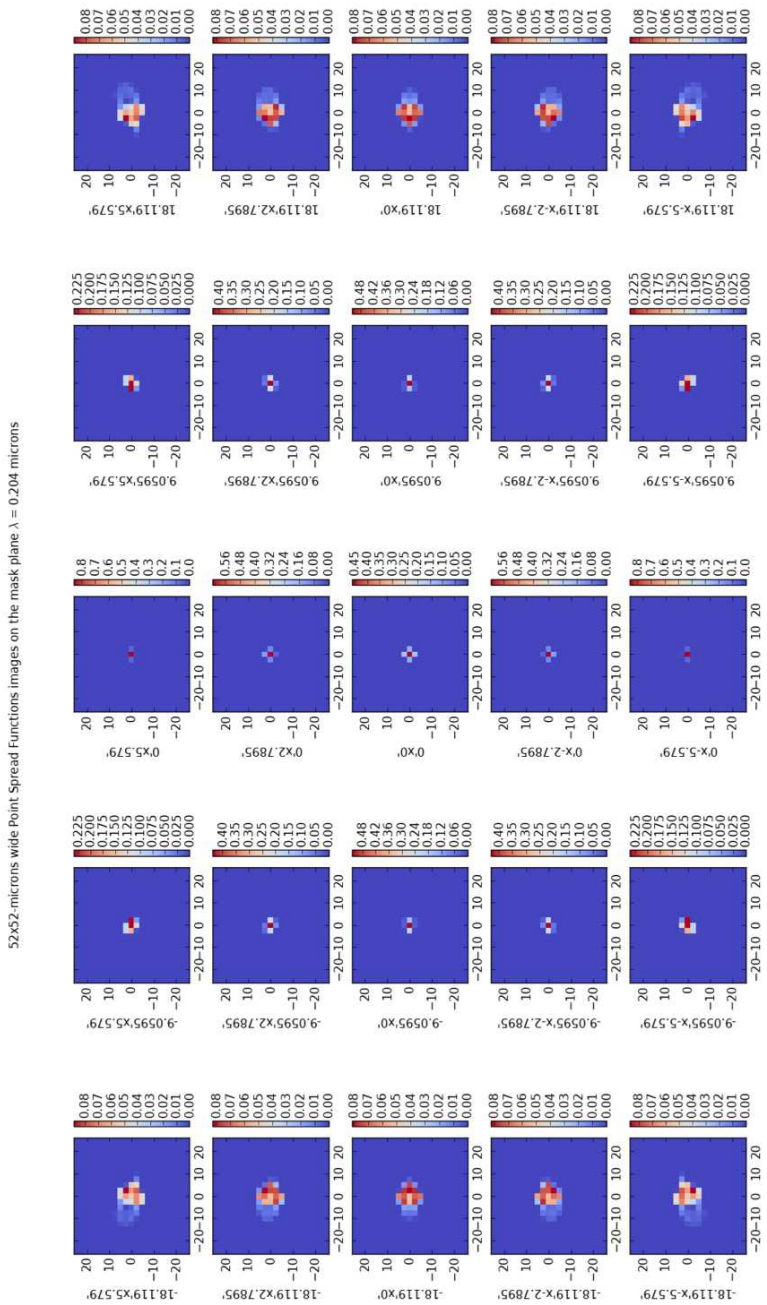

Figure 5.2.: PSF Images of the sky-to-slit mapping at 204nm, sampled on 5x5 positions on the field: {-18.12, -9.06, 0, 9.06, 18.12}x{-5.58, -2.79, 0, 2.79, 5.58} arcmin. These are computed from the PSF Rays of Fig. 5.1, and have been centered on each PSF centroid. Credit: Mège et al., 2015

5.1.1.2. Generating detector images

Once the set of PSFs is generated, for a specified version of the FIREBall-2 model on Zemax (for example, taking into account the actual distances measured during the integration of the instrument), it is possible to generate images on the detector from a simulated object in the sky (either a calibration tool or a realistic galactic emission model). The code includes a PSF interpolating device (called the PSFInterpoler), that will generate the instrument's PSF for any voxel of the mock cube. The interpolation relies on a polynomial fit of the centroid mapping $\vec{c}(\vec{\alpha} = (x, y), \lambda, ...)$, from which we can extract the first order derivative Jacobian matrix $J = (M, \vec{d})$ giving the spatial magnification matrix $M = \frac{\partial(c_x, c_y)}{\partial(x,y)}$ and the spectral dispersion vector $\vec{d} = \frac{\partial \vec{c}}{\partial \lambda}$. These quantities are used to derive an instrument-convolved image cube:

$$I_{\bar{\alpha},\bar{\lambda}}(\vec{\beta_*}, \lambda_*) = \mathcal{S}\ \Delta\Omega\ \sum_{\mathcal{R}_*} \eta^{tot}_{\bar{\alpha},\bar{\lambda}}(\vec{\beta_*}, \lambda_*)\ O_{\bar{\alpha},\bar{\lambda}}(\vec{\beta_*}, \lambda_*)\ \mathrm{PSFIMAGE}_{\bar{\alpha},\bar{\lambda}}(\vec{\beta} - \vec{\beta_*})\ [ph/s] \tag{5.1}$$

where $(\bar{\alpha}, \bar{\lambda})$ is the slit center location on the sky, $O_{\bar{\alpha},\bar{\lambda}}$ the detector-remapped object brightness distribution, $\mathcal{S}$ the gathering surface of the telescope, $\eta^{tot}_{\bar{\alpha},\bar{\lambda}}$ the total optical throughput and $\Delta\Omega$ the solid angle seen by the pixel on the source using the sky-to-detector inverse mapping: $\Delta\Omega = \det M^{-1}_{sd} \underline{\Delta\vec{\beta_*}} \Delta\lambda$, $\underline{\Delta\vec{\beta_*}}$ being the pixel area.

The detected 2D-image $D_{\bar{\alpha},\bar{\lambda}}(\vec{\beta_*})$ is then generated using a model for the detector:

$$D_{\bar{\alpha},\bar{\lambda}}(\vec{\beta_*}) = \sum_{\lambda} q_{det}(\lambda)\ I_{\bar{\alpha},\bar{\lambda}}(\vec{\beta_*}, \lambda_*)\ T_{exp} + \mathrm{CIC} + \mathrm{DC}\ \frac{T_{exp}}{3600}\ [e^-/px] \tag{5.2}$$

where $q_{det}(\lambda)$ is the Quantum Efficiency of the detector which is assumed to be spatially flat, T_{exp} is the exposition time in seconds, CIC is the Charge Induced Current of the detector[a] and DC is the Dark Current of the detector[b]. The Read Out noise is considered negligible.

5.1.2. New developments

The IMO has been revisited since the version described in Mège et al., 2015.

5.1.2.1. Updated optical efficiencies

The different optical efficiencies have been updated to the values measured on the instrument in the lab. These are classified with respect to the coating used of each surface. These values are gathered in Table 5.1 for the most part. The rest

[a] the default CIC charge is 0.0004 e^-/px/frame.
[b] the default DC is 0.06 e^-/px/hour.

Table 5.1.: Measured efficiencies of FIREBall-2 optics

optics	number of surfaces	eff	eff tot
large optics (siderostat and parabola)	2	0.90	0.81
field lens	2	0.94	0.88
Field corrector 1	1	0.925	0.925
Field corrector 2	1	0.92	0.92
Schmidt 2	1	0.92	0.92
Flat Folding 2	1	0.925	0.925

are given in Fig. 5.3, beside the grating's efficiency which has been introduced in much more details in the chapter 3. Regarding the detector, we have set the QE to 40% given some difficulties in the characterization of the device, but we aim at producing a QE of $\sim 60\%$ for FIREBall-2's flight.

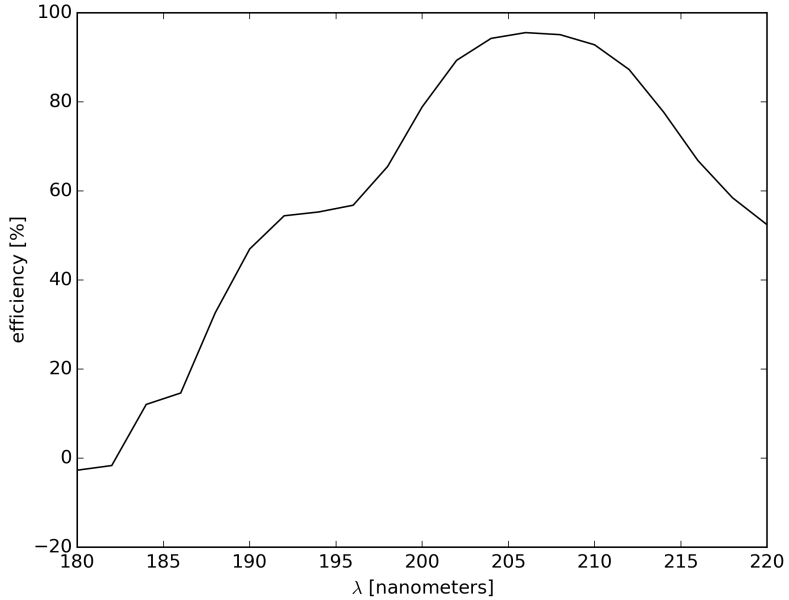

Figure 5.3.: Measured efficiency of the notched optics (Schmidt and Flat folding mirrors upstream of the grating). Credit: Mège et al., 2015

5.1.2.2. Field Corrector's aberration

An aberration from the focal corrector of the instrument has been detected post integration. Fig. 5.4 represents the PSF of such aberration, which is composed

of several clumps, originating from a jolt-like polishing of the mirrors creating several plane reflecting facets. We have accounted for this aberration in the IMO by spatially convolving the image at the Field Corrector level with this PSF downgraded to the cube resolution.

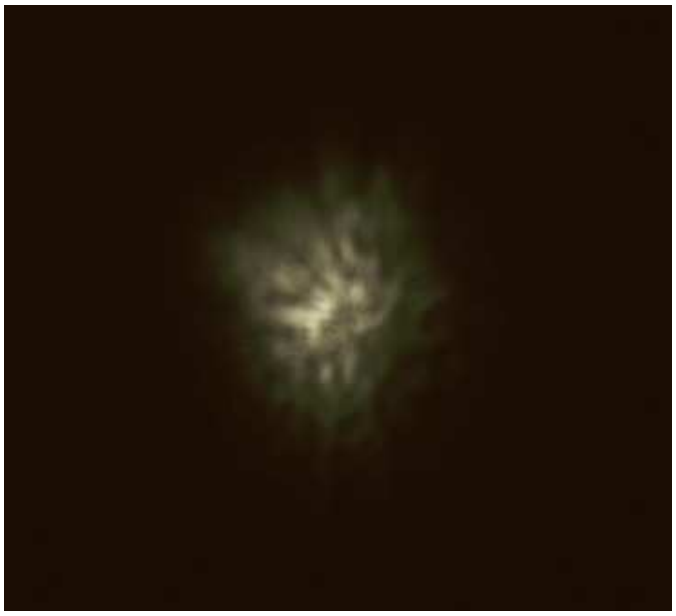

Figure 5.4.: Aberration measured from the Field Corrector (the image is about 9 arcsec on the side).

5.1.2.3. Slit thickness

Previously, the slit was modeled by a simple rectangular aperture at the mask level within the Zemax model. This meant that the photons traveled with any angular direction through the mask (left panel of Fig. 5.5). However, the real configuration actually limits the angular aperture on the mask given the properties of the slit (right panel of Fig. 5.5). We added to the IMO the option of a slit thickness of 50μm.

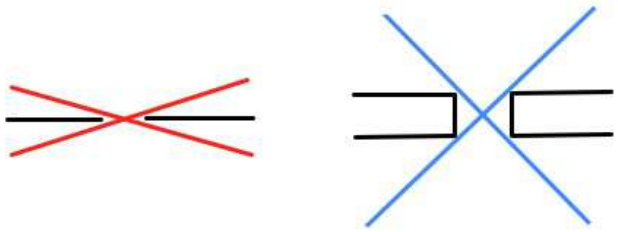

Figure 5.5.: Sketch representing the effect of the slit thickness on the angular selection of the photons through the slit. Left: Without thickness, the slits enables the photons to travel at any orientation. Right: The edges of the slits block the photons which are not within the blue lines.

5.1.2.4. Atmospheric transmission

A wavelength-dependent atmospheric transmission model, as described in Matuszewski, 2012 and considering 4 molecules, O_2, O_3, N_2O and CO_2, has been added (Fig. 5.6).

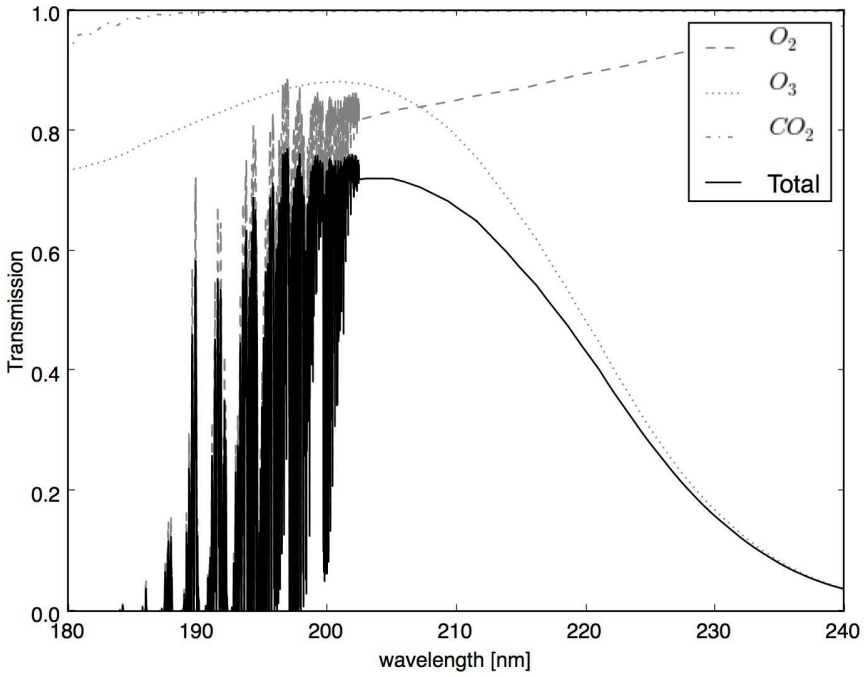

Figure 5.6.: Atmospheric transmission at 40km and 45°elevation

5.2. Simulating FIREBall-2 observations

We now combine the emission prescription presented in chapter 4 to the instrument model (IMO) described earlier to perform an end-to-end analysis of the observation of the CGM of low-redshift galaxies via the multi object slit spectrograph FIREBall-2.

5.2.1. Detector signal

Following the prescription described in section 4.2, we generate mock cubes of different emission lines for different sub-halos. The spatial resolution of these mock cubes is of 0.2 arcsec[c] and the spectral resolution is 0.034 Å. This choice has been made to over-sample the detector pixels by a factor of 5.

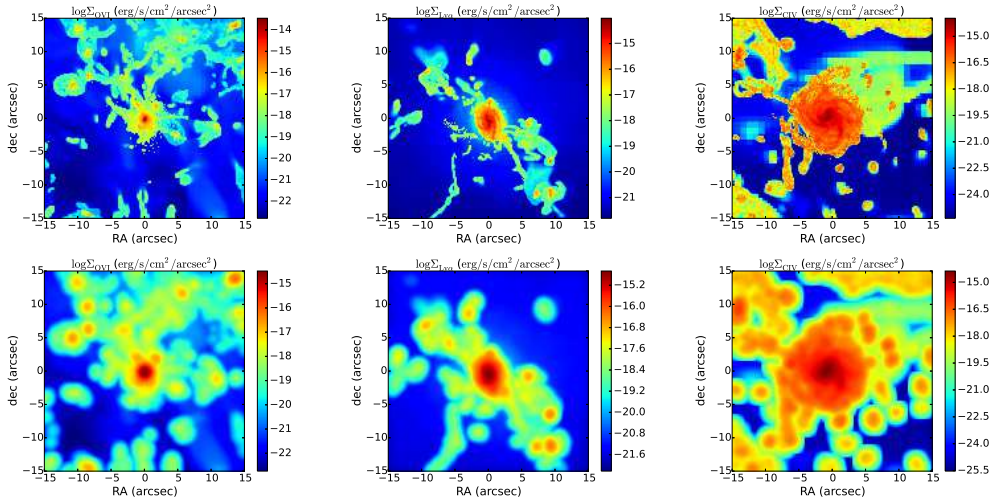

Figure 5.7.: SB projection maps of the main halo for OVI (left panels, z=1.0), Lyα (middle panels, z=0.67) and CIV (right panels, z=0.25). The top panels show the unconvolved mock cubes while the bottom panels show the same cubes convolved with a 1" FWHM PSF, corresponding to the convolution by the guidance of the gondola. The images are all 30" on a side. The pixel size is of 0.2", which corresponds to 2.3 comoving kpc/h for OVI, 1.67 comoving kpc/h for Lyα and 0.69 comoving kpc/h for CIV.

Fig. 5.7 shows the unconvolved (top panels) and convolved (bottom panels) projection of the mock cubes of the main halo for the three lines of interest. The left panels show the main halo SB at redshift z=1, color-coded with the OVI

[c] reaching the limit of the resolution of the high-resolution simulation at z=1.0

pixel luminosity. The middle panels show the main halo SB at z=0.67, color-coded with the Lyα pixel luminosity. The right panels show the main halo SB at z=0.25, color coded with the CIV pixel luminosity. The angular size of each projection is of 30 arcsec (the typical slit length will be of 25 arcsec).

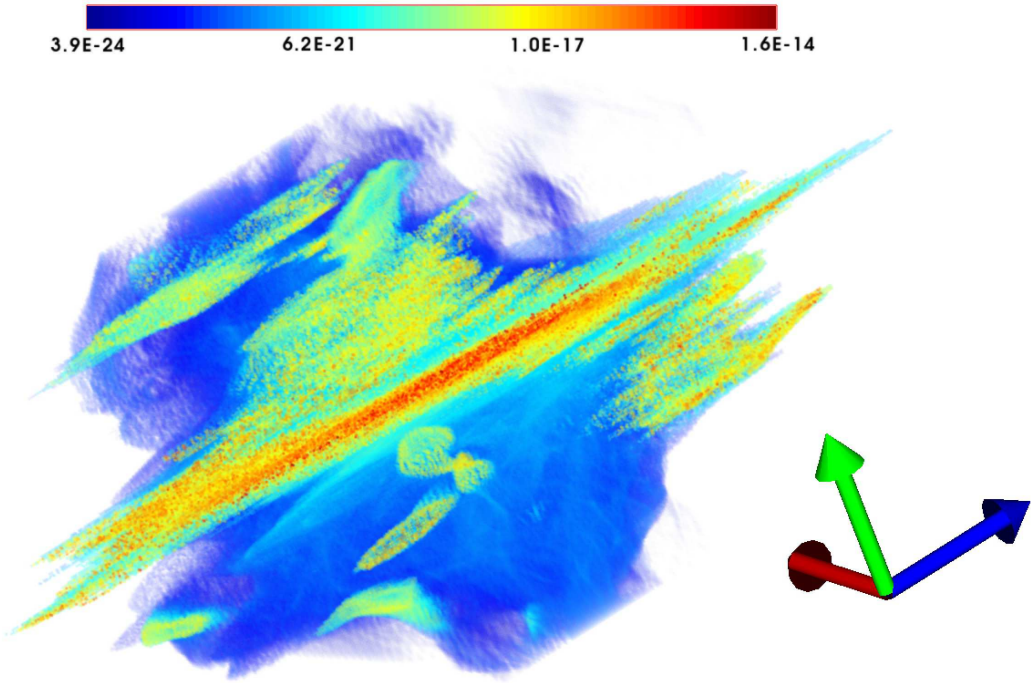

Figure 5.8.: 3-dimensional representation of the main halo Lyα unconvolved luminosity with $f_{esc} = 1\%$ (in flux units $\mathrm{erg/s/cm^2/Å/arcsec^2}$) using GLNemo2 software (Lambert et al., private communication). Only the Lyα emission is represented here. The blue arrow gives the spectral direction. The volume presented corresponds to an extraction of a sphere centered on the halo and of 15 arcsec radius (~ 100 kpc at z=0.67). The stretching in the wavelength direction (covering about 14 Å) comes from the peculiar velocity of the gas.

Part of the following work on signal analysis has been conducted in the context of an internship conducted by Vincent Picouet whom I have tutored during the last summer of my PhD.

All further analysis are made for a single wavelength (203nm) and for a single field position (the optical axis of the instrument). Here, we have chosen the simple case where the dispersion is along the horizontal axis on the detector (this is what the IMO predicts at the center of the field). We also assume an altitude of 40km and elevation of 45°for the atmospheric transmission model.

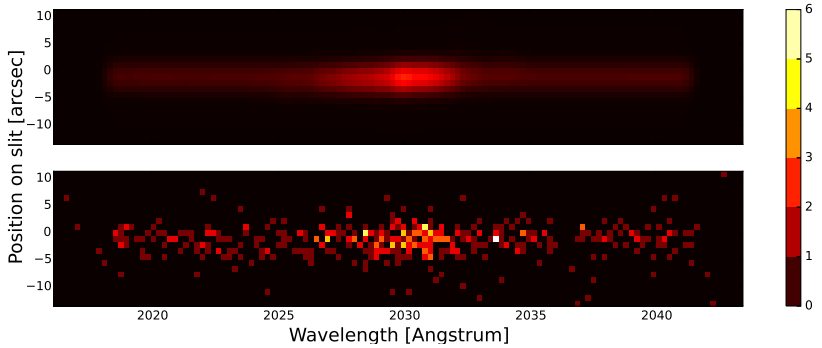

Figure 5.9.: Electronic density map derived from the instrument model for the analytic (top panel) and Poisson realized (bottom panel) 1-hour exposure observation of the Lyα emission, with $f_{esc}(Ly\alpha) = 1\%$, from the main halo at z=0.67. The color bar gives the number of electrons detected per pixel.

Fig. 5.9 shows the predicted electronic map on the detector for the 1-hour exposure observation of the Lyα emission line, using $f_{esc}(Ly\alpha) = 1\%$, and continuum for the simulated main halo at z=0.67. The total Lyα luminosity is $L_{Ly\alpha} = 3.3\ 10^{42}$ erg/s.

The top panel shows the analytic signal, while the bottom panel shows its Poissonian realization, accounting for the actual observation.

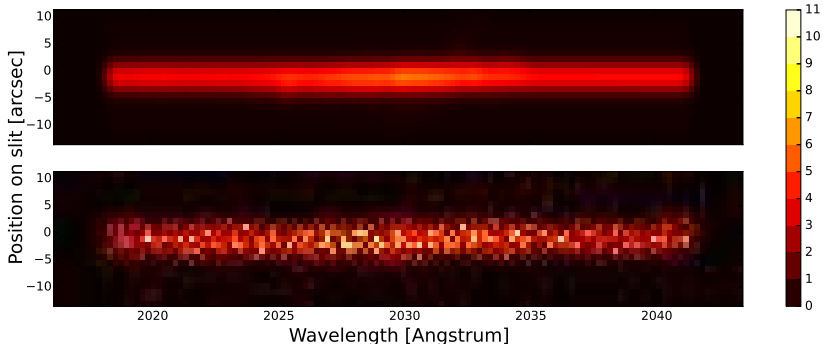

Figure 5.10.: Same as Fig. 5.9, but with the Lyα emission, with $f_{esc}(Ly\alpha) = 0.1\%$, and 7-hour exposure from the main halo at z=0.67.

Fig. 5.10 shows the same quantity as Fig. 5.9, but using $f_{esc}(Ly\alpha) = 0.1\%$ and 7-hour exposure. As the total Lyα luminosity decreases, the relative level of the continuum is enhanced, and the CGM emission appears less clearly. However, with such lowered Lyα escape fraction, the stellar contribution is diminished

and we can observe a differently shaped emission as the radiation from gravitational cooling and UVB fluorescence becomes predominant: from $\sim 30\%$ with $f_{esc}(Ly\alpha) = 1\%$, it goes to $> 50\%$ with $f_{esc}(Ly\alpha) = 0.1\%$ (Fig. 4.12). The total Lyα luminosity of the halo is $L_{Ly\alpha} = 1.3\ 10^{42}$ erg/s.

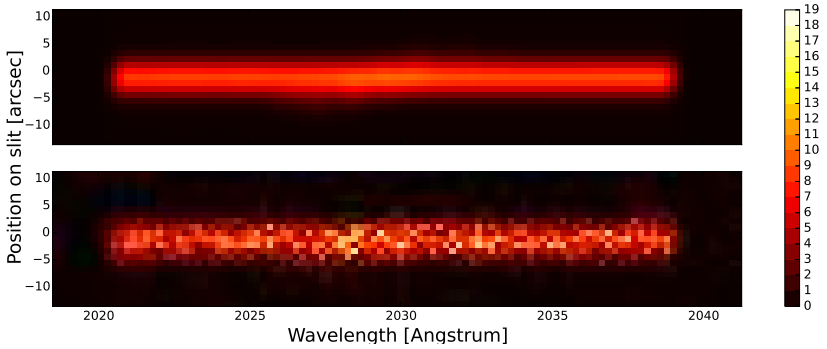

Figure 5.11.: Same as Fig. 5.9, but with the CIV emission and 7-hour exposure from the second main halo at z=0.25.

Fig. 5.11 show the predicted electronic map on the detector for the 7-hour exposure observation of the CIV emission line and continuum for the simulated second main halo[d] at z=0.25. The total CIV luminosity is $L_{CIV} = 9.72\ 10^{40}$ erg/s. The emission if bright given the long exposure but also because the halo is located at low-redshift where the flux is higher, and moreover the fraction of the slit occupied by the galaxy is also larger than higher-redshift objects.

However, the second brightest object in the z=1.0 snapshot of the high resolution simulation has a SFR lowered by a factor of 4 compared to that of the main halo. This results in the low CIV line luminosity computed above.

[d] A bug in our simulation chain prevented me from analyzing the main halo at z=0.25 before the submission of this manuscript, so I chose to perform the study on a slightly less massive halo.

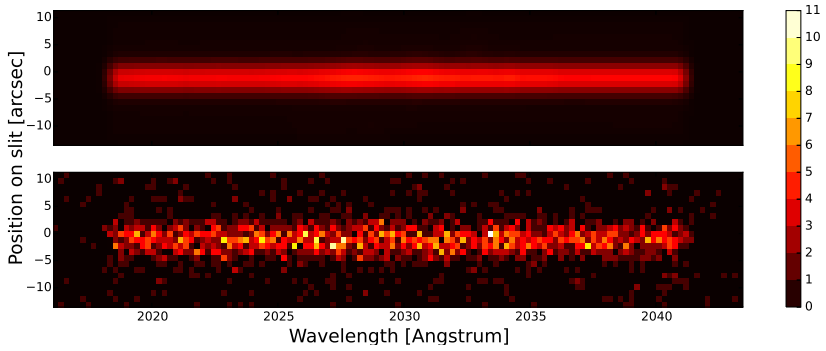

Figure 5.12.: Same as Fig. 5.9, but with the OVI emission and 7 hours exposure from the main halo at z=1.0.

Fig. 5.12 show the predicted electronic map on the detector for the 7-hour exposure observation of the OVI emission line and continuum for the simulated main halo at z=1.0. The total OVI luminosity is $\mathrm{L_{OVI}} = 1.42\ 10^{42}\ \mathrm{erg/s}$. It is fainter than the CIV object with the same exposure because of the higher redshift.

5.2.2. Signal to Noise

The total image is the additive contribution of the CGM, the continuum of the galaxy, the sky and the dark current from the detector: $\mathrm{Total} = \mathrm{CGM} + \mathrm{GAL} + \mathrm{SKY} + \mathrm{DARK}$. We are interested in deriving the signal to noise ration (SNR) of the emission coming from the CGM over the whole image acquired by the detector, that is isolating the CGM part from the total: $\mathrm{SNR} = \frac{\mathrm{CGM}}{\mathrm{NOISE}}$, with $\mathrm{CGM} = \mathrm{Total} - \mathrm{GAL} - \mathrm{SKY} - \mathrm{DARK}$.

To isolate the CGM emission from these background emissions, we need to estimate their contributions from the image or by other means. The dark current is considered known from the calibration of the detector, giving us $dark = 0.009\ e^{-}/px/frame$. The uncertainty on this estimator is neglected given it is weak and it can be measured over a large number pixels with respect to the dominant noise source which is the galaxy continuum. We first remove the dark from the signal.

We then estimate the profile of the continuum from regions free of emission lines, $\mathrm{P_{x,1}}$ and $\mathrm{P_{x,2}}$, by stacking the columns of pixels (without the dark) over about 10 columns in the dispersion direction:

$$\mathrm{P_{x,i}} = \frac{1}{\mathrm{N_\lambda}} \sum_{\lambda_\mathrm{i}} (\mathrm{d_{x,\lambda_i}} - \mathrm{dark_{x,\lambda}}) \tag{5.3}$$

For the purpose of this estimation, we assume that the profile is free from absorption/emission feature on these patches. This estimate accounts for both the

galaxy continuum and the UV sky background, the former assumed spatially and spectrally uniform. The variance of the estimated profiles is as follows:

$$\sigma^2_{\mathrm{P_{x,i}}} = \frac{1}{\mathrm{N}^2_\lambda} \sum_{\lambda_\mathrm{i}} \mathrm{d_{x,\lambda_i}} \tag{5.4}$$

taking $\sigma^2_{\mathrm{dark}} = 0$.

Each stacked profile is associated to the wavelengths λ_1 and λ_2 at the center of each patch. As the continuum (+ background) evolves relatively little over the narrow wavelength range (a few Å), we choose to interpolate it between λ_1 and λ_2 assuming a linear regression:

$$\hat{\mathrm{c}}_{\mathrm{x},\lambda} = (1-\alpha)\ \mathrm{P_{x,1}} + \alpha\ \mathrm{P_{x,2}} \tag{5.5}$$

with $\alpha = \frac{\lambda-\lambda_1}{\lambda_2-\lambda_1}$. The variance of this estimator is:

$$\sigma^2_{\mathrm{c_{x,\lambda}}} = (1-\alpha)^2\ \sigma^2_{\mathrm{P_{x,1}}} + \alpha^2\ \sigma^2_{\mathrm{P_{x,2}}} \tag{5.6}$$

Considering a Poissonian distribution for the noise, the variance on the measure is computed as the image $\sigma^2_{\mathrm{x},\lambda,\mathrm{meas}} = \mathrm{d_{x,\lambda}}$. We neglect the read out noise as we use the detector in counting mode: $\sigma^2_{RO} = 0$. The other sources of noise have been neglected as well, thus giving us the following Signal to Noise Ratio estimated per pixel:

$$\mathrm{SNR}^{\text{per pixel}}_{\mathrm{x},\lambda} = \frac{\mathrm{d_{x,\lambda}} - \mathrm{dark_{x,\lambda}} - \hat{\mathrm{c}}_{\mathrm{x},\lambda}}{\sqrt{\mathrm{d_{x,\lambda}} + \sigma^2_{\mathrm{c_{x,\lambda}}}}} \tag{5.7}$$

As the current pixel size on the detector oversamples the resolution, a more physically meaningful computation of the SNR must account for the actual resolution element. We therefore compute a SNR per resolution element by convolving the continuum-subtracted signal (and the corresponding noise) with the instrument's PSF normalized with the following formula: $\mathrm{h}'_\mathrm{i} = \frac{\sum_\mathrm{j} \mathrm{h_j}}{\sum_\mathrm{j} \mathrm{h}^2_\mathrm{j}}\ \mathrm{h_i}$ where $\mathrm{h_i}$ is the value of the PSF at pixel i. This relation enables to recover the energy from a dirac source after convolution. However, for a diffuse object, it overestimates it by a factor 2, giving a factor $\sqrt{2}$ over-estimate on the SNR per resolution element.

$$\mathrm{SNR}^{\mathrm{PRE}}_{\mathrm{x},\lambda} = \frac{\left((\mathrm{d} - \mathrm{dark} - \hat{\mathrm{c}}) * \mathrm{PSF}\right)_{\mathrm{x},\lambda}}{\sqrt{\left((\mathrm{d} + \sigma^2_\mathrm{c}) * \mathrm{PSF}\right)_{\mathrm{x},\lambda}}} \tag{5.8}$$

For all the following figures, the top panels represent the analytic solution while the lower panels represent the Poissonian realization, modeling a realistic observation. The left panels show the SNR per pixel and the right panels the SNR per resolution element.

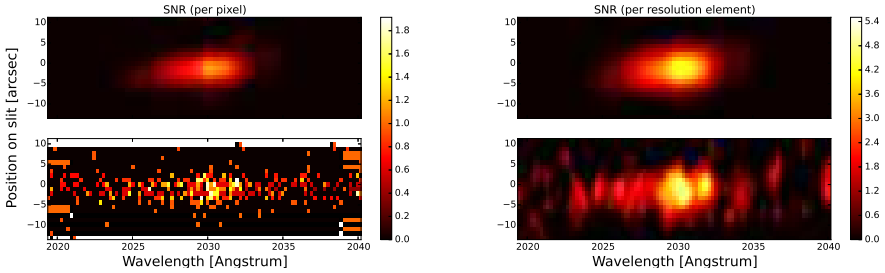

Figure 5.13.: 2D images of the SNR per pixel (left panels) and per resolution element (right panels) from the analytic image (top panels) and the Poisson realized image (bottom panels). This shows the results for the Lyα emission, using $f_{esc}(Ly\alpha) = 1\%$, and 1-hour exposure of the main halo at z=0.67

Fig. 5.13 shows the SNR per pixel and per resolution element for the continuum-substracted main halo Lyα emission with $f_{esc}(Ly\alpha) = 1\%$, for a 1-hour exposure. It shows that we are able to recover a SNR per resolution element > 5 on the position predicted by the analytic signal.

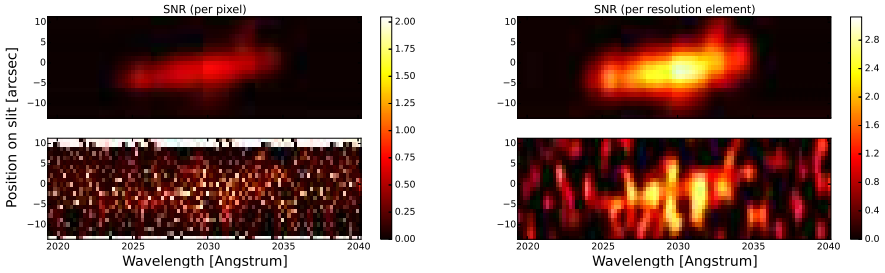

Figure 5.14.: Same as Fig. 5.13, but with the Lyα emission, with $f_{esc}(Ly\alpha) = 0.1\%$, and 7-hour exposure from the main halo at z=0.67.

Fig. 5.14 shows the SNR per pixel and per resolution element for the continuum-substracted main halo Lyα with $f_{esc}(Ly\alpha) = 0.1\%$ emission, for a 7-hour exposure. The profile of this line is very different from the $f_{esc}(Ly\alpha) = 1\%$ case, meaning that we are observing a different emission mechanism (probably the gravitational cooling). We reach a SNR per resolution element of 3 for the longest exposure possible with FIREBall-2. This means that the detection of Lyα CGM emission is closely related to the Lyα escape fraction of the target, and that the sole contribution of the cooling radiations and the fluorescence from the UVB will be a challenging observation given the current instrument.

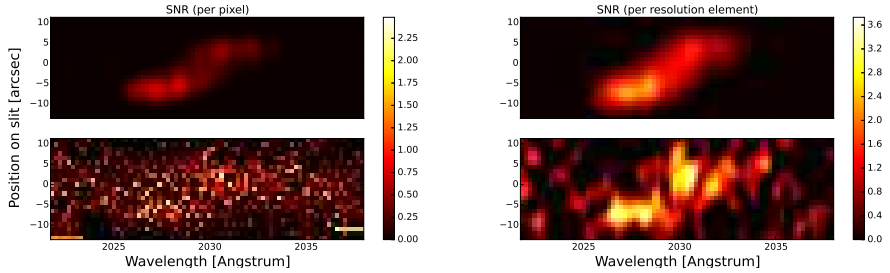

Figure 5.15.: Same as Fig. 5.13, but with the CIV emission and 7-hour exposure from the second main halo at z=0.25.

Fig. 5.15 shows the SNR per pixel and per resolution element for the continuum-substracted second main halo CIV emission, for an 7-hour exposure. The extended observed signal shapes approximately as the analytic one, however it is very low and we can only reach a SNR per resolution element of 3. This would be the best signal FIREBall-2 can produce given the single night exposure the balloon offers.

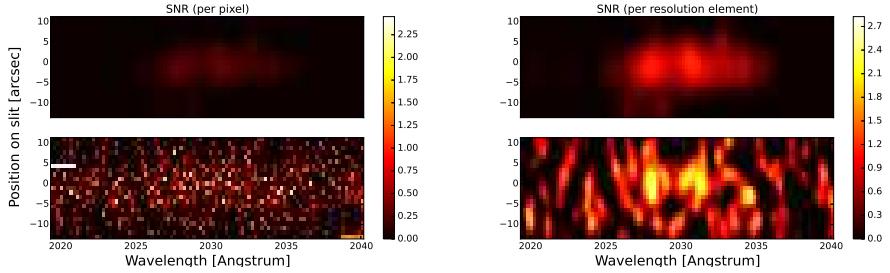

Figure 5.16.: Same as Fig. 5.13, but with the OVI emission and 7-hour exposure from the second main halo at z=1.0.

Fig. 5.16 shows the SNR per pixel and per resolution element for the continuum-substracted main halo OVI emission, for a 7-hour exposure. Similarly to the CIV 7-hour exposure, the signal shapes approximatively as the analytic one, but the maximum SNR per resolution element is about 3, which is challenging for any detection.

5.3. Conclusion

In this chapter, we analyzed the possible detection of CGM faint emission from low-redshift galaxies via the FIREBall-2 UV MOS. We used mock cubes of an emission model described in chapter 4 on an instrument model reproducing the output of the FIREBall-2 detector. The two dimensional analysis of the signal

tells us that the more massive objects can be observed in Lyα at redshift z=0.67 within the short time available for the balloon's flight, which is encouraging and enlightens the need for future development for the satellite version of the instrument, ISTOS. The detection appears more difficult for objects with low Lyα escape fraction. Our simulations indicate that the current version of the instrument and flight-plan will be challenged to detect the OVI and CIV emission lines (at redshift 1.0 and 0.25 respectively). Nevertheless, it is possible that the modeled fluxes are underestimated and further improvements in the emission model, such as the effect of radiative transfer of ionizing photons, or the presence of a bright source nearby the galaxy, could enhance the overall emission levels.

Conclusion

In this thesis, I have studied the CGM with two different but complementary techniques: absorption and emission. The former provides a high sensitivity for measuring densities of various elements in dense neutral hydrogen clouds but is limited to a sole line of sight to probe the galactic outskirts. The latter overcomes this issue with the possibility to map the emission out to large distances on the entire CGM, but it represents an observational challenge due to the low surface brightness at play. Both techniques are essential in our understanding of the gaseous and energetic exchanges mechanisms occurring within the CGM of galaxies.

Quasar absorption spectroscopy

Dense clouds of neutral hydrogen gas are observed in the vicinity of galaxy, and the study of these regions can bring valuable insights towards the gas content and the activity of a galaxy. In particular, I have developed a keen interest in studying the metallicity of such regions, as it gives a probe of many aspects of galaxy evolution such as the dust content, the star formation history or even the dynamics of the gas. In chapter 1, I studied a class of dense HI quasar absorbers that had been poorly considered until now: the sub-DLAs. Based on a large archive sample of UVES spectra, providing the required high resolution to resolve the sub-DLA damping wings and enabling metallicity measurements, I performed Voigt profile fits of 15 sub-DLAs and 7 DLAs in the redshift range $0.584 \leq z_{\rm abs} \leq 3.104$ and I gathered the most updated sample of 92 sub-DLAs and 362 DLAs from the literature. The newly measured sub-DLAs contributes substantially to the low-redshift range of sub-DLAs metallicity measurements, enabling to witness a bimodality in the sub-DLAs metallicity distribution at $z_{\rm abs} \leq 1.25$, using Fe as a metallicity indicator, which is known to be little affected by photo-ionization effects. Lehner, Howk, et al., 2013 interpreted the bimodality as a signature of accretion from the metal-poor absorbers and outflows from the metal-rich absorbers. However, the determination of the intrinsic metallicity of quasar absorbers remains a challenge as the elements suffer from dust depletion, which screens out the fraction of atoms locked onto dust grains. Out of the methods to derive the dust contents in a cloud, the comparison of the

abundances of elements with different dust depletion levels (i.e. Zn and Fe) is the most commonly used. Unfortunately, the derivation of Zn, which has a low cosmic abundance and long rest-frame wavelengths, is challenging in the case of sub-DLAs. I have extended this dust analysis relying on two elements to a larger number of elements, using a method described by Jenkins, 2009. Using a reference sample of 243 sight lines in our Galaxy, I derived a dust depletion factor of $\mathrm{F}^* = -0.34 \pm 0.19$ for the whole sample of sub-DLAs and of $\mathrm{F}^* = -0.70 \pm 0.06$ for the DLAs. This suggests that both classes of absorbers present an average extinction $\mathrm{A_V}$ below 0.01, and that sub-DLAs are more affected by dust depletion than their counterparts. Interestingly, these sub-DLAs seem to have a steeper metallicity evolution than DLAs, reaching solar metallicity at present day. This can be interpreted as a faster metal-enrichment or gas consumption within the sub-DLAs, further supporting the trend that they might be associated with gas flows.

The archive is growing significantly as the study of these quasar absorbers goes on. As a consequence, the database is prone to be furthermore extended, enabling one day analyses no longer restricted by poor statistics. In particular, the study of quasar absorbers with lower HI column densities, such as Lyman Limit Systems, presents interesting developments with such a database, and there is ongoing effort to measure and characterize such systems in order to confirm the bimodality observed at low redshifts.

FIREBall-2

The challenge to be able to observe the CGM in emission lies in the low surface brightness that requires large collective areas for a high enough sensitivity. Such facilities can '*easily*' be deployed on the ground, with instruments such as MUSE on the VLT in Chile, or the KCWI (Keck Cosmic Web Imager) at the W. M. Keck Observatory in Hawaii. These instruments are however limited to visible wavelengths as the atmospheric absorption prevents UV photons to reach the surface in a sufficient number, thus blocking the observation of the Universe younger than 10 Gyr[e]. I have dedicated the second part of this thesis to the study of the low-redshift CGM in emission via the FIREBall-2 balloon project. The balloon technology of FIREBall-2 offers many advantages such as the reduced timescale of the end-to-end project, the cost-effective and nonetheless cutting-edge technologies developments leading the possibility to observe the faint and diffuse emission from the CGM of galaxies at low redshifts via a Multi-Object UV spectrograph.

Gratings

[e]More than 70% of the Universe history!

Although I did not witness the balloon fly within this PhD, I actively contributed to the preparation of the instrument. In chapter 2, I presented the measurements and modeling of the flight grating of FIREBall-2. The grating is the one most critical optical component of the instrument as it is causing the majority of the light losses down to the detector. Using an innovative experimental set up, I have performed clean UV polarized measurements on 5 different gratings within 200 and 400nm. The flight grating shows promising performances under flight conditions, reaching efficiencies above 55% under flight conditions according to my model. I inferred that this might be due to an abnormally thin layer of coated aluminum. Moreover, I discovered that applying an optimized amount of $\mathrm{MgF_2}$ on the aluminum layer of the grating would rise the efficiency under flight conditions by about 10%. However, I was confronted with the difficulty of accurately controlling the deposition of coatings during the validation of this solution. Its final design shows also good performances but is expected to be less efficient than the baseline grating.

These developments are of prime interest in the perspective of more UV observations with the satellite version of FIREBall-2, ISTOS. Indeed, I have shown that the current technology of grating manufacturers is providing high efficiency at 200nm ($> 50\%$), and that there is room for further improvement at shorter wavelengths through $\mathrm{MgF_2}$ coating deposition. However, this calls for experimental solution to measure efficiencies at even shorter wavelengths, using for example nitrogen within the measurement device to prevent from oxygen absorption. Furthermore, the solutions are closely related to the knowledge of the actual amount of coating deposited onto the surface, and it would therefore be essential to actively work toward an accurate coating deposition in the future.

An end-to-end analysis of the $\mathrm{z} < 1$ CGM observations

In addition to the technical endeavor of developing cutting edge optical pieces with high sensitivity, a model for the observing potential of the instrument is crucial to optimize FIREBall-2 observational strategy. I have presented in chapter 4 the use of a high resolution hydrodynamical cosmological RAMSES simulation combined to a model for CGM emission, considering gravitational cooling, fluorescence from the metagalactic UV background and scattering of Lyα photons produced in the ISM region, to generate observational mock cubes of the CGM in emission. In the absence of low-redshift data, I compared these predictions to larger redshift observations. Despite the difficulty to properly account for the scattering of stellar Lyα photons, which requires full radiative transfer post-processing on the simulation, I recovered the continuum and the expected Lyα emission in the inner region, considering lower Lyα escape fractions than usually observed. Overall, my models predicts the contribution of cooling radiations and photo-ionization from the UV background to be important in the total budget of Lyα emission at z=0.67. This suggests that the mapping of the faint Lyα emission

from the CGM could unveil the physical properties of accretion of cold gas onto galaxies. Moreover, I find a discrepancy between the luminosity distribution of my simulated halos at z=0.67 and the emission spectroscopic observations perform by Wold et al., 2014. Indeed, the luminosities I derive seem to be 2 orders of magnitude below what is currently observed in emission. Of course, this means that the analysis performed here is conservative, and that we should expect more powerful emissions in reality, leading to much more detection than can be predicted from my model. It is nevertheless important to understand the possible origin to this large discrepancy. It could be that the objects composing the high end of this luminosity function are observed through holes of low dust and N(HI) column densities due to energetic feedback. These holes would have a much higher Lyα escape fraction that would boost the luminosity originating from ionizing photons. It could also be that these objects are in fact in the vicinity of a powerful quasar that would enhance the fluorescence from the CGM, as it has been observed already in a few examples. In short, the analysis performed here does not pretend to fully model the complex physics of CGM emission as it is not reproducing every possible source of emission (such as the scattering of continuum Lyα photons, or photon pumping, that could be donminating in some regions). However, the inconsistency observed between our model and the observations acknowledges the need for further understanding and modeling of the emission processes occurring within the CGM. This is to be addressed via the future observations of the emission of these regions, which will bring additional constraints to the emitted energy budget, and will eventually enable the mapping of the CGM emission and velocity field.

Chapter 5 focused on the observational possibilities of FIREBall-2. Mock observations of the modeled emission are fed to a realistic instrument model for FIREBall-2's detector output. This instrument model takes into account the actual optical design, the throughput of the entire optical chain, the atmospheric transmission and the dispersion induced by the grating to derive the distribution of the incoming photons onto the detector. It is a valuable tool for the preparation of the data analysis, the target selection and the observational strategy. Moreover, its modular architecture is of prime interest for further UV instrument developments. The end-to-end analysis predicts that the instrument is able to observe Lyα emission in the short observing time available from a balloon mission (typically less than 7 hours). I predicted the detection of a $\mathrm{M_{DM}} = 1.36\ 10^{13}\ \mathrm{M_\odot}$ halo at z=0.67, with a luminosity of a few $10^{42}\ \mathrm{erg/s}$, in an exposure time of a few hours. The signal to noise ratio, after a careful continuum and background subtraction, reached a value of 5 for a typical resolution element. Our model predicts that it will be challenging to establish a positive detection of the OVI and CIV emission lines at redshifts z=1.0 and z=0.25 respectively in current observing conditions. Furthermore, the instrument model is about to be adjusted according to ongoing calibrations. Its first practical use will be to validate different methods of detection (such as stacking) and it will serve as a useful tool for

data analysis after the flight. For example, it will be possible to study the dominance of the central source or the polarization of the CGM emission through the knowledge of the grating's polarization. Additional research on the simulation will also help preparing the selection of targets with the higher emission (e.g. high gas mass halos, high SFR halos, ...).

Consequently, the likelihood is that the next flight of FIREBall-2, scheduled for summer 2017, will be successful. Indeed, my model shows that the huge leap performed by the team in terms of optical design, efficiency improvements and pointing will lead to the detection of Lyα emission from the CGM of low-redshift galaxies. Besides, there is exciting science to come with more ambitious UV spectrograph projects such as ISTOS or LAEX (Lyman Alpha Explorer), currently under preparation for a future MIDEX NASA proposal.

To conclude, this thesis presents many interesting aspects of the current endeavor for the study of the CGM and its associated gaseous and energetic exchanges between galaxies and the IGM. From the study of a large sample of existing observations, through the participation of the design of a balloon-borne UV spectrograph and the prediction of its observing capabilities, I was able to highlight the diverse sources of scientific and technological difficulties still to be improved upon to reach a full understanding of the physical processes at play in the CGM.

Publications

Grange, R., Lemaitre, G. R., **Quiret, S.**, Milliard, B., Pascal, S. & Origné, A.
Multi object spectrograph of the Fireball balloon experiment.
In T. Takahashi, J.-W. A. den Herder, & M. Bautz (Eds.), SPIE (p. 914430). 2014.
http://doi.org/10.1117/12.2056388

Quiret, S., Milliard, B., Grange, R., Lemaitre, G. R., Caillat, A., Belhadi, M. & Cotel, A.
The FIREBall-2 UV sample grating efficiency at 200-208nm.
In T. Takahashi, J.-W. A. den Herder, & M. Bautz (Eds.), SPIE (p. 914432). 2014.
http://doi.org/10.1117/12.2056972

Mège, P., Pascal, S., **Quiret, S.**, Corlies, L., Vibert, D., Grange, R. & Milliard, B.
The UV multi-object slit-spectrograph FIREBall-2 simulator.
In O. H. Siegmund (Ed.), SPIE (p. 960110). 2015.
http://doi.org/10.1117/12.2206160

Kulkarni, V. P., Som, D., Morrison, S., Péroux, C., **Quiret, S.** & York, D. G.
Keck and VLT observations of super-damped Lyα absorbers at $z \sim$ 2-2.5: constraints on chemical compositions and physical conditions.
The Astrophysical Journal, 815, 24. 2015.
http://doi.org/10.1088/0004-637X/815/1/24

Morrison, S., Kulkarni, V. P., Som, D., DeMarcy, B., **Quiret, S.** & Péroux, C.
Element Abundances in a Gas-rich Galaxy at $z = 5$: Clues to the Early Chemical Enrichment of Galaxies.
The Astrophysical Journal, 830, 158.
10.3847/0004-637X/830/2/158

Péroux, C., **Quiret, S.**, Rahmani, H., Kulkarni, V. P., Epinat, B., Milliard, B., Straka, L. A., York, D. G., Rahmati, A. & Contini, T.
A SINFONI integral field spectroscopy survey for galaxy counterparts to damped Lyman α systems – VI. Metallicity and geometry as gas flow probes.
Monthly Notices of the Royal Astronomical Society, 457, 903–916. 2016.
http://doi.org/10.1093/mnras/stw016

Quiret, S., Péroux, C., Zafar, T., Kulkarni, V. P., Jenkins, E. B., Milliard, B., Rahmani, H., Popping, A., Rao, S. M., Turnshek, D. A. & Monier, E. M.
The ESO UVES advanced data products quasar sample – VI. Sub-damped Lyman α metallicity measurements and the circumgalactic medium.
Monthly Notices of the Royal Astronomical Society, 458, 4074–4121. 2016.
http://doi.org/10.1093/mnras/stw524

Rahmani, H., Péroux, C., Turnshek, D. A., Rao, S. M., **Quiret, S.**, Hamilton, T. S., Kulkarni, V. P., Monier, E. M. & Zafar, T.
A study of the circumgalactic medium at $z \sim 0.6$ using damped Lyman α galaxies.
Monthly Notices of the Royal Astronomical Society, 463, 980–1007. 2016.
http://doi.org/10.1093/mnras/stw1965

Zafar, T., Møller, P., Péroux, C., **Quiret, S.**, Fynbo, J. P. U., Ledoux, C. & Deharveng, J.-M.
The ESO UVES Advanced Data Products Quasar Sample-V. Identifying the Galaxy Counterpart to the sub-Damped Lyα System towards Q2239-2949.
Monthly Notices of the Royal Astronomical Society, Accepted, 2016
arXiv:1611.00091

Péroux, C., Rahmani, H., **Quiret, S.**, Pettini, M., Kulkarni, V. P., York, D. G., Straka, L., Husemann, B. & Milliard, B.
Nature of the Absorbing Gas associated with a Galaxy Group at $z\sim0.4$.
Monthly Notices of the Royal Astronomical Society, 464, 2053-2065. 2017
http://doi.org/10.1093/mnras/stw2444

Appendices

Appendix A: An introduction to absorption physics

A.1. Basic absorption physics

Quasars are extremely bright, point source-like, objects. Before reaching our telescopes, their photon go through a majority of ionized gas. When they go though a region of neutral hydrogen (typically in the CGM of a galaxy, where the gas can be self-shielded from the background ionizing sources) they are absorbed, mostly at the $Ly\alpha$ wavelength, which corresponds to the the first level of Hydrogen ionization (about 66% of the energy level transitions): 1216Å. Then, as the photon finishes its journey toward our telescope, the absorbed line gets *redshifted* as a consequence of the expansion of the Universe:

$$\lambda_{obs} = (1 + z_{abs})\lambda_{rest} \tag{A.1}$$

where λ_{obs} is the observed wavelength of the absorption, λ_{rest} is the rest frame wavelength of the transition responsible for the absorption and z_{abs} is the redshift of the absorbing system.

One way to characterize an absorption line is through its observed equivalent width W_{obs}: it is defined as the width of a rectangle of height 1 for which the area is equal to the area between the absorbed spectrum (normalized to its continuum) and 1. It is defined as:

$$W_{obs} = \int \frac{I_c - I}{I_c} d\lambda = \int (1 - e^{-\tau(\lambda)}) d\lambda \tag{A.2}$$

where I is the observed spectral intensity, I_c is the spectral intensity that would be measured without absorption (continuum) and $\tau(\lambda)$ is the optical depth, defined as $\tau(\lambda) = -\ln(I(\lambda)/I_c(\lambda))$.

We can estimate the optical depth $\tau(\lambda)$ measured by an observer in the frame of reference R by assuming a Gaussian velocity distribution among the atoms in the cloud, with v_0 as mean velocity relative to R. Indeed, considering the absorption process of an atom of velocity v and frequency ν having a cross section

of $\sigma(\nu)$, we have:

$$\tau(\nu) = N\frac{1}{\sqrt{\pi}b}\int_{\infty}^{\infty}\sigma(\nu')e^{-\frac{(v-v_0)^2}{b^2}}dv \tag{A.3}$$

where N is the column density[a] for the considered ion in the cloud, b the Doppler parameter[b], $\nu' = \frac{\nu}{1-v/c}$ the Doppler shifted frequency of the atom (v being positive when the atom moves away from the observer).

The absorption cross section of an atomic transition can be characterized via a Lorentzian profile, given an oscillator strength f (the probability for the atom to go from its current ionized state to an other), an attenuation parameter γ and a central frequency ν_0 corresponding to the transition frequency:

$$\sigma(\nu) = f\frac{1}{4\pi\epsilon_0}\frac{\pi e^2}{m_e c}\frac{1}{\pi}\frac{\frac{\gamma}{4\pi}}{(\nu-\nu_0)^2+(\frac{\gamma}{4\pi})^2} \tag{A.6}$$

The Doppler parameter b is related to the Doppler width W_d and the Gaussian width σ by the following formula:

$$W_d = \sqrt{2}\sigma = \frac{\nu_0}{c}b \tag{A.7}$$

Considering $v \ll c$, $\nu' \approx \nu(1+v/c)$, and using equations A.3 and A.6, we get:

$$\tau(\lambda) = \frac{e^2}{4\sqrt{\pi}\epsilon_0 m_e c}\frac{Nf\lambda}{b}H(a,u) \tag{A.8}$$

where $H(a,u)$ is the Voigt function:

$$H(a,u) = \frac{a}{\pi}\int_{\infty}^{\infty}\frac{e^{-y^2}}{(u-y)^2+a^2} \tag{A.9}$$

with $a = \frac{\lambda\gamma}{4\pi b}$ being a factor related to the ratio between the Lorentzian and Gaussian linewidths, and $u = -\frac{c}{b}\left(1+\frac{v_0}{c}-\frac{\lambda}{\lambda_0}\right)$ corresponding to the frequency

[a] The column density is the density integrated along the line of sight and has units of $atom/cm^{-2}$.

[b] The Doppler parameter b is the quadratic sum of a thermal and a turbulent contribution:

$$b^2 = b_{th}^2 + b_{turb}^2 \tag{A.4}$$

As the dynamics of the gas are usually not known in details such as to provide relevant information about the turbulent contribution, we use the b parameter to derive an upper limit to the temperature of the gas using the following formula:

$$b_{th} = \sqrt{\frac{2kT}{m}} = 12.8[km/s^{-2}]\sqrt{\left(\frac{T[K]}{10^4}\right)\frac{1}{A}} \tag{A.5}$$

where k is the Boltzmann constant, T the temperature of the cloud in K, m the mass of an atom and A its atomic number.

and velocity offsets from the line center in units of the Gaussian broadening linewidth. This Voigt profile is the convolution between a Gaussian profile (emerging from the movements of the atoms in the cloud) and a Lorentzian profile (emerging from the absorption process itself).

Using the definition of the classical electron radius $r_e = \frac{1}{4\pi\epsilon_0}\frac{e^2}{m_e c} = 2.8179\,10^{-15} m$, we can formulate equation A.8 as

$$\tau(\lambda) = \sqrt{\pi} c r_e 10^{11} \frac{f N[cm^{-2}]\lambda[\text{Å}]}{b[km.s^{-1}]} H(a,u) \tag{A.10}$$

The Curve of Growth (Fig. A.1) links the equivalent width W_{obs}, the column density $N(X)$ and the Doppler parameter b, with three different regimes in regards of $N(X)$:

- for $N < 10^{12} cm^{-2}$, W_{obs} is proportional to $N(X)$. This is the linear regime.
- for $10^{12} < N < 10^{19} cm^{-2}$, it is not $N(X)$ but the b parameter that controls W_{obs}. This is the flat regime, in which the absorption is saturated.
- for $N > 10^{19} cm^{-2}$, the absorption profile develops damped wings. This is the damped regime.

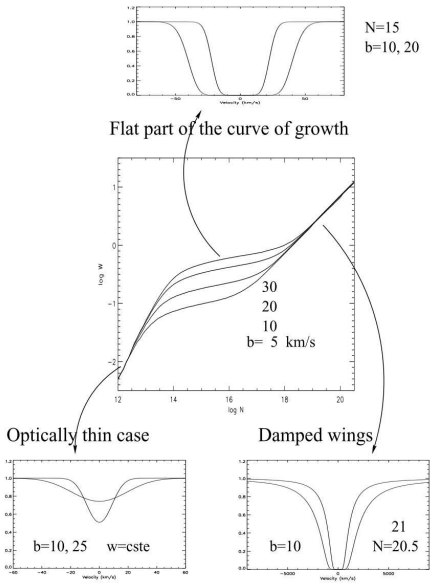

Figure A.1.: Curve of Growth which relates the Equivalent Width to the column density and the Doppler parameter of a Voigt profile. There are 3 regimes to consider according to the column density: the linear regime, the flat regime and the damped regime, . Credit: Petitjean, 1998

A.2. The Distribution of N(HI): from the forest to the DLAs

The large range of column densities covered by the curve of growth (10^{11-21} cm^{-2}) calls for a classification of these absorbers, according to their neutral hydrogen column density.

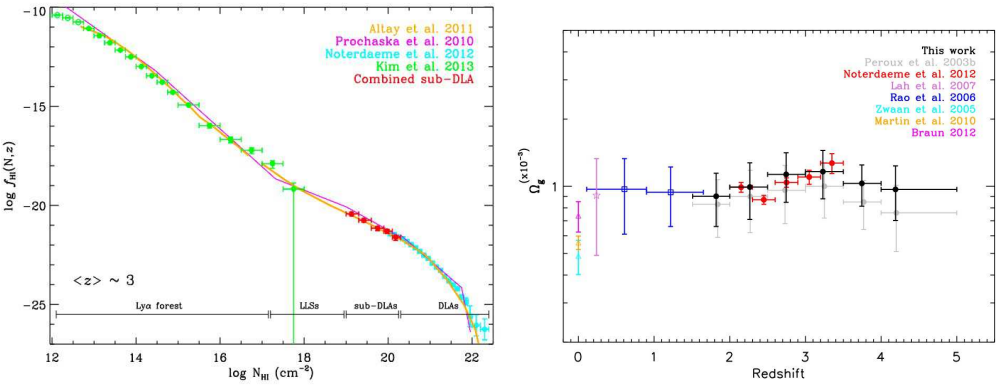

Figure A.2.: Left: NHI distribution function f_{HI}. Right: Ω_g evolution with redshift. Credit: Zafar, Popping, et al., 2013

Figure A.2 shows the N(HI) distribution function, $f_{HI}(N, z)$, derived by Zafar, Popping, et al., 2013 for $1.51 < z < 5.00$. It represents the number of absorbers per unit column density per unit path length. This quantity is important because it gives a diagnostic of the distribution of gas densities in the Universe from which we can derive the cosmological mass density of neutral gas Ω_g by integrating it from N_{min} to N_{max} (Wolfe, Gawiser, et al., 2005):

$$\Omega_g = \frac{H_0}{c}\frac{\mu m_H}{\rho_{crit}} \int_{N_{min}}^{N_{max}} dN N f(N, z) \tag{A.11}$$

where $\mu = 1.3$ is the mean molecular weight of the gas (including helium), $\rho_{crit} = 3H_0^2/8\pi G$ is the current critical mass density, m_H is the hydrogen mass and H_0 is the Hubble constant.

Ω_g is a key parameter in the study of the evolution of galaxies as it tells us how the density of neutral hydrogen evolves with cosmic time. Indeed, we expect that with decreasing redshift (and thus with increasing time from the Big Bang), the amount of neutral hydrogen would decrease, as a result of galaxy formation and evolution (neutral hydrogen is the fuel of star formation). Surprisingly, Zafar, Popping, et al., 2013 observed no evolution of Ω_g with redshift (up to $z = 5$), both for DLA and sub-DLA populations. This means that some mechanism, such

as replenishment of gas through accretion of matter from the filaments, must keep Ω_g constant with cosmic time.

The Lyman α forest can be observed in a quasar's spectrum, bluewards of its Lyα emission peak at $\lambda_{Ly\alpha} = (1 + z_{QSO}) \times 1216$[Å] (see figure 0.6). It is composed of many optically thin absorption lines, corresponding to absorption of the neutral hydrogen in the Lyman series redshifted at redshifts lower than z_{QSO} (because the absorbing systems are located in the line of sight, between us and the quasar).

Typically, the absorbing systems responsible for the forest have column densities for hydrogen, N(HI), up to 10^{17} atoms per cm^2, and would be the signature of the filaments of the cosmic web (which are mostly ionized). According to Penton, Stocke, et al. 2004, the Lyα forest contributes up to $\sim 10\%$ of the baryon budget at the present time (z=0).

When N(HI) is above 10^{17} atoms per cm^2, we start to witness different effects on the spectra. Indeed, every photon with a wavelength below 912 Å (corresponding to the Lyman limit), is likely to be absorbed by any hydrogen atom. If we have a dense enough cloud with a column density N(HI) above 10^{17} atoms per cm^2, there will be a sudden fall in the spectrum at $(1 + z_{abs}) \times 912$Å. These systems are called strong absorbers.

We can consider three different strong absorbers:

- systems with $log(N(HI)) > 17cm^{-2}$ are called the Lyman Limit Systems (LLS) and are observable from the fall in the quasar spectrum at $(1+z_{abs}) \times 912$Å
- systems with $\log N(HI) > 20.3cm^{-2}$ are called the Damped Lyman Absorbers (DLA) (see the review from Wolfe, Gawiser, et al. (2005))
- systems with $19 < log(N(HI)) < 20.3cm^{-2}$ are called the sub-DLA systems.

The DLAs and sub-DLAs are both identified via a typical wide and damped Lyα absorption line (in the forest), displayed on figure 0.7. They lie in the damped part of the Curve of Growth. They are called 'Damped' because of the shape of their absorption profile, which happens to be very saturated, with characteristic damping wings. The wings of the absorption profile give us all the information needed, as they do not depend much on the Doppler parameter (we usually use $b = 20km.s^{-2}$ for the sub-DLAs and $b = 30km.s^{-2}$ for the DLAs, Zafar, Popping, et al., 2013) and are well constrained by the column density $N(HI)$.

Recent studies give a better account of the baryons: $28\% \pm 11\%$ in the photoionized Lyα forest, $25\% \pm 8\%$ in the WHIM (Warm Hot Intergalactic Medium) and $18\% \pm 4\%$ in the galaxies, groups, clusters and the CGM (Shull, Smith, et al. (2012)).

Appendix B: Absorption

B.1. Multi-Element Analysis

B.1.1. Derivation of F_*

Jenkins, 2009 proposed to use the abundances of different elements (namely C, N, O, Mg, Si, P, Cl, Ti, Cr, Mn, Fe, Ni, Cu, Zn, Ge, Kr and S) to compare the dust depletion of dense neutral hydrogen systems to that of the Interstellar Medium (ISM) of our Galaxy. Specifically, the depletion $[X_{gas}/H]$ described in Jenkins, 2009 is the difference between the observed abundance of element X normalized to the total hydrogen abundance in both neutral and molecular phases, $N(H) = N(H\,I) + 2N(H_2)$, and its intrinsic abundance (assumed to be solar, initially):

$$[X_{gas}/H] = \log(X/H)_{obs} - \log(X/H)_{\odot} \tag{B.1}$$

Using 243 sight lines in our Galaxy, Jenkins, 2009 linearly fits the following formula:

$$[X_{gas}/H]_{fit} = [X_{gas}/H]_0 + A_X F_* \tag{B.2}$$

where F_* is defined as the line-of-sight depletion factor[a], A_X as the propensity of the element X to increase the absolute value of its particular depletion level as F_* becomes larger and $[X_{gas}/H]_0$ as the depletion for element X when $F_* = 0$. This equation can linearly be rewritten as:

$$[X_{gas}/H]_{fit} = B_X + A_X(F_* - z_X) \tag{B.3}$$

where F_* has its zero-point reference displaced to an intermediate value z_X (unique to element X), B_X being the depletion at $F_* = z_X$. The three parameters, A_X B_X and z_X, are then solved for each element (Table 4 of Jenkins, 2009).

In the case of DLAs and sub-DLAs[b], releasing the hypothesis of solar metallicity,

[a] We stress that this definition is based on calibration of F_* against the descriptive summary definitions reported in the review article by Savage et al., 1996.

[b] We note that the measured molecular hydrogen fraction for DLAs is rather low and that this fraction is not correlated with the HI column density (Ledoux, Petitjean, and Srianand, 2003; Noterdaeme, Ledoux, Petitjean, and Srianand, 2008). Therefore, the definition $N(H) = N(H\,I) + 2N(H_2)$ still holds for the present study.

equation B.1 can be rewritten as follows:

$$[\mathrm{X_{gas}/H}] = \log(\mathrm{X/H})_{\mathrm{obs}} - \log(\mathrm{X/H})_{\mathrm{intrinsic}} \tag{B.4}$$

where $\log(\mathrm{X/H})_{\mathrm{intrinsic}}$ is the abundance of element X in the absence of depletion. Equation B.3 then becomes:

$$[\mathrm{X/H}]_{\mathrm{obs}} - \mathrm{B_X} + \mathrm{A_X z_X} = [\mathrm{X/H}]_{\mathrm{intrinsic}} + \mathrm{A_X F_*} \tag{B.5}$$

where $[\mathrm{X/H}]_{\mathrm{obs}}$ is the metallicity compared to solar as we measure it (hence affected by depletion) and $[\mathrm{X/H}]_{\mathrm{intrinsic}}$ is the intrinsic metallicity compared to solar of the system derived from element X (corrected for depletion). We derive $\mathrm{F_*}$ by linearly fitting the left hand side of equation B.5 as a function of $\mathrm{A_X}$, thus providing an estimate of the intrinsic metallicity.

B.1.2. Derivation of $\mathrm{A_V}$

Our study relates to the rest frame extinction $\mathrm{A_V}$ through equation 3 of Vladilo, Centurión, et al., 2006, which scales $\mathrm{A_V}$ to the dust-phase column density of iron $\widehat{\mathrm{N_{Fe}}}$. Assuming that zinc is completely undepleted, and that the intrinsic ratio $\mathrm{Zn/Fe}$ ratio in DLAs and sub-DLAs is solar, we can express $\widehat{\mathrm{N_{Fe}}}$ as the following:

$$\widehat{\mathrm{N_{Fe}}} = \mathrm{f_{Fe} N_{Zn}} \left(\frac{\mathrm{Fe}}{\mathrm{Zn}}\right)_{\odot} \tag{B.6}$$

where $\mathrm{f_{Fe}} = 1 - 10^{\delta_{\mathrm{Fe}}}$ is the fraction of iron in dust form. We can assume $\delta_{\mathrm{Fe}} = [\mathrm{Fe/Zn}]_{\mathrm{obs}}$. To recover $\mathrm{N_{Zn}}$, we use the assumption that $[\mathrm{Zn/H}] = [\mathrm{X/H}]$, with $[\mathrm{X/H}]$ being the metallicity derived for each system using the ion X (when Zn is not detected). We obtain the following expression:

$$\log \widehat{\mathrm{N_{Fe}}} = \log\left(1 - 10^{[\mathrm{Fe/Zn}]_{\mathrm{obs}}}\right) + \log(\mathrm{N_X}) - \log\left(\frac{\mathrm{N_X}}{\mathrm{N_{Fe}}}\right)_{\odot} \tag{B.7}$$

where $\mathrm{N_X}$ is the column density of the ion used for the metallicity derivation for a given system.

We can use equation B.5 to derive an estimate of the quantity $[\mathrm{Fe/Zn}]_{\mathrm{J}}$ from the Jenkins analysis:

$$[\mathrm{Fe/Zn}]_{\mathrm{J}} = (-1.01 \pm 0.07) + (-0.68 \pm 0.08)\mathrm{F_*} \tag{B.8}$$

This results in $\langle[\mathrm{Fe/Zn}]\rangle_{\mathrm{J,\,sub-DLA}} = -0.78 \pm 0.15$ and $\langle[\mathrm{Fe/Zn}]\rangle_{\mathrm{J,\,DLA}} = -0.53 \pm 0.10$. Using a bootstrap method, we derive $\left\langle \log \widehat{\mathrm{N_{Fe}}} \right\rangle_{\mathrm{sub-DLA}} = 14.38 \pm 0.80$ and $\left\langle \log \widehat{\mathrm{N_{Fe}}} \right\rangle_{\mathrm{DLA}} = 14.73 \pm 0.85$. Based on Fig. 4 from Vladilo, Centurión, et al.,

2006, we can estimate the rest frame extinction $\log A_V$ from $\log \widehat{N_{Fe}}$. For both populations, the value of $\left\langle \log \widehat{N_{Fe}} \right\rangle$ falls below the range of MW data used to derive the correlation, giving low values of $\langle \log A_V \rangle \lesssim -2$ mag. This suggests that the dust reddening is not observed in the current quasar selection.

B.2. Individual objects

This Appendix summarizes a description of the individual systems as well as figures and tables providing the Voigt profile parameters for the low, intermediate and high-ionization species when available. For the following figures, we use z_{abs} from the literature as the zero velocity component.

B.2.1. QSOJ0008-2900 $z_{em} = 2.645$, $z_{abs} = 2.254$, $\log N(HI) = 20.22 \pm 0.10$

The EUADP spectrum for this absorber covers multiple low-ionization transitions including FeII $\lambda\lambda\lambda\lambda$ 2374, 2382, 2586, 2600, SiII λ 1526, and the saturated MgII doublet $\lambda\lambda$ 2796, 2803. The velocity profiles are well fitted with 5 components. The fit to the Fe lines is found to be consistent with the non-detection of FeII λ 2260. The resulting total column density of Fe is $\log N(FeII) = 13.78 \pm 0.01$. By comparing the detected SiII λ 1526 line with the weak SiII λ 1808 transition, we deduce that the former is slightly contaminated. An estimation on the column density based on SiII λ 1808 gives $\log N(SiII) = 14.40 \pm 0.1$. This total column density is confirmed with the apparent optical depth method applied on SiII λ 1808 from $v = -72$ km/s and $v = +10$ km/s. Because it is saturated, the MgII doublet is fitted fixing the number of components and parameters to the low-ionization lines. The result provides a lower limit to the Mg column density of $\log N(MgII) > 15.1$. The non-detection of CrII λ 2062, ZnII λ 2026 and MnII λ 2576 leads to the determination of the following upper limits: $\log N(CrII) < 12.37$, $\log N(ZnII) < 11.68$ and $\log N(MnII) < 12.02$.

In addition to these low-ionization ions, the quasar spectrum covers high-ionization species including the SiIV doublet $\lambda\lambda$ 1393 and 1402. However, the bluest SiIV line lies on the Lyα emission line of the quasar thus complicating the quasar continuum placement. Therefore the reddest component of the SiIV doublet is used to model the Voigt profile. In addition, the intermediate-ionization lines of AlIII $\lambda\lambda$ 1854 and 1862 present a similar velocity profile to the SiIV doublet. Therefore, the fit is performed using these transitions simultaneously. A satisfactory 3-component fit leads to the following column densities: $\log N(SiIV) = 13.72 \pm 0.03$ and $\log N(AlIII) = 12.39 \pm 0.04$.

The parameter fits are summarised in Table B.1 and Voigt profile fits are shown in Fig. B.1.

Table B.1.: Voigt profile fit parameters to the low- and high-ionisation species for the z_{abs}=2.645 log N(H I)=20.22 ± 0.10 absorber towards QSO J0008-2900. In this table and in the following ones, the values with no uncertainties have been manually fixed to improve the fitting process.

Comp.	z_{abs}	b km s^{-1}	Ion	log N cm^{-2}
1	2.25337	4.5 ± 0.2	FeII	12.95 ± 0.01
			SiII	13.70
2	2.25352	2.8 ± 0.2	FeII	13.00 ± 0.01
			SiII	13.80
3	2.25367	4.0 ± 0.2	FeII	13.24 ± 0.01
			SiII	13.85
4	2.25380	5.0 ± 0.3	FeII	13.20 ± 0.02
			SiII	13.40
5	2.25392	5.3 ± 0.3	FeII	12.91 ± 0.02
			SiII	13.60
1	2.25332	16.1 ± 2.7	SiIV	13.19 ± 0.05
			AlIII	11.74 ± 0.10
2	2.25366	9.0 ± 1.1	SiIV	13.42 ± 0.05
			AlIII	12.07 ± 0.06
3	2.25389	9.2 ± 1.9	SiIV	13.05 ± 0.08
			AlIII	11.88 ± 0.08

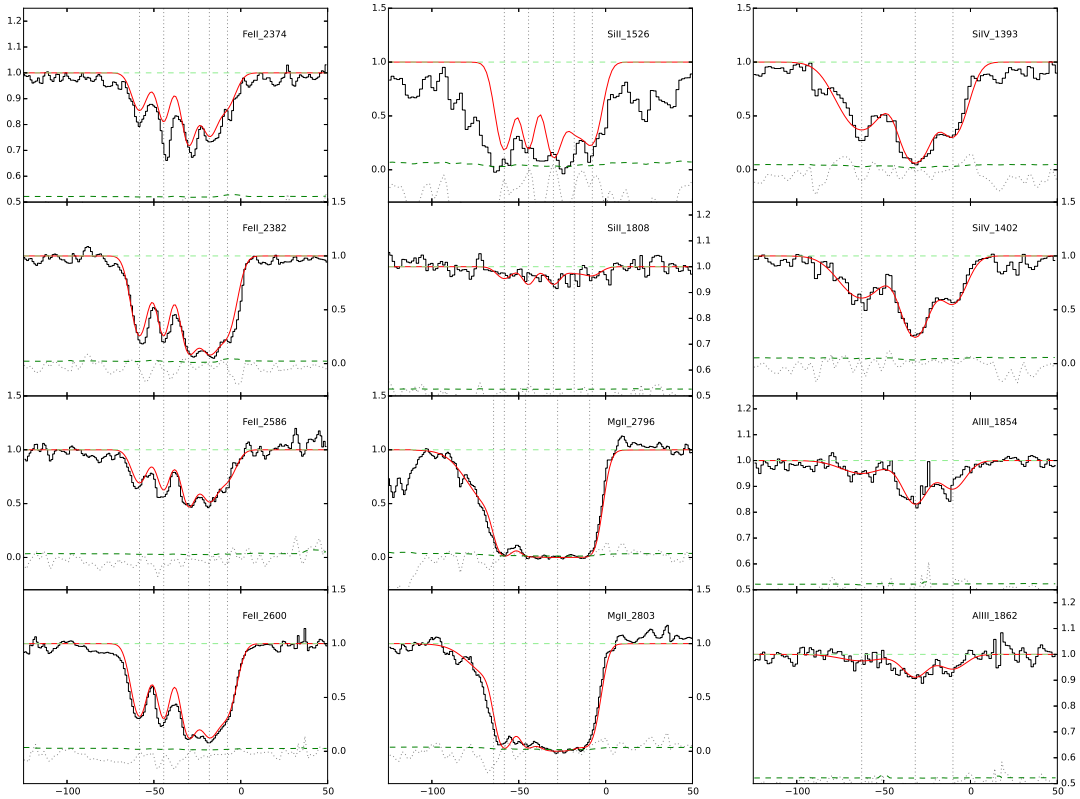

Figure B.1.: Fit to the low-ionization transitions of the $z_{abs} = 2.254$, log N(H I) = 20.22 ± 0.10 absorber towards QSOJ0008-2900 (see Table B.1). In this and the following figures, the Voigt profile fits are overlaid in red above the observed quasar spectrum (black) and the green horizontal line indicates the normalised flux level to one. The zero velocity corresponds to the absorption redshift listed in Table 1.1 and the vertical dotted lines correspond to the redshift of the fitted components. We warn the reader that the y-axis varies from one panel to another in order to optimise for each transitions so that weaker lines can be readily seen.

Table B.2.: Voigt profile fit parameters to the low-ionization species for the z_{abs}=2.491 log N(H I)=19.94±0.11 absorber towards QSO J0008-2901.

Comp.	z_{abs}	b km s^{-1}	Ion	log N cm^{-2}
1	2.49046	1.6 ± 0.2	FeII	12.60 ± 0.07
			SII	12.98 ± 0.91
			OI	13.32 ± 1.54
2	2.49054	4.1 ± 0.1	FeII	13.61 ± 0.02
			SII	13.58 ± 0.02
			OI	15.31 ± 0.24

B.2.2. QSOJ0008-2901 $z_{em} = 2.607$, $z_{abs} = 2.491$, $\log N(HI) = 19.94 \pm 0.11$

In this case, the quasar spectrum is of modest SNR. The wavelength coverage includes low-ionization lines of FeII $\lambda\lambda\lambda\lambda$ 2260, 2344, 2382, 2586, SII λ 1259 and OI λ 1039. A two-component fit is used given the asymmetrical shape of the FeII and SII lines. The resulting column densities are log N(FeII)$= 13.65 \pm 0.02$, log N(OI)$= 15.31 \pm 0.24$ and log N(SII)$= 13.68 \pm 0.18$. Finally, we used the non-detection of the following transitions to derive upper limits on the column densities: CrII λ 2062 log N(CrII)< 12.9, NiII λ 1741 log N(NiII)< 13.29, ZnII λ 2026 log N(ZnII)< 12.12 and AlIII λ 1854 log N(AlII)< 12.2.

The EUADP quasar spectrum does not cover the CIV doublet for this absorber. In addition, the high-ionization SiIV doublet $\lambda\lambda$ 1393 and 1402 is covered but no satisfactory fit could be determined given the low SNR of the quasar spectrum in this region.

The resulting parameter fits are summarised in Table B.2 and Voigt profile fits are shown in Fig. B.2.

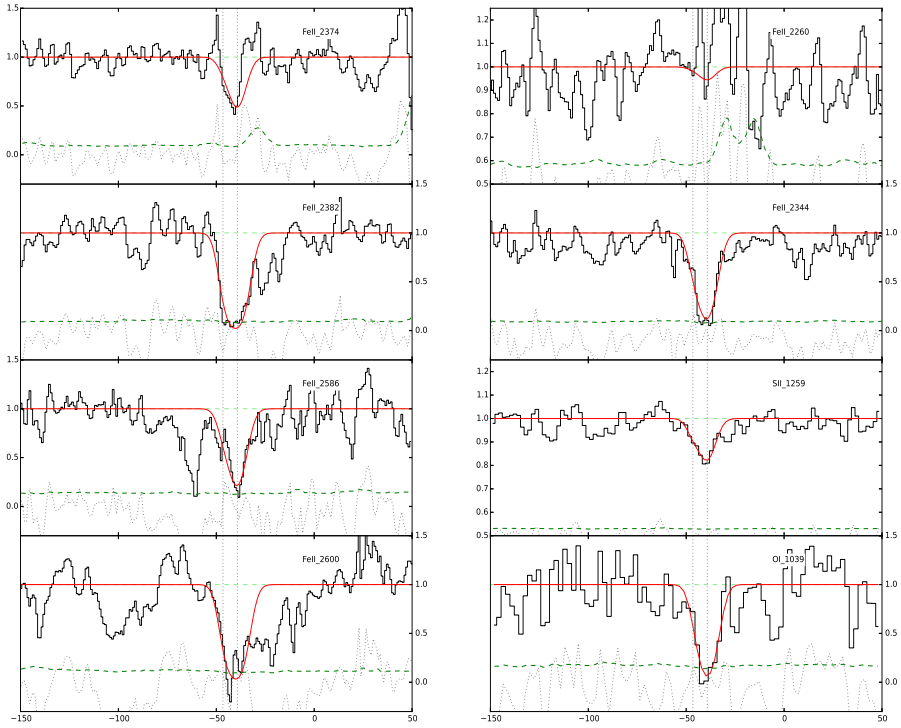

Figure B.2.: QSOJ0008-2901 $z_{abs} = 2.607$

B.2.3. QSO J0018-0913 $z_{em} = 0.75593$, $z_{abs} = 0.584$, $\log N(HI) = 20.11 \pm 0.10$

We detect in this low-redshift absorber's spectrum the following low-ionization ions: FeII $\lambda\lambda\lambda$ 2344 2374 and 2382. The profile is fitted using 11 components, spread over a velocity range of about $200 km/s$, resulting in an abundance for FeII of $\log N(FeII) = 13.87 \pm 0.03$. The main component is located on the blue edge of the profile and is accounting for about 40% of the total abundance. Also, we derive upper limits from non detection of ZnII λ 2026, $\log N(ZnII) < 12.41$, CrII λ 2056, $\log N(CrII) < 12.97$, TiII λ 3384, $\log N(TiII) < 11.57$, MgI λ 2026, $\log N(MgI) < 13.04$, NaI λ 3303.3 and $\log N(NaI) < 13.15$.

The metallicity for this low-redshift sub-DLA is surprisingly low (even considering the α-enhancement correction of $\sim .4$ dex), $[Fe/H] = -1.70 \pm 0.13$. It may be an effect of dust depletion, but we are unable to conclude on this particular issue due to the low number of detected ions. The metallicity derived here is

Table B.3.: Voigt profile fit parameters to the low-ionization species for the z_{abs}=0.584 log N(H I)=20.11 ± 0.1 absorber towards QSO J0018-0913.

Comp.	z_{abs}	b km s^{-1}	Ion	log N cm^{-2}
1	0.58304	5.4 ± 0.3	FeII	13.51 ± 0.04
2	0.58322	13.0 ± 5.4	FeII	12.60 ± 0.14
3	0.58332	2.5 ± 0.7	FeII	12.90 ± 0.09
4	0.58339	3.1 ± 5.3	FeII	12.28 ± 0.13
5	0.58346	3.3 ± 1.2	FeII	12.78 ± 0.06
6	0.58353	3.5 ± 3.5	FeII	11.96 ± 0.17
7	0.58365	13.4 ± 14.9	FeII	12.15 ± 0.43
8	0.58378	3.8 ± 2.1	FeII	12.69 ± 0.10
9	0.58386	2.0 ± 3.1	FeII	12.33 ± 0.19
10	0.58397	6.7 ± 0.8	FeII	12.98 ± 0.03
11	0.58406	3.8 ± 1.2	FeII	12.57 ± 0.05

therefore to be considered as a lower limit.

There is no coverage of the high-ionization ions due to the low redshift of the absorber.

The parameter fits of the individual components are listed in Table B.3 and the corresponding Voigt profile fits are shown in Fig. B.3.

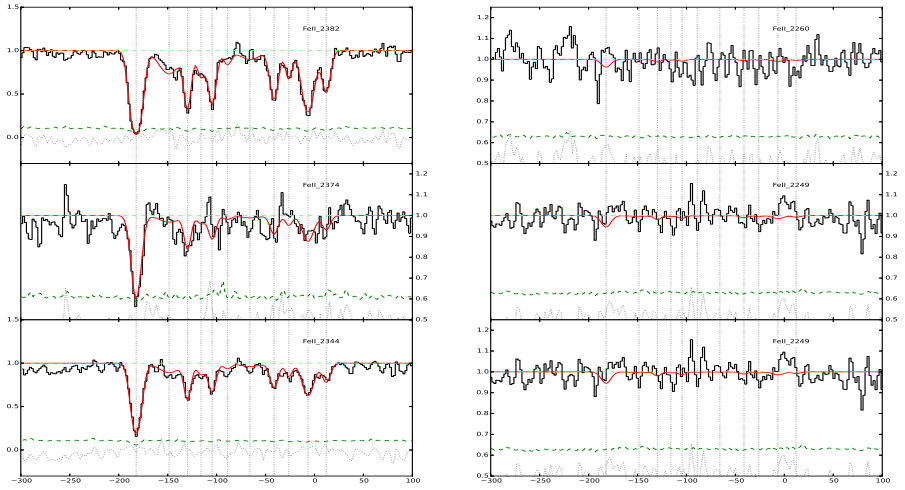

Figure B.3.: QSOJ0018-0913 $z_{abs} = 0.584$

B.2.4. QSOJ0041-4936 $z_{em} = 3.24$, $z_{abs} = 2.248$, $\log N(HI) = 20.46 \pm 0.13$

This spectrum covers many low-ionization transitions associated with the absorber: SII λ 1259, ZnII λ 2026, FeII λ 1608, SiII $\lambda\lambda$ 1808, 1526 and AlII λ 1670. The velocity profile can be conveniently separated into a group of red and blue components. The overall profile is well fitted with 4 components. Interestingly, the blue group which is weaker than its red counterpart is only detected in SII λ 1259, SiII λ 1526 and AlII λ 1670. Conversely, the red group of components is saturated in the case of the last two transitions. Therefore, these two groups are fitted separately: the blue-component group is fitted with two components using the lines of SiII λ 1526 and AlII λ 1670. The SII λ 1259 line is too blended to provide useful information and we derive an upper limit of $\log N(SII) < 14.82$. The red-component group includes ZnII λ 2026, FeII λ 1608 and SiII λ 1808. It is also fitted with two components given the asymmetrical profile of FeII λ 1608. A fifth component redward of the profile is considered for SII λ 1526 and AlII λ 1670. The resulting column densities are: $\log$ N(FeII)$=14.43 \pm 0.04$, $\log$ N(ZnII)$=11.70 \pm 0.10$, $\log$ N(SiII)$=14.78 \pm 0.03$, $\log$ N(NiII)$=13.07 \pm 0.07$ and $\log$ N(CrII)$=13.12 \pm 0.45$. We detect four NI absorption lines NI $\lambda\lambda\lambda\lambda$ 1199.5, 1134.1, 1134.4 and 1134.9. The profile is fitted with the low-ionization profile in this case. In spite of the modest SNR, a satisfactory fit is found for NI $\lambda\lambda\lambda$ 1134.1, 1134.9 and 1199.5, while the remaining line (NI λ 1134.4) appears to be blended. The resulting column density is $\log$ N(NI)$=14.03 \pm 0.03$. Finally, the AlII λ 1670 line is saturated thus providing a lower limit on the column density: $\log N(AlII) > 14.06$.

Regarding the high-ionization ions, the CIV doublet $\lambda\lambda$ 1548 and 1550 is covered by the EUADP spectrum. In addition, the intermediate-ionization AlIII transitions $\lambda\lambda$ 1854 and 1862 are present and match well the high-ionization profile. In the case of the CIV doublet, the CIV λ 1550 is blended with a broad line in the blue part ($v < -120 km/s$), whereas CIV λ 1548 seems blended in the red part ($v > -120 km/s$). In addition, the AlIII transition shows absorption features in the red part of the profile only. A 6-component profile is used to fit the red part of the profile (using transitions from CIV λ 1550, AlIII $\lambda\lambda$ 1862 and 1854) and one-component is used to fit the blue part of the profile (using CIV λ 1548 at $v \sim -240 km/s$). This results in an estimated column density of AlIII $\log N(AlIII) = 12.90 \pm 0.01$ and a lower limit (blending) for CIV $\log N(CIV) > 14.56$.

The parameter fits are summarised in Table B.4 and Voigt profile fits are shown in Fig. B.4.

Table B.4.: Voigt profile fit parameters to the low-, intermediate- and high-ionization species for the z_{abs}=2.248 log N(H I)=20.46 ± 0.13 absorber towards QSO J0041-4936.

Comp.	z_{abs}	b	Ion	log N
1	2.24785	4.6 ± 0.8	FeII	12.01 ± 0.35
			ZnII	–
			SiII	12.85 ± 0.04
			NiII	–
			CrII	–
			AlII	11.28 ± 0.05
			SII	< 13.24
			NI	12.38 ± 0.17
2	2.24799	7.3 ± 0.4	FeII	12.01 ± 0.35
			ZnII	–
			SiII	13.12 ± 0.02
			NiII	–
			CrII	–
			AlII	11.78 ± 0.02
			SII	< 14.04
			NI	12.80 ± 0.07
3	2.24840	10.2 ± 0.9	FeII	13.71 ± 0.05
			ZnII	11.03 ± 0.36
			SiII	14.35 ± 0.06
			NiII	12.80 ± 0.10
			CrII	12.73 ± 0.91
			AlII	> 13.11
			SII	< 14.38
			NI	12.58 ± 0.15
4	2.24852	3.8 ± 0.2	FeII	14.33 ± 0.05
			ZnII	11.59 ± 0.09
			SiII	14.54 ± 0.04
			NiII	12.74 ± 0.09
			CrII	12.89 ± 0.44
			AlII	> 15.13
			SII	< 14.48
			NI	14.25 ± 0.04
5	2.24866	8.0 ± 0.3	FeII	–
			ZnII	–
			SiII	13.13 ± 0.02
			NiII	–

Continued on next page

Table B.4 – *Continued from previous page*

Comp.	z_{abs}	b	Ion	log N
			CrII	–
			AlII	12.09 ± 0.02
			SII	–
			NI	–
1	2.24547	3.5 ± 0.5	CIV	12.84 ± 0.02
			AlIII	–
2	2.24696	4.1 ± 0.4	CIV	13.21 ± 0.01
			AlIII	–
3	2.24757	12.1 ± 0.7	CIV	13.24 ± 0.01
			AlIII	11.25 ± 0.06
4	2.24797	13.1 ± 0.1	CIV	14.32 ± 0.01
			AlIII	12.28 ± 0.01
5	2.24835	8.7 ± 0.3	CIV	13.58 ± 0.10
			AlIII	12.37 ± 0.01
6	2.24845	19.6 ± 0.4	CIV	13.87 ± 0.01
			AlIII	12.36 ± 0.01
7	2.24853	2.6 ± 0.7	CIV	–
			AlIII	12.08 ± 0.01

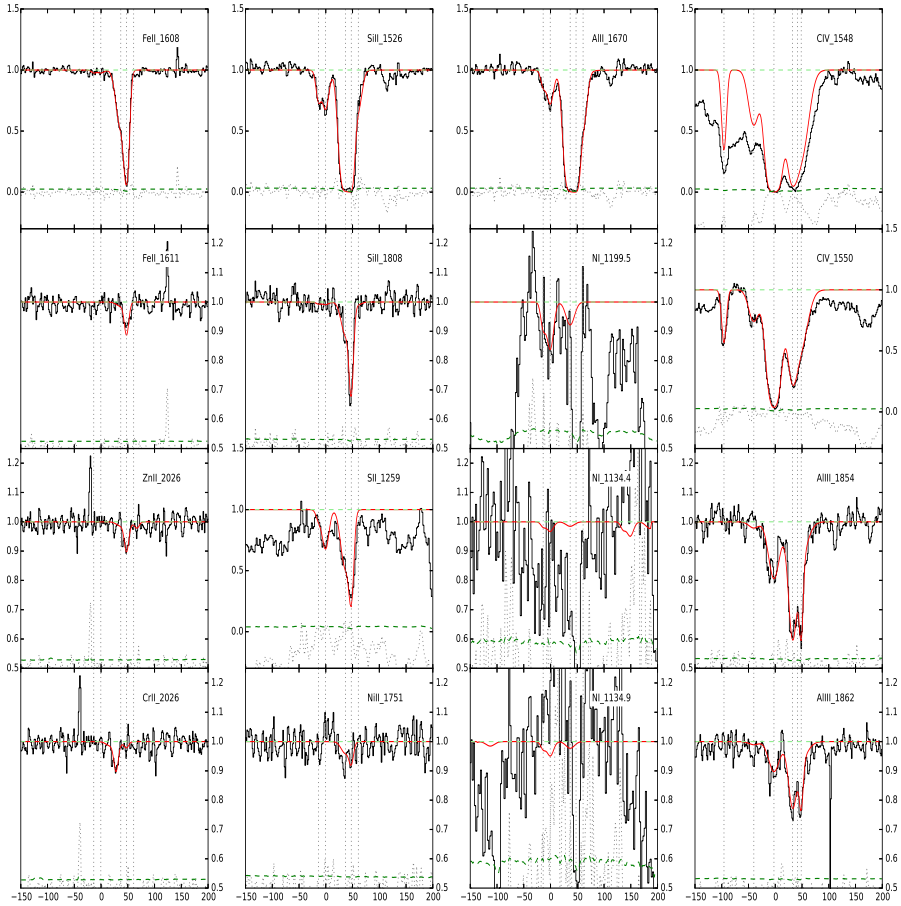

Figure B.4.: QSOJ0041-4936 $z_{abs} = 2.248$

B.2.5. QSO B0128-2150 $z_{em} = 1.9$, $z_{abs} = 1.857$, $\log N(HI) = 20.21 \pm 0.09$

For this low-redshift absorber, the EUADP spectrum covers a number of the low-ionization ions including FeII $\lambda\lambda\lambda$ 2374 2260 2249, NiII $\lambda\lambda\lambda$ 1751 1741 1709, SII $\lambda\lambda\lambda$ 1259 1253 1250 and SiII λ 1808. The detected intermediate-ionization transitions, AlIII $\lambda\lambda$ 1854 and 1862 show the same velocity profile as the low-ionization ions. A 5-component Voigt profile is used to fit FeII $\lambda\lambda$ 2374 2249, SiII λ 1808 SII λ1259, AlIII λ 1854 and NiII λ 1709. The full absorption profile extends to a velocity range of about 100 km/s. The resulting total column densities

are log N(FeII)=14.44 ± 0.01, log N(SiII)=14.82 ± 0.02, log N(SII)=14.33 ± 0.03, log N(NiII)=13.26 ± 0.05 and log N(AlIII)=12.78 ± 0.01. In addition, CII λ 1334 is detected but, as often in DLAs, heavily saturated. Finally, the non-detection of both ZnII λ 2062 and MgI λ 1827 provides robust column density upper limits: $\log N(ZnII) < 12.26$, and $\log \mathrm{N(MgI)} < 13.21$.

We note that no high-ionization species are covered by this spectrum.

The parameter fits are summarised in Table B.5 and Voigt profile fits are shown in Fig. B.5.

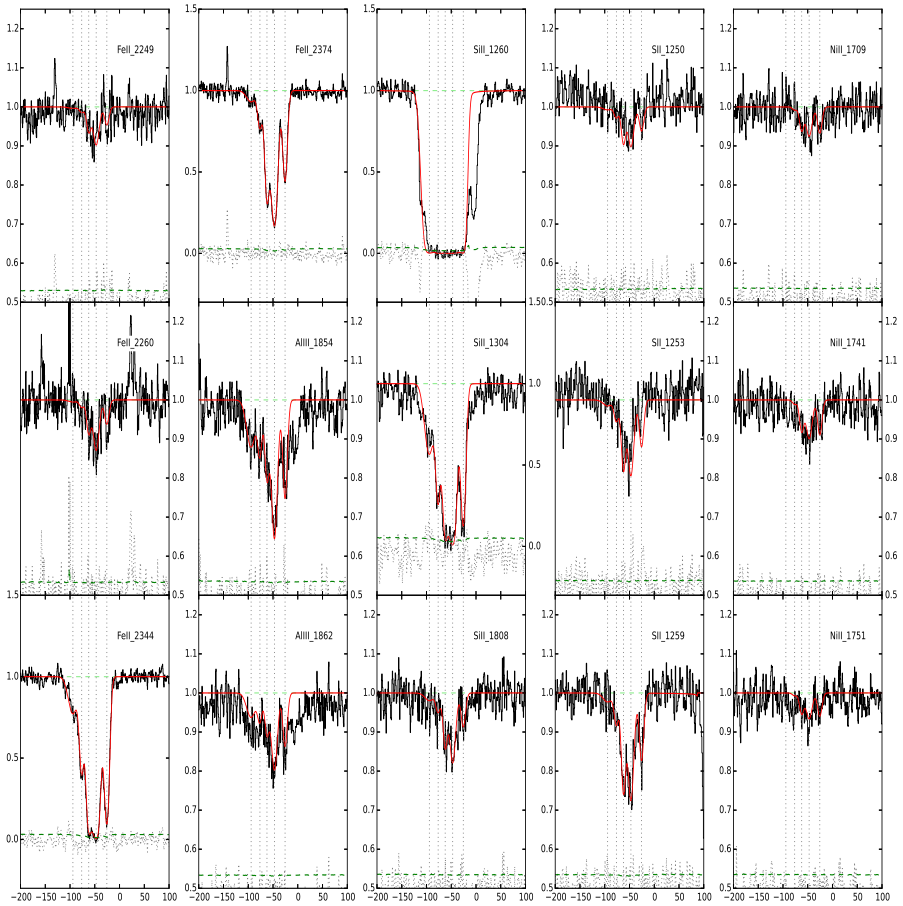

Figure B.5.: QSOB0128-2150 $z_{\mathrm{abs}} = 1.857$

Table B.5.: Voigt profile fit parameters to the low-ionization species for the z_{abs}=1.857 log N(H I)=20.21±0.09 absorber towards QSO B0128-2150.

Comp.	z_{abs}	b km s^{-1}	Ion	log N cm^{-2}
1	1.85610	11.8 ± 2.1	FeII	12.91 ± 0.06
			SiII	13.93 ± 0.10
			SII	12.98 ± 0.29
			AlIII	12.02 ± 0.05
			NiII	–
2	1.85627	4.5 ± 0.7	FeII	13.16 ± 0.04
			SiII	13.71 ± 0.12
			SII	13.23 ± 0.12
			AlIII	11.76 ± 0.07
			NiII	11.80 ± 0.67
3	1.85641	4.3 ± 0.3	FeII	13.82 ± 0.01
			SiII	14.19 ± 0.04
			SII	13.77 ± 0.04
			AlIII	11.94 ± 0.03
			NiII	12.66 ± 0.1
4	1.85655	7.0 ± 0.2	FeII	14.14 ± 0.01
			SiII	14.44 ± 0.01
			SII	13.94 ± 0.03
			AlIII	12.37 ± 0.01
			NiII	12.89 ± 0.06
5	1.85676	4.6 ± 0.2	FeII	13.69 ± 0.01
			SiII	13.99 ± 0.05
			SII	13.60 ± 0.05
			AlIII	12.08 ± 0.02
			NiII	12.73 ± 0.08

Table B.6.: Voigt profile fit parameters to the low-ionization species for the z_{abs}=0.647 log N(H I)=20.60±0.12 absorber towards QSO J0132-0823.

Comp.	z_{abs}	b km s^{-1}	Ion	log N cm^{-2}
1	0.64612	10.7 ± 2.3	FeII	13.38 ± 0.08
			TiII	11.53 ± 0.44
			MgI	10.62 ± 1.76
2	0.64635	15.6 ± 1.2	FeII	14.72 ± 0.09
			TiII	12.15 ± 0.10
			MgI	12.37 ± 0.04
3	0.64658	14.4 ± 2.1	FeII	14.52 ± 0.11
			TiII	11.75 ± 0.21
			MgI	12.13 ± 0.06
4	0.64677	10.8 ± 3.0	FeII	13.35 ± 0.13
			TiII	11.12 ± 0.77
			MgI	11.43 ± 0.19

B.2.6. QSO J0132-0823 $z_{\rm em} = 1.121$, $z_{\rm abs} = 0.6467$, $\log {\rm N(HI)} = 20.60 \pm 0.12$

A few ions are covered and detected in this low-redshift absorber's spectrum: FeII $\lambda\lambda$ 2249 2260, MgI λ 2582 and TiII $\lambda\lambda$ 3242 and 3384. The absorption is weak, we use the MgI profile to derive the two main components. The saturated FeII λ 2344 unveils two weak components on either side of the profile. This results in abundances of FeII $\log {\rm N(FeII)} = 14.96 \pm 0.07$, of TiII $\log {\rm N(TiII)} = 12.39 \pm 0.11$ and of MgI $\log {\rm N(MgI)} = 12.60 \pm 0.04$.

The overall SNR (< 10) gives a reasonable upper limit for CrII, using CrII λ 2056, of $\log {\rm N(CrII)} < 13.17$. ZnII and CII are also covered, but the best upper limits we can derive are above 16.30.

There is no coverage of the high-ionization ions due to the low redshift of the absorber.

The parameter fits of the individual components are listed in Table B.6 and the corresponding Voigt profile fits are shown in Fig. B.6.

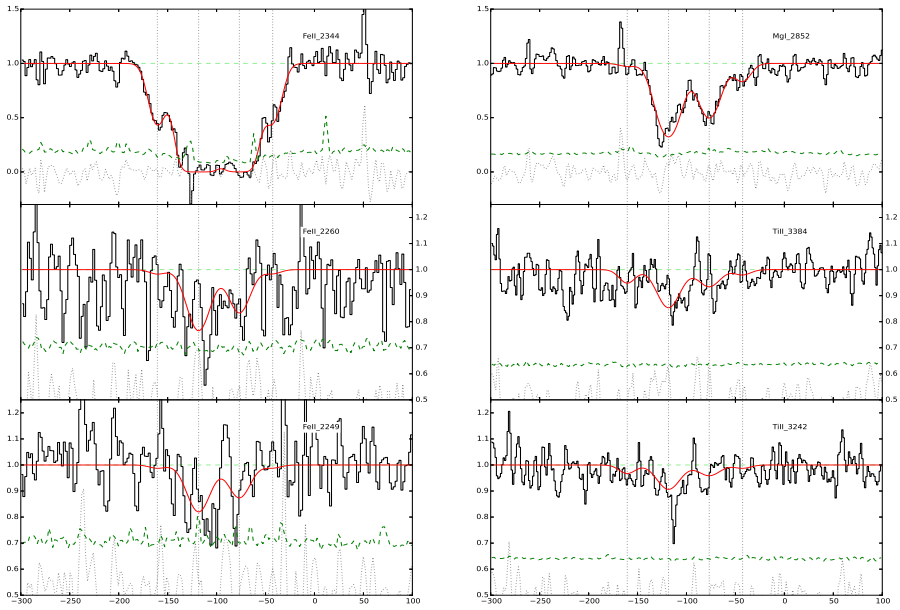

Figure B.6.: QSOJ0132-0823 $z_{abs} = 0.6467$

B.2.7. QSO B0307-195B $z_{em} = 2.122$, $z_{abs} = 1.788$, $\log N(HI) = 19.0 \pm 0.10$

Many low-ionization ions are detected in this low-redshift absorber including MgI λ 2852, FeII $\lambda\lambda\lambda\lambda\lambda$ 2374, 1608, 2586, 2344, 2382, 2600, SiII $\lambda\lambda\lambda$ 1808, 1304, 1526, MgII $\lambda\lambda$ 2803, 2796, AlII λ 1670, AlIII $\lambda\lambda$ 1862, 1854, CIV $\lambda\lambda$ 1550, 1548 and SiIV $\lambda\lambda$ 1402, 1393. The absorption profile presents two distinct parts, one in the red (5 components), the other one in the blue (3 components), with a total velocity ranging about 300 km/s. The fit is performed using the transitions which are free from any saturation i.e. FeII $\lambda\lambda\lambda$ 2374 1608 2586, SiII λ 1808 and MgI λ 2852. The FeII λ 2586 line in particular is not considered for the final fits given the medium quality of the EUADP spectrum around $v = 50 km/s$. The resulting total column densities are: $\log$ N(FeII)$=14.48 \pm 0.004$, $\log$ N(SiII)$=15.0 \pm 0.01$ and $\log$ N(MgI)$=12.54 \pm 0.01$. In addition to these measures, the non-detection of CrII λ 2056, MnII λ 2594, NiII λ 1751, and ZnII λ 2062 is used to derive the following upper limits $\log N(CrII) < 12.77$, $\log N(MnII) < 12.13$, $\log N(NiII) < 13.22$ and $\log N(ZnII) < 12.18$.

The high-ionization doublets of CIV $\lambda\lambda$ 1548 1550 and SiIV $\lambda\lambda$ 1393 and 1402 are detected in the spectrum albeit indicating strong saturation. A 7-component

profile is used to fit these four transitions resulting in lower limits to the total column densities of $\log \mathrm{N(SiIV)} > 14.55$ and $\log \mathrm{N(CIV)} > 15.13$. Interestingly, in this absorber, the velocity range of the high-ionization ion profile matches the one from the low-ionization ions extending to about 300 km/s.

The resulting parameter fits for the low- and high-ionization profiles are listed in Table B.7 and the corresponding Voigt profile fits are shown in Fig. B.7.

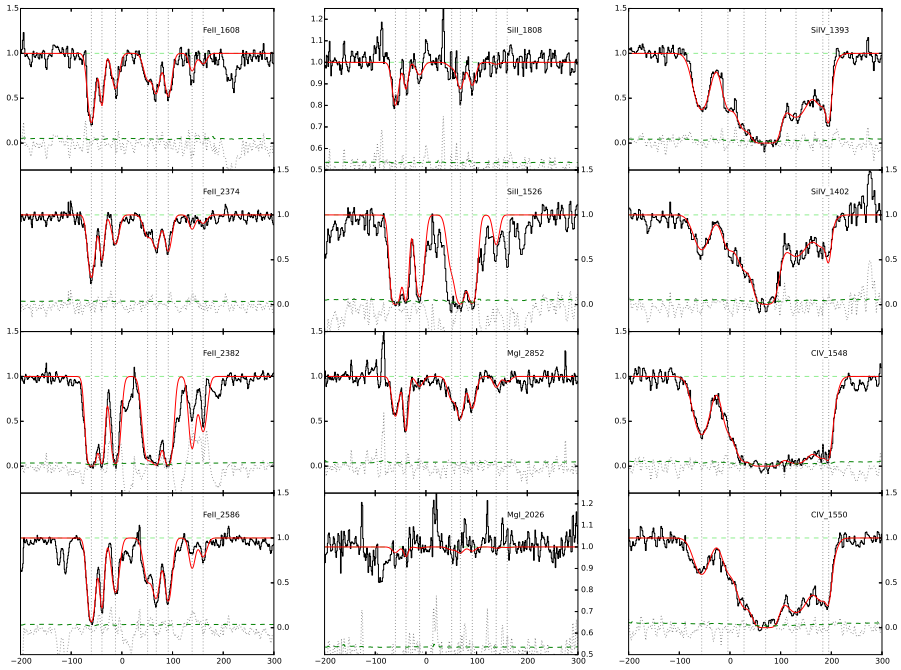

Figure B.7.: QSOB0307-195B $z_{abs} = 1.788$

B.2.8. QSO J0427-1302 $z_{em} = 2.166$, $z_{abs} = 1.562$, $\log \mathrm{N(HI)} = 19.35 \pm 0.10$

The low-ionization transitions in this low-redshift system are well fitted with two components, the redshift and Doppler parameter of which are fixed by a simultaneous fit of FeII $\lambda\lambda\lambda\lambda$ 2344, 2382, 2586, 2600 and AlII λ 1670. The 2-component fit shows an interesting asymmetric distribution of FeII and AlII abundances: the blue component is stronger for FeII while the red component is stronger for AlII. The resulting column densities are $\log$ N(FeII)$=12.23 \pm 0.04$ and $\log$ N(AlII)$=11.78 \pm 0.1$. In addition, the non detection of CrII λ 2056, MgI λ 2026, MnII λ 2576, NiII λ 1741, and ZnII λ 2026 leads to the following

Table B.7.: Voigt profile fit parameters to the low- and high-ionization species for the z_{abs}=1.788 log N(H I)=19.00 ± 0.10 absorber towards QSO B0307-195B.

Comp.	z_{abs}	b km s^{-1}	Ion	log N cm^{-2}
1	1.78744	7.8 ± 0.1	FeII	13.99 ± 0.01
			SiII	14.53 ± 0.01
			MgI	11.83 ± 0.01
2	1.78763	4.3 ± 0.1	FeII	13.61 ± 0.01
			SiII	14.14 ± 0.03
			MgI	11.90 ± 0.01
3	1.78788	8.6 ± 0.4	FeII	13.54 ± 0.01
			SiII	13.99 ± 0.04
			MgI	11.16 ± 0.03
4	1.78847	9.9 ± 0.1	FeII	13.42 ± 0.02
			SiII	13.60 ± 0.11
			MgI	11.61 ± 0.01
5	1.78863	8.2 ± 0.2	FeII	13.58 ± 0.01
			SiII	14.31 ± 0.02
			MgI	11.87 ± 0.01
6	1.78885	8.2 ± 0.2	FeII	13.64 ± 0.01
			SiII	14.25 ± 0.02
			MgI	11.72 ± 0.01
7	1.78929	7.0 ± 0.7	FeII	13.11 ± 0.03
			SiII	13.13 ± 0.26
			MgI	11.14 ± 0.03
8	1.78949	8.9 ± 2.0	FeII	12.95 ± 0.05
			SiII	–
			MgI	10.90 ± 0.07
1	1.78748	19.8 ± 0.3	SiIV	13.27 ± 0.01
			CIV	13.68 ± 0.01
2	1.78796	15.1 ± 0.6	SiIV	13.10 ± 0.03
			CIV	13.46 ± 0.03
3	1.78826	18.6 ± 1.1	SiIV	13.50 ± 0.03
			CIV	14.08 ± 0.03
4	1.78865	19.8 ± 0.5	SiIV	14.37 ± 0.02
			CIV	14.89 ± 0.02
5	1.78921	32.5 ± 1.3	SiIV	13.58 ± 0.02
			CIV	14.42 ± 0.01
6	1.78970	18.9 ± 0.6	SiIV	13.15 ± 0.02
			CIV	13.97 ± 0.02
7	1.78981	5.0 ± 0.3	SiIV	12.78 ± 0.02
			CIV	13.25 ± 0.04

Table B.8.: Voigt profile fit parameters to the low- and high-ionization species for the z_{abs}=1.562 log N(H I)=19.35 ± 0.10 absorber towards QSO J0427-1302.

Comp.	z_{abs}	b km s^{-1}	Ion	log N cm^{-2}
1	1.5631845	7.2 ± 1.4	AlII	11.78 ± 0.10
			FeII	-
2	1.5632172	2.9 ± 0.6	AlII	-
			FeII	12.23 ± 0.04
1	1.56065	17.4 ± 2.7	SiIV	12.96 ± 0.08
2	1.56075	3.1 ± 2.4	SiIV	12.31 ± 0.22
3	1.56089	4.6 ± 1.0	SiIV	12.73 ± 0.06
4	1.56101	1.5 ± 0.7	SiIV	12.93 ± 0.62
5	1.56126	23.8 ± 8.3	SiIV	12.85 ± 0.12
6	1.56143	1.2 ± 2.0	SiIV	12.13 ± 0.39
7	1.56165	12.8 ± 1.0	SiIV	13.27 ± 0.03
8	1.56197	12.7 ± 1.8	SiIV	12.81 ± 0.04
9	1.56228	6.4 ± 2.5	SiIV	12.33 ± 0.08
10	1.56270	25.4 ± 5.2	SiIV	12.49 ± 0.08
11	1.56309	2.0 ± 2.0	SiIV	12.35 ± 0.17
12	1.56321	6.4 ± 0.6	SiIV	13.15 ± 0.03

upper limits: $\log \mathrm{N(CrII)} < 12.39$, $\log \mathrm{N(MgI)} < 12.38$, $\log \mathrm{N(MnII)} < 11.84$, $\log \mathrm{N(NiII)} < 13.23$ and $\log \mathrm{N(ZnII)} < 11.75$.

In addition to these low-ionization transitions, the EUADP spectrum covers several high-ionization species. The doublet of CIV $\lambda\lambda$ 1550, 1548 and SiIV $\lambda\lambda$ 1393 and 1402 expand a velocity range of about 250 km/s. The CIV transitions are strongly saturated and SiIV λ 1402 appears to be blended (greater absorption in spite of a lower oscillation factor than SiIV λ 1393). Thus the fit is performed using the SiIV λ 1393 line, considering a total of 12 components, with the redder one being associated with the low-ionization profile (v $\sim$140 km/s). Many of the strongest components fitted for SiIV λ 1393 match the velocity profiles of the CIV doublet. We obtain $\log \mathrm{N(SiIV)} = 13.9 \pm 0.07$.

The parameter fits are listed in Table B.8 and the corresponding Voigt profile fits are shown in Fig. B.8.

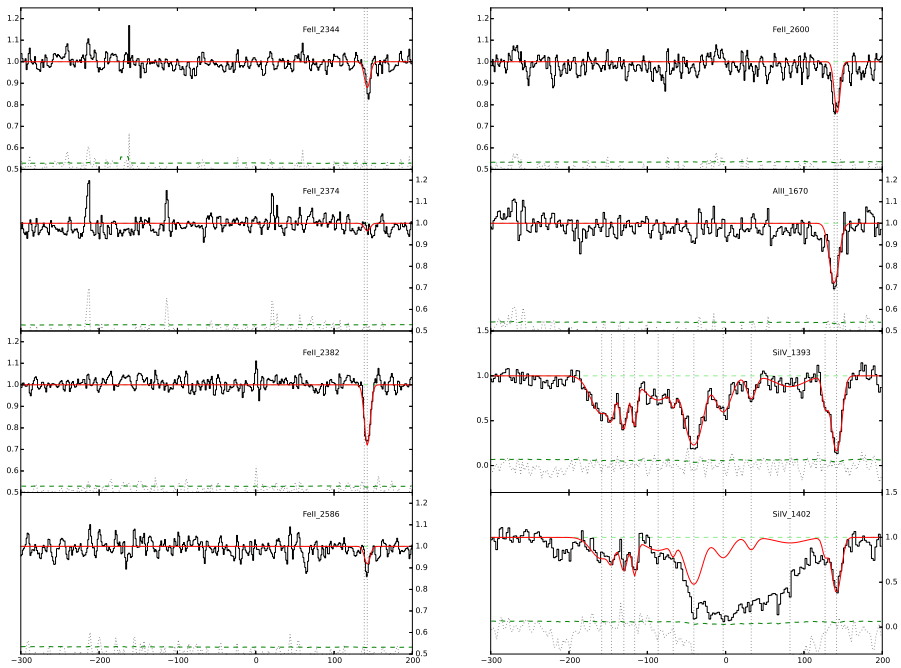

Figure B.8.: QSOJ0427-1302 $z_{abs} = 1.562$

B.2.9. QSO PKS0454-220 $z_{em} = 0.534$, $z_{abs} = 0.474$, $\log N(HI) = 19.45 \pm 0.03$

This low-redshift absorption system contains a great number of transitions including three MnII lines: MnII $\lambda\lambda\lambda$ 2576, 2594, 2606, and seven FeII lines (four of which are saturated): FeII $\lambda\lambda\lambda\lambda\lambda\lambda\lambda$ 2249, 2260, 2374, 2344, 2382, 2586 and 2600. It is interesting to notice the presence of a component in the blue part of the saturated lines which is not detected in the weaker transitions. Therefore, the fit is performed in two separate steps: on one hand the unsaturated lines are used to constrain the strongest components, on the other hand, this solution is applied to the saturated profiles to check its validity and to constrain the blue component. The absorption profile results in a total of seven components (five strong components as well as one blue and one red additional weaker components), spread in a velocity range of about 150 km/s. The column densities derived are $\log$ N(FeII)$=14.71 \pm 0.01$ and $\log$ N(MnII)$=12.58 \pm 0.01$.

In this EUADP spectrum, no high-ionisation transitions are covered for this low-redshift absorber.

Table B.9.: Voigt profile fit parameters to the low-ionization species for the z_{abs}=0.474 log N(H I)=19.45 ± 0.03 absorber towards QSO PKS 0454-220.

Comp.	z_{abs}	b km s^{-1}	Ion	log N cm^{-2}
1	0.47405	14.3 ± 0.6	FeII	12.39 ± 0.02
			MnII	11.12 ± 0.07
2	0.47422	14.5 ± 0.2	FeII	13.38 ± 0.01
			MnII	11.46 ± 0.03
3	0.47432	4.0 ± 0.1	FeII	14.00 ± 0.02
			MnII	11.65 ± 0.02
4	0.47439	10.0 ± 0.2	FeII	14.26 ± 0.01
			MnII	12.09 ± 0.01
5	0.47448	18.5 ± 0.2	FeII	14.12 ± 0.01
			MnII	12.03 ± 0.01
6	0.47466	6.5 ± 0.1	FeII	13.81 ± 0.01
			MnII	11.48 ± 0.04
7	0.47468	14.9 ± 0.3	FeII	13.11 ± 0.04
			MnII	11.50 ± 0.06

The parameter fits are summarised in Table B.9 and Voigt profile fits are shown in Fig. B.9.

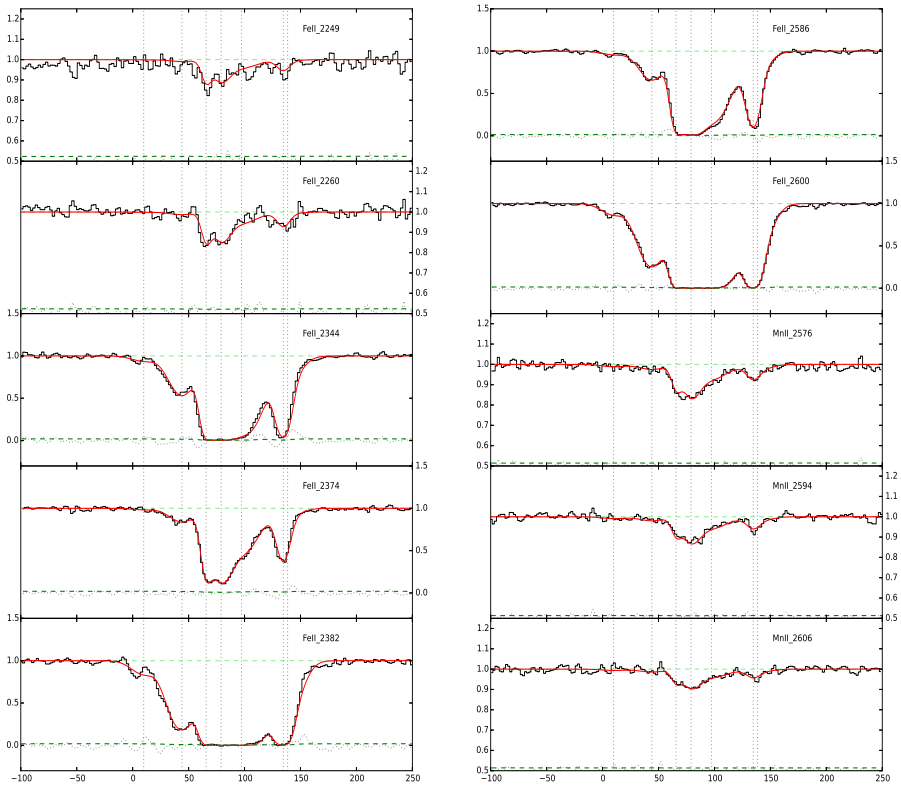

Figure B.9.: QSOPKS0454-220 $z_{abs} = 0.474$

B.2.10. QSOJ0600-5040 $z_{em} = 3.13$, $z_{abs} = 2.149$, $\log N(HI) = 20.4 \pm 0.12$

The EUADP spectrum for this absorber covers many low-ionization transitions including FeII $\lambda\lambda$ 1608, 1611, AlII λ 1670, SiII $\lambda\lambda\lambda$ 1193, 1526, 1304, 1808, ZnII λ 2062, CrII $\lambda\lambda$ 2062, 2026, NiII $\lambda\lambda\lambda$ 1709, 1741 and 1751. The absorption profile is clearly multi-component and covers a large velocity range of about 100 km/s based on the strongest transitions (namely AlII λ 1670, FeII λ 1608, SiII $\lambda\lambda\lambda$ 1193, 1526 and 1304). The profile is well fitted with four components. This velocity profile is then applied to the weakest ZnII λ 2026 line. It reveals a blend in the first two components related to the CrII λ 2062 line which is therefore fitted simultaneously. The AlII λ 1670 line is saturated, leading to a lower limit estimate in the column density of $\log N(AlII) > 14.33$ based on the

four component profile (redshifts and Doppler parameters) described above. The AlIII $\lambda\lambda$ 1854 and 1862 profiles follow the low-ionization ions. However, a blend in AlIII λ 1854 complicates the fit so that the velocity of the first component is fixed to the value derived above. The resulting column densities are: $\log$ N(FeII)$=14.84 \pm 0.03$, $\log$ N(SiII)$=15.08 \pm 0.01$, $\log$ N(NiII)$=13.62 \pm 0.02$, $\log$ N(CrII)$=13.10 \pm 0.01$, $\log$ N(ZnII)$=12.11 \pm 0.03$ and $\log$ N(AlIII)$=12.78 \pm 0.01$.

In this EUADP spectrum, the high-ionization ions SiIV $\lambda\lambda$ 1393, 1402, and CIV $\lambda\lambda$ 1548 and 1550 are covered but are located in the forest, and hence suffer from important blending.

The parameter fits are summarized in Table B.10 and Voigt profile fits are shown in Fig. B.10.

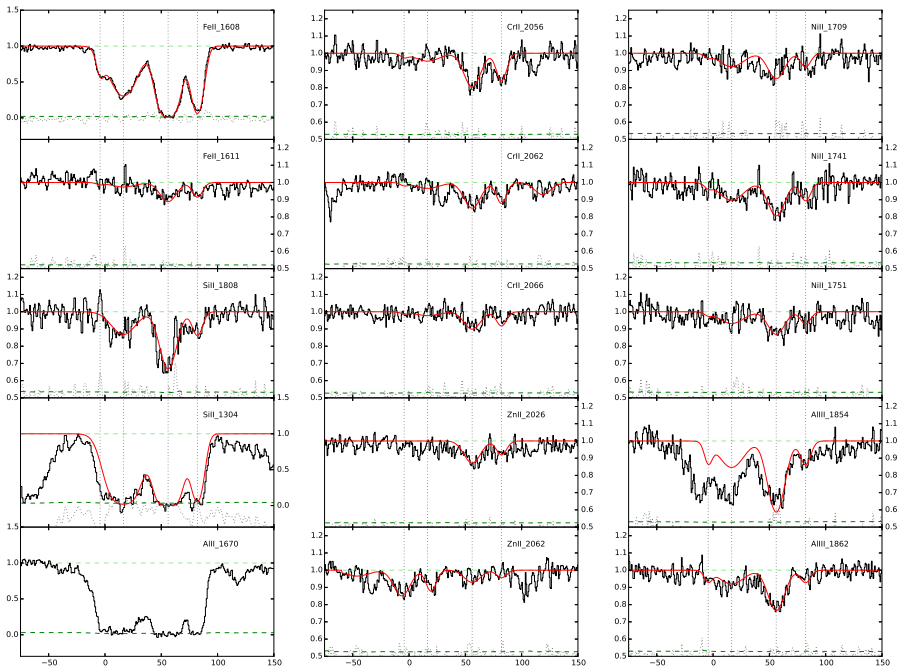

Figure B.10.: QSOJ0600-5040 $z_{abs} = 2.149$

B.2.11. QSO B1036-2257 $z_{em} = 3.13$, $z_{abs} = 2.533$, $\log N(HI) = 19.3 \pm 0.10$

A large number of low-ionisation elements are detected in the EUADP spectrum including SiII $\lambda\lambda\lambda\lambda$ 1190, 1193, 1260, 1526, CII $\lambda\lambda$ 1036, 1334, MgII $\lambda\lambda$ 2803 and 2796, AlII λ 1670, AlIII λ 1862 and FeII $\lambda\lambda$ 2382, 2600. Based on the SiII

Table B.10.: Voigt profile fit parameters to the low- and intermediate-ionization species for the z_{abs}=2.533 log N(H I)=20.4 ± 0.12 absorber towards QSO J060008.1-504036.

Comp.	z_{abs}	b km s^{-1}	Ion	log N cm^{-2}
1	2.14895	2.2 ± 0.7	FeII	13.22 ± 0.04
			SiII	–
			NiII	12.06 ± 0.18
			CrII	11.50 ± 0.22
			ZnII	–
			AlIII	11.60 ± 0.02
			AlII	> 14.2
2	2.14917	14.1 ± 0.4	FeII	14.1 ± 0.01
			SiII	14.55 ± 0.02
			NiII	13.16 ± 0.03
			CrII	12.33 ± 0.06
			ZnII	–
			AlIII	12.20 ± 0.01
			AlII	> 13.1
3	2.14959	9.1 ± 0.3	FeII	14.58 ± 0.01
			SiII	14.84 ± 0.01
			NiII	13.29 ± 0.02
			CrII	12.83 ± 0.01
			ZnII	11.97 ± 0.03
			AlIII	12.54 ± 0.01
			AlII	> 13.50
4	2.14986	4.7 ± 0.3	FeII	14.26 ± 0.06
			SiII	14.21 ± 0.03
			NiII	12.81 ± 0.04
			CrII	12.54 ± 0.02
			ZnII	11.56 ± 0.06
			AlIII	11.79 ± 0.02
			AlII	> 13.10

$\lambda\lambda$ 1193 and 1260 lines which are free from any saturation and blending, eleven components are used to fit the absorption profile. The low-ionization transitions for this system cover a large velocity range of about 200 km/s. The strongest components of this profile are used to fit AlII λ 1670, FeII $\lambda\lambda$ 2600, 2382 and AlIII λ 1862. The resulting column densities are $\log$ N(SiII)$=13.64 \pm 0.01$, $\log$ N(AlII)$=12.52 \pm 0.01$, $\log$ N(AlIII)$=12.89 \pm 0.02$ and $\log$ N(FeII)$=12.93 \pm 0.01$. The profile estimated from the weakest transition is then used to fit the saturated CII λ 1334 revealing a $12^{\rm th}$ component around $v = 0$ km/s. A manual fit using CII $\lambda\lambda$ 1036 and 1334 and the previous solution provides the following lower limit for CII $\log \mathrm{N(CII)} > 15.98$. Nevertheless, both lines are contaminated with unrelated absorbers, which prevents us from deriving a robust estimate of the lower limit in CII.

A great number of high-ionization lines are detected in this EUADP spectra including OVI $\lambda\lambda$ 1031, 1037, NV $\lambda\lambda$ 1238, 1242, CIV $\lambda\lambda$ 1548, 1550, SiIV $\lambda\lambda$ 1393 and 1402. A number of these lines are located in the Lyman-α forest (SiIV doublet, NV λ1242 and OVI λ 1031) and therefore appear to be blended. The CIV doublet is saturated in this case, such that only a lower limit is derived. Only the OVI λ 1037 and NV λ 1238 lines appear free from any saturation or blending, preventing from performing a reasonable fit. A three-component profile is used to fit SiIV λ 1393. The resulting component velocities and Doppler parameters are then used to fit the other lines available. The resulting column densities are $\log$ N(SiIV)$=13.71 \pm 0.01$, $\log$ N(CIV)> 17.42.

The parameter fits of the individual components are listed in Table B.11 and the corresponding Voigt profile fits are shown in Fig. B.11.

Table B.11.: Voigt profile fit parameters to the low- and high-ionization species for the $z_{\rm abs}$=2.533 log N(H I)$=19.30 \pm 0.10$ absorber towards QSO B1036-2257.

Comp.	z_{abs}	b	Ion	log N
1	2.53132	5.4 ± 0.1	SiII	13.19 ± 0.01
			FeII	12.65 ± 0.01
			AlII	12.16 ± 0.01
			MgII	13.20 ± 0.04
			CII	14.00
2	2.53152	11.3 ± 0.4	SiII	12.87 ± 0.03
			FeII	$-$
			AlII	11.77 ± 0.03
			MgII	12.71 ± 0.03
			CII	13.81 ± 0.01
3	2.53178	2.2 ± 0.2	SiII	11.80 ± 0.10
			FeII	$-$

Continued on next page

Table B.11 – *Continued from previous page*

Comp.	z_{abs}	b	Ion	log N
			AlII	11.14 ± 0.03
			MgII	11.49 ± 0.21
			CII	12.7
4	2.53197	2.1 ± 0.2	SiII	12.47 ± 0.06
			FeII	–
			AlII	11.32 ± 0.02
			MgII	12.37 ± 0.06
			CII	13.60
5	2.53220	4.3 ± 2.1	SiII	11.49 ± 0.13
			FeII	–
			AlII	–
			MgII	11.19 ± 0.43
			CII	13.00
6	2.53248	5.3 ± 0.9	SiII	12.09 ± 0.04
			FeII	–
			AlII	–
			MgII	12.11 ± 0.07
			CII	14.00
7	2.53275	7.8 ± 2.3	SiII	11.95 ± 0.05
			FeII	–
			AlII	–
			MgII	11.27 ± 0.48
			CII	> 15.90
8	2.53291	7.1 ± 1.5	SiII	12.09 ± 0.04
			FeII	–
			AlII	–
			MgII	12.11 ± 0.07
			CII	> 15.00
9	2.53313	4.0 ± 2.0	SiII	11.60 ± 0.04
			FeII	–
			AlII	–
			MgII	12.14 ± 0.06
			CII	> 14.30
10	2.53332	5.6 ± 0.3	SiII	12.65 ± 0.01
			FeII	12.31 ± 0.01
			AlII	–
			MgII	12.52 ± 0.04
			CII	13.8
11	2.53356	5.9 ± 0.7	SiII	12.32 ± 0.03
			FeII	–

Continued on next page

Table B.11 – *Continued from previous page*

Comp.	z_{abs}	b	Ion	log N
			AlII	11.42 ± 0.02
			MgII	12.35 ± 0.04
			CII	13.55
12	2.53382	5.0 ± 0.2	SiII	12.82 ± 0.01
			FeII	12.30 ± 0.01
			AlII	11.80 ± 0.01
			MgII	12.58 ± 0.03
			CII	13.70
1	2.53143	12.9 ± 0.6	CIV	12.97 ± 0.02
			SiIV	12.83 ± 0.02
2	2.53158	7.8 ± 0.4	CIV	12.98 ± 0.02
			SiIV	12.74 ± 0.02
3	2.53192	11.6 ± 0.8	CIV	12.83 ± 0.02
			SiIV	12.32 ± 0.04
4	2.53294	13.2 ± 2.5	CIV	13.9 ± 0.01
			SiIV	12.91 ± 0.01
5	2.53314	6.0 ± 2.3	CIV	> 13.85
			SiIV	12.78 ± 0.02
6	2.53340	5.4 ± 4.4	CIV	> 16.57
			SiIV	12.98 ± 0.01
7	2.53358	3.0 ± 2.6	CIV	> 17.35
			SiIV	13.15 ± 0.01

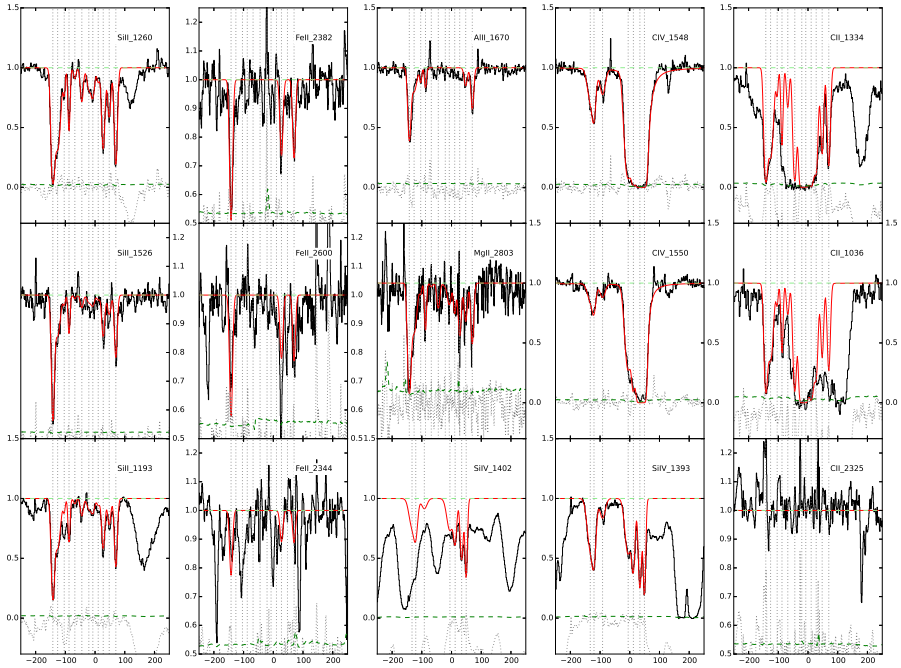

Figure B.11.: QSOB1036-2257 $z_{abs} = 2.533$

B.2.12. QSO J115538.6+053050 $z_{em} = 3.475$, $z_{abs} = 3.327$, $\log N(HI) = 21.0 \pm 0.10$

Many ions are detected in this absorber, such as SiII λ 1808, SII $\lambda\lambda\lambda$ 1259 1253 1250, AlIII $\lambda\lambda$ 1854 1862, NiII $\lambda\lambda$ 1370 1317, CIV $\lambda\lambda$ 1548 1550 and SiIV $\lambda\lambda$ 1393 and 1402. The low- and intermediate-ionization ions show a similar profile (strong absorption line near $v = 65$ km/s) and are therefore fitted together with a 7-component profile. Only the non-saturated lines, NiII $\lambda\lambda$ 1370 1317, SiII λ 1808 and SII λ 1253 are used in the derivation of the parameter. The ions AlII λ 1670, CII $\lambda\lambda$ 1036 and 1334 are also detected but not fitted due to strong saturation. AlIII have not been fitted due to a blend in the AlIII λ 1862 line. The resulting abundances for the low-ionization ions are $\log$ N(SiII)$=15.93 \pm 0.01$, $\log$ N(SII)$=15.31 \pm 0.01$ and $\log$ N(NiII)$=13.74 \pm 0.01$. A non-detection from MgI λ 1827 gives the following upper limit: $\log N(\mathrm{MgI}) < 13.33$.

The high-ionization ions CIV $\lambda\lambda$ 1548 1550 and SiIV $\lambda\lambda$ 1402 are fitted using a 3-component profile, extending to about 200 km/s. SiIV λ 1393 is not considered for the fit as it is blended blueward the bluest component of the fit ($v \sim 150$

km/s). This gives the following abundances for the high-ionization transitions: log N(CIV)=13.71 ± 0.01 and log N(SiIV)=13.56 ± 0.01. We note that, although the reddest components for both low- and high-ionization profiles have velocities that differ by about 20 km/s, they both stand out from the bluer absorption profile.

The parameter fits of the individual components are listed in Table B.12 and the corresponding Voigt profile fits are shown in Fig. B.12.

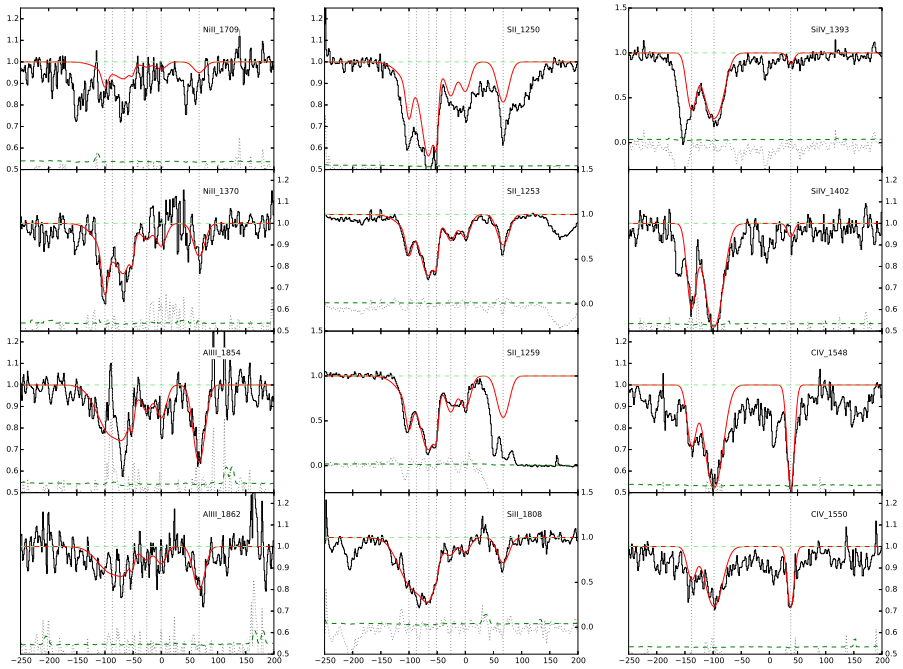

Figure B.12.: QSOJ115538.6+053050 $z_{abs} = 3.327$

B.2.13. QSO LBQS 1232+0815 $z_{em} = 2.57$, $z_{abs} = 1.72$, $\log N(HI) = 19.48 \pm 0.13$

The EUADP spectrum for this DLA absorber covers the following low- and intermediate-ionization transitions: FeII $\lambda\lambda\lambda\lambda$ 2382, 2374, 2344, 1608, AlIII $\lambda\lambda$ 1862, 1854, SiII $\lambda\lambda$ 1526 (blended) and 1808. It also covers CII λ 1334, which is saturated. The low- and intermediate-ionization profiles are well fitted together with the transitions FeII $\lambda\lambda$ 2382, 2344, AlIII $\lambda\lambda$ 1854, 1862 and SiII λ 1808 using 6 components spread over $\sim$ 200 km/s, resulting in the following abundances log N(FeII)=13.50 ± 0.01, log N(SiII) = 14.41 ± 0.01 and log N(AlIII)=13.28 ± 0.01.

Table B.12.: Voigt profile fit parameters to the low- and high-ionization species for the z_{abs}=3.327 log N(H I)=21.0 ± 0.10 absorber towards QSO J115538.6+053050.

Comp.	z_{abs}	b km s^{-1}	Ion	log N cm^{-2}
1	3.32555	5.9 ± 0.1	NiII	12.84 ± 0.01
			SII	14.14 ± 0.01
			SiII	–
			AlIII	–
2	3.32575	33.8 ± 0.1	NiII	13.35 ± 0.01
			SII	14.66 ± 0.01
			SiII	15.72 ± 0.01
			AlIII	12.77 ± 0.01
3	3.32606	13.6 ± 0.1	NiII	12.88 ± 0.01
			SII	14.83 ± 0.01
			SiII	15.20 ± 0.01
			AlIII	11.96 ± 0.01
4	3.32626	2.0 ± 0.1	NiII	12.27 ± 0.02
			SII	14.16 ± 0.02
			SiII	13.96 ± 0.03
			AlIII	11.55 ± 0.04
5	3.32663	10.7 ± 0.2	NiII	12.48 ± 0.01
			SII	14.27 ± 0.01
			SiII	14.55 ± 0.01
			AlIII	11.94 ± 0.02
6	3.32700	11.6 ± 0.1	NiII	12.71 ± 0.01
			SII	14.25 ± 0.01
			SiII	14.57 ± 0.01
			AlIII	12.12 ± 0.01
7	3.32797	13.2 ± 0.1	NiII	12.93 ± 0.01
			SII	14.45 ± 0.01
			SiII	14.89 ± 0.01
			AlIII	12.60 ± 0.01
1	3.32500	10	CIV	12.9 ± 0.02
			SiIV	13.00 ± 0.01
2	3.32558	20	CIV	13.48 ± 0.02
			SiIV	13.40 ± 0.01
3	3.32755	7	CIV	13.10 ± 0.01
			SiIV	12.00 ± 0.02

Table B.13.: Voigt profile fit parameters to the low–ionization species for the z_{abs}=1.72 log N(H I)=19.48 ± 0.13 absorber towards QSO LBQS 1232+0815.

Comp.	z_{abs}	b km s^{-1}	Ion	log N cm^{-2}
1	1.71942	7.7 ± 0.1	FeII	13.17 ± 0.01
			AlIII	12.61 ± 0.01
			SiII	14.10 ± 0.01
2	1.71958	4.6 ± 0.4	FeII	12.15 ± 0.02
			AlIII	11.96 ± 0.02
			SiII	13.20 ± 0.02
3	1.71995	8.2 ± 0.6	FeII	12.07 ± 0.03
			AlIII	12.04 ± 0.02
			SiII	13.06 ± 0.02
4	1.72014	8.8 ± 0.1	FeII	13.02 ± 0.01
			AlIII	12.90
			SiII	14.01 ± 0.01
5	1.72036	7.1 ± 0.3	FeII	12.16 ± 0.02
			AlIII	12.37 ± 0.01
			SiII	–
6	1.72094	18.3 ± 0.6	FeII	12.33 ± 0.02
			AlIII	12.41 ± 0.01
			SiII	–
1	1.71946	23.3 ± 0.3	SiIV	13.47 ± 0.01
2	1.72008	14.5 ± 0.5	SiIV	> 14.50
3	1.72032	14.2 ± 0.5	SiIV	> 13.82
4	1.72089	10.5 ± 0.3	SiIV	13.49 ± 0.01
5	1.72104	27.8 ± 0.6	SiIV	13.41 ± 0.01

We derived upper limits from non detection for SII λ 1253, $\log \mathrm{N(SII)} < 14.18$, CrII λ 2056, $\log \mathrm{N(CrII)} < 12.38$, MgI λ 2026, $\log \mathrm{N(MgI)} < 12.21$, NiII λ 1751, $\log \mathrm{N(NiII)} < 13.05$, and ZnII λ 2026, $\log \mathrm{N(ZnII)} < 11.58$.

The high-ionization ions detected in the spectrum are SiIV $\lambda\lambda$ 1393, 1402, CIV $\lambda\lambda$ 1548 and 1550. The CIV transition lines are highly saturated and contaminated by an apparent blend, they are therefore not consider for the fit. From the less saturated SiIV transition lines, a 5-component profile provides the following lower limit $\log \mathrm{N(SiIV)} > 14.67$. We notice that the low- and high-ionization ions seem to share the same components.

The parameter fits of the individual components are listed in Table B.13 and the corresponding Voigt profile fits are shown in Fig. B.13.

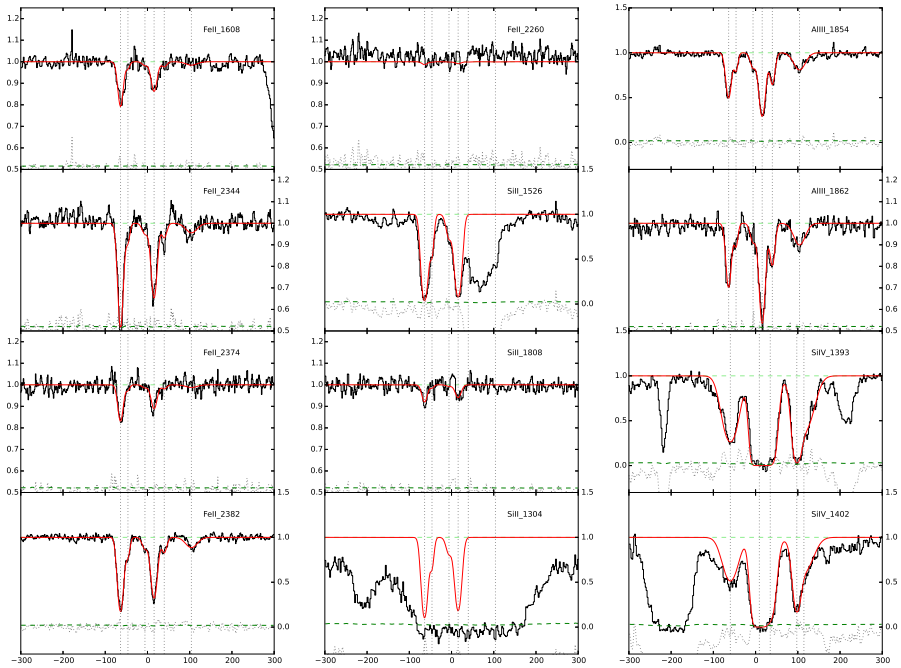

Figure B.13.: QSOLBQS1232+0815 $z_{abs} = 1.72$

B.2.14. QSO J1330-2522 $z_{em} = 3.91$, $z_{abs} = 2.654$, $\log N(HI) = 19.56 \pm 0.13$

This EUADP spectrum covers six ions, SiIV $\lambda\lambda$ 1393, 1402, SiII λ 1526, AlII λ 1670, AlIII $\lambda\lambda$ 1854 and 1862. Many of these transitions are blended and/or saturated, such that only AlII λ 1670 and AlIII λ 1854 have been fitted. The asymmetry of both lines suggests a 2-component profile, resulting in the following abundances: $\log$ N(AlIII)$=12.62\pm0.02$ and $\log$ N(AlII)$=12.18\pm0.2$. We derive an upper limit from non detection of NiII λ 1741: $\log N(\mathrm{NiII}) < 13.22$.

In this spectrum, the high-ionization ions SiIV $\lambda\lambda$ 1393, 1402 and CIV $\lambda\lambda$ 1548 and 1550 are covered but suffer from severe blending, such that no fit has been performed.

The parameter fits of the individual components are listed in Table B.14 and the corresponding Voigt profile fits are shown in Fig. B.14.

Table B.14.: Voigt profile fit parameters to the low- and intermediate-ionization species for the z_{abs}=2.654 log N(H I)=19.56 $\pm$ 0.13 absorber towards QSO J1330-2522.

Comp.	z_{abs}	b km s^{-1}	Ion	log N cm^{-2}
1	2.65414	6.7	AlII	12.16 ± 0.02
			AlIII	12.55 ± 0.02
2	2.65433	2.0	AlII	10.90 ± 0.21
			AlIII	11.79 ± 0.08

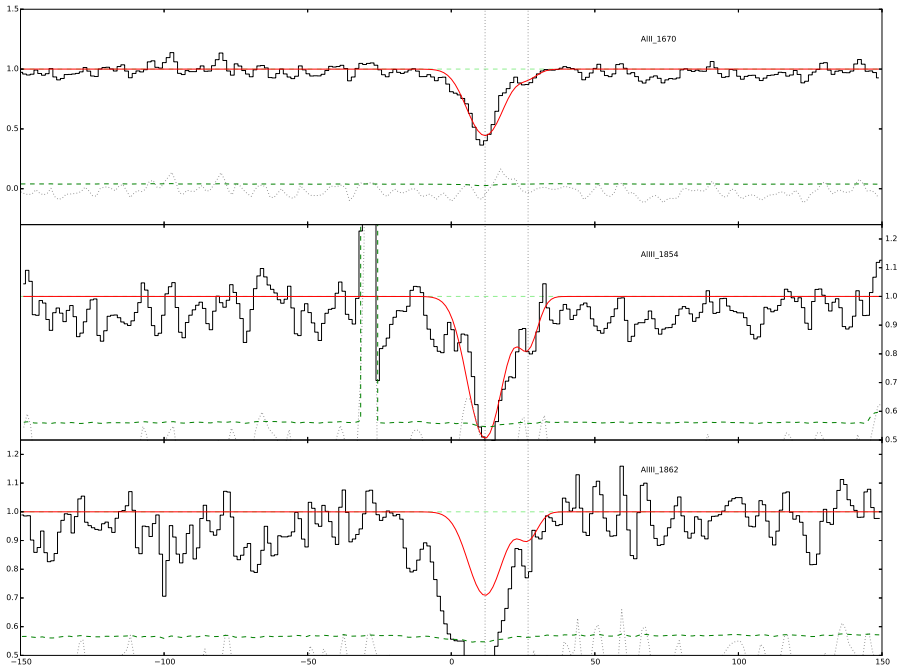

Figure B.14.: QSOJ1330-2522 $z_{abs} = 2.654$

B.2.15. QSO J1356-1101 $z_{em} = 3.006$, $z_{abs} = 2.397$, $\log N(HI) = 19.85 \pm 0.08$

The spectrum covers four FeII lines and two SiIV lines associated with the absorber: FeII $\lambda\lambda\lambda\lambda$ 2600 2344 2382 2586 and SiIV $\lambda\lambda$ 1393 and 1402. The low-

Table B.15.: Voigt profile fit parameters to the low-ionization species for the z_{abs}=2.397 log N(H I)=19.85 ± 0.08 absorber towards QSO J1356-1101.

Comp.	z_{abs}	b km s^{-1}	Ion	log N cm^{-2}
1	2.39339	11.0 ± 0.3	FeII	12.81 ± 0.01
2	2.39621	14.8 ± 1.4	FeII	11.99 ± 0.08
3	2.39629	4.5 ± 0.3	FeII	12.44 ± 0.02
4	2.39669	61.1 ± 5.4	FeII	12.63 ± 0.04
5	2.39677	5.8 ± 0.1	FeII	12.95 ± 0.01
6	2.39706	2.4 ± 0.3	FeII	12.44 ± 0.02
7	2.39714	2.6 ± 0.6	FeII	12.10 ± 0.02

ionization profile is well fitted with a 6-component profile in the red, and a single blue component isolated from the red group of components by about 250km/s. The resulting column density is $\log \mathrm{N(FeII)} = 13.44 \pm 0.01$. We derived upper limits from the non-detection of several transitions: CrII λ 2056, $\log \mathrm{N(CrII)} < 12.64$, MnII λ 2576, $\log \mathrm{N(MnII)} < 12.07$, NiII λ 1317, $\log \mathrm{N(NiII)} < 12.76$, and ZnII λ 2062, $\log \mathrm{N(ZnII)} < 12.38$.

The high-ionization ion SiIV $\lambda\lambda$ 1393 and 1402 is detected but not fitted because it is heavily saturated.

The parameter fits of the individual components are listed in Table B.15 and the corresponding Voigt profile fits are shown in Fig. B.15.

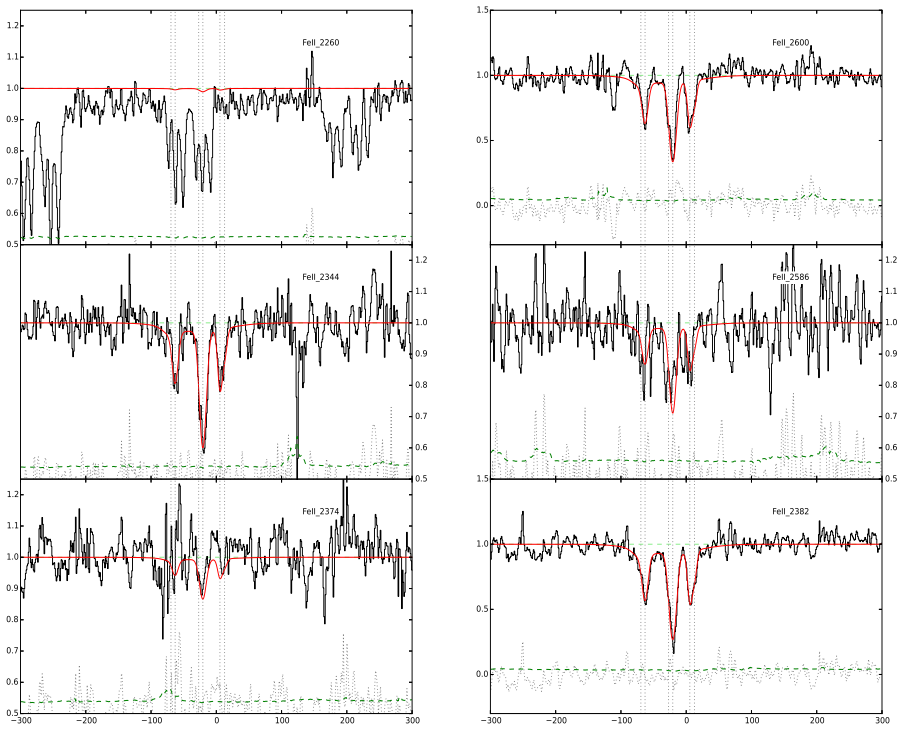

Figure B.15.: QSOJ1356-1101 $z_{abs} = 2.397$

B.2.16. QSO J1621-0042 $z_{em} = 3.7$, $z_{abs} = 3.104$, $\log N(HI) = 19.7 \pm 0.20$

The EUADP spectrum probing this high-redshift subDLA covers many transitions associated with the absorber such as FeII $\lambda\lambda$ 1608, 1611, CII $\lambda\lambda$ 1036, 1334, SII $\lambda\lambda\lambda$ 1250, 1253, 1259, SiII $\lambda\lambda\lambda\lambda\lambda$ 1190, 1193, 1260, 1304, 1526, SiIV $\lambda\lambda$ 1393, 1402 (partly), CIV $\lambda\lambda$ 1548 and 1550. Most of these lines are heavily blended (SiII $\lambda\lambda\lambda$ 1190, 1304, 1260) or saturated (CII $\lambda\lambda$ 1334 and 1036), but the wide coverage and SNR of the spectrum provide enough elements to derive the different parameters.

The low-ionization ions are fitted with a 12-component profile, with a broad velocity range (about 400 km/s). The component with the highest velocity ($v \sim 400$ km/s) is identified in three transitions: SiII $\lambda\lambda$ 1190 and CII λ 1334. The low velocity components are less affected by the blending and are therefore well fitted, but the information about the group of component between $v \sim 100$ km/s

and $\mathrm{v} \sim 250$ km/s are only derived from FeII λ 1608 and SiII λ 1526. For CII in particular, this group of component is saturated so that a lower limit is derived based on the low velocity components $\log \mathrm{N(CII)} < 14.41$. The SII line is most probably blended as its profile does not match the other low-ionization ions. The resulting abundances for the low-ionization ions are $\log \mathrm{N(FeII)} = 13.30 \pm 0.04$ and $\log \mathrm{N(SiII)} = 13.78 \pm 0.03$.

The high-ionization ion components are also detected with a broad velocity range (400km/s). The EUADP spectrum does not fully cover the SiIV λ 1402 transition, thus preventing a proper fit. However, the blue part of SiIV λ 1402 matches the blue parts of SiIV λ 1393 and the CIV lines, confirming the detection of SiIV and CIV. It is interesting to note that in this case no satisfactory solutions could be found to fit simultaneously the SiIV and CIV doublets. To check the wavelength calibration of the spectrum, the SiII $\lambda\lambda$ 1526 and 1190 lines (which fall on two different arm of the spectrograph) are fitted independently. The redshifts determined for these transitions are consistent with each other ($\mathrm{z} = 3.10408$ and $\mathrm{z} = 3.10409$) thus indicating no systematic shift in the spectrum. Therefore, the SiIV and CIV transitions are fitted separately, with different Doppler parameters and velocities as seen in Table B.16. The 14-component fit results in $\log \mathrm{N(SiIV)} = 14.24 \pm 0.03$ and $\log \mathrm{N(CIV)} = 14.71 \pm 0.01$.

The parameter fits of the individual components are listed in Table B.16 and the corresponding Voigt profile fits are shown in Fig. B.16.

Table B.16.: Voigt profile fit parameters to the low- and high-ionization species for the z_{abs}=3.104 log N(H I)=19.7 ± 0.20 absorber towards QSO J1621-0042.

Comp.	z_{abs}	b km s^{-1}	Ion	log N cm^{-2}	Comp.	z_{abs}	b km s^{-1}	Ion	log N cm^{-2}
1	3.10394	3.7 ± 0.7	FeII	12.62 ± 0.06	1	3.10509	7.0 ± 1.0	SiIV	12.77 ± 0.07
			SiII	12.95 ± 0.03		3.10541	24.6 ± 1.0	CIV	13.49 ± 0.21
			CII	13.90 ± 0.03	2	3.10530	7.9 ± 3	SiIV	12.69 ± 0.18
2	3.10407	2.7 ± 0.5	FeII	13.03 ± 0.04		3.10539	6.4 ± 3.4	CIV	12.13 ± 0.21
			SiII	13.55 ± 0.03	3	3.10564	12.0 ± 2.8	SiIV	13.47 ± 0.09
			CII	14.00 ± 0.17		3.10568	8.5 ± 1.0	CIV	13.16 ± 0.05
3	3.10415	8.4 ± 2	FeII	12.32 ± 0.19	4	3.10588	6.1 ± 1.9	SiIV	13.40 ± 0.12
			SiII	12.93 ± 0.15		3.10592	9.0 ± 0.6	CIV	13.64 ± 0.04
			CII	13.57 ± 0.02	5	3.10607	7.5 ± 1.7	SiIV	13.52 ± 0.09
4	3.10438	6.0 ± 1.1	FeII	12.28 ± 0.11		3.10612	7.9 ± 0.6	CIV	13.69 ± 0.05
			SiII	12.73 ± 0.06	6	3.10631	8.1 ± 1.5	SiIV	13.16 ± 0.10
			CII	13.47 ± 0.01		3.10632	8.6 ± 0.5	CIV	13.36 ± 0.05
5	3.10462	7.3 ± 1.4	FeII	11.95 ± 0.21	7	3.10657	15.0 ± 1.6	SiIV	13.10 ± 0.06
			SiII	12.37 ± 0.06		3.10659	21.5 ± 0.7	CIV	13.70 ± 0.02
			CII	13.00 ± 0.01	8	3.10709	9.3 ± 1.2	SiIV	12.51 ± 0.04
6	3.10523	6.1 ± 0.13	FeII	13.28 ± 0.01		3.10712	12.1 ± 0.4	CIV	13.24 ± 0.02
			SiII	13.74 ± 0.01	9	3.10742	7.9 ± 1.1	SiIV	12.40 ± 0.04
			CII	–		3.10746	9.3 ± 0.4	CIV	12.95 ± 0.02
7	3.10563	7.9 ± 0.23	FeII	13.16 ± 0.02	10	3.10780	6.0 ± 0.6	SiIV	12.50 ± 0.02
			SiII	13.73 ± 0.03		3.10785	12.2 ± 0.2	CIV	13.27 ± 0.01
			CII	–	11	3.10836	6.5 ± 0.7	SiIV	12.61 ± 0.03
8	3.10593	20.0 ± 1.08	FeII	13.07 ± 0.05		3.10842	10.4 ± 0.2	CIV	13.63 ± 0.01
			SiII	13.73 ± 0.03	12	3.10859	5.7 ± 1.2	SiIV	12.49 ± 0.07
			CII	–		3.10865	5.5 ± 0.3	CIV	13.43 ± 0.02
9	3.10601	5.0	FeII	13.10 ± 0.02	13	3.10883	10.6 ± 2.1	SiIV	12.53 ± 0.07
			SiII	13.66 ± 0.02		3.10887	10.4 ± 0.3	CIV	13.76 ± 0.01
			CII	–	14	3.10922	7.5 ± 0.3	SiIV	13.47 ± 0.03
10	3.10618	0.9 ± 0.2	FeII	–		3.10928	14.1 ± 0.1	CIV	14.12 ± 0.01
			SiII	13.39 ± 0.25					
			CII	–					
11	3.10743	6.1 ± 0.29	FeII	12.47 ± 0.06					
			SiII	12.93 ± 0.01					
			CII	–					
12	3.10926	2.5 ± 0.25	FeII	10.84 ± 1.99					
			SiII	12.77 ± 0.01					
			CII	–					

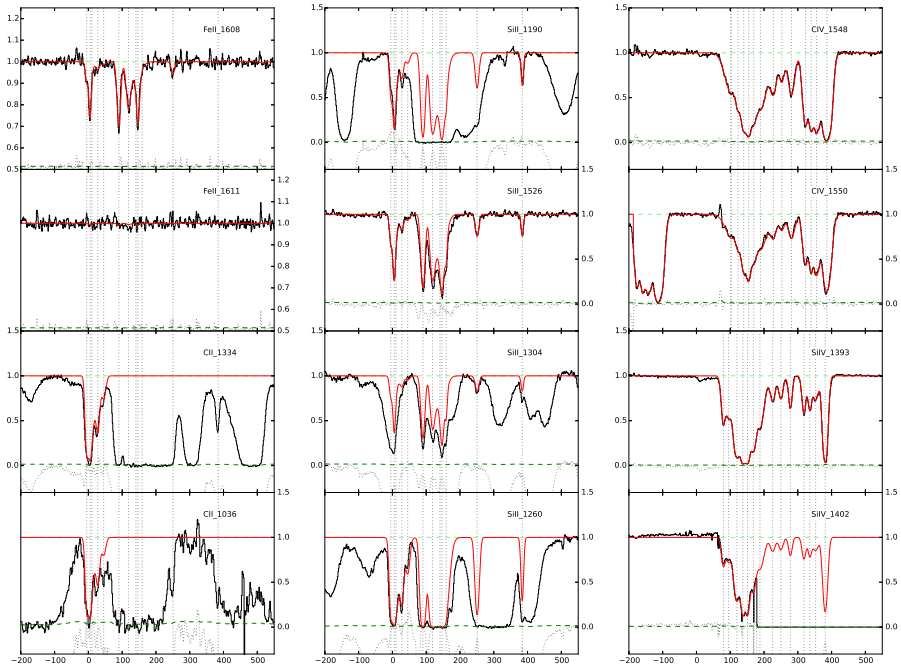

Figure B.16.: QSOJ1621-0042 $z_{abs} = 3.104$

B.2.17. QSO 4C12.59 $z_{em} = 1.792$, $z_{abs} = 0.531$, $\log N(HI) = 20.7 \pm 0.09$

This very low-redshift DLA absorber presents a few absorption features in the EUADP spectrum partly due the limited wavelength coverage and an overall low SNR. The FeII ion is detected in the following transitions FeII $\lambda\lambda\lambda$ 2344, 2382 and 2374. The FeII λ 2382 line is saturated. A satisfactory fit for the remaining transitions FeII $\lambda\lambda$ 2374 and 2344 is found with six components. The resulting column density is $\log N(\mathrm{FeII}) = 14.26 \pm 0.08$. The CII λ 2325 line is covered but not detected. The resulting upper limit is $\log N(\mathrm{CII}) < 11.36$.

No high-ionization ions are covered in this EUADP spectrum.

The parameter fits of the individual components are listed in Table B.17 and the corresponding Voigt profile fits are shown in Fig. B.17.

Table B.17.: Voigt profile fit parameters to the low-ionization species for the z_{abs}=0.531 log N(H I)=20.7 ± 0.09 absorber towards QSO 4C 12.59.

Comp.	z_{abs}	b km s^{-1}	Ion	log N cm^{-2}
1	0.53123	7.0 ± 1.3	FeII	13.20 ± 0.08
2	0.53130	4.6 ± 1.4	FeII	13.58 ± 0.08
3	0.53135	4.0 ± 1.1	FeII	13.68 ± 0.10
4	0.53143	13.9 ± 4.1	FeII	13.59 ± 0.26
5	0.53143	6.8 ± 1.4	FeII	13.47 ± 0.28
6	0.53156	6.3 ± 1.8	FeII	13.06 ± 0.12

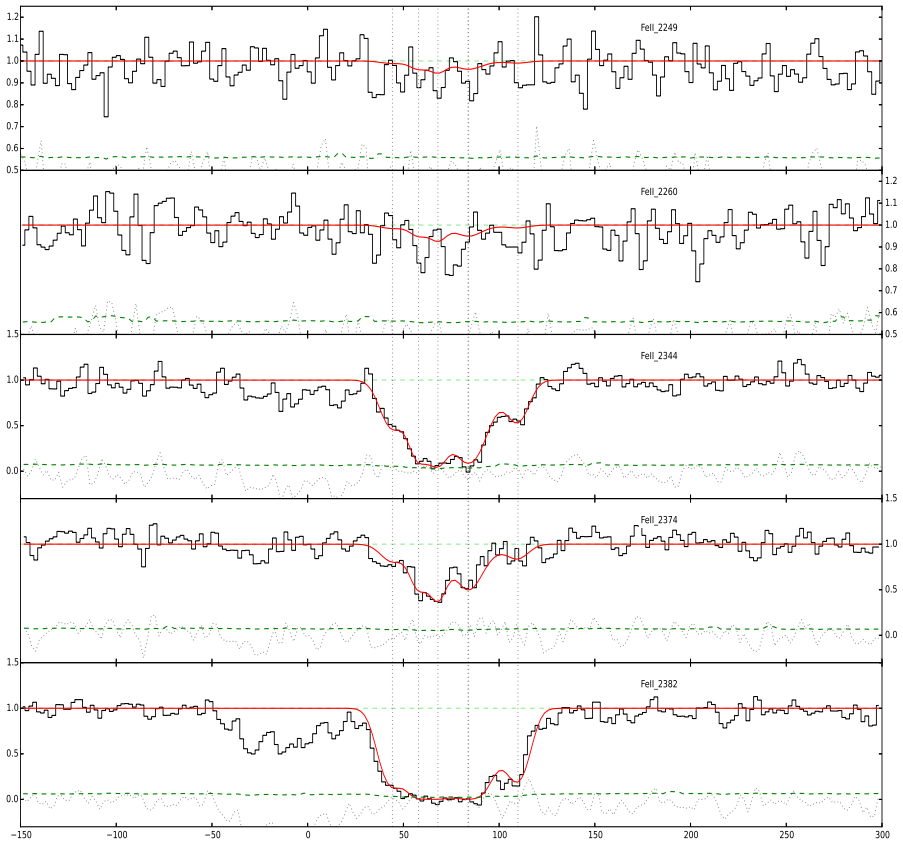

Figure B.17.: QSO4C12.59 $z_{abs} = 0.531$

B.2.18. QSO LBQS2114-4347 $z_{em} = 2.04$, $z_{abs} = 1.912$, $\log N(HI) = 19.5 \pm 0.10$

The EUADP spectrum of this quasar covers the following low-ionization ions: SiII $\lambda\lambda$ 1304 1526, MgII $\lambda\lambda$ 2796 2803, FeII $\lambda\lambda\lambda\lambda\lambda$ 2600 1608 2260 2344 2374 2586, AlII λ 1670 and CII λ 1334. An 11-component fit is used to describe the lines free from saturations and blends, namely SiII $\lambda\lambda$ 1526 1304 and FeII $\lambda\lambda\lambda$ 1608 2374 and 2586.

This results in the following column densities: $\log N(\mathrm{SiII}) = 14.39 \pm 0.02$, $\log N(\mathrm{FeII}) = 14.02 \pm 0.01$, $\log N(\mathrm{AlII}) = 13.00 \pm 0.01$ and $\log N(\mathrm{MgII}) = 14.40 \pm 0.01$. In addition, the non-detections in the spectrum provide further upper limits as follows: AlIII λ 1854, $\log N(\mathrm{AlIII}) < 12.09$, CrII λ 2056, $\log N(\mathrm{CrII}) < 12.77$, MnII λ 2576, $\log N(\mathrm{MnII}) < 12.24$, NiII λ 1317, $\log N(\mathrm{NiII}) < 12.88$, SII λ 1253, $\log N(\mathrm{SII}) < 13.97$, and ZnII λ 2026, $\log N(\mathrm{ZnII}) < 12.17$.

A 4-component profile is used to fit the high-ionization ions: CIV $\lambda\lambda$ 1548 1550 and SiIV $\lambda\lambda$ 1393 and 1402. The resulting column densities are $\log N(\mathrm{SiIV}) = 13.43 \pm 0.01$ and $\log N(\mathrm{CIV}) = 14.39 \pm 0.01$.

The parameter fits of the individual components are listed in Table B.18 and the corresponding Voigt profile fits are shown in Fig. B.18.

Table B.18.: Voigt profile fit parameters to the low- and high-ionization species for the z_{abs}=1.912 log N(H I)=19.5 ± 0.10 absorber towards QSO LBQS 2114-4347.

Comp.	z_{abs}	b	Ion	log N
1	1.9109296	6.7 ± 0.1	SiII	13.16 ± 0.03
			FeII	12.65 ± 0.01
			AlII	11.70 ± 0.02
			MgII	12.92 ± 0.01
2	1.9111506	3.0 ± 0.1	SiII	12.53 ± 0.01
			FeII	12.11 ± 0.01
			AlII	10.84 ± 0.01
			MgII	11.76 ± 0.01
3	1.9113052	4.6 ± 0.1	SiII	13.44 ± 0.01
			FeII	13.18 ± 0.01
			AlII	12.10 ± 0.01
			MgII	13.23 ± 0.01
4	1.91146	12.3 ± 0.1	SiII	12.96 ± 0.01
			FeII	–
			AlII	11.66 ± 0.01
			MgII	12.53 ± 0.01
5	1.91148	3.7 ± 0.1	SiII	12.79 ± 0.04

Continued on next page

Table B.18 – *Continued from previous page*

Comp.	z_{abs}	b	Ion	log N
			FeII	12.38 ± 0.01
			AlII	11.75 ± 0.01
			MgII	12.69 ± 0.01
6	1.91165	5.5 ± 0.1	SiII	13.00 ± 0.03
			FeII	12.30 ± 0.01
			AlII	11.43 ± 0.02
			MgII	12.55 ± 0.01
7	1.91185	4.1 ± 0.1	SiII	14.08 ± 0.02
			FeII	13.77 ± 0.01
			AlII	12.69 ± 0.01
			MgII	14.21 ± 0.01
8	1.91205	6.7 ± 0.1	SiII	13.37 ± 0.20
			FeII	12.88 ± 0.01
			AlII	11.73 ± 0.01
			MgII	13.12 ± 0.01
9	1.91221	4.0 ± 1.0	SiII	13.17 ± 0.02
			FeII	12.59 ± 0.01
			AlII	11.81 ± 0.01
			MgII	13.14 ± 0.01
10	1.91232	0.9 ± 0.1	SiII	12.25 ± 0.01
			FeII	12.41 ± 0.01
			AlII	10.91 ± 0.01
			MgII	13.08 ± 0.01
11	1.91252	6.3 ± 1.0	SiII	13.24 ± 0.02
			FeII	12.78 ± 0.01
			AlII	11.84 ± 0.01
			MgII	13.05 ± 0.01
1	1.91173	16.3 ± 0.3	CIV	14.19 ± 0.01
			SiIV	12.97 ± 0.01
2	1.91199	8.5 ± 0.3	CIV	13.63 ± 0.02
			SiIV	12.65 ± 0.02
3	1.91224	12.3 ± 0.8	CIV	13.18 ± 0.03
			SiIV	12.63 ± 0.02
4	1.91252	8.8 ± 0.2	CIV	13.49 ± 0.01
			SiIV	12.97 ± 0.01

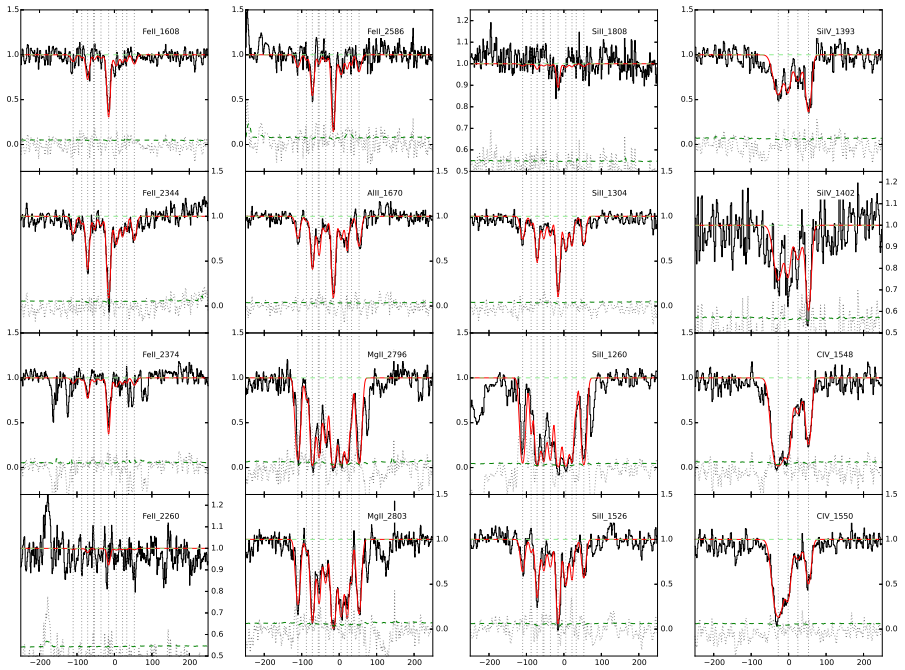

Figure B.18.: QSOLBQS2114-4347 $z_{abs} = 1.912$

B.2.19. QSO B2126-15 $z_{em} = 3.268$, $z_{abs} = 2.638$, $\log N(HI) = 19.25 \pm 0.15$

This EUADP spectrum covers the following transitions associated with the absorber: NiII $\lambda\lambda\lambda$ 1709 1741 1751, SiII λ 1808, FeII $\lambda\lambda\lambda\lambda\lambda$ 2586 1608 2249 2600 2382 and AlIII $\lambda\lambda$I 1854 and 1862. The good quality of the spectrum and the presence of non blended lines enables a robust 3-component fit of the low-ionization ions with FeII $\lambda\lambda$ 1608 2586, SiII λ 1808 and NiII $\lambda\lambda\lambda$ 1741 1751 and 1709. The apparent shift in FeII λ 2586 is thought to originate from a poor continuum fit. The resulting abundances are $\log N(FeII) = 14.05 \pm 0.01$, $\log N(SiII) = 14.67 \pm 0.02$, $\log N(NiII) = 13.15 \pm 0.01$. We derive an upper limit from the non detection of ZnII λ 2026: $\log N(ZnII) < 11.58$.

The intermediate-ionization transitions AlIII $\lambda\lambda$ 1854 and 1862 do not share the same absorption profile as the low-ionization ions (except for the strong narrow line in the middle of both profiles). These are therefore fitted separately with a 5-component profile. The resulting column density is $\log N(AlIII) = 13.24 \pm 0.02$.

Table B.19.: Voigt profile fit parameters to the low- and intermediate-ionization species for the z_{abs}=2.638 log N(H I)=19.25 ± 0.15 absorber towards QSO B2126-15.

Comp.	z_{abs}	b km s^{-1}	Ion	log N cm^{-2}
1	2.63767	17.8 ± 0.1	FeII	13.77 ± 0.01
			SiII	14.38 ± 0.02
			NiII	12.66 ± 0.02
2	2.63799	4.1 ± 0.1	FeII	13.39 ± 0.01
			SiII	13.80 ± 0.05
			NiII	12.47 ± 0.01
3	2.63807	19.3 ± 0.3	FeII	13.45 ± 0.01
			SiII	14.21 ± 0.03
			NiII	12.83 ± 0.02
1	2.63758	9.9 ± 0.5	AlIII	12.38 ± 0.02
2	2.63784	13.3 ± 0.2	AlIII	12.84 ± 0.01
3	2.63802	4.2 ± 0.5	AlIII	12.34 ± 0.05
4	2.63818	10.3 ± 0.8	AlIII	12.52 ± 0.08
5	2.63827	11.75 ± 1.8	AlIII	12.43 ± 0.11

The high-ionization transitions SiIV $\lambda\lambda$ 1398 and 1402 are clearly detected. However these lines are both blended and saturated, so that no fit are attempted.

The parameter fits of the individual components are listed in Table B.19 and the corresponding Voigt profile fits are shown in Fig. B.19.

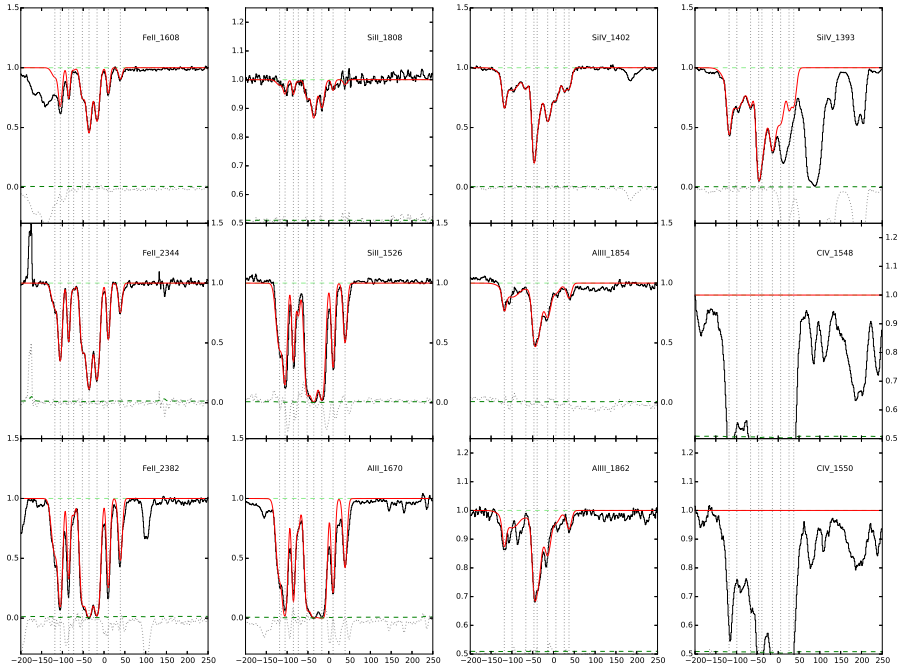

Figure B.19.: QSOB2126-15 $z_{abs} = 2.638$

B.2.20. QSO B2126-15 $z_{em} = 3.268$, $z_{abs} = 2.769$, $\log N(HI) = 19.2 \pm 0.15$

Many lines associated to the absorber are detected in this EUADP spectrum: FeII $\lambda\lambda\lambda\lambda\lambda\lambda\lambda$ 2586 2374 2344 1608 1144 2382 2600, SiII $\lambda\lambda\lambda$ 1808 1526 1190, CII $\lambda\lambda$ 1334 1036, AlII λ 1670, AlIII $\lambda\lambda$ 1862 1854, CIV $\lambda\lambda$ 1550 1548 and SiIV $\lambda\lambda$ 1402 and 1393.

The low-ionization ions are fitted considering the non blended lines, FeII λ 2344, SiII $\lambda\lambda$ 1808, 1526 and AlII λ 1670. This resulted in a 9-component profile with a $250 km/s$ velocity range. The transition FeII λ 2374 is not considered for the final fit due to the complexity in the continuum placement in this portion of the spectrum. The CII line is strongly saturated and therefore no fit could be performed on this transition. The AlII λ 1670 transition is saturated, therefore resulting in a lower limit for the column density ($\log N(AlII) < 14.05$). The fit results in the following column densities: $\log N(FeII) = 14.17 \pm 0.01$ and $\log N(SiII) = 14.79 \pm 0.01$. In addition, the non-detections led to the following upper limits: CrII λ 2056, $\log N(CrII) < 12.40$, MnII λ 2606, $\log N(MnII) < 12.28$,

and ZnII λ 2062, $\log \mathrm{N(ZnII)} < 11.95$.

The intermediate- and high-ionization ions AlIII $\lambda\lambda$ 1854 1862 and SiIV λ 1402 are fitted together given the similarities in their absorption profile. The SiIV λ 1393 transition is not considered because of an unidentified blending in the red part of the profile. The blending does not match any transition from the absorber at redshift $\mathrm{z_{abs}} = 2.638$. The 9-component profile of about $200\mathrm{km/s}$ and results in the following column densities $\log \mathrm{N(SiIV)} = 13.84 \pm 0.13$ and $\log \mathrm{N(AlIII)} = 13.11 \pm 0.01$. The CIV doublet is also covered by the data but the CIV λ 1548 line is saturated and both profiles show evidence for the presence of blending. It is interesting to note that the CIV doublet presents some components far in the red (up to $\sim 240\mathrm{km/s}$) which are not seen in SiIV. The OVI $\lambda\lambda$ 1031 and 1037 lines are also detected, but they are blended as often the case in the Lyα forest.

The parameter fits of the individual components are listed in Table B.20 and the corresponding Voigt profile fits are shown in Fig. B.20.

Table B.20.: Voigt profile fit parameters to the low- and high- and intermediate-ionization species for the $\mathrm{z_{abs}}$=2.769 log N(H I)=19.20 ± 0.15 absorber towards QSO B2126-15.

Comp.	z_{abs}	b	Ion	log N
1	2.76751	9.4 ± 0.8	FeII	12.78 ± 0.01
			SiII	13.52 ± 0.01
			AlII	12.40 ± 0.01
2	2.76768	4.4 ± 0.1	FeII	13.23 ± 0.01
			SiII	13.70 ± 0.01
			AlII	13.07 ± 0.01
3	2.76793	2.1 ± 0.2	FeII	13.06 ± 0.01
			SiII	13.64 ± 0.07
			AlII	13.42 ± 0.01
4	2.76808	3.7 ± 1.4	FeII	11.91 ± 0.05
			SiII	12.87 ± 0.01
			AlII	11.58 ± 0.01
5	2.76835	6.2 ± 0.2	FeII	13.19 ± 0.01
			SiII	13.94 ± 0.05
			AlII	12.65 ± 0.01
6	2.76855	7 ± 0.2	FeII	13.67 ± 0.01
			SiII	14.30 ± 0.02
			AlII	13.13 ± 0.01
7	2.76879	6.8 ± 0.1	FeII	13.54 ± 0.01
			SiII	14.15 ± 0.03
			AlII	13.70 ± 0.01

Continued on next page

Table B.20 – *Continued from previous page*

Comp.	z_{abs}	b	Ion	log N
8	2.76913	3.2 ± 0.2	FeII	12.99 ± 0.01
			SiII	13.55 ± 0.09
			AlII	12.45 ± 0.01
9	2.76949	4.4 ± 0.3	FeII	12.65 ± 0.01
			SiII	13.26 ± 0.01
			AlII	12.10 ± 0.01
1	2.76751	4.9 ± 0.9	SiIV	12.55 ± 0.06
			AlIII	11.91 ± 0.02
2	2.76775	26.3 ± 2.5	SiIV	13.02 ± 0.04
			AlIII	12.33 ± 0.01
3	2.76816	7.3 ± 6.9	SiIV	12.37 ± 0.47
			AlIII	11.02 ± 0.11
4	2.76841	4.6 ± 2.9	SiIV	13.17 ± 0.38
			AlIII	12.01 ± 0.02
5	2.76851	12.0 ± 6.2	SiIV	13.18 ± 0.46
			AlIII	12.72 ± 0.01
6	2.76882	9.1 ± 1.7	SiIV	13.02 ± 0.10
			AlIII	12.32 ± 0.01
7	2.76907	12.4 ± 4.3	SiIV	12.88 ± 0.15
			AlIII	11.87 ± 0.02
8	2.76933	4.7 ± 3.9	SiIV	12.30 ± 0.36
			AlIII	10.70 ± 0.21
9	2.76947	7.0 ± 2.6	SiIV	12.47 ± 0.18
			AlIII	11.85 ± 0.02

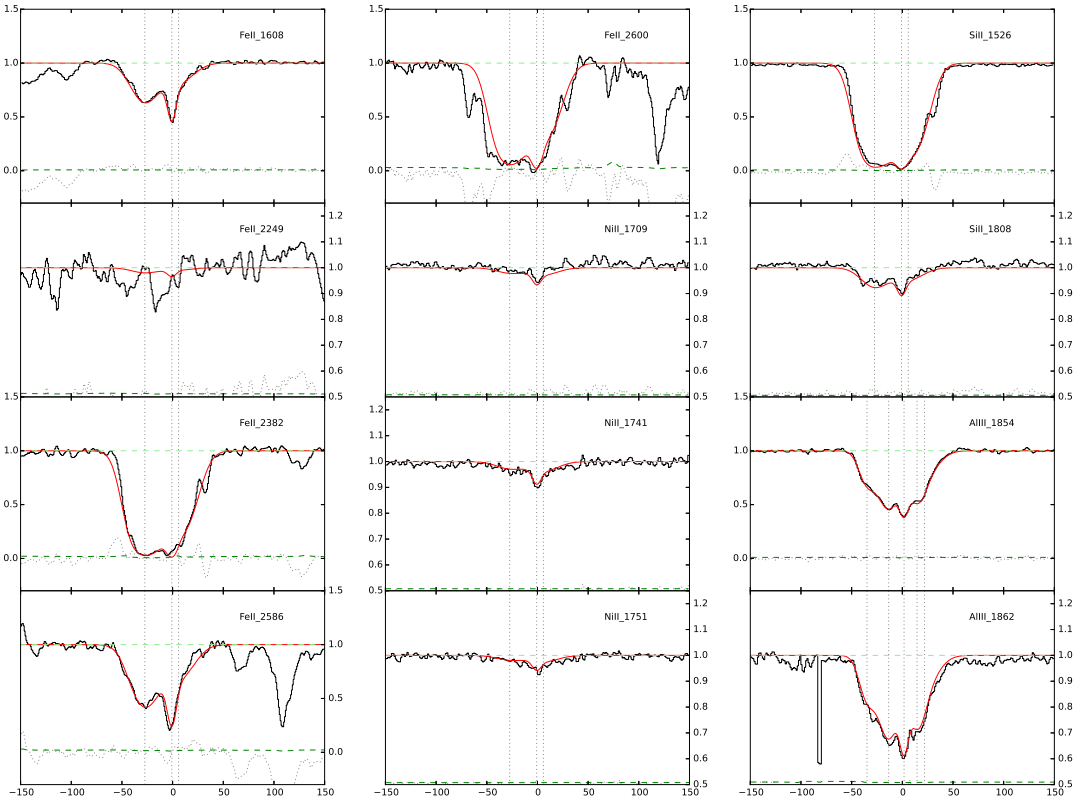

Figure B.20.: QSOB2126-15 $z_{abs} = 2.769$

B.2.21. QSO LBQS2132-4321 $z_{em} = 2.42$, $z_{abs} = 1.916$, $\log N(HI) = 20.74 \pm 0.09$

This EUADP spectrum provides the coverage of many ions associated to the absorber, often free from blending and with a good SNR. The low-ionization ions detected are SiII $\lambda\lambda\lambda\lambda\lambda\lambda$ 1190 1304 1808 1253 1250 1260 1193, FeII $\lambda\lambda\lambda$ 1608 2260 2249, CrII λ 2056, NiII $\lambda\lambda$ 1741 1709, ZnII λ 2026 and SII $\lambda\lambda$ 1250 and 1253. The profile presents two distinct groups of components spread over about 300 km/s: the weak components, only detected in large oscillator strength ions and the strong components, detected in all low-ionization ions and saturated otherwise. Therefore, the column densities of the strongest components are measured from the small oscillator strength ions only. We fit SiII λ 1808, FeII λ 2260, CrII $\lambda\lambda$ 2056 2026, NiII $\lambda\lambda$ 1741 1709 and ZnII λ 2026 with four compo-

nents. The intermediate ion AlIII λ 1854 which presents the same components (among others) is added to the fit. The remaining weak group is fitted with 3 components for SiII, AlIII and FeII. In this latter fit, some parameters such as the Doppler-parameter are fixed during the process because of a rather low SNR and/or blending. We detected a contamination in the third component of SiII λ 1808, based on SiII $\lambda\lambda$ 1526 and 1304, we therefore fitted the first three red components fixing the doppler parameter and column density of the third component of SiII. The fit results in the following column densities: $\log \mathrm{N(SiII)} = 15.75 \pm 0.02$, $\log \mathrm{N(FeII)} = 15.06 \pm 0.04$, $\log \mathrm{N(CrII)} = 13.38 \pm 0.03$, $\log \mathrm{N(NiII)} = 13.80 \pm 0.03$, $\log \mathrm{N(ZnII)} = 12.69 \pm 0.02$ and $\log \mathrm{N(AlIII)} = 13.18 \pm 0.03$. For SII $\lambda\lambda$ 1250 and 1253, a blend in the blue part of the absorption prevent from fitting the full profile. However, a lower limit is derived from the fit of the strong component in the red based on the other elements. The resulting column density is $\log \mathrm{N(SII)} > 14.90$.

The spectrum cover several high-ionization ions: CIV $\lambda\lambda$ 1550, 1548 and SiIV $\lambda\lambda$ 1393 and 1402. However, no satisfactory fit could be found for the CIV doublet because of the low SNR in this portion of the spectrum. On the contrary, a 4-component profile is derived for the SiIV λ 1402. It is also interesting to note that the velocity components are quite similar to the low-ionization ions components. The SiIV λ 1393 line suffers from a blend and again a limited SNR, so that the fit is performed with fix parameters but for the second Doppler-parameter. This fit results in $\log \mathrm{N(SiIV)} = 14.2 \pm 0.01$.

The parameter fits of the individual components are listed in Table B.21 and the corresponding Voigt profile fits are shown in Fig. B.21.

Table B.21.: Voigt profile fit parameters to the low- and high-ionization species for the z_{abs}=1.916 log N(H I)=20.74 ± 0.09 absorber towards QSO LBQS 2132-432.

Comp.	z_{abs}	b	Ion	log N
1	1.91433	15.60 ± 1.2	SiII	14.82 ± 0.04
			FeII	14.42 ± 0.06
			CrII	12.63 ± 0.05
			NiII	13.04 ± 0.08
			ZnII	11.43 ± 0.17
			AlIII	12.77 ± 0.02
2	1.91454	8.9 ± 0.4	SiII	15.03 ± 0.02
			FeII	14.57 ± 0.03
			CrII	12.81 ± 0.03
			NiII	13.30 ± 0.03
			ZnII	12.15 ± 0.03
			AlIII	12.58 ± 0.02

Continued on next page

Table B.21 – *Continued from previous page*

Comp.	z_{abs}	b	Ion	log N
3	1.91478	7.00	SiII	14.80
			FeII	14.22 ± 0.06
			CrII	12.69 ± 0.03
			NiII	13.05 ± 0.05
			ZnII	12.00 ± 0.04
			AlIII	12.48 ± 0.02
4	1.91562	6.0	SiII	13.74 ± 0.02
			FeII	12.40 ± 0.32
			CrII	–
			NiII	–
			ZnII	–
			AlIII	12.15 ± 0.03
5	1.91585	7.0	SiII	13.9 ± 0.02
			FeII	13.26 ± 0.05
			CrII	–
			NiII	–
			ZnII	–
			AlIII	12.29 ± 0.03
6	1.91599	3.0	SiII	13.07 ± 0.06
			FeII	12.52 ± 0.22
			CrII	–
			NiII	–
			ZnII	–
			AlIII	11.60 ± 0.10
7	1.91647	5.2 ± 0.3	SiII	15.01 ± 0.02
			FeII	14.41 ± 0.05
			CrII	12.74 ± 0.04
			NiII	13.21 ± 0.04
			ZnII	12.28 ± 0.02
			AlIII	12.19 ± 0.03
1	1.91431	17.8 ± 0.3	SiV	13.90 ± 0.01
2	1.91474	16.5 ± 0.5	SiV	13.46 ± 0.01
3	1.91567	11.1 ± 0.8	SiV	13.40 ± 0.07
4	1.91582	19.4 ± 1.1	SiV	13.40 ± 0.05

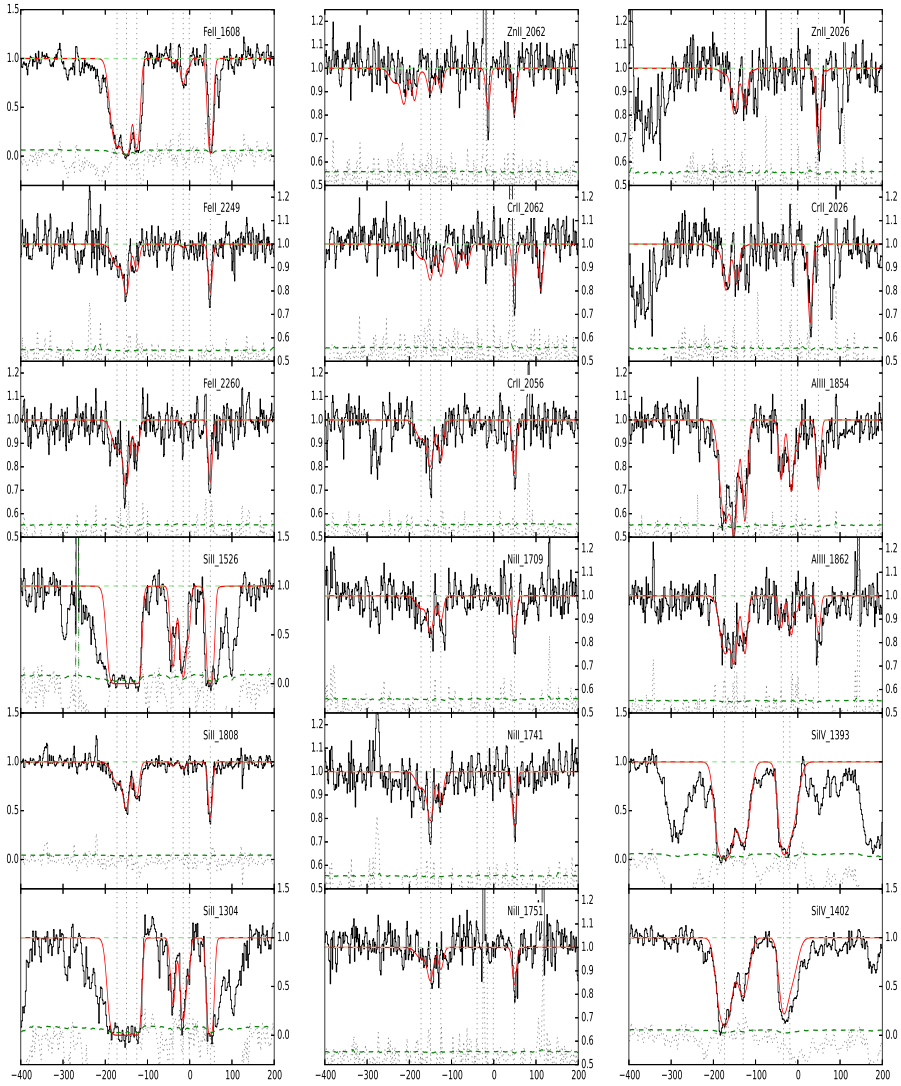

Figure B.21.: QSOLBQS2132-4321 $z_{abs} = 1.916$

B.2.22. QSO B2318-1107 $z_{em} = 2.96$, $z_{abs} = 1.629$, $\log N(HI) = 20.52 \pm 0.14$

A broad variety of ions are covered in the EUADP spectrum of this low-redshift absorber. The low-ionization ions detected are FeII $\lambda\lambda\lambda$ 2260, 2249 2374, MnII λ 2576, AlII λ 1670, CII λ 1334, SiII $\lambda\lambda\lambda$ 1260, 1304 and 1526. The profile of the CII line appears to be saturated and blended from a comparison with other low-ionisation ions. This line is therefore not considered for a fit. Likewise, the SiII lines are saturated and are not fitted. The AlII λ 1670 line appears to be blended (strong absorption on the blue side of the line), and therefore only an upper limit is available: $\log N(\mathrm{AlII}) < 14.93$. FeII and MnII are well fitted with 2 components (from the asymmetry of FeII λ 2249): resulting in $\log N(\mathrm{FeII}) = 14.14 \pm 0.02$ and $\log N(\mathrm{MnII}) = 11.78 \pm 0.04$. Also, we derive upper limits from non detection of SII λ 1250, $\log N(\mathrm{SII}) < 14.54$, CrII λ 2062, $\log N(\mathrm{CrII}) < 12.47$, ZnII λ 2026, $\log N(\mathrm{ZnII}) < 11.74$, MgI λ 2026 and $\log N(\mathrm{MgI}) < 12.37$.

The detected intermediate-ionization transitions are AlIII $\lambda\lambda$ 1854 and 1862. The absorption profiles differ significantly from the high- or the low-ionization ions (red component stronger than the blue one). The fit is thus performed separately with two components. The resulting column density is $\log N(\mathrm{AlIII}) = 12.17 \pm 0.02$.

The high-ionization ions detected are SiIV $\lambda\lambda$ 1393, 1402 and CIV $\lambda\lambda$ 1548 (saturated) and 1550. The position of the SiIV lines (on the red wing of the Lya absorber for λ 1393 and blended from the forest for λ 1402) prevents a robust fit for the SiIV lines. Similarly to the low-ionization ions, the asymmetry of CIV λ 1550 suggests a 2-component profile. We derive an upper limit for CIV from a 2-component fit of CIV λ 1550, as the saturated CIV λ 1548 brings no constraints on possible contamination of CIV λ 1550. We obtain $\log N(\mathrm{CIV}) < 14.10$.

The parameter fits of the individual components are listed in Table B.22 and the corresponding Voigt profile fits are shown in Fig. B.22.

Table B.22.: Voigt profile fit parameters to the low- and high-ionization species for the z_{abs}=1.629 log N(H I)=20.52 ± 0.14 absorber towards QSO B2318-1107.

Comp.	z_{abs}	b km s^{-1}	Ion	log N cm^{-2}
1	1.62908	4.7 ± 0.3	FeII	14.05 ± 0.01
			MnII	11.67 ± 0.04
			AlII	12.06 ± 0.10
2	1.62915	1.4 ± 0.4	FeII	13.42 ± 0.08
			MnII	11.13 ± 0.12
			AlII	14.93 ± 0.40
1	1.62898	24.2 ± 15.0	AlIII	11.60 ± 0.35
2	1.62909	8.0 ± 1.4	AlIII	12.03 ± 0.11
1	1.62895	2.7 ± 3.2	CIV	13.21 ± 0.17
2	1.62904	19.8 ± 1.1	CIV	14.04 ± 0.03

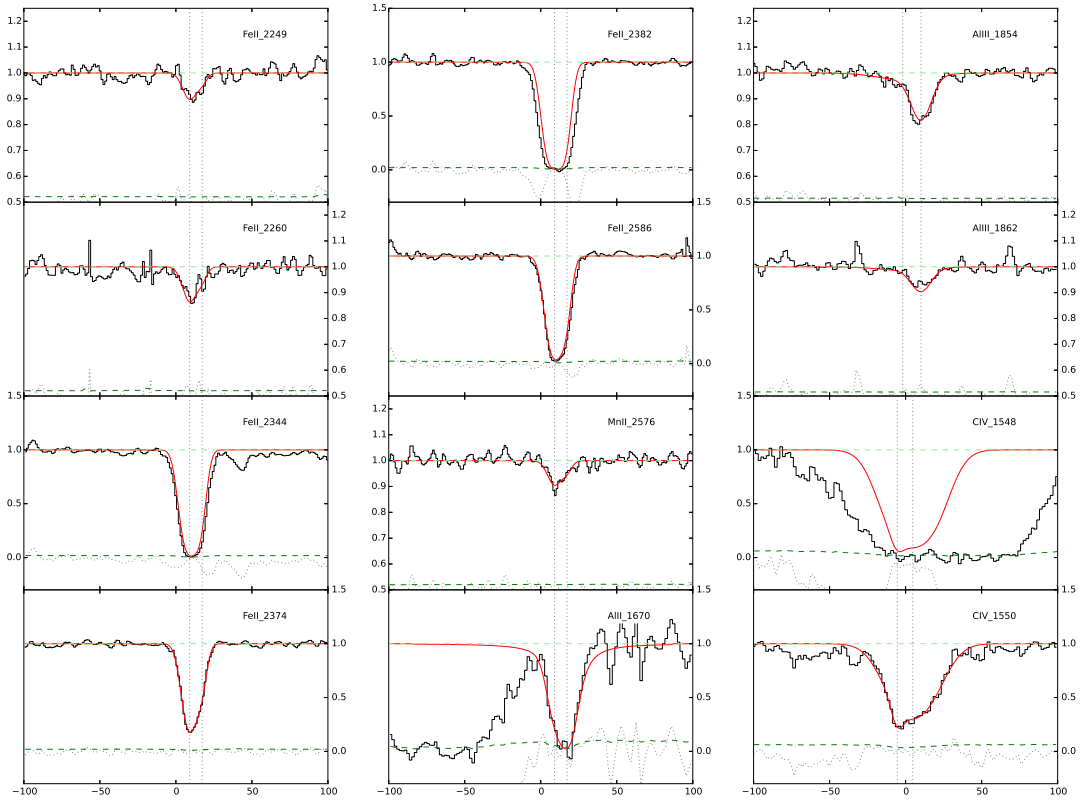

Figure B.22.: QSOB2318-1107 $z_{abs} = 1.629$

B.3. EUADP+ Sample

This Appendix presents the full list of damped and sub-damped absorbers identified in the EUADP+. We compile estimates of abundances from various references in the literature, as specified in the last column. We list the column density of ZnII, FeII and SII, as well as estimates of their metallicity based on the ion specified. The online version of this table includes a more complete list of ions (Quiret, Péroux, et al., 2016).

Table B.23.: Full list of damped and sub-damped absorbers identified in the EUADP+, with the column densities of ZnII, FeII and SII, as well as estimates of their metallicity based on the ion specified.

QSO name	$z_{\rm abs}$	log N(HI)	log N(Zn)	log N(Fe)	log N(S)	[X/H]	X	Ref
CTQ418	2.5100	20.50 ± 0.07	-	14.07 ± 0.03	13.99 ± 0.06	-1.63 ± 0.09	SII	43
CTQ418	2.4300	20.68 ± 0.07	-	13.91 ± 0.05	13.97 ± 0.03	-1.83 ± 0.08	SII	43
QXO0001	3.0000	20.70 ± 0.05	-	< 15.09	-	-1.62 ± 0.05	OI	92
Q0000-262	3.3900	21.41 ± 0.08	12.01 ± 0.05	14.87 ± 0.03	-	-1.96 ± 0.09	ZnII	62, 90
QSO J0003-2323	2.1870	19.60 ± 0.40	< 11.04	13.22 ± 0.12	< 13.12	-1.76 ± 0.42	OI	103
Q0005+0524	0.8514	19.08 ± 0.04	< 11.24	13.79 ± 0.01	-	-0.47 ± 0.18	FeII	60
PSS0007+2417	3.5000	21.10 ± 0.10	< 12.39	> 14.63	-	-1.53 ± 0.11	SiII	94
PSS0007+2417	3.8400	20.85 ± 0.15	-	13.91 ± 0.03	-	-2.12 ± 0.24	FeII	94
J0007+0041	4.7300	20.65 ± 0.20	-	-	-	-2.19 ± 0.20	SiII	99
QSO J0008-2900	2.2540	20.22 ± 0.10	< 11.68	13.78 ± 0.01	-	-1.33 ± 0.14	SiII	114
QSO J0008-2901	2.4910	19.94 ± 0.11	< 12.12	13.65 ± 0.02	13.68 ± 0.18	-1.32 ± 0.26	OI	114
J0008-0958	1.7700	20.85 ± 0.15	13.31 ± 0.05	15.62 ± 0.05	15.84 ± 0.05	-0.10 ± 0.16	ZnII	44, 3, 4, 5
LBQS 0009-0138	1.3860	20.26 ± 0.02	< 11.55	14.25 ± 0.01	-	-1.32 ± 0.04	SiII	60

Continued on next page

Table B.23 – *Continued from previous page*

QSO name	$z_{\rm abs}$	log N(HI)	log N(Zn)	log N(Fe)	log N(S)	[X/H]	X	Reference
LBQS 0010-0012	2.0250	20.95 ± 0.10	12.19 ± 0.05	15.18 ± 0.03	14.98 ± 0.05	-1.32 ± 0.11	ZnII	52, 110
Q0012-0122	1.3862	20.26 ± 0.02	< 11.55	14.24 ± 0.01	-	-1.34 ± 0.08	SiII	60
LBQS 0013-0029	1.9730	20.83 ± 0.05	12.74 ± 0.05	14.81 ± 0.03	15.28 ± 0.03	-0.65 ± 0.07	ZnII	76, 110, 44
LBQS 0018+0026	0.5200	19.54 ± 0.03	-	13.17 ± 0.04	-	-1.55 ± 0.19	FeII	32
LBQS 0018+0026	0.9400	19.38 ± 0.15	< 11.64	14.62 ± 0.04	-	0.06 ± 0.24	FeII	32
J001855-091351	0.5840	20.11 ± 0.10	< 12.41	13.87 ± 0.03	-	-1.42 ± 0.21	FeII	114
Q0019-15	3.4400	20.92 ± 0.10	-	> 14.79	-	-1.01 ± 0.11	SiII	89, 90
Q0021+0104	1.3259	20.04 ± 0.11	< 11.48	14.69 ± 0.01	-	-0.53 ± 0.21	FeII	60
Q0021+0104	1.5756	20.48 ± 0.15	< 11.95	14.61 ± 0.02	-	-1.11 ± 0.15	SiII	60
J0021+0043	0.9424	19.38 ± 0.13	< 11.64	15.06 ± 0.14	-	0.50 ± 0.26	FeII	26
QSO B0027-1836	2.4020	21.75 ± 0.10	12.79 ± 0.02	14.97 ± 0.02	15.23 ± 0.02	-1.52 ± 0.10	ZnII	64
J0035-0918	2.3400	20.55 ± 0.10	-	13.07 ± 0.04	< 13.13	-2.69 ± 0.17	OI	17
QSO B0039-3354	2.2240	20.60 ± 0.10	-	14.41 ± 0.03	-	-1.27 ± 0.11	SiII	66
J004054.7-091526	4.7400	20.55 ± 0.15	-	14.05 ± 0.06	-	-1.93 ± 0.15	SiII	98
J0040-0915	4.7394	20.30 ± 0.15	-	14.05 ± 0.06	-	-1.43 ± 0.24	FeII	98
QSO J0041-4936	2.2480	20.46 ± 0.13	11.70 ± 0.10	14.42 ± 0.04	< 14.82	-1.32 ± 0.16	ZnII	114
LBQS 0042-2930	1.8090	20.40 ± 0.10	-	-	-	-1.21 ± 0.12	SiII	37
LBQS 0042-2930	1.9360	20.50 ± 0.10	-	-	-	-1.23 ± 0.11	SiII	37
J0044+0018	1.7300	20.35 ± 0.10	< 12.61	> 14.77	15.27 ± 0.05	-0.20 ± 0.11	SII	3, 4, 5
Q0049-2820	2.0700	20.45 ± 0.10	-	14.50 ± 0.02	-	-1.26 ± 0.11	SiII	67

Continued on next page

Table B.23 – *Continued from previous page*

QSO name	$z_{\rm abs}$	log N(HI)	log N(Zn)	log N(Fe)	log N(S)	[X/H]	X	Reference
QSO B0058-292	2.6710	21.10 ± 0.10	12.23 ± 0.05	14.75 ± 0.03	14.92 ± 0.03	-1.43 ± 0.11	ZnII	51, 110
J0058+0115	2.0100	21.10 ± 0.15	12.95 ± 0.05	15.18 ± 0.05	15.40 ± 0.05	-0.71 ± 0.16	ZnII	3, 4, 5
QSO B0100+1300	2.3090	21.35 ± 0.08	12.49 ± 0.02	15.10 ± 0.04	15.09 ± 0.06	-1.42 ± 0.08	ZnII	89, 22
QSO J0105-1846	2.3700	21.00 ± 0.08	11.77 ± 0.11	14.47 ± 0.10	14.30 ± 0.04	-1.79 ± 0.14	ZnII	51, 110
QSO J0105-1846	2.9260	20.00 ± 0.10	-	13.80 ± 0.03	13.82 ± 0.03	-1.56 ± 0.13	OI	66
B0105-008	1.3700	21.70 ± 0.15	12.93 ± 0.04	15.59 ± 0.03	-	-1.33 ± 0.16	ZnII	35
QSO B0112-30	2.4180	20.50 ± 0.08	-	13.33 ± 0.04	14.44 ± 0.03	-2.24 ± 0.11	OI	77
QSO B0112-30	2.7020	20.30 ± 0.10	-	14.77 ± 0.07	-	-0.44 ± 0.13	SiII	51, 110
Q0112+030	2.4200	20.90 ± 0.10	-	14.85 ± 0.01	14.79 ± 0.05	-1.23 ± 0.11	SII	110, 52, 67
QSO B0122-005	1.7610	20.78 ± 0.07	-	15.10 ± 0.10	-	-0.87 ± 0.11	SiII	33
QSO B0122-005	2.0100	20.04 ± 0.07	< 11.40	13.69 ± 0.07	-	-1.88 ± 0.09	SiII	33
QSO J0123-0058	1.4090	20.08 ± 0.09	12.23 ± 0.10	14.98 ± 0.02	-	-0.41 ± 0.13	ZnII	74
QSO J0124+0044	2.9880	19.18 ± 0.10	-	< 13.55	< 14.27	-0.57 ± 0.16	SiII	73
QSO J0124+0044	3.0780	20.21 ± 0.10	-	< 14.13	-	-0.59 ± 0.40	SiII	73
QSO B0128-2150	1.8570	20.21 ± 0.09	< 12.26	14.44 ± 0.01	14.33 ± 0.03	-1.00 ± 0.09	SII	114
J013209-082349	0.6470	20.60 ± 0.12	-	14.96 ± 0.07	-	-0.82 ± 0.23	FeII	114
QSO J0133+0400	3.6920	20.68 ± 0.15	-	13.51 ± 0.07	-	-0.96 ± 0.16	SiII	93
QSO J0133+0400	3.7730	20.55 ± 0.13	< 13.10	> 14.87	-	-0.59 ± 0.13	SiII	93
QSO J0133+0400	3.9950	19.94 ± 0.15	-	< 13.43	-	-1.54 ± 0.20	SiII	73

Continued on next page

Table B.23 – *Continued from previous page*

QSO name	$z_{\rm abs}$	log N(HI)	log N(Zn)	log N(Fe)	log N(S)	[X/H]	X	Reference
PSS0133+0400	3.6900	20.70 ± 0.10	-	13.57 ± 0.04	< 13.35	-2.31 ± 0.21	FeII	93, 77
PSS0133+0400	3.7700	20.60 ± 0.10	< 13.10	> 14.87	-	-0.65 ± 0.10	SiII	93, 67
QSO J0134+0051	0.8420	19.93 ± 0.13	< 12.17	14.47 ± 0.01	-	-0.64 ± 0.22	FeII	72
PSS0134+3317	3.7600	20.85 ± 0.08	-	-	-	-2.69 ± 0.09	AlII	93
QSO B0135-42	3.1010	19.81 ± 0.10	-	13.67 ± 0.11	-	-1.21 ± 0.27	SiII	73
QSO B0135-42	3.6650	19.11 ± 0.10	-	< 13.47	-	-2.42 ± 0.16	OI	73
Q0135-273	2.8000	21.00 ± 0.10	-	14.77 ± 0.03	14.80 ± 0.02	-1.32 ± 0.10	SII	110, 52, 67
Q0135-273	2.1100	20.30 ± 0.15	-	-	14.38 ± 0.06	-1.04 ± 0.16	SII	52
QSO J0138-0005	0.7820	19.81 ± 0.09	12.69 ± 0.05	< 15.17	-	0.32 ± 0.10	ZnII	74
J0140-0839	3.7000	20.75 ± 0.15	-	< 12.73	< 13.33	-2.75 ± 0.15	OI	34
UM673A	1.6300	20.70 ± 0.10	11.43 ± 0.15	14.59 ± 0.03	14.53 ± 0.00	-1.83 ± 0.18	ZnII	15
J0142+0023	3.3500	20.38 ± 0.05	< 11.50	13.70 ± 0.10	13.26 ± 0.06	-2.24 ± 0.08	SII	34
Q0149+33	2.1400	20.50 ± 0.10	11.50 ± 0.10	14.20 ± 0.02	< 14.80	-1.56 ± 0.14	ZnII	89, 11, 90
Q0151+0448	1.9300	20.36 ± 0.10	< 11.81	13.70 ± 0.01	< 13.47	-1.86 ± 0.11	SiII	34, 118
QSO J0157-0048	1.4160	19.90 ± 0.07	12.12 ± 0.07	14.57 ± 0.03	-	-0.34 ± 0.10	ZnII	32
QSO B0201+113	3.3850	21.26 ± 0.08	-	15.35 ± 0.05	15.21 ± 0.11	-1.17 ± 0.14	SII	29

Continued on next page

Table B.23 – *Continued from previous page*

QSO name	$z_{\rm abs}$	log N(HI)	log N(Zn)	log N(Fe)	log N(S)	[X/H]	X	Reference
Q0201+365	2.4600	20.38 ± 0.05	12.47 ± 0.05	15.01 ± 0.01	15.29 ± 0.01	-0.47 ± 0.07	ZnII	87, 79, 90, 92, 3, 4, 5
Q0201+1120	3.3900	21.26 ± 0.10	-	15.35 ± 0.10	15.21 ± 0.10	-1.17 ± 0.14	SII	29
QSO J0209+0517	3.6660	20.47 ± 0.10	-	13.63 ± 0.05	-	-2.01 ± 0.21	FeII	93
QSO J0209+0517	3.8630	20.55 ± 0.10	-	< 13.34	-	-2.60 ± 0.11	SiII	93
PSS0209+0517	3.6700	20.45 ± 0.10	-	13.64 ± 0.05	-	-1.99 ± 0.21	FeII	93
J0211+1241	2.6000	20.60 ± 0.15	-	15.06 ± 0.05	-	-0.58 ± 0.17	SiII	3, 4, 5
QSO B0216+0803	1.7690	20.20 ± 0.10	11.90 ± 0.06	14.53 ± 0.09	-	-0.86 ± 0.12	ZnII	57
QSO B0216+0803	2.2930	20.45 ± 0.16	12.47 ± 0.05	14.88 ± 0.02	15.04 ± 0.02	-0.54 ± 0.17	ZnII	57, 117
QSO J0217+0144	1.3450	19.89 ± 0.09	-	14.38 ± 0.10	-	-1.11 ± 0.10	MgII	6, 7
SDSS0225+0054	2.7100	21.00 ± 0.15	12.89 ± 0.11	15.30 ± 0.08	-	-0.67 ± 0.19	ZnII	44
J0233+0103	1.7900	20.60 ± 0.15	-	14.62 ± 0.05	-	-1.34 ± 0.16	SiII	3, 4, 5
J0234-0751	2.3200	20.90 ± 0.10	-	14.18 ± 0.03	14.18 ± 0.03	-1.84 ± 0.10	SII	28
AO0235+164	0.5200	21.70 ± 0.10	-	15.30 ± 0.40	-	-1.58 ± 0.45	FeII	13
QSO B0237-2322	1.3650	19.30 ± 0.30	-	14.13 ± 0.01	-	0.08 ± 0.30	SiII	111
QSO B0237-2322	1.6720	19.65 ± 0.10	11.84 ± 0.09	14.57 ± 0.02	-	-0.37 ± 0.13	ZnII	35
Q0242-2917	2.5600	20.90 ± 0.10	-	14.36 ± 0.03	14.11 ± 0.02	-1.91 ± 0.10	SII	67
QSO B0244-1249	1.8630	19.48 ± 0.18	< 11.50	< 13.90	-	-0.79 ± 0.27	SiII	33
QSO B0253+0058	0.7250	20.70 ± 0.17	13.19 ± 0.04	15.13 ± 0.30	-	-0.07 ± 0.17	ZnII	72

Continued on next page

Table B.23 – *Continued from previous page*

QSO name	$z_{\rm abs}$	log N(HI)	log N(Zn)	log N(Fe)	log N(S)	[X/H]	X	Reference
QSO B0254-404	2.0460	20.45 ± 0.08	-	14.17 ± 0.03	14.14 ± 0.04	-1.43 ± 0.09	SII	66
J0255+00	3.9200	21.30 ± 0.05	-	14.75 ± 0.09	14.72 ± 0.01	-1.70 ± 0.05	SII	90
J0255+00	3.2500	20.70 ± 0.10	-	14.76 ± 0.01	-	-0.89 ± 0.11	SiII	90
Q0300-3152	2.1800	20.80 ± 0.10	-	14.21 ± 0.02	14.20 ± 0.03	-1.72 ± 0.10	SII	67
Q0302-223	1.0100	20.36 ± 0.11	12.45 ± 0.06	14.67 ± 0.05	-	-0.47 ± 0.13	ZnII	82
QSO B0307-195B	1.7880	19.00 ± 0.10	< 12.18	14.48 ± 0.00	-	0.49 ± 0.10	SiII	114
J0307-4945	4.4700	20.67 ± 0.09	-	14.21 ± 0.17	< 15.46	-1.45 ± 0.19	OI	20
TXS0311+430	2.2900	20.30 ± 0.00	< 12.50	14.85 ± 0.20	-	-0.63 ± 0.27	FeII	32, 32
J0311-1722	3.7300	20.30 ± 0.06	-	< 13.76	-	-2.29 ± 0.10	OI	16
QSO J0332-4455	2.6560	19.82 ± 0.05	-	13.51 ± 0.05	-	-1.67 ± 0.06	OI	36
QSO B0335-122	3.1780	20.65 ± 0.07	< 12.25	13.70 ± 0.04	-	-2.44 ± 0.10	SiII	1, 67
QSO B0336-017	3.0620	21.20 ± 0.09	-	14.90 ± 0.03	14.99 ± 0.01	-1.33 ± 0.09	SII	90
0338-0005	2.9090	21.10 ± 0.10	< 12.47	15.02 ± 0.06	15.19 ± 0.01	-1.03 ± 0.10	SII	95
QSO B0347-383	3.0250	20.63 ± 0.09	12.23 ± 0.12	14.47 ± 0.01	14.73 ± 0.01	-0.96 ± 0.15	ZnII	90, 51
QSO J0354-2724	1.4050	20.18 ± 0.15	12.73 ± 0.03	15.10 ± 0.03	-	-0.01 ± 0.15	ZnII	59
B0405-331	2.5700	20.60 ± 0.10	< 12.74	14.31 ± 0.00	-	-1.40 ± 0.10	SiII	1
Q0405-443	2.5500	21.13 ± 0.10	12.44 ± 0.05	14.95 ± 0.06	14.82 ± 0.06	-1.25 ± 0.11	ZnII	55, 110
Q0405-443	2.6200	20.47 ± 0.10	-	13.60 ± 0.02	< 14.34	-1.97 ± 0.10	OI	55, 110, 68, 112
QSO J0407-4410	1.9130	20.80 ± 0.10	12.44 ± 0.05	-	-	-0.92 ± 0.11	ZnII	52

Continued on next page

Table B.23 – *Continued from previous page*

QSO name	$z_{\rm abs}$	log N(HI)	log N(Zn)	log N(Fe)	log N(S)	[X/H]	X	Reference
QSO J0407-4410	2.5510	21.13 ± 0.10	12.44 ± 0.05	14.95 ± 0.06	14.82 ± 0.06	-1.25 ± 0.11	ZnII	55, 110
QSO J0407-4410	2.5950	21.09 ± 0.10	12.68 ± 0.02	15.15 ± 0.02	15.19 ± 0.05	-0.97 ± 0.10	ZnII	55, 110
QSO J0407-4410	2.6210	20.45 ± 0.10	-	13.60 ± 0.02	< 14.34	-1.95 ± 0.10	OI	55, 110
Q0421-2624	2.1600	20.65 ± 0.10	-	13.97 ± 0.01	-	-1.81 ± 0.10	SiII	67
QSO J0422-3844	3.0820	19.37 ± 0.02	-	13.96 ± 0.10	-	-0.69 ± 0.04	OI	10
Q0425-5214	2.2200	20.30 ± 0.10	-	13.96 ± 0.03	14.07 ± 0.03	-1.35 ± 0.10	SII	67
BRJ0426-2202	2.9800	21.50 ± 0.15	< 12.17	14.15 ± 0.07	-	-2.53 ± 0.24	FeII	93
QSO J0427-1302	1.5620	19.35 ± 0.10	< 11.75	12.23 ± 0.04	-	-2.30 ± 0.21	FeII	114
QSO J0427-1302	1.4080	19.04 ± 0.04	< 11.09	13.33 ± 0.02	-	-0.99 ± 0.06	SiII	60
Q0432-4401	2.3000	20.95 ± 0.10	< 12.20	14.87 ± 0.10	-	-1.18 ± 0.12	SiII	1, 67, 119
QSO B0438-43	2.3470	20.78 ± 0.12	12.72 ± 0.03	-	-	-0.62 ± 0.12	ZnII	1
PKS 0439-433	0.1012	19.63 ± 0.15	-	14.92 ± 0.03	15.03 ± 0.03	0.28 ± 0.15	SII	105
QSO B0449-1645	1.0070	20.98 ± 0.07	12.62 ± 0.07	15.09 ± 0.01	-	-0.92 ± 0.10	ZnII	74
QSO B0450-1310B	2.0670	20.50 ± 0.07	-	14.29 ± 0.03	14.18 ± 0.06	-2.13 ± 0.08	OI	24, 119
PKS 0454-220	0.4740	19.45 ± 0.03	-	14.71 ± 0.01	15.06 ± 0.04	0.49 ± 0.05	SII	114
Q0454+039	0.8600	20.69 ± 0.06	12.33 ± 0.08	-	-	-0.92 ± 0.10	ZnII	82
4C-02.19	2.0400	21.70 ± 0.10	13.13 ± 0.05	15.38 ± 0.05	-	-1.13 ± 0.11	ZnII	42
QSO B0512-3329	0.9310	20.49 ± 0.08	-	14.47 ± 0.06	-	-1.20 ± 0.21	FeII	56
QSO B0515-4414	1.1510	19.88 ± 0.05	12.22 ± 0.04	14.31 ± 0.03	-	-0.22 ± 0.06	ZnII	97, 122

Continued on next page

Table B.23 – *Continued from previous page*

QSO name	$z_{\rm abs}$	log N(HI)	log N(Zn)	log N(Fe)	log N(S)	[X/H]	X	Reference
HE0512-3329A	0.9300	20.49 ± 0.08	-	14.47 ± 0.06	-	-1.20 ± 0.21	FeII	56
HE0515-4414	1.1500	20.45 ± 0.15	12.11 ± 0.04	14.31 ± 0.20	-	-0.90 ± 0.16	ZnII	123
QSO B0528-2505	2.1410	20.70 ± 0.08	13.00 ± 0.03	14.94 ± 0.26	14.83 ± 0.04	-0.26 ± 0.09	ZnII	57, 12
QSO B0528-2505	2.8110	21.11 ± 0.07	13.27 ± 0.03	15.47 ± 0.02	15.56 ± 0.02	-0.40 ± 0.08	ZnII	107, 57, 12
QSO B0551-36	1.9620	20.50 ± 0.08	13.02 ± 0.05	15.05 ± 0.05	15.38 ± 0.11	-0.04 ± 0.09	ZnII	49
J060008.1-504036	2.1490	20.40 ± 0.12	12.11 ± 0.03	14.84 ± 0.03	-	-0.85 ± 0.12	ZnII	114
QSO B0642-5038	2.6590	20.95 ± 0.08	12.50 ± 0.06	15.10 ± 0.04	-	-1.01 ± 0.10	ZnII	66, 119
Q0738+313	0.0900	21.18 ± 0.06	< 12.66	15.02 ± 0.15	-	-1.34 ± 0.24	FeII	58, 47
HS0741+4741	3.0200	20.48 ± 0.10	-	14.05 ± 0.01	14.00 ± 0.02	-1.60 ± 0.10	SII	90, 92
J0747+4434	4.0196	20.95 ± 0.15	-	> 14.32	-	-2.50 ± 0.20	NiII	98
FJ0747+2739	3.9000	20.50 ± 0.10	< 12.40	< 13.80	< 14.36	-1.98 ± 0.10	SiII	93
J0759+1800	4.6577	20.85 ± 0.15	-	< 15.16	14.26 ± 0.05	-1.71 ± 0.16	SII	98
SDSS0759+3129	3.0300	20.60 ± 0.10	-	13.80 ± 0.20	-	-2.01 ± 0.32	SiII	70
PSSJ0808+52	3.1100	20.65 ± 0.07	< 12.13	14.17 ± 0.04	-	-1.56 ± 0.14	SiII	91, 93
FJ0812+32	2.0700	21.00 ± 0.10	12.21 ± 0.02	14.89 ± 0.02	-	-1.35 ± 0.10	ZnII	95, 43

Continued on next page

Table B.23 – *Continued from previous page*

QSO name	$z_{\rm abs}$	log N(HI)	log N(Zn)	log N(Fe)	log N(S)	[X/H]	X	Reference
FJ0812+32	2.6300	21.35 ± 0.10	13.15 ± 0.05	15.09 ± 0.05	15.63 ± 0.07	-0.76 ± 0.11	ZnII	93, 95, 3, 4, 5
J0815+1037	1.8500	20.30 ± 0.15	-	> 14.87	-	-0.43 ± 0.47	SiII	3, 4, 5
J0816+1446	3.2900	22.00 ± 0.10	13.53 ± 0.00	15.89 ± 0.00	-	-1.03 ± 0.10	ZnII	41
J0817+1351	4.2584	21.30 ± 0.15	-	15.45 ± 0.06	15.30 ± 0.02	-1.12 ± 0.15	SII	98
J0824+1302	4.4700	20.65 ± 0.20	-	13.60 ± 0.08	-	-2.32 ± 0.21	SiII	99
J0825+3544	3.2073	20.30 ± 0.10	-	13.77 ± 0.03	-	-1.71 ± 0.21	FeII	98
J0825+3544	3.6567	21.25 ± 0.10	-	> 14.65	-	-1.83 ± 0.13	SiII	98
J0825+5127	3.3180	20.85 ± 0.10	-	14.22 ± 0.01	-	-1.67 ± 0.14	SiII	98
Q0826-2230	0.9110	19.04 ± 0.04	12.71 ± 0.08	13.57 ± 0.06	-	1.11 ± 0.09	ZnII	60
Q0827+243	0.5200	20.30 ± 0.05	< 12.80	14.59 ± 0.02	-	-0.89 ± 0.19	FeII	58, 45
J0831+4046	4.3440	20.75 ± 0.15	-	13.79 ± 0.07	-	-2.36 ± 0.15	SiII	98
J0834+2140	3.7102	20.85 ± 0.10	-	14.44 ± 0.02	-	-1.59 ± 0.21	FeII	98
J0834+2140	4.3900	21.00 ± 0.20	-	14.76 ± 0.02	14.85 ± 0.04	-1.27 ± 0.20	SII	98
J0834+2140	4.4610	20.30 ± 0.15	-	13.71 ± 0.07	< 14.13	-1.86 ± 0.16	SiII	98
Q0836+11	2.4700	20.58 ± 0.10	< 12.12	14.68 ± 0.01	< 14.66	-1.10 ± 0.11	SiII	90, 92
J0839+3524	4.2800	20.30 ± 0.15	-	14.30 ± 0.04	-	-1.18 ± 0.24	FeII	98
QSO B0841+129	1.8640	21.00 ± 0.10	-	-	14.82 ± 0.05	-1.30 ± 0.11	SII	52
QSO B0841+129	2.3750	21.05 ± 0.10	12.12 ± 0.05	14.76 ± 0.11	14.69 ± 0.15	-1.50 ± 0.11	ZnII	89, 119

Continued on next page

Table B.23 – *Continued from previous page*

QSO name	$z_{\rm abs}$	log N(HI)	log N(Zn)	log N(Fe)	log N(S)	[X/H]	X	Reference
QSO B0841+129	2.4760	20.80 ± 0.10	11.69 ± 0.05	14.43 ± 0.03	14.48 ± 0.12	-1.67 ± 0.11	ZnII	89, 24
SDSS0844+5153	2.7700	21.45 ± 0.15	-	15.29 ± 0.06	-	-0.99 ± 0.15	SiII	44
J0900+42	3.2500	20.30 ± 0.10	-	14.54 ± 0.01	14.65 ± 0.01	-0.77 ± 0.10	SII	95, 43
J0909+3303	3.6584	20.55 ± 0.10	-	14.43 ± 0.01	14.51 ± 0.04	-1.16 ± 0.11	SII	98
QSO B0913+0715	2.6180	20.35 ± 0.10	< 11.90	12.99 ± 0.01	13.88 ± 0.03	-2.41 ± 0.10	OI	84, 77
B0913+003	2.7400	20.74 ± 0.10	< 12.82	14.60 ± 0.00	-	-1.47 ± 0.10	SiII	1
Q0918+1636	2.4100	21.26 ± 0.06	13.23 ± 0.18	15.51 ± 0.23	-	-0.59 ± 0.19	ZnII	39
Q0918+1636	2.5800	20.96 ± 0.05	13.40 ± 0.01	15.43 ± 0.01	15.82 ± 0.01	-0.12 ± 0.05	ZnII	38
J0925+4004	0.2477	19.55 ± 0.15	-	14.22 ± 0.09	< 14.72	-0.29 ± 0.17	OI	2
J0927+5823	1.6400	20.40 ± 0.25	13.29 ± 0.05	> 15.27	15.61 ± 0.05	0.33 ± 0.25	ZnII	3, 4, 5
J0928+6025	0.1538	19.35 ± 0.15	-	14.90 ± 0.08	< 14.65	0.37 ± 0.25	FeII	2
SDSS0928+0939	2.9100	20.75 ± 0.15	-	14.10 ± 0.30	-	-1.83 ± 0.38	FeII	70
Q0930+28	3.2400	20.35 ± 0.10	-	13.49 ± 0.03	-	-2.07 ± 0.10	SiII	92, 93
QSO B0933-333	2.6820	20.50 ± 0.10	< 11.99	14.46 ± 0.08	-	-1.22 ± 0.12	SiII	1, 66
Q0933+733	1.4800	21.62 ± 0.10	12.71 ± 0.02	15.19 ± 0.01	-	-1.47 ± 0.10	ZnII	101
Q0935+417	1.3700	20.52 ± 0.10	12.26 ± 0.02	14.82 ± 0.10	-	-0.82 ± 0.10	ZnII	61, 79, 100
Q0948+433	1.2300	21.62 ± 0.06	13.15 ± 0.01	15.56 ± 0.01	-	-1.03 ± 0.06	ZnII	101
QSO B0951-0450	3.2350	20.25 ± 0.10	-	13.49 ± 0.03	-	-1.97 ± 0.10	SiII	93
QSO B0951-0450	3.8580	20.60 ± 0.10	-	14.06 ± 0.06	-	-1.47 ± 0.10	SiII	89

Continued on next page

Table B.23 – *Continued from previous page*

QSO name	$z_{\rm abs}$	log N(HI)	log N(Zn)	log N(Fe)	log N(S)	[X/H]	X	Reference
QSO B0951-0450	4.2030	20.55 ± 0.10	-	13.07 ± 0.19	< 13.89	-2.55 ± 0.10	OI	89
BR0951-04	3.8600	20.60 ± 0.10	-	14.06 ± 0.06	-	-1.46 ± 0.10	SiII	89, 90
QSO B0952+179	0.2380	21.32 ± 0.05	12.93 ± 0.04	-	-	-0.95 ± 0.06	ZnII	47
QSO B0952-0115	4.0240	20.55 ± 0.10	-	14.19 ± 0.08	-	-2.61 ± 0.11	SiII	90
PC0953+4749	4.2400	20.90 ± 0.15	-	13.90 ± 0.07	-	-2.18 ± 0.15	SiII	106, 93
PC0953+4749	3.8900	21.20 ± 0.10	-	15.09 ± 0.10	-	-1.29 ± 0.23	FeII	106, 93
PSSJ0957+33	3.2800	20.45 ± 0.08	< 12.13	14.37 ± 0.02	< 14.58	-1.08 ± 0.09	SiII	90, 93
PSSJ0957+33	4.1800	20.70 ± 0.10	-	14.13 ± 0.05	14.39 ± 0.06	-1.43 ± 0.12	SII	90, 93
J0958+0145	1.9300	20.40 ± 0.10	< 12.00	14.23 ± 0.05	14.44 ± 0.05	-1.08 ± 0.11	SII	3, 4, 5
J1001+5944	0.3035	19.32 ± 0.10	-	14.30 ± 0.04	< 14.53	-0.37 ± 0.10	OI	2
SDSS1003+5520	2.5000	20.35 ± 0.15	-	12.90 ± 0.30	-	-2.06 ± 0.34	SiII	70
J1004+0018	2.6900	21.39 ± 0.10	-	14.71 ± 0.04	14.70 ± 0.02	-1.81 ± 0.10	SII	28
J1004+0018	2.5400	21.30 ± 0.10	-	15.13 ± 0.02	15.09 ± 0.01	-1.33 ± 0.10	SII	28
Q1007+0042	1.0400	21.15 ± 0.20	13.27 ± 0.04	-	-	-0.44 ± 0.20	ZnII	63
Q1008+36	2.8000	20.70 ± 0.05	-	< 15.11	-	-1.75 ± 0.05	SiII	43
QSO J1009-0026	0.8400	20.20 ± 0.07	< 11.85	14.37 ± 0.03	-	-1.01 ± 0.19	FeII	59
QSO J1009-0026	0.8800	19.48 ± 0.08	12.38 ± 0.04	15.33 ± 0.06	-	0.34 ± 0.09	ZnII	59
J1009+0713	0.1140	20.68 ± 0.10	-	15.29 ± 0.17	15.25 ± 0.12	-0.55 ± 0.16	SII	2

Continued on next page

Table B.23 – *Continued from previous page*

QSO name	$z_{\rm abs}$	log N(HI)	log N(Zn)	log N(Fe)	log N(S)	[X/H]	X	Reference
Q1010+0003	1.2700	21.52 ± 0.07	12.96 ± 0.06	15.26 ± 0.05	-	-1.12 ± 0.09	ZnII	58, 63, 3, 4, 5
J1013+4240	4.7979	20.60 ± 0.15	-	-	-	-2.14 ± 0.15	SiII	98
J1013+5615	2.2800	20.70 ± 0.15	13.56 ± 0.05	> 15.45	-	0.30 ± 0.16	ZnII	3, 4, 5
BRI1013+0035	3.1000	21.10 ± 0.10	13.33 ± 0.02	15.18 ± 0.05	-	-0.33 ± 0.10	ZnII	95
J1017+6116	2.7684	20.60 ± 0.10	-	13.76 ± 0.05	-	-2.71 ± 0.10	OI	98
Q1021+30	2.9500	20.70 ± 0.10	< 12.23	14.04 ± 0.01	13.87 ± 0.07	-1.95 ± 0.12	SII	93, 95
J1024+0600	1.9000	20.60 ± 0.15	-	15.27 ± 0.08	15.45 ± 0.05	-0.27 ± 0.16	SII	3, 4, 5
LBQS 1026-0045B	0.6320	19.95 ± 0.07	12.46 ± 0.16	15.11 ± 0.06	-	-0.05 ± 0.17	ZnII	32
LBQS 1026-0045B	0.7090	20.04 ± 0.06	< 12.51	15.10 ± 0.03	-	-0.12 ± 0.19	FeII	32
J1028-0100	0.6321	19.95 ± 0.07	< 12.38	15.08 ± 0.08	-	-0.05 ± 0.21	FeII	26
J1028-0100	0.7089	20.04 ± 0.06	< 12.49	15.12 ± 0.07	-	-0.10 ± 0.20	FeII	26
SDSS1031+4055	2.5700	20.55 ± 0.10	-	13.80 ± 0.20	-	-1.93 ± 0.29	FeII	70
QSO B1036-2257	2.5330	19.30 ± 0.10	< 11.74	12.93 ± 0.01	-	-1.33 ± 0.10	MgII	114
QSO B1036-2257	2.7770	20.93 ± 0.05	< 12.36	14.68 ± 0.01	14.79 ± 0.02	-1.26 ± 0.05	SII	120, 52, 67
Q1037+0028	1.4244	20.04 ± 0.12	< 12.04	14.84 ± 0.02	-	-0.46 ± 0.12	SiII	60
J1037+0139	2.7000	20.50 ± 0.08	-	13.53 ± 0.02	-	-2.13 ± 0.09	OI	16, 70
QSO J1039-2719	2.1390	19.70 ± 0.05	12.09 ± 0.04	14.56 ± 0.02	14.82 ± 0.04	-0.17 ± 0.06	ZnII	109

Continued on next page

Table B.23 – *Continued from previous page*

QSO name	$z_{\rm abs}$	log N(HI)	log N(Zn)	log N(Fe)	log N(S)	[X/H]	X	Reference
J1042+3107	4.0865	20.75 ± 0.10	-	14.22 ± 0.03	-	-1.95 ± 0.10	SiII	98
J1042+0628	1.9400	20.70 ± 0.15	-	15.00 ± 0.15	15.08 ± 0.05	-0.74 ± 0.16	SII	3, 4, 5
SDSS1042+0117	2.2700	20.75 ± 0.15	< 12.74	15.08 ± 0.13	-	-0.79 ± 0.17	SiII	44
SDSS1043+6151	2.7900	20.60 ± 0.15	-	14.00 ± 0.20	-	-2.01 ± 0.34	SiII	70
QSO B1045+056	0.9510	19.28 ± 0.02	< 11.70	13.49 ± 0.08	-	-0.97 ± 0.20	FeII	58
SDSS1048+3911	2.3000	20.70 ± 0.10	-	13.70 ± 0.20	-	-2.31 ± 0.32	SiII	70
J1049-0110	1.6600	20.35 ± 0.15	13.14 ± 0.05	15.17 ± 0.05	15.47 ± 0.05	0.23 ± 0.16	ZnII	3, 4, 5
J1051+3107	4.1392	20.70 ± 0.20	-	13.95 ± 0.03	13.86 ± 0.08	-1.96 ± 0.22	SII	98
J1051+3545	4.3498	20.45 ± 0.10	-	13.66 ± 0.05	-	-1.88 ± 0.10	SiII	98
J1051+3545	4.8206	20.35 ± 0.10	-	-	-	-2.28 ± 0.10	SiII	98
Q1054-0020	0.8301	18.95 ± 0.18	< 11.76	14.33 ± 0.01	-	0.20 ± 0.25	FeII	60
Q1054-0020	0.9514	19.28 ± 0.02	< 11.70	13.66 ± 0.01	-	-0.80 ± 0.18	FeII	60
J1054+1633	3.8400	20.65 ± 0.20	-	13.58 ± 0.07	-	-2.25 ± 0.28	FeII	99
J1054+1633	4.8200	20.65 ± 0.20	-	-	-	-2.17 ± 0.20	SiII	99
J1054+1633	4.1400	20.65 ± 0.20	-	-	-	-0.35 ± 0.20	SiII	99
QSO B1055-301	1.9040	21.54 ± 0.10	12.91 ± 0.03	-	-	-1.19 ± 0.10	ZnII	1
Q1055+46	3.3200	20.34 ± 0.10	-	13.94 ± 0.06	-	-1.60 ± 0.15	SiII	91, 43
J1056+1208	1.6100	21.45 ± 0.15	13.76 ± 0.05	15.81 ± 0.05	> 16.15	-0.25 ± 0.16	ZnII	3, 4, 5
J1100+1122	4.3947	21.74 ± 0.10	-	15.21 ± 0.09	-	-1.71 ± 0.22	FeII	98
QSO B1101-26	1.8380	19.50 ± 0.05	< 11.27	13.51 ± 0.02	13.66 ± 0.11	-1.64 ± 0.10	OI	22
J1101+0531	4.3446	21.30 ± 0.10	-	15.19 ± 0.14	-	-1.07 ± 0.12	SiII	98
QSO B1104-181	1.6610	20.85 ± 0.01	12.48 ± 0.01	14.77 ± 0.02	-	-0.93 ± 0.01	ZnII	53

Continued on next page

Table B.23 – *Continued from previous page*

QSO name	$z_{\rm abs}$	log N(HI)	log N(Zn)	log N(Fe)	log N(S)	[X/H]	X	Reference
J1106+1044	1.8200	20.50 ± 0.15	-	> 15.15	15.33 ± 0.05	-0.29 ± 0.16	SII	3, 4, 5
QSO J1107+0048	0.7400	21.00 ± 0.04	13.06 ± 0.15	15.53 ± 0.02	-	-0.50 ± 0.16	ZnII	72, 122
QSO B1108-07	3.4820	19.95 ± 0.07	-	-	-	-1.57 ± 0.09	SiII	52
QSO B1108-07	3.6080	20.37 ± 0.07	-	13.88 ± 0.01	-	-1.69 ± 0.08	OI	90, 77
J1111+3509	4.0520	20.80 ± 0.15	-	14.13 ± 0.05	< 14.34	-1.95 ± 0.16	SiII	98
Q1111-152	3.2700	21.30 ± 0.05	12.32 ± 0.10	14.81 ± 0.01	14.62 ± 0.04	-1.54 ± 0.11	ZnII	52, 67, 120, 119
SDSS1116+4118A	2.6600	20.48 ± 0.10	12.40 ± 0.20	14.36 ± 0.10	-	-0.64 ± 0.22	ZnII	31
BR1117-1329	3.3500	20.84 ± 0.12	12.26 ± 0.03	14.83 ± 0.03	-	-1.14 ± 0.12	ZnII	71, 110
HE1122-1649	0.6800	20.45 ± 0.05	< 11.76	14.55 ± 0.01	-	-0.60 ± 0.13	SiII	123, 50
Q1127-145	0.3100	21.70 ± 0.08	13.53 ± 0.13	> 15.16	-	-0.73 ± 0.15	ZnII	45
J1131+6044	2.8800	20.50 ± 0.15	-	13.76 ± 0.03	< 13.29	-1.52 ± 0.20	SiII	34
HS1132+2243	2.7800	21.00 ± 0.07	< 11.99	14.02 ± 0.01	14.07 ± 0.06	-2.05 ± 0.09	SII	93
J1132+1209	4.3800	20.65 ± 0.20	-	13.78 ± 0.07	-	-2.05 ± 0.28	FeII	99
J1132+1209	5.0200	20.65 ± 0.20	-	< 13.55	-	-2.66 ± 0.20	SiII	99
J1135-0010	2.2100	22.05 ± 0.10	13.62 ± 0.03	15.76 ± 0.03	> 16.19	-0.99 ± 0.10	ZnII	48, 69
Q1137+3907	0.7200	21.10 ± 0.10	13.43 ± 0.05	15.45 ± 0.05	-	-0.23 ± 0.11	ZnII	58

Continued on next page

Table B.23 – *Continued from previous page*

QSO name	$z_{\rm abs}$	log N(HI)	log N(Zn)	log N(Fe)	log N(S)	[X/H]	X	Reference
J1142+0701	1.8400	21.50 ± 0.15	13.29 ± 0.05	15.47 ± 0.05	-	-0.77 ± 0.16	ZnII	3, 4, 5
QSO B1151+068	1.7750	21.30 ± 0.08	12.34 ± 0.08	-	-	-1.52 ± 0.11	ZnII	80
J115538.6+053050	3.3270	21.00 ± 0.10	-	-	15.31 ± 0.00	-0.81 ± 0.10	SII	114
J1155+3510	2.7582	21.00 ± 0.10	-	< 14.73	14.77 ± 0.01	-1.35 ± 0.10	SII	98
J1155+0530	2.6100	20.37 ± 0.11	-	-	-	-1.57 ± 0.16	SiII	119
J1155+0530	3.3300	21.05 ± 0.10	12.89 ± 0.07	15.37 ± 0.05	15.40 ± 0.05	-0.72 ± 0.12	ZnII	3, 4, 5
Q1157+014	1.9400	21.70 ± 0.10	13.11 ± 0.06	15.49 ± 0.05	> 15.16	-1.15 ± 0.12	ZnII	75, 24, 25, 3, 4, 5
J1200+4015	3.2200	20.85 ± 0.10	12.86 ± 0.04	15.31 ± 0.04	15.36 ± 0.01	-0.55 ± 0.11	ZnII	98
J1200+4618	4.4765	20.50 ± 0.15	-	14.27 ± 0.02	-	-1.41 ± 0.24	FeII	98
J1201+2117	3.7975	21.35 ± 0.15	-	15.56 ± 0.04	-	-0.75 ± 0.15	SiII	98
J1201+2117	4.1578	20.60 ± 0.15	-	13.76 ± 0.03	-	-2.38 ± 0.15	SiII	98
QSO B1202-074	4.3830	20.55 ± 0.16	-	13.88 ± 0.11	-	-1.49 ± 0.17	OI	57, 106, 27
J1202+3235	4.7955	21.10 ± 0.15	-	13.90 ± 0.03	-	-2.38 ± 0.24	FeII	98
J1202+3235	5.0647	20.30 ± 0.15	-	-	-	-2.66 ± 0.16	SiII	98
J1204-0021	3.6400	20.65 ± 0.20	-	13.85 ± 0.04	-	-1.98 ± 0.27	FeII	99
J120550.2+020131	1.7470	20.40 ± 0.10	12.08 ± 0.08	-	-	-0.88 ± 0.13	ZnII	37
J1208+0010	5.0800	20.65 ± 0.20	-	13.27 ± 0.08	-	-2.41 ± 0.20	SiII	99
QSO B1209+0919	2.5840	21.40 ± 0.10	12.98 ± 0.05	15.25 ± 0.03	-	-0.98 ± 0.11	ZnII	95

Continued on next page

Table B.23 – *Continued from previous page*

QSO name	$z_{\rm abs}$	log N(HI)	log N(Zn)	log N(Fe)	log N(S)	[X/H]	X	Reference
LBQS 1210+1731	1.8920	20.70 ± 0.08	12.37 ± 0.03	14.95 ± 0.06	14.96 ± 0.03	-0.89 ± 0.09	ZnII	90, 24
Q1215-0034	1.5543	19.56 ± 0.02	< 11.63	14.39 ± 0.01	-	-0.35 ± 0.18	FeII	60
Q1215+33	2.0000	20.95 ± 0.07	12.33 ± 0.05	14.75 ± 0.05	< 15.36	-1.18 ± 0.09	ZnII	89, 11, 90, 91
PG1216+069	0.0063	19.32 ± 0.03	-	13.23 ± 0.14	-	-1.69 ± 0.06	OI	115
J1219+1603	3.0000	20.35 ± 0.10	-	13.80 ± 0.10	-	-2.52 ± 0.35	OI	70
QSO B1220-1800	2.1120	20.12 ± 0.07	-	14.36 ± 0.04	14.53 ± 0.04	-0.71 ± 0.08	SII	66
Q1220-0040	0.9746	20.20 ± 0.07	< 11.69	14.34 ± 0.02	-	-1.04 ± 0.19	FeII	60
J1221+4445	4.8100	20.65 ± 0.20	-	14.35 ± 0.06	-	-2.21 ± 0.20	SiII	99
LBQS 1223+1753	2.4660	21.40 ± 0.10	12.55 ± 0.03	15.16 ± 0.02	15.14 ± 0.04	-1.41 ± 0.10	ZnII	90, 110
LBQS 1223+1753	2.5570	19.32 ± 0.15	< 11.51	13.98 ± 0.03	-	-0.45 ± 0.15	SiII	22
Q1224+0037	1.2300	20.88 ± 0.05	< 11.89	> 15.11	-	-1.29 ± 0.09	SiII	59
Q1225+0035	0.7700	21.38 ± 0.11	< 13.01	15.69 ± 0.03	-	-0.87 ± 0.21	FeII	58, 63
PHL 1226	0.1602	19.48 ± 0.10	-	14.76 ± 0.18	14.84 ± 0.11	0.24 ± 0.15	SII	105
QSO B1228-113	2.1930	20.60 ± 0.10	13.01 ± 0.04	-	-	-0.15 ± 0.11	ZnII	1
Q1228+1018	0.9376	19.41 ± 0.02	< 11.67	14.58 ± 0.01	-	-0.01 ± 0.18	FeII	60
PKS1229-021	0.4000	20.75 ± 0.07	12.92 ± 0.10	< 14.95	-	-0.39 ± 0.12	ZnII	8
QSO B1230-101	1.9310	20.48 ± 0.10	12.94 ± 0.05	-	-	-0.10 ± 0.11	ZnII	1
LBQS 1232+0815	1.7200	19.48 ± 0.13	< 11.58	13.50 ± 0.01	< 14.19	-0.58 ± 0.13	SiII	114

Continued on next page

Table B.23 – *Continued from previous page*

QSO name	$z_{\rm abs}$	log N(HI)	log N(Zn)	log N(Fe)	log N(S)	[X/H]	X	Reference
LBQS 1232+0815	2.3340	20.90 ± 0.04	12.64 ± 0.09	14.68 ± 0.08	14.83 ± 0.10	-0.82 ± 0.10	ZnII	108, 40, 12, 120
J1238+3437	2.4714	20.80 ± 0.10	-	14.06 ± 0.03	13.91 ± 0.11	-2.01 ± 0.15	SII	98
J1240+1455	3.1100	21.30 ± 0.20	12.90 ± 0.07	14.60 ± 0.03	15.56 ± 0.02	-0.96 ± 0.21	ZnII	34
J1241+4617	2.6674	20.70 ± 0.10	-	14.02 ± 0.04	-	-2.18 ± 0.10	SiII	98
LBQS1242+0006	1.8200	20.45 ± 0.10	-	-	-	-1.20 ± 0.15	SiII	119
J1245+3822	4.4500	20.65 ± 0.20	-	< 13.93	-	-2.14 ± 0.20	SiII	99
LBQS 1246-0217	1.7810	21.45 ± 0.00	13.01 ± 0.05	15.47 ± 0.02	-	-1.00 ± 0.05	ZnII	44
J1248+3110	3.6973	20.60 ± 0.10	-	14.11 ± 0.03	-	-1.67 ± 0.21	FeII	98
SDSS1249-0233	1.7800	21.45 ± 0.15	13.15 ± 0.05	15.47 ± 0.02	15.53 ± 0.05	-0.86 ± 0.16	ZnII	44, 3, 4, 5
SDSS1251+4120	2.7300	21.10 ± 0.10	-	14.20 ± 0.30	-	-2.71 ± 0.32	SiII	70
J1253+1046	4.6001	20.30 ± 0.15	-	14.09 ± 0.03	-	-1.39 ± 0.24	FeII	98
PSS1253-0228	2.7800	21.85 ± 0.20	12.77 ± 0.07	15.36 ± 0.04	-	-1.64 ± 0.21	ZnII	93
J1257-0111	4.0208	20.30 ± 0.10	-	13.65 ± 0.07	< 13.90	-1.56 ± 0.10	SiII	98
J1304+1202	2.9131	20.55 ± 0.15	< 11.83	13.72 ± 0.04	14.05 ± 0.05	-1.62 ± 0.16	SII	98
J1304+1202	2.9289	20.30 ± 0.15	< 11.95	13.85 ± 0.03	13.91 ± 0.04	-1.51 ± 0.16	SII	98
J1305+0924	2.0200	20.40 ± 0.15	-	15.21 ± 0.14	15.39 ± 0.05	-0.13 ± 0.16	SII	3, 4, 5
J1310+5424	1.8000	21.45 ± 0.15	13.57 ± 0.05	15.64 ± 0.05	> 16.05	-0.44 ± 0.16	ZnII	3, 4, 5
J1323-0021	0.7160	20.21 ± 0.20	13.43 ± 0.05	15.15 ± 0.03	-	0.66 ± 0.21	ZnII	72
Q1323-0021	0.7200	20.54 ± 0.15	13.29 ± 0.21	-	-	0.19 ± 0.26	ZnII	63

Continued on next page

Table B.23 – *Continued from previous page*

QSO name	$z_{\rm abs}$	log N(HI)	log N(Zn)	log N(Fe)	log N(S)	[X/H]	X	Reference
SDSS1325+1255	3.5500	20.50 ± 0.15	-	< 13.69	-	-2.51 ± 0.25	SiII	70
Q1328+307	0.6900	21.25 ± 0.10	12.72 ± 0.10	14.98 ± 0.10	-	-1.09 ± 0.14	ZnII	79, 8, 50
QSO J1330-2522	2.6540	19.56 ± 0.13	-	-	-	-1.83 ± 0.13	AlII	114
Q1330-2056	0.8526	19.40 ± 0.02	< 11.96	13.80 ± 0.01	-	-0.78 ± 0.18	FeII	60
QSO B1331+170	1.7760	21.15 ± 0.07	12.61 ± 0.01	14.60 ± 0.00	15.08 ± 0.11	-1.10 ± 0.07	ZnII	89, 22
J1335+0824	1.8600	20.65 ± 0.15	-	> 15.17	15.29 ± 0.05	-0.48 ± 0.16	SII	3, 4, 5
Q1337+113	2.8000	21.00 ± 0.08	< 12.25	14.33 ± 0.01	14.33 ± 0.02	-1.95 ± 0.11	OI	93, 110, 52, 95, 77, 67
J1340+1106	2.8000	21.00 ± 0.06	-	14.32 ± 0.01	14.30 ± 0.02	-1.65 ± 0.07	OI	16
J1340+3926	4.8300	20.65 ± 0.20	-	14.33 ± 0.05	-	-1.50 ± 0.27	FeII	99
QSO J1342-1355	3.1180	20.05 ± 0.08	-	13.93 ± 0.03	13.83 ± 0.03	-1.22 ± 0.08	OI	77
J1345+2329	5.0100	20.65 ± 0.20	-	-	14.66 ± 0.05	-1.11 ± 0.21	SII	99
BRI1346-03	3.7400	20.72 ± 0.10	-	< 14.13	-	-2.28 ± 0.10	SiII	89, 90
SDSS1350+5952	2.7600	20.65 ± 0.10	-	13.50 ± 0.20	-	-2.33 ± 0.29	FeII	70
J1353+5328	2.8349	20.80 ± 0.10	-	> 14.46	14.57 ± 0.02	-1.35 ± 0.10	SII	98
Q1354+258	1.4200	21.54 ± 0.06	12.59 ± 0.08	15.01 ± 0.04	-	-1.51 ± 0.10	ZnII	81
PKS1354-17	2.7800	20.30 ± 0.15	-	13.37 ± 0.08	-	-1.83 ± 0.16	SiII	93
QSO J1356-1101	2.3970	19.85 ± 0.08	< 12.38	13.44 ± 0.01	-	-1.59 ± 0.20	FeII	114

Continued on next page

Table B.23 – *Continued from previous page*

QSO name	$z_{\rm abs}$	log N(HI)	log N(Zn)	log N(Fe)	log N(S)	[X/H]	X	Reference
QSO J1356-1101	2.5010	20.44 ± 0.05	< 11.70	14.36 ± 0.08	14.27 ± 0.09	-1.29 ± 0.10	SII	1, 66
QSO J1356-1101	2.9670	20.80 ± 0.10	< 11.93	14.63 ± 0.05	-	-1.35 ± 0.12	SiII	1, 66
J1358+0349	2.8500	20.50 ± 0.10	-	13.01 ± 0.05	-	-2.81 ± 0.27	OI	70
J1358+6522	3.0700	20.35 ± 0.15	-	< 12.80	-	-3.01 ± 0.17	OI	70, 18
QSO B1409+0930	2.0190	20.65 ± 0.10	11.63 ± 0.10	-	-	-1.58 ± 0.14	ZnII	52
QSO B1409+0930	2.4560	20.53 ± 0.08	-	13.74 ± 0.02	-	-2.07 ± 0.10	OI	83
QSO B1409+0930	2.6680	19.80 ± 0.08	< 11.22	14.02 ± 0.13	13.54 ± 0.06	-1.18 ± 0.14	OI	83, 22
J1412+0624	4.1095	20.40 ± 0.15	-	13.83 ± 0.08	-	-1.75 ± 0.25	FeII	98
J1417+4132	1.9500	21.45 ± 0.25	13.55 ± 0.05	15.58 ± 0.05	> 15.80	-0.46 ± 0.25	ZnII	3, 4, 5
J1418+3142	3.9600	20.65 ± 0.20	-	< 15.78	-	-0.39 ± 0.20	SiII	99
J1419+0829	3.0500	20.40 ± 0.03	-	13.54 ± 0.03	-	-1.92 ± 0.04	OI	16, 86
QSO J1421-0643	3.4480	20.40 ± 0.10	< 11.98	14.18 ± 0.08	-	-1.29 ± 0.13	SiII	1, 66
Q1425+6039	2.8300	20.30 ± 0.04	12.18 ± 0.04	14.48 ± 0.01	-	-0.68 ± 0.06	ZnII	57, 91, 92, 95
J1431+3952	0.6000	21.20 ± 0.10	13.03 ± 0.19	15.15 ± 0.11	-	-0.73 ± 0.21	ZnII	35
PSS1432+39	3.2700	21.25 ± 0.10	< 12.65	> 14.93	-	-1.09 ± 0.11	SiII	93
J1435+3604	0.2026	19.80 ± 0.10	-	14.20 ± 0.08	14.60 ± 0.12	-0.32 ± 0.16	SII	2
SDSS1435+0420	1.6600	21.25 ± 0.15	< 13.21	15.70 ± 0.07	-	-0.84 ± 0.17	SiII	44
J1435+5359	2.3400	21.05 ± 0.10	-	-	14.78 ± 0.05	-1.39 ± 0.11	SII	43
Q1436-0051	0.7377	20.08 ± 0.11	12.67 ± 0.05	14.94 ± 0.02	-	0.03 ± 0.12	ZnII	60

Continued on next page

Table B.23 – *Continued from previous page*

QSO name	$z_{\rm abs}$	log N(HI)	log N(Zn)	log N(Fe)	log N(S)	[X/H]	X	Reference
J1437+2323	4.8000	20.65 ± 0.20	-	-	-	-2.34 ± 0.20	SiII	99
J1438+4314	4.3990	20.89 ± 0.15	-	14.42 ± 0.01	14.73 ± 0.01	-1.28 ± 0.15	SII	98
QSO J1439+1117	2.4180	20.10 ± 0.10	12.93 ± 0.04	14.28 ± 0.05	15.27 ± 0.06	0.27 ± 0.11	ZnII	66
SDSS1440+0637	2.5200	21.00 ± 0.15	-	14.50 ± 0.30	-	-2.31 ± 0.34	SiII	70
QSO J1443+2724	4.2240	20.95 ± 0.10	12.99 ± 0.03	15.33 ± 0.03	15.52 ± 0.01	-0.52 ± 0.10	ZnII	90, 66, 52
LBQS 1444+0126	2.0870	20.25 ± 0.07	12.12 ± 0.15	14.41 ± 0.03	14.62 ± 0.08	-0.69 ± 0.17	ZnII	51, 22
Q1451+123	2.4700	20.39 ± 0.10	-	13.36 ± 0.07	< 13.55	-1.90 ± 0.16	SiII	75, 110
Q1451+123	2.2600	20.30 ± 0.15	11.85 ± 0.11	14.33 ± 0.07	-	-1.01 ± 0.19	ZnII	22
J1454+0941	1.7900	20.50 ± 0.15	12.72 ± 0.05	15.02 ± 0.12	15.25 ± 0.06	-0.34 ± 0.16	ZnII	3, 4, 5
Q1455-0045	1.0929	20.08 ± 0.06	< 11.91	14.57 ± 0.01	-	-0.95 ± 0.12	SiII	60
J1456+0407	2.6700	20.35 ± 0.10	-	13.00 ± 0.10	-	-2.49 ± 0.30	OI	70
Q1501+0019	1.4800	20.85 ± 0.13	12.93 ± 0.06	-	-	-0.48 ± 0.14	ZnII	58
Q1502+4837	2.5700	20.30 ± 0.15	-	14.15 ± 0.12	-	-1.57 ± 0.17	SiII	93
PSS1506+5220	3.2200	20.67 ± 0.07	< 12.11	13.71 ± 0.03	-	-2.30 ± 0.07	SiII	93
J1507+4406	3.0644	20.75 ± 0.10	-	14.03 ± 0.03	13.97 ± 0.10	-1.90 ± 0.14	SII	98
J1509+1113	2.0300	21.30 ± 0.15	-	15.48 ± 0.07	15.69 ± 0.05	-0.73 ± 0.16	SII	3, 4, 5
PSS1535+2943	3.7600	20.40 ± 0.15	-	-	-	-1.97 ± 0.16	SiII	94
J1541+3153	2.4435	20.95 ± 0.10	12.03 ± 0.11	14.50 ± 0.11	-	-1.48 ± 0.15	ZnII	98
SBS1543+393	0.0100	20.42 ± 0.04	-	-	15.19 ± 0.04	-0.35 ± 0.06	SII	9
J1553+3548	0.0830	19.55 ± 0.15	-	14.01 ± 0.07	< 14.24	-0.84 ± 0.16	SiII	2

Continued on next page

Table B.23 – *Continued from previous page*

QSO name	$z_{\rm abs}$	log N(HI)	log N(Zn)	log N(Fe)	log N(S)	[X/H]	X	Reference
J1555+4800	2.3900	21.50 ± 0.15	< 13.95	15.84 ± 0.05	> 15.88	-0.46 ± 0.16	SiII	3, 4, 5
SDSS1557+2320	3.5400	20.65 ± 0.10	-	13.50 ± 0.30	-	-2.24 ± 0.15	OI	70
SDSSJ1558+4053	2.5500	20.30 ± 0.04	-	13.07 ± 0.06	-	-2.45 ± 0.06	OI	85
J1558-0031	2.7000	20.67 ± 0.05	-	14.11 ± 0.03	14.07 ± 0.02	-1.72 ± 0.05	SII	43
PHL 1598	0.4297	19.18 ± 0.03	-	-	14.36 ± 0.05	0.06 ± 0.06	SII	105
J1604+3951	3.1600	21.75 ± 0.20	13.12 ± 0.05	15.47 ± 0.05	15.71 ± 0.05	-1.19 ± 0.21	ZnII	34, 3, 4, 5
J1607+1604	4.4741	20.30 ± 0.15	-	14.03 ± 0.06	-	-1.71 ± 0.15	SiII	98
SDSS1610+4724	2.5100	21.15 ± 0.15	13.56 ± 0.05	15.62 ± 0.05	> 16.01	-0.15 ± 0.16	ZnII	44, 3, 4, 5
J1616+4154	0.3211	20.60 ± 0.20	-	15.02 ± 0.05	15.37 ± 0.11	-0.35 ± 0.23	SII	2
J1619+3342	0.0963	20.55 ± 0.10	-	14.38 ± 0.15	15.08 ± 0.09	-0.59 ± 0.13	SII	2
QSO J1621-0042	3.1040	19.70 ± 0.20	-	13.30 ± 0.04	-	-1.43 ± 0.20	SiII	114
3C336	0.6600	20.36 ± 0.10	-	14.59 ± 0.11	-	-0.95 ± 0.23	FeII	113, 14, 50
J1623+0718	1.3400	21.35 ± 0.10	12.91 ± 0.09	15.28 ± 0.05	-	-1.00 ± 0.13	ZnII	35
J1626+2751	4.3110	21.34 ± 0.15	-	15.33 ± 0.06	-	-1.19 ± 0.24	FeII	98
J1626+2751	4.4975	21.39 ± 0.15	-	14.08 ± 0.02	-	-2.49 ± 0.24	FeII	98
J1626+2751	5.1791	20.94 ± 0.15	-	> 14.59	14.60 ± 0.02	-1.46 ± 0.15	SII	98
J1626+2858	4.6100	20.65 ± 0.20	-	-	-	-2.73 ± 0.22	SiII	99
J1629+0913	1.9000	20.80 ± 0.10	12.68 ± 0.08	> 14.93	15.24 ± 0.05	-0.68 ± 0.13	ZnII	3, 4, 5

Continued on next page

Table B.23 – *Continued from previous page*

QSO name	$z_{\rm abs}$	log N(HI)	log N(Zn)	log N(Fe)	log N(S)	[X/H]	X	Reference
4C 12.59	0.5310	20.70 ± 0.09	-	14.26 ± 0.08	-	-1.62 ± 0.22	FeII	114
4C 12.59	0.9000	19.70 ± 0.04	< 12.18	14.17 ± 0.03	-	-0.71 ± 0.19	FeII	60
J1637+2901	3.5000	20.70 ± 0.10	-	13.84 ± 0.10	-	-3.10 ± 0.22	OI	70
J1654+2227	4.0022	20.60 ± 0.15	-	14.09 ± 0.03	-	-1.69 ± 0.24	FeII	98
SDSS1709+3417	2.5300	20.45 ± 0.15	-	14.30 ± 0.20	-	-1.46 ± 0.25	SiII	70
SDSS1709+3417	3.0100	20.40 ± 0.10	-	13.90 ± 0.20	-	-1.68 ± 0.29	FeII	70
J1712+5755	2.2500	20.60 ± 0.10	-	14.49 ± 0.02	-	-1.19 ± 0.12	SiII	43
Q1715+4606	0.6500	20.44 ± 0.10	< 12.87	14.94 ± 0.03	-	-0.68 ± 0.21	FeII	58
PSS1715+3809	3.3400	21.05 ± 0.12	< 12.11	13.74 ± 0.04	-	-2.49 ± 0.22	FeII	94
Q1727+5302	1.0300	21.41 ± 0.15	12.76 ± 0.24	14.81 ± 0.01	-	-1.21 ± 0.28	ZnII	116, 63
Q1727+5302	0.9400	21.16 ± 0.10	13.25 ± 0.11	15.29 ± 0.01	-	-0.47 ± 0.15	ZnII	116, 63
Q1733+5533	1.0000	20.70 ± 0.10	< 12.11	-	-	-0.73 ± 0.12	SiII	58, 63
SDSS1737+5828	4.7400	20.65 ± 0.10	-	13.30 ± 0.10	-	-2.53 ± 0.23	FeII	106
J1737+5828	4.7400	20.65 ± 0.20	-	-	-	-2.23 ± 0.21	SiII	99
Q1755+578	1.9700	21.40 ± 0.15	13.85 ± 0.05	15.79 ± 0.05	> 16.12	-0.11 ± 0.16	ZnII	3, 4, 5
Q1759+75	2.6300	20.76 ± 0.05	> 11.65	15.08 ± 0.02	15.24 ± 0.01	-0.64 ± 0.05	SII	89, 90, 43
PSS1802+5616	3.8100	20.35 ± 0.20	-	13.67 ± 0.10	-	-1.99 ± 0.22	SiII	94
PSS1802+5616	3.5500	20.50 ± 0.10	< 12.63	14.08 ± 0.06	-	-1.60 ± 0.21	FeII	94
PSS1802+5616	3.3900	20.30 ± 0.10	< 12.41	14.26 ± 0.04	-	-1.22 ± 0.21	FeII	94
QSO B2000-330	3.1720	19.75 ± 0.15	-	< 12.86	-	-2.29 ± 0.15	OI	96

Continued on next page

Table B.23 – *Continued from previous page*

QSO name	$z_{\rm abs}$	log N(HI)	log N(Zn)	log N(Fe)	log N(S)	[X/H]	X	Reference
QSO B2000-330	3.1880	19.80 ± 0.15	-	13.69 ± 0.04	-	-1.34 ± 0.15	SiII	96
QSO B2000-330	3.1920	19.10 ± 0.15	-	13.49 ± 0.07	-	-0.48 ± 0.15	SiII	96
J2036-0553	2.2800	21.20 ± 0.15	-	14.68 ± 0.11	-	-1.67 ± 0.16	SiII	43
Q2051+1950	1.1157	20.00 ± 0.15	12.90 ± 0.10	15.02 ± 0.02	-	0.34 ± 0.18	ZnII	60
SDSS2059-0529	2.2100	20.80 ± 0.20	12.94 ± 0.11	15.00 ± 0.11	-	-0.42 ± 0.23	ZnII	44
Q2059-360	3.0800	20.98 ± 0.08	-	14.52 ± 0.07	14.41 ± 0.04	-1.58 ± 0.09	OI	75, 110, 77
SDSS2100-0641	3.0900	21.05 ± 0.15	13.24 ± 0.05	15.37 ± 0.05	15.49 ± 0.05	-0.37 ± 0.16	ZnII	44, 3, 4, 5
LBQS 2114-4347	1.9120	19.50 ± 0.10	< 12.17	14.02 ± 0.01	< 13.97	-0.70 ± 0.10	MgII	114
QSO J2119-3536	1.9960	20.10 ± 0.07	12.30 ± 0.09	14.77 ± 0.09	< 14.95	-0.36 ± 0.11	ZnII	22
QSO B2126-15	2.6380	19.25 ± 0.15	< 11.58	14.05 ± 0.01	-	-0.09 ± 0.15	SiII	114
QSO B2126-15	2.7690	19.20 ± 0.15	< 11.95	14.17 ± 0.00	-	0.08 ± 0.15	SiII	114
LBQS 2132-4321	1.9160	20.74 ± 0.09	12.66 ± 0.02	15.03 ± 0.02	> 14.90	-0.64 ± 0.09	ZnII	114
LBQS 2138-4427	2.3830	20.60 ± 0.05	12.05 ± 0.07	-	-	-1.11 ± 0.09	ZnII	52
LBQS 2138-4427	2.8520	20.98 ± 0.05	11.99 ± 0.05	14.65 ± 0.02	14.50 ± 0.02	-1.55 ± 0.07	ZnII	51, 110
J2144-0632	4.1300	20.40 ± 0.15	-	< 13.51	-	-2.37 ± 0.47	OI	70
PSSJ2155+1358	3.3200	20.50 ± 0.15	12.05 ± 0.32	14.51 ± 0.13	-	-1.01 ± 0.35	ZnII	19, 93
LBQS 2206-1958A	2.0760	20.44 ± 0.05	< 11.20	13.33 ± 0.01	-	-2.08 ± 0.06	OI	84

Continued on next page

Table B.23 – *Continued from previous page*

QSO name	$z_{\rm abs}$	log N(HI)	log N(Zn)	log N(Fe)	log N(S)	[X/H]	X	Reference
Q2206-199	1.9200	20.68 ± 0.03	12.91 ± 0.01	15.30 ± 0.02	15.42 ± 0.02	-0.33 ± 0.03	ZnII	88, 90, 91, 117
QSO B2222-396	2.1540	20.85 ± 0.10	-	14.42 ± 0.03	14.08 ± 0.02	-1.89 ± 0.10	SII	66
SDSS2222-0946	2.3500	20.50 ± 0.15	< 12.78	15.06 ± 0.08	15.37 ± 0.05	-0.25 ± 0.16	SII	44, 3, 4, 46, 5
Q2223+20	3.1200	20.30 ± 0.10	-	13.32 ± 0.06	-	-2.17 ± 0.11	SiII	93
Q2228-3954	2.1000	21.20 ± 0.10	12.51 ± 0.06	15.17 ± 0.02	-	-1.25 ± 0.12	ZnII	67
LBQS 2230+0232	1.8640	20.83 ± 0.10	12.80 ± 0.03	15.19 ± 0.02	15.29 ± 0.10	-0.59 ± 0.10	ZnII	89, 90, 91, 24, 25, 3, 4, 5
Q2231-00	2.0700	20.53 ± 0.08	12.30 ± 0.05	14.83 ± 0.03	15.10 ± 0.15	-0.79 ± 0.09	ZnII	89, 90, 21, 23
QSO B2237-0607	4.0790	20.55 ± 0.10	-	13.85 ± 0.11	-	-1.79 ± 0.10	SiII	57, 106, 43
J223941.8-294955	1.8250	19.84 ± 0.14	12.76 ± 0.06	14.33 ± 0.04	-	0.36 ± 0.15	ZnII	24

Continued on next page

Table B.23 – *Continued from previous page*

QSO name	$z_{\rm abs}$	log N(HI)	log N(Zn)	log N(Fe)	log N(S)	[X/H]	X	Reference
J2241+1225	2.4200	21.15 ± 0.15	-	15.02 ± 0.08	> 15.01	-1.31 ± 0.25	FeII	3, 4, 5
PSS2241+1352	4.2800	21.15 ± 0.10	-	> 14.65	14.58 ± 0.03	-1.69 ± 0.10	SII	93
HE2243-6031	2.3300	20.67 ± 0.02	12.22 ± 0.03	14.92 ± 0.01	14.88 ± 0.01	-1.01 ± 0.04	ZnII	54
J2252+1425	4.7475	20.60 ± 0.15	-	13.98 ± 0.11	< 14.41	-1.80 ± 0.26	FeII	98
QSO B2311-373	2.1820	20.48 ± 0.13	< 11.82	14.23 ± 0.04	-	-1.45 ± 0.15	SiII	1, 66
B2314-409	1.8600	20.90 ± 0.10	12.52 ± 0.10	15.08 ± 0.10	15.10 ± 0.15	-0.94 ± 0.14	ZnII	30
PSS2315+0921	3.4300	21.10 ± 0.20	-	> 14.63	-	-1.46 ± 0.21	SiII	94
QSO B2318-1107	1.6290	20.52 ± 0.14	< 11.74	14.14 ± 0.02	< 14.54	-1.56 ± 0.23	FeII	114
QSO B2318-1107	1.9890	20.68 ± 0.05	12.50 ± 0.03	14.91 ± 0.01	15.09 ± 0.02	-0.74 ± 0.06	ZnII	64
J2321+1421	2.5700	20.70 ± 0.05	< 11.84	14.18 ± 0.03	< 13.60	-1.76 ± 0.06	SiII	34
PSS2323+2758	3.6800	20.95 ± 0.10	-	13.32 ± 0.13	-	-2.54 ± 0.10	SiII	93
QSO J2328+0022	0.6520	20.32 ± 0.07	12.43 ± 0.15	14.84 ± 0.01	-	-0.45 ± 0.17	ZnII	72
QSO B2332-094	3.0570	20.50 ± 0.07	< 12.17	14.34 ± 0.03	14.34 ± 0.18	-1.24 ± 0.07	OI	51, 93, 77, 119
J233544.2+150118	0.6800	19.70 ± 0.30	12.37 ± 0.04	14.83 ± 0.03	-	0.11 ± 0.30	ZnII	74
J2340-00	2.0500	20.35 ± 0.15	12.63 ± 0.07	14.98 ± 0.05	14.95 ± 0.05	-0.28 ± 0.17	ZnII	95, 3, 4, 5
Q2342+34	2.9100	21.10 ± 0.10	< 12.60	14.91 ± 0.07	15.19 ± 0.05	-1.03 ± 0.11	SII	93, 95, 3, 4, 120, 5

Continued on next page

Table B.23 – *Continued from previous page*

QSO name	$z_{\rm abs}$	log N(HI)	log N(Zn)	log N(Fe)	log N(S)	[X/H]	X	Reference
QSO B2343+125	2.4310	20.40 ± 0.07	12.20 ± 0.07	14.52 ± 0.02	14.66 ± 0.02	-0.76 ± 0.10	ZnII	64
Q2344+12	2.5400	20.36 ± 0.10	-	14.03 ± 0.03	< 14.20	-1.69 ± 0.10	SiII	90, 92
PSSJ2344+0342	3.2200	21.25 ± 0.08	12.23 ± 0.30	15.06 ± 0.15	-	-1.58 ± 0.31	ZnII	19, 93
QSO J2346+1247	2.5690	20.98 ± 0.04	12.88 ± 0.06	15.24 ± 0.04	15.38 ± 0.05	-0.66 ± 0.07	ZnII	104
QSO B2348-0180	2.4260	20.50 ± 0.10	< 11.20	14.83 ± 0.07	15.06 ± 0.10	-0.56 ± 0.14	SII	65
QSO B2348-0180	2.6150	21.30 ± 0.08	< 11.87	14.57 ± 0.09	-	-1.92 ± 0.11	SiII	90
QSO B2348-147	2.2790	20.56 ± 0.08	< 11.28	13.79 ± 0.02	13.72 ± 0.12	-1.95 ± 0.14	SII	89, 24
Q2352-0028	0.8730	19.18 ± 0.09	< 11.67	13.48 ± 0.02	-	-0.88 ± 0.20	FeII	60
Q2352-0028	1.0318	19.81 ± 0.13	< 11.93	14.91 ± 0.01	-	0.17 ± 0.13	SiII	60
Q2352-0028	1.2467	19.60 ± 0.24	< 11.53	14.21 ± 0.01	-	-0.57 ± 0.30	FeII	60
Q2353-0028	0.6000	21.54 ± 0.15	13.25 ± 0.29	-	-	-0.85 ± 0.33	ZnII	63
B2355-106	1.1700	21.00 ± 0.10	12.76 ± 0.17	15.08 ± 0.10	-	-0.80 ± 0.20	ZnII	35
LBQS 2359-0216	2.0950	20.65 ± 0.10	12.60 ± 0.03	14.51 ± 0.03	-	-0.61 ± 0.10	ZnII	89
LBQS 2359-0216	2.1540	20.30 ± 0.10	< 11.90	13.89 ± 0.03	-	-1.49 ± 0.10	SiII	89

References: 1: Akerman et al. 2005, 2: Battisti et al. 2012, 3: Berg, Ellison, Venn, et al. 2013, 4: Berg, Neeleman, et al. 2015, 5: Berg, Ellison, Prochaska, et al. 2015, 6: Bergeron et al. 1986, 7: Blades et al. 1982, 8: Boissé et al. 1998, 9: Bowen et al. 2005, 10: Carswell et al. 1996, 11: Centurion, Bonifacio, et al. 2000, 12: Centurion, Molaro, et al. 2003, 13: Chen et al. 2005, 14: Churchill et al. 2000, 15: Cooke, Pettini, Steidel, King, et al. 2010, 16: Cooke, Pettini, Steidel, Rudie, and Nissen 2011, 17: Cooke, Pettini, Steidel, Rudie, and Jorgenson 2011, 18: Cooke, Pettini, and Murphy 2012, 19: Dessauge-Zavadsky (unpublished), 20: Dessauges-Zavadsky, D'Odorico, et al. 2001, 21: Dessauges-Zavadsky, Prochaska, and D'Odorico 2002, 22: Dessauges-Zavadsky, Péroux, et al. 2003, 23: Dessauges-Zavadsky et al. 2004, 24: Dessauges-Zavadsky, Prochaska, D'Odorico, et al. 2006, 25: Dessauges-Zavadsky et al. 2007, 26: Dessauges-Zavadsky,

Ellison, et al. 2009, 27: D'Odorico and Molaro 2004, 28: Dutta et al. 2014, 29: Ellison, Pettini, et al. 2001, 30: Ellison and Lopez 2001, 31: Ellison, Hennawi, et al. 2007, 32: Ellison, York, et al. 2008, 33: Ellison and Lopez 2009, 34: Ellison, Prochaska, et al. 2010, 35: Ellison, Kanekar, et al. 2012, 36: Fox, Petitjean, et al. 2007, 37: Fox, Prochaska, et al. 2009, 38: Fynbo, Ledoux, et al. 2011, 39: Fynbo, Geier, et al. 2013, 40: Ge et al. 2001, 41: Guimarães et al. 2012, 42: Heinmüller et al. 2006, 43: Henry et al. 2007, 44: Herbert-Fort et al. 2006, 45: Kanekar et al. 2014, 46: Krogager, Fynbo, Ledoux, et al. 2013, 47: Kulkarni, Fall, et al. 2005, 48: Kulkarni, Meiring, et al. 2012, 49: Ledoux, Srianand, et al. 2002, 50: Ledoux, Bergeron, et al. 2002, 51: Ledoux, Petitjean, and Srianand 2003, 52: Ledoux, Petitjean, Fynbo, et al. 2006, 53: Lopez, Reimers, Rauch, et al. 1999, 54: Lopez, Reimers, D'Odorico, et al. 2002, 55: Lopez and Ellison 2003, 56: Lopez, Reimers, Gregg, et al. 2005, 57: Lu et al. 1996, 58: Meiring, Kulkarni, et al. 2006, 59: Meiring, Lauroesch, Kulkarni, Péroux, Khare, York, and Crotts 2007, 60: Meiring, Lauroesch, Kulkarni, Péroux, Khare, and York 2009, 61: Meyer et al. 1995, 62: Molaro et al. 2000, 63: Nestor et al. 2008, 64: Noterdaeme, Ledoux, Petitjean, Le Petit, et al. 2007, 65: Noterdaeme, Petitjean, Srianand, et al. 2007, 66: Noterdaeme, Petitjean, Ledoux, et al. 2008, 67: Noterdaeme, Ledoux, Petitjean, and Srianand 2008, 68: Noterdaeme, López, et al. 2012, 69: Noterdaeme, Laursen, et al. 2012, 70: Penprase et al. 2010, 71: Peroux et al. 2002, 72: Péroux, Kulkarni, Meiring, et al. 2006, 73: Péroux et al. 2007, 74: Péroux, Meiring, Kulkarni, Khare, et al. 2008, 75: Petitjean et al. 2000, 76: Petitjean et al. 2002, 77: Petitjean, Ledoux, et al. 2008, 78: Pettini, Smith, Hunstead, et al. 1994, 79: Pettini, King, et al. 1997, 80: Pettini, Smith, King, et al. 1997, 81: Pettini, Ellison, Steidel, and Bowen 1999, 82: Pettini, Ellison, Steidel, Shapley, et al. 2000, 83: Pettini, Ellison, Bergeron, et al. 2002, 84: Pettini, Zych, Murphy, et al. 2008, 85: Pettini, Zych, Steidel, et al. 2008, 86: Pettini and Cooke 2012, 87: Prochaska and Wolfe 1996, 88: Prochaska and Wolfe 1997a, 89: Prochaska and Wolfe 1999, 90: Prochaska and Wolfe 2002, 91: Prochaska, Gawiser, and Wolfe 2001, 92: Prochaska, Henry, et al. 2002, 93: Prochaska, Gawiser, Wolfe, et al. 2003, 94: Prochaska, Castro, et al. 2003, 95: Prochaska, Wolfe, et al. 2007, 96: Prochter et al. 2010, 97: Quast et al. 2008, 98: Rafelski, Wolfe, et al. 2012, 99: Rafelski, Neeleman, et al. 2014, 100: Rao and Turnshek 2000, 101: Rao, Prochaska, et al. 2005, 102: Rao, Turnshek, and Nestor 2006, 103: Richter et al. 2005, 104: Rix et al. 2007, 105: Som, Kulkarni, Meiring, York, Péroux, Lauroesch, et al. 2015, 106: Songaila et al. 2002, 107: Srianand and Petitjean 1998, 108: Srianand, Petitjean, and Ledoux 2000, 109: Srianand and Petitjean 2001, 110: Srianand, Petitjean, Ledoux, et al. 2005, 111: Srianand, Gupta, and Petitjean 2007, 112: Srianand, Gupta, Petitjean, et al. 2012, 113: Steidel, Dickinson, et al. 1997, 114: This work (Quiret, Péroux, et al., 2016), 115: Tripp, Jenkins, et al. 2005, 116: Turnshek, Rao, et al. 2004, 117: Vladilo, Abate, et al. 2011, 118: Zafar, Watson, et al. 2011, 119: Zafar, Centurion, et al. 2014, 120: Zafar, Vladilo, et al. 2014, 121: Zafar et al. (in prep), 122: Zych et al. 2009, 123: Varga

et al. 2000

Bibliography

[1] K. L. Adelberger, a. E. Shapley, C. C. Steidel, et al. “The Connection Between Galaxies and Intergalactic Absorption Lines at Redshift $2 < \mathrm{z} < 3$”. In: *Astrophys. J.* 629 (2005), pp. 636–653.

[2] Kurt L Adelberger, Charles C Steidel, Alice E Shapley, et al. “Galaxies and Intergalactic Matter at Redshift z $\sim$ 3: Overview”. In: *Astrophys. J.* 584.1 (Feb. 2003), pp. 45–75.

[3] Oscar Agertz, Romain Teyssier, and Ben Moore. “The formation of disc galaxies in a ΛCDM universe”. In: *Mon. Not. R. Astron. Soc.* 410.2 (Jan. 2011), pp. 1391–1408.

[4] Chris J. Akerman, Sara L. Ellison, Max Pettini, et al. “Zn and Cr abundances in damped Lyman alpha systems from the CORALS survey”. In: *Astron. Astrophys.* 440.2 (Sept. 2005), pp. 499–509.

[5] R. Alpher, H. Bethe, and G. Gamow. “The Origin of Chemical Elements”. In: *Phys. Rev.* 73.7 (Apr. 1948), pp. 803–804.

[6] Ralph A. Alpher and Robert C. Herman. “On the Relative Abundance of the Elements”. In: *Phys. Rev.* 74.12 (Dec. 1948), pp. 1737–1742.

[7] M. Asplund, N. Grevesse, a. J. Sauval, et al. “The chemical composition of the Sun”. In: *Annu. Rev. Astron. Astrophys* 47 (2009), pp. 481–522.

[8] Hakim Atek, Daniel Kunth, Daniel Schaerer, et al. “Empirical estimate of Lya escape fraction in a statistical sample of Lya emitters”. In: *Astron. Astrophys.* 506.2 (Nov. 2009), pp. L1–L4.

[9] D. Aubert, C. Pichon, and S. Colombi. “The origin and implications of dark matter anisotropic cosmic infall on”. In: *Mon. Not. R. Astron. Soc.* 352.2 (Aug. 2004), pp. 376–398.

[10] R Bacon, J Brinchmann, J Richard, et al. “The MUSE 3D view of the Hubble Deep Field South”. In: *Astron. Astrophys.* 575 (2014), A75.

[11] John N. Bahcall and Lyman Jr. Spitzer. “Absorption Lines Produced by Galactic Halos”. In: *Astrophys. J.* 156 (May 1969), p. L63.

[12] B Barbuy, V Hill, M Zoccali, et al. “Zinc abundances in Galactic bulge field red giants : Implications for DLA systems”. In: (2015).

[13] K. A. Barger, L. M. Haffner, B. P. Wakker, et al. “PRESENT-DAY GALACTIC EVOLUTION: LOW-METALLICITY, WARM, IONIZED GAS INFLOW ASSOCIATED WITH HIGH-VELOCITY CLOUD COMPLEX A”. In: *Astrophys. J.* 761.2 (Dec. 2012), p. 145.

[14] a. J. Battisti, J. D. Meiring, T. M. Tripp, et al. “THE FIRST OBSERVATIONS OF LOW-REDSHIFT DAMPED Lya SYSTEMS WITH THE COSMIC ORIGINS SPECTROGRAPH: CHEMICAL ABUNDANCES AND AFFILIATED GALAXIES”. In: *Astrophys. J.* 744.2 (2012), p. 93.

[15] Amber Bauermeister, Leo Blitz, and Chung-Pei Ma. “The Gas Consumption History to redshift 4”. In: *Astrophys. J.* 717.2008 (2010), pp. 323–332.

[16] T. A. M. Berg, S. L. Ellison, K. A. Venn, et al. “A search for boron in damped Lya systems”. In: *Mon. Not. R. Astron. Soc.* 434.4 (2013), pp. 2892–2906.

[17] Trystyn A M Berg, Sara L Ellison, J Xavier Prochaska, et al. “The chemistry of the most metal-rich damped Lyman a systems at z $\sim$ 2 – II. Context with the Local Group”. In: *Mon. Not. R. Astron. Soc.* 452.4 (Oct. 2015), pp. 4326–4346.

[18] Trystyn A. M. Berg, Marcel Neeleman, J. Xavier Prochaska, et al. “The Most Metal-rich Damped Lya Systems at z $>$ 1.5 I: The Data”. In: *Publ. Astron. Soc. Pacific* 127.948 (Feb. 2015), pp. 167–210.

[19] J. Bergeron and S. Dodorico. “Ionization state of the absorption systems in the BL Lac object 0215 + 015 and properties of low-excitation absorbers”. In: *Mon. Not. R. Astron. Soc.* 220 (1986), pp. 833–843.

[20] S. Bertone, a. Aguirre, and J. Schaye. “How the diffuse Universe cools”. In: *Mon. Not. R. Astron. Soc.* 430.4 (Feb. 2013), pp. 3292–3313.

[21] Serena Bertone and Joop Schaye. “Rest-frame ultraviolet line emission from the intergalactic medium at”. In: *Mon. Not. R. Astron. Soc.* 419.1 (Jan. 2012), pp. 780–798.

[22] Serena Bertone, Joop Schaye, C M Booth, et al. “Metal-line emission from the warm-hot intergalactic medium - II. Ultraviolet”. In: *Mon. Not. R. Astron. Soc.* 408.2 (Oct. 2010), pp. 1120–1138.

[23] Serena Bertone, Joop Schaye, Claudio Dalla Vecchia, et al. “Metal-line emission from the warm-hot intergalactic medium - I. Soft X-rays”. In: *Mon. Not. R. Astron. Soc.* 407.1 (Sept. 2010), pp. 544–566.

[24] Yuval Birnboim and Avishai Dekel. “Virial shocks in galactic haloes?” In: *Mon. Not. R. Astron. Soc.* 345.1 (Oct. 2003), pp. 349–364.

[25] J. C. Blades, R. W. Hunstead, H. S. Murdoch, et al. “Optical absorption lines in the high redshift BL Lac object 0215 + 015”. In: *Mon. Not. R. Astron. Soc.* 200 (1982), pp. 1091–1111.

[26] Patrick Boissé, Vincent Le Brun, Jacqueline Bergeron, et al. “A HST Spectroscopic study of QSOs with intermediate redshift damped Lyman-alpha systems”. In: *Astron. Astrophys.* 333 (Jan. 1998), p. 23.

[27] H. Bondi and T. Gold. “The Steady-State Theory of the Expanding Universe”. In: *Mon. Not. R. Astron. Soc.* 108.3 (June 1948), pp. 252–270.

[28] R. Bordoloi, S. J. Lilly, C. Knobel, et al. “THE RADIAL AND AZIMUTHAL PROFILES OF Mg II ABSORPTION AROUND $0.5 < z < 0.9$ zCOSMOS GALAXIES OF DIFFERENT COLORS, MASSES, AND ENVIRONMENTS”. In: *Astrophys. J.* 743.1 (Dec. 2011), p. 10.

[29] Elena Borisova, Sebastiano Cantalupo, Simon J. Lilly, et al. “UBIQUITOUS GIANT Ly a NEBULAE AROUND THE BRIGHTEST QUASARS AT $z \sim 3.5$ REVEALED WITH MUSE”. In: *Astrophys. J.* 831.1 (Oct. 2016), p. 39.

[30] N Bouché, M T Murphy, G G Kacprzak, et al. “Signatures of cool gas fueling a star-forming galaxy at redshift 2.3.” In: *Science* 341.6141 (July 2013), pp. 50–3.

[31] N. Bouché, M.T. Murphy, C. Péroux, et al. “Are strong Mg II absorbers the signature of outflows?” In: *New Astron. Rev.* 51.1-2 (Feb. 2007), pp. 131–134.

[32] Nicolas Bouché, W. Hohensee, R. Vargas, et al. “Physical properties of galactic winds using background quasars”. In: *Mon. Not. R. Astron. Soc.* 426.2 (Oct. 2012), pp. 801–815.

[33] Nicolas Bouché, M T Murphy, G G Kacprzak, et al. “Signatures of cool gas fueling a star-forming galaxy at redshift 2.3.” In: *Science* 341.6141 (July 2013), pp. 50–3.

[34] David V Bowen, Edward B Jenkins, Max Pettini, et al. “A Comparison of Absorption and Emission Line Abundances in the Nearby Damped Lya Galaxy SBS 1543+593”. In: *Astrophys. J.* 635.2 (Dec. 2005), pp. 880–893.

[35] Daniela Calzetti, Lee Armus, Ralph C Bohlin, et al. “The Dust Content and Opacity of Actively Star-forming Galaxies”. In: *Astrophys. J.* 533.2 (Apr. 2000), pp. 682–695.

[36] Sebastiano Cantalupo, Fabrizio Arrigoni-Battaia, J Xavier Prochaska, et al. “A cosmic web filament revealed in Lyman-a emission around a luminous high-redshift quasar.” In: *Nature* 506.7486 (2014), pp. 63–6.

[37] Sebastiano Cantalupo, Cristiano Porciani, Simon J. Lilly, et al. “Fluorescent Lya Emission from the High Redshift Intergalactic Medium”. In: *Astrophys. J.* 628.1 (2005), pp. 61–75.

[38] R. F. Carswell, J. K. Webb, K. M. Lanzetta, et al. “The high-redshift deuterium abundance: the z=3.086 absorption complex towards Q 0420-388”. In: *Mon. Not. R. Astron. Soc.* 278 (1996), pp. 506–512.

[39] a J Caruso, G H Mount, and B E Woodgate. “Absolute S- and P-plane polarization efficiencies for high frequency holographic gratings in the VUV.” In: *Appl. Opt.* 20.10 (1981), pp. 1764–76.

[40] Renyue Cen and Taotao Fang. “Where Are the Baryons? III. Nonequilibrium Effects and Observables”. In: *Astrophys. J.* 650.2 (Oct. 2006), pp. 573–591.

[41] Renyue Cen and Jeremiah P. Ostriker. “Where Are the Baryons? II. Feedback Effects”. In: *Astrophys. J.* 650.2 (Oct. 2006), pp. 560–572.

[42] M. Centurion, P. Molaro, G. Vladilo, et al. “Early stages of nitrogen enrichment in galaxies: Clues from measurements in damped Lyman a systems”. In: *Astron. Astrophys.* 403.1 (May 2003), pp. 55–72.

[43] Miriam Centurion, Piercarlo Bonifacio, Paolo Molaro, et al. “Chemical Evolution of Damped Lyα Galaxies: The [S/Zn] Abundance Ratio at Redshift $>$2”. In: *Astrophys. J.* 536.2 (June 2000), pp. 540–549.

[44] Daniel Ceverino and Anatoly Klypin. “THE ROLE OF STELLAR FEEDBACK IN THE FORMATION OF GALAXIES”. In: *Astrophys. J.* 695.1 (Apr. 2009), pp. 292–309.

[45] Jane C. Charlton and Christopher W. Churchill. “Quasistellar Objects: Intervening Absorption Lines”. In: *Encycl. Astron. Astrophys.* (May 2000), p. 15.

[46] H.-W. Chen, R.$\sim$C. Kennicutt, and M Rauch. “Abundance Profiles and Kinematics of Damped Lyman-alpha Absorbing Galaxies at z $<$ 0.65”. In: *Astrophys. J.* 620 (2005), p. 703.

[47] L. Christensen, P Møller, J P U Fynbo, et al. “Verifying the mass-metallicity relation in damped Lyman-alpha selected galaxies at $0.1 < z < 3.2$”. In: 000.April (Apr. 2014), p. 15.

[48] Christopher W Churchill, Richard R Mellon, Jane C Charlton, et al. “Low- and High-Ionization Absorption Properties of Mg II Absorption–selected Galaxies at Intermediate Redshifts. II. Taxonomy, Kinematics, and Galaxies”. In: *Astrophys. J.* 543.2 (Nov. 2000), pp. 577–598.

[49] Ryan Cooke, Max Pettini, and Michael T. Murphy. “A new candidate for probing Population III nucleosynthesis with carbon-enhanced damped Lya systems”. In: *Mon. Not. R. Astron. Soc.* 425.1 (Sept. 2012), pp. 347–354.

[50] Ryan Cooke, Max Pettini, Charles C. Steidel, Lindsay J. King, et al. “A newly discovered DLA and associated Lyα emission in the spectra of the gravitationally lensed quasar UM 673A,B”. In: *Mon. Not. R. Astron. Soc.* 409.2 (Dec. 2010), pp. 679–693.

[51] Ryan Cooke, Max Pettini, Charles C. Steidel, Gwen C. Rudie, and Regina A. Jorgenson. “A carbon-enhanced metal-poor damped Lyα system: probing gas from Population III nucleosynthesis?” In: *Mon. Not. R. Astron. Soc.* 412 (Dec. 2011), pp. 1047–1058.

[52] Ryan Cooke, Max Pettini, Charles C. Steidel, Gwen C. Rudie, and Poul E. Nissen. “The most metal-poor damped Lya systems: insights into chemical evolution in the very metal-poor regime”. In: *Mon. Not. R. Astron. Soc.* 417.2 (Oct. 2011), pp. 1534–1558.

[53] Tiago Costa, Debora Sijacki, and Martin G. Haehnelt. “Feedback from active galactic nuclei: energy- versus momentum-driving”. In: *Mon. Not. R. Astron. Soc.* 444.3 (Sept. 2014), pp. 2355–2376.

[54] Donald P. Cox. “The Three-Phase Interstellar Medium Revisited”. In: *Annu. Rev. Astron. Astrophys.* 43.1 (Sept. 2005), pp. 337–385.

[55] G. Cresci, V. Mainieri, M. Brusa, et al. “BLOWIN’ IN THE WIND: BOTH “NEGATIVE” AND “POSITIVE” FEEDBACK IN AN OBSCURED HIGH- z QUASAR”. In: *Astrophys. J.* 799.1 (Jan. 2015), p. 82.

[56] Neil H. M. Crighton, Joseph F. Hennawi, and J. Xavier Prochaska. “METAL-POOR, COOL GAS IN THE CIRCUMGALACTIC MEDIUM OF A z = 2.4 STAR-FORMING GALAXY: DIRECT EVIDENCE FOR COLD ACCRETION?” In: *Astrophys. J.* 776.2 (2013), p. L18.

[57] Neil H M Crighton, Joseph F Hennawi, Robert A Simcoe, et al. “Metal-enriched, sub-kiloparsec gas clumps in the circumgalactic medium of a faint z = 2.5 galaxy”. In: June (June 2014), p. 17.

[58] O. Cucciati, L. Tresse, O. Ilbert, et al. “The star formation rate density and dust attenuation evolution over 12 Gyr with the VVDS surveys”. In: *Astron. Astrophys.* 539 (Mar. 2012), A31.

[59] Charles W. Danforth, Brian A. Keeney, Evan M. Tilton, et al. “AN HST /COS SURVEY OF THE LOW-REDSHIFT INTERGALACTIC MEDIUM. I. SURVEY, METHODOLOGY, AND OVERALL RESULTS”. In: *Astrophys. J.* 817.2 (Jan. 2016), p. 111.

[60] Romeel Dave, Renyue Cen, Jeremiah P. Ostriker, et al. “Baryons in the Warm-Hot Intergalactic Medium”. In: *Astrophys. J.* 552.2 (May 2001), pp. 473–483.

[61] A De Cia, C Ledoux, S Savaglio, et al. “Dust-to-metal ratios in damped Lyman- a absorbers”. In: *Astron. Astrophys.* 560 (Dec. 2013), A88.

[62] A. Dekel and Y. Birnboim. “Galaxy bimodality due to cold flows and shock heating”. In: *Mon. Not. R. Astron. Soc.* 368.1 (2006), pp. 2–20.

[63] M. Dessauges-Zavadsky, F Calura, J X Prochaska, et al. “A comprehensive set of elemental abundances in damped Lya systems: Revealing the nature of these high-redshift galaxies”. In: *Astron. Astrophys.* 416.1 (Mar. 2004), pp. 79–110.

[64] M. Dessauges-Zavadsky, F Calura, J X Prochaska, et al. “A new comprehensive set of elemental abundances in DLAs”. In: *Astron. Astrophys.* 470.2 (Aug. 2007), pp. 431–448.

[65] M. Dessauges-Zavadsky, S. D’Odorico, R. G. McMahon, et al. “UVES observations of a damped Lya system at z abs = 4.466 towards the quasar APM BR J0307-4945”. In: *Astron. Astrophys.* 370.2 (May 2001), pp. 426–435.

[66] M. Dessauges-Zavadsky, C. Péroux, T.-S. Kim, et al. “A homogeneous sample of sub-damped Lyman alpha systems - I. Construction of the sample and chemical abundance measurements”. In: *Mon. Not. R. Astron. Soc.* 345.2 (Oct. 2003), pp. 447–479.

[67] M. Dessauges-Zavadsky, J. X. Prochaska, and S. D’Odorico. “New detections of Mn, Ti and Mg in damped Lya systems: Toward reconciling the dust/nucleosynthesis degeneracy”. In: *Astron. Astrophys.* 391.3 (Sept. 2002), pp. 801–807.

[68] M. Dessauges-Zavadsky, J X Prochaska, S. D’Odorico, et al. “A new comprehensive set of elemental abundances in DLAs”. In: *Astron. Astrophys.* 445.1 (Jan. 2006), pp. 93–113.

[69] Miroslava Dessauges-Zavadsky, Sara L. Ellison, and Michael T. Murphy. *Revisiting the origin of the high metallicities of sub-damped Lyman-alpha systems*. 2009.

[70] Mark Dijkstra and Roban Kramer. “Line transfer through clumpy, large scale outflows: Ly a absorption and haloes around star forming galaxies”. In: *Mon. Not. R. Astron. Soc.* 424.3 (Aug. 2012), pp. 1672–1693.

[71] Mark Dijkstra and Abraham Loeb. “Lya blobs as an observational signature of cold accretion streams into galaxies”. In: *Mon. Not. R. Astron. Soc.* 400.2 (Dec. 2009), pp. 1109–1120.

[72] V. D’Odorico, G. Cupani, S. Cristiani, et al. “Metals in the IGM approaching the re-ionization epoch: Results from X-shooter at the VLT”. In: *Mon. Not. R. Astron. Soc.* 435.2 (2013), pp. 1198–1232.

[73] V D’Odorico and P Molaro. “Hints of star formation at z >6: The chemical abundances of the DLA system in the QSO BRI1202-0725 (z abs =4.383)”. In: *Astron. Astrophys.* 415.3 (Mar. 2004), pp. 879–884.

[74] Valentina D'Odorico, Francesco Calura, Stefano Cristiani, et al. "The rise of the C IV mass density at z <2.5". In: *Mon. Not. R. Astron. Soc.* 401.4 (2010), pp. 2715–2721.

[75] Bruce Draine. *Physics of the Interstellar and Intergalactic Medium*. 2011.

[76] R. Dutta, R. Srianand, H. Rahmani, et al. "A study of low-metallicity DLAs at high redshift and C II* as a probe of their physical conditions". In: *Mon. Not. R. Astron. Soc.* 440.1 (2014), pp. 307–326.

[77] S. L. Ellison, J. F. Hennawi, C. L. Martin, et al. "Coincident, 100 kpc scale damped Ly absorption towards a binary QSO: how large are galaxies at z 3?" In: *Mon. Not. R. Astron. Soc.* 378.3 (July 2007), pp. 801–818.

[78] S. L. Ellison and S. Lopez. "Unusual metal abundances in a pair of damped Lyman alpha systems at z ?2". In: *Astron. Astrophys.* 380.1 (Dec. 2001), pp. 117–122.

[79] Sara L. Ellison, Nissim Kanekar, J. Xavier Prochaska, et al. "Hi content, metallicities and spin temperatures of damped and sub-damped Lya systems in the redshift desert ($0.6 < z_{abs} < 1.7$)". In: *Mon. Not. R. Astron. Soc.* 424.1 (2012), pp. 293–312.

[80] Sara L. Ellison and Sebastian Lopez. "Assessing the dust selection bias in quasar absorbers at $0.7 < z < 1.6$: Zn/Fe abundances in a radio-selected sample". In: *Mon. Not. R. Astron. Soc.* 397.1 (2009), pp. 467–478.

[81] Sara L. Ellison, Max Pettini, Charles C. Steidel, et al. "An Imaging and Spectroscopic Study of the z=3.38639 Damped Lyman Alpha System in Q0201+1120: Clues to Star Formation Rate at High Redshift". In: *Astrophys. J.* 549 (2001), pp. 770–779.

[82] Sara L. Ellison, J. Xavier Prochaska, Joseph Hennawi, et al. "The nature of proximate damped Lyman a systems". In: *Mon. Not. R. Astron. Soc.* 406 (May 2010), pp. 1435–1459.

[83] Sara L. Ellison, Brian a. York, Max Pettini, et al. "A search for damped Lyman a systems towards radio-loud quasars I: The optical survey". In: *Mon. Not. R. Astron. Soc.* 388.3 (2008), pp. 1349–1360.

[84] Dawn K. Erb, Anna M. Quider, Alaina L. Henry, et al. "GALACTIC OUTFLOWS IN ABSORPTION AND EMISSION: NEAR-ULTRAVIOLET SPECTROSCOPY OF GALAXIES AT $1 < z < 2$". In: *Astrophys. J.* 759.1 (Nov. 2012), p. 26.

[85] Dawn K. Erb, Alice E. Shapley, Max Pettini, et al. "The Mass-Metallicity Relation at z >2". In: *Astrophys. J.* 644.2 (June 2006), pp. 813–828.

[86] S M Fall and G Efstathiou. "Formation and rotation of disc galaxies with haloes". In: *R. Astron. Soc.* 193 (1980), p. 189.

[87] Mark a. Fardal, Neal Katz, Jeffrey P. Gardner, et al. “Cooling Radiation and the Lya Luminosity of Forming Galaxies”. In: *Astrophys. J.* 562.2 (Dec. 2001), pp. 605–617.

[88] C.-A. Faucher-Giguere, P. F. Hopkins, D. Kere, et al. “Neutral hydrogen in galaxy haloes at the peak of the cosmic star formation history”. In: *Mon. Not. R. Astron. Soc.* 449.1 (2015), pp. 987–1003.

[89] Claude André Faucher-Giguere and Dušan Kereš. “The small covering factor of cold accretion streams”. In: *Mon. Not. R. Astron. Soc. Lett.* 412.1 (2011), pp. L118–L122.

[90] Claude-Andre Faucher-Giguere, Dusan Keres, Mark Dijkstra, et al. “Ly alpha COOLING EMISSION FROM GALAXY FORMATION”. In: *Astrophys. J.* 725.1 (2010), pp. 633–657.

[91] John J. Feldmeier, Alex Hagen, Robin Ciardullo, et al. “SEARCHING FOR NEUTRAL HYDROGEN HALOS AROUND z $\sim$ 2.1 AND z $\sim$ 3.1 Lya EMITTING GALAXIES”. In: *Astrophys. J.* 776.2 (2013), p. 75.

[92] G. J. Ferland, K. T. Korista, D. A. Verner, et al. “CLOUDY 90: Numerical Simulation of Plasmas and Their Spectra”. In: *Publ. Astron. Soc. Pacific* 110.749 (July 1998), pp. 761–778.

[93] A Fontana and P Ballester. “FITLYMAN: A Midas Tool for the Analysis of Absorption Spectra”. In: *The Messenger* 80 (1995), pp. 37–41.

[94] Andrew J Fox, Patrick Petitjean, Cédric Ledoux, et al. “Multiphase Plasma in Sub-Damped Lya Systems: A Hidden Metal Reservoir”. In: *Astrophys. J.* 668.1 (Oct. 2007), pp. L15–L18.

[95] Andrew J. Fox, J. Xavier Prochaska, Cédric Ledoux, et al. “Metal-enriched plasma in protogalactic halos”. In: *Astron. Astrophys.* 503.3 (Sept. 2009), pp. 731–746.

[96] Anne Fox and Philipp Richter. “A high-redshift quasar absorber without C IV. A galactic outflow caught in the act?” In: *Astron. & Astrophys.* 588 (Apr. 2016), A94.

[97] S. Frank and C. Péroux. “Searching for dust reddening in SDSS spectra with damped Lyman a systems”. In: *Mon. Not. R. Astron. Soc.* 406.4 (2010), pp. 2235–2248.

[98] S Frank, Y Rasera, D Vibert, et al. “Observable signatures of the low-z circumgalactic and intergalactic media: ultraviolet line emission in simulations”. In: *Mon. Not. R. Astron. Soc.* 420.2 (Feb. 2012), pp. 1731–1753.

[99] F Fraternali, A. Marasco, L. Armillotta, et al. “Galactic hail: the origin of the high-velocity cloud complex C”. In: *Mon. Not. R. Astron. Soc. Lett.* 447.1 (Dec. 2014), pp. L70–L74.

[100] Michele Fumagalli, John M. O'Meara, and J. Xavier Prochaska. "The physical properties of z $>$ 2 Lyman limit systems: new constraints for feedback and accretion models". In: *Mon. Not. R. Astron. Soc.* 455.4 (Feb. 2016), pp. 4100–4121.

[101] Michele Fumagalli, J. Xavier Prochaska, Daniel Kasen, et al. "Absorption-line systems in simulated galaxies fed by cold streams". In: *Mon. Not. R. Astron. Soc.* 418.3 (2011), pp. 1796–1821.

[102] Steven R. Furlanetto, Joop Schaye, Volker Springel, et al. "Ultraviolet Line Emission from Metals in the Low-Redshift Intergalactic Medium". In: *Astrophys. J.* 606.1 (May 2004), pp. 221–236.

[103] Steven R. Furlanetto, Joop Schaye, Volker Springel, et al. "Lya Emission from Structure Formation". In: *Astrophys. J.* 622.1 (2005), pp. 7–27.

[104] J. P. U. Fynbo, S. J. Geier, L. Christensen, et al. "On the two high-metallicity DLAs at z = 2.412 and 2.583 towards Q 0918+1636". In: *Mon. Not. R. Astron. Soc.* 436.1 (Nov. 2013), pp. 361–370.

[105] J. P. U. Fynbo, C. Ledoux, P. Noterdaeme, et al. "Galaxy counterparts of metal-rich damped Lyα absorbers - II. A solar-metallicity and dusty DLA at zabs= 2.58". In: *Mon. Not. R. Astron. Soc.* 413.4 (June 2011), pp. 2481–2488.

[106] J.-R. Gauthier, H.-W. Chen, K. L. Cooksey, et al. "Halo masses of Mg II absorbers at z 0.5 from Sloan Digital Sky Survey Data Release 7". In: *Mon. Not. R. Astron. Soc.* 439.1 (2014), pp. 342–353.

[107] Jian Ge, Jill Bechtold, and Varsha P. Kulkarni. "H2, C I, Metallicity, and Dust Depletion in the z = 2.34 Damped Lya Absorption System toward QSO 1232+0815". In: *Astrophys. J.* 547.1 (2001), pp. L1–L5.

[108] Shy Genel, Nicolas Bouché, Thorsten Naab, et al. "the Growth of Dark Matter Halos: Evidence for Significant Smooth Accretion". In: *Astrophys. J.* 719.1 (Aug. 2010), pp. 229–239.

[109] Mauro Giavalisco, Anuradha Koratkar, and Daniela Calzetti. "Obscuration of LYa Photons in Star-forming Galaxies". In: *Astrophys. J.* 466 (Aug. 1996), p. 831.

[110] Mauro Giavalisco, Eros Vanzella, Sara Salimbeni, et al. "DISCOVERY OF COLD, PRISTINE GAS POSSIBLY ACCRETING ONTO AN OVERDENSITY OF STAR-FORMING GALAXIES AT REDSHIFT z $\sim$ 1.6". In: *Astrophys. J.* 743.1 (Dec. 2011), p. 95.

[111] Leonid I Goray. "Numerical modeling of coated gratings in sensitive cases". In: (2002), pp. 1–15.

[112] Leonid I Goray, Ivan G Kuznetsov, Sergey Yu Sadov, et al. “Multilayer resonant subwavelength gratings: effects of waveguide modes and real groove profiles.” In: *J. Opt. Soc. Am. A. Opt. Image Sci. Vis.* 23.1 (Jan. 2006), pp. 155–65.

[113] F. Governato, C. Brook, L. Mayer, et al. “Bulgeless dwarf galaxies and dark matter cores from supernova-driven outflows”. In: *Nature* 463.7278 (Jan. 2010), pp. 203–206.

[114] R. Grange, G. R. Lemaitre, S. Quiret, et al. “Multi object spectrograph of the Fireball balloon experiment”. In: ed. by Tadayuki Takahashi, Jan-Willem A. den Herder, and Mark Bautz. July 2014, p. 914430.

[115] R. Grange, B. Milliard, G. Lemaitre, et al. “Fireball multi object spectrograph: as-built optic performances”. In: *SPIE 9905*. Ed. by Jan-Willem A. den Herder, Tadayuki Takahashi, and Marshall Bautz. July 2016, p. 990531.

[116] Robert Grange, Bruno Milliard, Ryan McLean, et al. “Three-dimensional spectroscopy with a fiber-fed NUV spectrograph”. In: ed. by Oswald H. W. Siegmund. Aug. 2005, p. 589812.

[117] D. E. Gray. “American Institute of Physics (AIP). Handbook”. In: *AIP Adv.* 1972.

[118] N. Grevesse, M. Asplund, a. J. Sauval, et al. “The chemical composition of the Sun”. In: *Astrophys. Space Sci.* 328.1 (2010), pp. 179–183.

[119] R. Guimarães, P. Noterdaeme, P. Petitjean, et al. “METALLICITIES, DUST, AND MOLECULAR CONTENT OF A QSO-DAMPED Lya SYSTEM REACHING log N (H I) = 22: AN ANALOG TO GRB-DLAs”. In: *Astron. J.* 143.6 (June 2012), p. 147.

[120] Francesco Haardt and Piero Madau. “RADIATIVE TRANSFER IN A CLUMPY UNIVERSE. IV. NEW SYNTHESIS MODELS OF THE COSMIC UV/X-RAY BACKGROUND”. In: *Astrophys. J.* 746.2 (Feb. 2012), p. 125.

[121] M Haardt and P Madau. *Clusters of Galaxies and the High Redshift Universe Observed in X-rays, Recent Results of XMM-Newton and Chandra, XXXVIth Rencontres de Moriond, XXIst Moriond Astrophysics Meeting, March 10–17, 2001, Savoie, France, available online at: http://moriond.in2*. 2001.

[122] Martin G. Haehnelt, Matthias Steinmetz, and Michael Rauch. “Damped Lya Absorber at High Redshift: Large Disks or Galactic Building Blocks?” In: *Astrophys. J.* 495.2 (Mar. 1998), pp. 647–658.

[123] Z. Hafen, C. -A. Faucher-Giguere, D. Angles-Alcazar, et al. “Low-Redshift Lyman Limit Systems as Diagnostics of Cosmological Inflows and Outflows”. In: (Aug. 2016).

[124] O. Hahn and T. Abel. *MUSIC: MUlti-Scale Initial Conditions*. 2013.

[125] Erika T. Hamden, April D. Jewell, Samuel Gordon, et al. “High efficiency CCD detectors at UV wavelengths”. In: ed. by Tadayuki Takahashi, Jan-Willem A. den Herder, and Mark Bautz. July 2014, p. 91442X.

[126] Matthew Hayes, Daniel Schaerer, Göran Östlin, et al. “ON THE REDSHIFT EVOLUTION OF THE Lya ESCAPE FRACTION AND THE DUST CONTENT OF GALAXIES”. In: *Astrophys. J.* 730.1 (Mar. 2011), p. 8.

[127] Timothy M. Heckman, Lee Armus, and George K. Miley. “On the nature and implications of starburst-driven galactic superwinds”. In: *Astrophys. J. Suppl. Ser.* 74 (Dec. 1990), p. 833.

[128] J. Heinmüller, Patrick Petitjean, Cedric Ledoux, et al. “Kinematics and star formation activity in the z abs = 2.03954 damped Lyman-a system towards PKS 0458–020”. In: *Astron. Astrophys.* 449.1 (Apr. 2006), pp. 33–39.

[129] R. B. C. Henry and Jason X. Prochaska. “The Chemical Evolution of High- z Galaxies from the Relative Abundances of N, Si, S, and Fe in Damped Lya Systems”. In: *Publ. Astron. Soc. Pacific* 119.859 (Sept. 2007), pp. 962–979.

[130] Stéphane Herbert-Fort, Jason X. Prochaska, Miroslava Dessauges-Zavadsky, et al. “The Metal-strong Damped Lya Systems”. In: *Publ. Astron. Soc. Pacific* 118.846 (Aug. 2006), pp. 1077–1097.

[131] a. M. Hopkins, N. M. McClure-Griffiths, and B. M. Gaensler. “Linked Evolution of Gas and Star Formation in Galaxies Over Cosmic History”. In: *Astrophys. J.* 682.1 (July 2008), pp. L13–L16.

[132] F. Hoyle. “A New Model for the Expanding Universe”. In: *Mon. Not. R. Astron. Soc.* 108.5 (Oct. 1948), pp. 372–382.

[133] M.∼C. Hutley. “Diffraction Gratings (Techniques of Physics)”. In: *Diffr. Gratings (Techniques Physics)*. Academic Presse, 1982. Chap. Diffractio.

[134] Inc. International Intellectual Group. *PCGrate - http://www.pcgrate.com/*. 1996.

[135] Edward B Jenkins. “A UNIFIED REPRESENTATION OF GAS-PHASE ELEMENT DEPLETIONS IN THE INTERSTELLAR MEDIUM”. In: *Astrophys. J.* 700.2 (Aug. 2009), pp. 1299–1348.

[136] April D. Jewell, Erika T. Hamden, Hwei Ru Ong, et al. “Detector performance for the FIREBall-2 UV experiment”. In: ed. by Oswald H. Siegmund. Aug. 2015, 96010N.

[137] Glenn G. Kacprzak, Christopher W. Churchill, and Nikole M. Nielsen. “TRACING OUTFLOWS AND ACCRETION: A BIMODAL AZIMUTHAL DEPENDENCE OF Mg II ABSORPTION”. In: *Astrophys. J.* 760.1 (Nov. 2012), p. L7.

[138] Glenn G. Kacprzak, Crystal L. Martin, Nicolas Bouché, et al. “NEW PERSPECTIVE ON GALAXY OUTFLOWS FROM THE FIRST DETECTION OF BOTH INTRINSIC AND TRAVERSE METAL-LINE ABSORPTION”. In: *Astrophys. J.* 792.1 (Aug. 2014), p. L12.

[139] N. Kanekar, J. X. Prochaska, A. Smette, et al. “The spin temperature of high-redshift damped Lyman systems”. In: *Mon. Not. R. Astron. Soc.* 438.3 (2014), pp. 2131–2166.

[140] Robert C. Kennicutt. “STAR FORMATION IN GALAXIES ALONG THE HUBBLE SEQUENCE”. In: *Annu. Rev. Astron. Astrophys.* 36.1 (Sept. 1998), pp. 189–231.

[141] D. Keres, Neal Katz, David H. Weinberg, et al. “How do galaxies get their gas?” In: *Mon. Not. R. Astron. Soc.* 363.1 (Oct. 2005), pp. 2–28.

[142] P. Khare, V. P. Kulkarni, C. Péroux, et al. “The nature of damped Lyman a and sub-damped Lyman a absorbers”. In: *Astron. Astrophys.* 464.2 (Mar. 2007), pp. 487–493.

[143] Pushpa Khare, Daniel Vanden Berk, Donald G. York, et al. “Exploring the dust content of Sloan Digital Sky Survey Data Release 7 damped Lyman a systems at”. In: *Mon. Not. R. Astron. Soc.* 419.2 (2012), pp. 1028–1039.

[144] Romas Kisielius, Varsha P. Kulkarni, Gary J. Ferland, Pavel Bogdanovich, and Matt L. Lykins. “ATOMIC DATA FOR S II—TOWARD BETTER DIAGNOSTICS OF CHEMICAL EVOLUTION IN HIGH-REDSHIFT GALAXIES”. In: *Astrophys. J.* 780.1 (2014), p. 76.

[145] Romas Kisielius, Varsha P Kulkarni, Gary J Ferland, Pavel Bogdanovich, Debopam Som, et al. “ATOMIC DATA FOR ZN II: IMPROVING SPECTRAL DIAGNOSTICS OF CHEMICAL EVOLUTION IN HIGH-REDSHIFT GALAXIES”. In: *Astrophys. J.* 804.1 (2015), p. 76.

[146] Juna A. Kollmeier, David H. Weinberg, Benjamin D. Oppenheimer, et al. “THE PHOTON UNDERPRODUCTION CRISIS”. In: *Astrophys. J.* 789.2 (July 2014), p. L32.

[147] Juna A Kollmeier, Zheng Zheng, Romeel Davé, et al. “Lya emission from cosmic structure. I. Fluorescence”. In: *Astrophys. J.* 708.2 (Jan. 2010), pp. 1048–1075.

[148] J.-K. Krogager, J. P. U. Fynbo, C. Ledoux, et al. “Comprehensive study of a z = 2.35 DLA Galaxy: mass, metallicity, age, morphology and SFR from HST and VLT”. In: *Mon. Not. R. Astron. Soc.* 433.4 (Aug. 2013), pp. 3091–3102.

[149] J.-K. Krogager, J P U Fynbo, P Noterdaeme, et al. “A quasar reddened by a sub-parsec-sized, metal-rich and dusty cloud in a damped Lyman α absorber at z = 2.13”. In: *Mon. Not. R. Astron. Soc.* 455.3 (Jan. 2016), pp. 2698–2711.

[150] J.-K. Krogager, S. Geier, J. P. U. Fynbo, et al. “THE HIGH A V Quasar Survey: Reddened Quasi-Stellar Objects selected from optical/near-infrared photometry. II.” In: *Astrophys. J. Suppl. Ser.* 217.1 (Mar. 2015), p. 5.

[151] V. P. Kulkarni, P. Khare, C. Péroux, et al. “The Role of Sub–Damped Lya Absorbers in the Cosmic Evolution of Metals”. In: *Astrophys. J.* 661.1 (May 2007), pp. 88–94.

[152] Varsha P Kulkarni, S. Michael Fall, James T Lauroesch, et al. “Hubble Space Telescope Observations of Element Abundances in Low-Redshift Damped Lya Galaxies and Implications for the Global Metallicity-Redshift Relation”. In: *Astrophys. J.* 618.1 (Jan. 2005), pp. 68–90.

[153] Varsha P. Kulkarni, Pushpa Khare, Debopam Som, et al. “Do damped and sub-damped Lyman-alpha absorbers arise in galaxies of different masses?” In: *New Astron.* 15.8 (Nov. 2010), pp. 735–743.

[154] Varsha P. Kulkarni, Joseph Meiring, Debopam Som, et al. “A super-damped Lya QSO absorber at z = 2.2”. In: *Astrophys. J.* 749.2 (Apr. 2012), p. 176.

[155] Daniel Kunth, Claus Leitherer, J Miguel Mas-Hesse, et al. “The First Deep Advanced Camera for Surveys Lya Images of Local Starburst Galaxies”. In: *Astrophys. J.* 597.1 (2003), pp. 263–268.

[156] Ivan G. Kuznetsov, Erik Wilkinson, David a. Content, et al. “Grating efficiencies comparison study: calculations versus metrology for various types of high groove density gratings”. In: 5178 (Jan. 2004). Ed. by Mark A. Kahan, pp. 267–277.

[157] Ethan Lake, Zheng Zheng, Renyue Cen, et al. “On the diffuse lyman-alpha halo around lyman-alpha emitting galaxies”. In: (2015).

[158] Kenneth M. Lanzetta, Arthur M. Wolfe, and David A. Turnshek. “The IUE Survey for Damped Lyman- alpha and Lyman-Limit Absorption Systems: Evolution of the Gaseous Content of the Universe”. In: *Astrophys. J.* 440 (Feb. 1995), p. 435.

[159] Peter Laursen and Jesper Sommer-Larsen. “Lya Resonant Scattering in Young Galaxies: Predictions from Cosmological Simulations”. In: *Astrophys. J.* 657.2 (Mar. 2007), pp. L69–L72.

[160] H.∼S. Leavitt and E.∼C. Pickering. “Periods of 25 Variable Stars in the Small Magellanic Cloud.” In: *Harvard Coll. Obs. Circ.* 173.9 (1912), pp. 1–3.

[161] C. Ledoux, J. Bergeron, and P. Petitjean. “Dust depletion and abundance pattern in damped Lyman-alpha systems: a sample of Mn and Ti abundances at $z < 2.2$”. In: *Eur. Sp. Agency, (Special Publ. ESA SP* 815.419 (2002), p. 17.

[162] C. Ledoux, P. Petitjean, J. P. U. Fynbo, et al. “Velocity-metallicity correlation for high- z DLA galaxies: evidence of a mass-metallicity relation?” In: *Astron. Astrophys.* 457.1 (Oct. 2006), pp. 71–78.

[163] C. Ledoux, P. Petitjean, and R. Srianand. “The Very Large Telescope Ultraviolet and Visible Echelle Spectrograph survey for molecular hydrogen in high-redshift damped Lyman systems”. In: *Mon. Not. R. Astron. Soc.* 346.1 (Nov. 2003), pp. 209–228.

[164] C. Ledoux, R. Srianand, and P. Petitjean. “Detection of molecular hydrogen in a near Solar-metallicity damped Lyman-? system at z abs ? 2 toward Q?0551-366”. In: *Astron. Astrophys.* 396.2 (Dec. 2002), pp. 429–429.

[165] N Lehner, J C Howk, T M Tripp, et al. “The bimodal metallicity distribution of the cool circumgalactic medium at z $<$ 1”. In: *Astrophys. J.* 770.2 (June 2013), p. 138.

[166] Nicolas Lehner, John M. O’Meara, Andrew J Fox, et al. “Galactic and Circumgalactic OVI and its Impact on the Cosmological Metal and Baryon Budgets at $2 < z < 3.5$”. In: *Astrophys. J.* 3 (Jan. 2014).

[167] Nicolas Lehner, John M. O’Meara, J. Christopher Howk, et al. “The Cosmic Evolution of the Metallicity Distribution of Ionized Gas Traced by Lyman Limit Systems”. In: (2016).

[168] G R Lemaitre, R Grange, S Quiret, et al. “Multi Object Spectrograph of the Fireball-II Balloon Experiment”. In: *OSA Proc. Conf. OF&T* (2014), pp. 5–7.

[169] Georges Lemaître. “Un univers homogène de masse constante et de rayon croissant, rendant compte de la vitesse radiale des nébuleuses extra-galactiques”. In: *Ann. la Société Sci. Bruxelles* 47A (Aug. 1927), pp. 49–59.

[170] Gérard René Lemaitre. *Astronomical Optics and Elasticity Theory*. Astronomy and Astrophysics Library. Berlin, Heidelberg: Springer Berlin Heidelberg, 2009.

[171] J Lequeux, M Peimbert, J. F. Rayo, et al. “Chemical Composition and Evolution of Irregular and Blue Compact Galaxies”. In: *Astron. Astrophys.* 80.2 (1979), pp. 155–166.

[172] E G Loewen and M Neviere. “Simple selection rules for VUV and XUV diffraction gratings.” In: *Appl. Opt.* 17.7 (Apr. 1978), pp. 1087–92.

[173] E G Loewen and M Nevière. “Dielectric coated gratings: a curious property.” In: *Appl. Opt.* 16.11 (Nov. 1977), pp. 3009–11.

[174] E G Loewen, M Nevière, and D Maystre. “Grating efficiency theory as it applies to blazed and holographic gratings.” In: *Appl. Opt.* 16.10 (Oct. 1977), pp. 2711–21.

[175] S. Lopez, D. Reimers, S. D'Odorico, et al. "Metal abundances and ionization conditions in a possibly dust-free damped Ly??system at z=2.3". In: *Astron. Astrophys.* 385.3 (Apr. 2002), pp. 778–792.

[176] Sebastian Lopez and Sara L. Ellison. "Distinct abundance patterns in multiple damped Ly? galaxies: Evidence for truncated star formation?" In: *Astron. Astrophys.* 403.2 (May 2003), pp. 573–584.

[177] Sebastian Lopez, Dieter Reimers, Michael D. Gregg, et al. "Metal Abundances in a Damped Lyα System along Two Lines of Sight at z = 0.93". In: *Astrophys. J.* 626.2 (June 2005), pp. 767–775.

[178] Sebastian Lopez, Dieter Reimers, Michael Rauch, et al. "First Comparison of Ionization and Metallicity in Two Lines of Sight Toward HE 1104-1805 AB at z=1.66". In: 10.Paper I (1999), p. 49.

[179] Limin Lu, Wallace L. W. Sargent, Thomas A Barlow, et al. "Abundances at High Redshifts: The Chemical Enrichment History Of Damped Lyman a Galaxies". In: *Astrophys. J. Suppl. Ser.* 107.2 (Dec. 1996), pp. 475–519.

[180] Britt F. Lundgren, Robert J. Brunner, Donald G. York, et al. "A Cross-Correlation Analysis of Mg II Absorption Line Systems and Luminous Red Galaxies from the SDSS DR5". In: *Astrophys. J.* 698 (2009), pp. 819–839.

[181] Natasha Maddox, Paul C. Hewett, Céline Péroux, et al. "The large area KX quasar catalogue - I. Analysis of the photometric redshift selection and the complete quasar catalogue". In: *Mon. Not. R. Astron. Soc.* 424.4 (Aug. 2012), pp. 2876–2895.

[182] Robert A. Malaney and Brian Chaboyer. "Star Formation and Chemical Evolution in Damped LY alpha Clouds". In: *Astrophys. J.* 462 (May 1996), p. 57.

[183] Crystal L. Martin. "Mapping Large-Scale Gaseous Outflows in Ultraluminous Infrared Galaxies with Keck II ESI Spectra: Spatial Extent of the Outflow". In: *Astrophys. J.* 621 (2005), pp. 227–245.

[184] Crystal L. Martin, Alice E. Shapley, Alison L. Coil, et al. "DEMOGRAPHICS AND PHYSICAL PROPERTIES OF GAS OUTFLOWS/INFLOWS AT $0.4 < z < 1.4$". In: *Astrophys. J.* 760.2 (2012), p. 127.

[185] D. Christopher Martin, Daphne Chang, Matt Matuszewski, Patrick Morrissey, Shahin Rahman, Anna Moore, and Charles C. Steidel. "IGM emission observations with the Cosmic Web Imager. I. The Circum-QSO Medium of QSO 1549+19, and evidence for filamentary inflow". In: *Astrophys. J.* 786.2 (May 2014), p. 106.

[186] D. Christopher Martin, Daphne Chang, Matt Matuszewski, Patrick Morrissey, Shahin Rahman, Anna Moore, Charles C. Steidel, and Yuichi Matsuda. “INTERGALACTIC MEDIUM EMISSION OBSERVATIONS WITH THE COSMIC WEB IMAGER. II. DISCOVERY OF EXTENDED, KINEMATICALLY LINKED EMISSION AROUND SSA22 Lya BLOB 2”. In: *Astrophys. J.* 786.2 (May 2014), p. 107.

[187] Y. Matsuda, T. Yamada, T. Hayashino, et al. “Diffuse Lya haloes around Lya emitters at z=3: Do dark matter distributions determine the Lya spatial extents?” In: *Mon. Not. R. Astron. Soc.* 425.2 (2012), pp. 878–883.

[188] Jorryt Matthee, David Sobral, Ivan Oteo, et al. “The CALYMHA survey: Lya escape fraction and its dependence on galaxy properties at z = 2.23”. In: *Mon. Not. R. Astron. Soc.* 458.1 (2016), pp. 449–467.

[189] Mateusz Konrad Matuszewski. “The Faint Intergalactic Redshifted Emission Balloon and the Cosmic Web Imager : Two Integral Field Spectrographs Designed to Study Emission from the Intergalactic Medium Thesis by”. PhD thesis. 2012.

[190] Daniel Maystre. *Plasmonics*. Ed. by Stefan Enoch and Nicolas Bonod. Vol. 167. Springer Series in Optical Sciences. Berlin, Heidelberg: Springer Berlin Heidelberg, 2012.

[191] P. Mège, S Pascal, S Quiret, et al. “The UV multi-object slit-spectrograph FIREBall-2 simulator”. In: *SPIE*. Ed. by Oswald H. Siegmund. Aug. 2015, p. 960110.

[192] Avery Meiksin. “Colour corrections for high-redshift objects due to intergalactic attenuation”. In: *Mon. Not. R. Astron. Soc.* 365.3 (Jan. 2006), pp. 807–812.

[193] J. D. Meiring, V. P. Kulkarni, P. Khare, et al. “Elemental abundance measurements in low-redshift damped Lyman absorbers”. In: *Mon. Not. R. Astron. Soc.* 370.1 (July 2006), pp. 43–62.

[194] J. D. Meiring, J. T. Lauroesch, V. P. Kulkarni, C. Péroux, P. Khare, D. G. York, and a. P. S. Crotts. “New abundance determinations in z $<$ 1.5 QSO absorbers: seven sub-DLAs and one DLA”. In: *Mon. Not. R. Astron. Soc.* 376.2 (Apr. 2007), pp. 557–572.

[195] Joseph D. Meiring, James T. Lauroesch, Varsha P. Kulkarni, Celine Péroux, Pushpa Khare, and Donald G. York. “A MIKE + UVES survey of sub-damped Lyman α systems at z $<$ 1.5”. In: *Mon. Not. R. Astron. Soc.* 397.4 (Aug. 2009), pp. 2037–2048.

[196] David M. Meyer, Kenneth M. Lanzetta, and Arthur M. Wolfe. “The Iron Group Abundance Pattern of the Damped Lyman-Alpha Absorber at z = 1.3726 toward the QSO 0935+417”. In: *Astrophys. J.* 451.1 (Sept. 1995), pp. 1–5.

[197] Bruno Milliard, D Christopher Martin, David Schiminovich, et al. “FIREBALL : The Faint Intergalactic medium Redshifted Emission Balloon – Overview and 1st Science Flight Results”. In: ed. by Monique Arnaud, Stephen S. Murray, and Tadayuki Takahashi. July 2010, pages.

[198] Nikola Milutinovic, Sara L. Ellison, J. Xavier Prochaska, et al. “Ionization corrections in a multiphase interstellar medium: Lessons from a z $\sim$ 2 sub-DLA”. In: *Mon. Not. R. Astron. Soc.* 408.4 (2010), pp. 2071–2082.

[199] Paolo Molaro, Piercarlo Bonifacio, Miriam Centurion, et al. “UVES Observations of QSO 0000-2620: Oxygen and Zinc Abundances in the Damped Lyα Galaxy at z abs = 3.3901”. In: *Astrophys. J.* 541.1 (Sept. 2000), pp. 54–60.

[200] P. Moller, J. P. U. Fynbo, C. Ledoux, et al. “Mass-metallicity relation from z = 5 to the present: evidence for a transition in the mode of galaxy growth at z = 2.6 due to the end of sustained primordial gas infall”. In: *Mon. Not. R. Astron. Soc.* 430.4 (Feb. 2013), pp. 2680–2687.

[201] R. Momose, M. Ouchi, K. Nakajima, et al. “Diffuse Lya haloes around galaxies at z = 2.2-6.6: implications for galaxy formation and cosmic reionization”. In: *Mon. Not. R. Astron. Soc.* 442.1 (2014), pp. 110–120.

[202] Johan Montel, Frédéri Mirc, Etienne Pérot, et al. “Design and improvements of the Attitude Control System of the FIREBall balloon experiment”. In: *SPIE 9905*. Ed. by Jan-Willem A. den Herder, Tadayuki Takahashi, and Marshall Bautz. July 2016, p. 99053I.

[203] Donald C Morton. “Atomic Data for Resonance Absorption Lines. III. Wavelengths Longward of the Lyman Limit for the Elements Hydrogen to Gallium”. In: *Astrophys. J. Suppl. Ser.* 149.1 (Nov. 2003), pp. 205–238.

[204] Marcel Neeleman, Arthur M. Wolfe, J. Xavier Prochaska, et al. “The fundamental plane of Lya systems”. In: *Astrophys. J.* 769.1 (May 2013), p. 54.

[205] D. Nelson, A. Pillepich, S. Genel, et al. “The illustris simulation: Public data release”. In: *Astron. Comput.* 13 (Nov. 2015), pp. 12–37.

[206] Dylan Nelson, Shy Genel, Annalisa Pillepich, et al. “Zooming in on accretion – I. The structure of halo gas”. In: *Mon. Not. R. Astron. Soc.* 460.3 (Aug. 2016), pp. 2881–2904.

[207] Daniel B. Nestor, Max Pettini, Paul C. Hewett, et al. “Measurements of Ca II absorption, metals and dust in a sample of z $\sim$ 1 DLAs and subDLAs”. In: *Mon. Not. R. Astron. Soc.* 390.4 (2008), pp. 1670–1682.

[208] Sarah F. Newman, Reinhard Genzel, Natascha M. Förster-Schreiber, et al. "THE SINS/zC-SINF SURVEY of $z \sim 2$ GALAXY KINEMATICS: OUTFLOW PROPERTIES". In: *Astrophys. J.* 761.1 (Dec. 2012), p. 43.

[209] P Noterdaeme, P Laursen, P Petitjean, et al. "Discovery of a compact gas-rich damped Lyman- a galaxy at z = 2.2 : evidence of a starburst-driven outflow". In: *Astron. Astrophys.* 540 (Mar. 2012), A63.

[210] P Noterdaeme, C Ledoux, P Petitjean, F. Le Petit, et al. "Excitation mechanisms in newly discovered H 2 -bearing damped Lyman-α clouds: systems with low molecular fractions". In: *Astron. Astrophys.* 474.2 (Nov. 2007), pp. 393–407.

[211] P. Noterdaeme, C. Ledoux, P. Petitjean, and R. Srianand. "Molecular hydrogen in high-redshift damped Lyman-a systems: the VLT/UVES database". In: *Astron. Astrophys.* 481.2 (2008), pp. 327–336.

[212] P Noterdaeme, S. López, V Dumont, et al. "Deuterium at high redshift". In: *Astron. Astrophys.* 542 (June 2012), p. L33.

[213] P. Noterdaeme, P. Petitjean, W. C. Carithers, et al. "Column density distribution and cosmological mass density of neutral gas: Sloan Digital Sky Survey-III Data Release 9". In: *Astron. Astrophys.* 547 (Oct. 2012), p. L1.

[214] P. Noterdaeme, P. Petitjean, C. Ledoux, et al. "HD molecules at high redshift". In: *Astron. Astrophys.* 491.2 (2008), pp. 397–400.

[215] P. Noterdaeme, P. Petitjean, R. Srianand, et al. "Physical conditions in the neutral interstellar medium at z = 2.43 toward Q 2348-011". In: *Astron. Astrophys.* 469 (2007), pp. 425–436.

[216] P. Ocvirk, C. Pichon, and R. Teyssier. "Bimodal gas accretion in the Horizon-MareNostrum galaxy formation simulation". In: *Mon. Not. R. Astron. Soc.* 390.4 (2008), pp. 1326–1338.

[217] J. M. O'Meara, N Lehner, J C Howk, et al. "THE FIRST DATA RELEASE OF THE KODIAQ SURVEY". In: *Astron. J.* 150.4 (Sept. 2015), p. 111.

[218] Benjamin D. Oppenheimer, Romeel Davé, Dušan Kereš, et al. "Feedback and recycled wind accretion: assembling the z= 0 galaxy mass function". In: *Mon. Not. R. Astron. Soc.* 406.4 (Aug. 2010), pp. 2325–2338.

[219] E. D. Palik. "Handbook of optical constants of solids II". In: *Bost. Acad. Press. 1991, Ed. by Palik, Edward D.* 1991.

[220] Yichuan C. Pei and S. Michael Fall. "Cosmic Chemical Evolution". In: *Astrophys. J.* 454 (Nov. 1995), p. 69.

[221] Yichuan C. Pei, S. Michael Fall, and Michael G. Hauser. "Cosmic Histories of Stars, Gas, Heavy Elements, and Dust in Galaxies". In: *Astrophys. J.* 522.2 (Sept. 1999), pp. 604–626.

[222] Bryan E. Penprase, J. Xavier Prochaska, Wallace L. W. Sargent, et al. “KECK ECHELLETTE SPECTROGRAPH AND IMAGER OBSERVATIONS OF METAL-POOR DAMPED Lya SYSTEMS”. In: *Astrophys. J.* 721.1 (Sept. 2010), pp. 1–25.

[223] Steven V. Penton, J. Michael Shull, and John T. Stocke. “The Local Lya Forest. II. Distribution of HI Absorbers, Doppler Widths, and Baryon Content”. In: *Astrophys. J.* 544.1 (Nov. 2000), pp. 150–175.

[224] Steven V Penton, John T Stocke, and J Michael Shull. “THE LOCAL L y FOREST . IV . SPACE TELESCOPE IMAGING SPECTROGRAPH G140M SPECTRA AND RESULTS ON THE DISTRIBUTION AND BARYON CONTENT OF H i ABSORBERS 1”. In: *Astrophys. J.* 152 (2004), pp. 29–62.

[225] Perkin Elmer. *Lambda 900 User Manual*. Tech. rep. 2001.

[226] S. Perlmutter, G. Aldering, G. Goldhaber, et al. “Measurements of Omega and Lambda from 42 High-Redshift Supernovae”. In: *Astrophys. J.* 517.2 (June 1999), pp. 565–586.

[227] C. Péroux, V. P. Kulkarni, J. Meiring, et al. “The Most Metal-Rich Intervening Quasar Absorber Known”. In: *Astron. Astrophys.* 450 (2006), pp. 53–57.

[228] C. Péroux, J. D. Meiring, V. P. Kulkarni, R. Ferlet, et al. “Metal-rich damped / subdamped Lyman a quasar absorbers at z $<$ 1”. In: *Mon. Not. R. Astron. Soc.* 372.1 (2006), pp. 369–380.

[229] C. Péroux, J. D. Meiring, V. P. Kulkarni, P. Khare, et al. “Metal abundances at z $<$ 1.5: New measurements in sub-damped Lyman a absorbers”. In: *Mon. Not. R. Astron. Soc.* 386.4 (2008), pp. 2209–2220.

[230] Céline Péroux. “Properties of Lya absorbers at high redshift”. PhD thesis. 2001.

[231] Céline Péroux, Nicolas Bouché, Varsha P. Kulkarni, et al. “A SINFONI integral field spectroscopy survey for galaxy counterparts to damped Lya systems - II. Dynamical properties of the galaxies towards Q0302 - 223 and Q1009 - 0026”. In: *Mon. Not. R. Astron. Soc.* 410.4 (Feb. 2011), pp. 2251–2256.

[232] Céline Péroux, Miroslava Dessauges-Zavadsky, Sandro D’Odorico, et al. “A homogeneous sample of sub-damped Lyman a systems - III. Total gas mass”. In: *Mon. Not. R. Astron. Soc.* 363.2 (2005), pp. 479–495.

[233] Céline Péroux, Miroslava Dessauges-Zavadsky, Sandro D’Odorico, et al. “A homogeneous sample of sub-damped Lyman α systems - IV. Global metallicity evolution”. In: *Mon. Not. R. Astron. Soc.* 382.1 (2007), pp. 177–193.

[234] Céline Péroux, Varsha P. Kulkarni, and Donald G. York. “A SINFONI integral field spectroscopy survey for galaxy counterparts to damped lyman a systems - v. neutral and ionized-phase metallicities”. In: *Mon. Not. R. Astron. Soc.* 437.4 (2014), pp. 3144–3158.

[235] Celine Peroux, Patrick Petitjean, Bastien Aracil, et al. “A new measurement of zinc metallicity in a DLA at z=3.35”. In: *New Astron.* 7.January 2014 (2002), pp. 1–15.

[236] Céline Péroux, Samuel Quiret, Hadi Rahmani, et al. “A SINFONI integral field spectroscopy survey for galaxy counterparts to damped Lyman a systems – VI. Metallicity and geometry as gas flow probes”. In: *Mon. Not. R. Astron. Soc.* 457.1 (Mar. 2016), pp. 903–916.

[237] P Petitjean, C Ledoux, and R Srianand. “The nitrogen and oxygen abundances in the neutral gas at high redshift”. In: *Astron. Astrophys.* 480 (2008), p. 349.

[238] P Petitjean, R Srianand, and C Ledoux. “ASTRONOMY AND Letter to the Editor Molecular hydrogen and the nature of damped Lyman- a systems”. In: *Astron. Astrophys.* 364 (2000), pp. 26–30.

[239] Patrick Petitjean. “QSO Absorption Line Systems”. In: 1 (Oct. 1998), p. 24.

[240] Patrick Petitjean, R. Srianand, and Cédric Ledoux. “Molecular hydrogen at z=1.973 toward Q0013-004: Dust depletion pattern in damped Lyman-alpha systems”. In: *Mon. Not. R. Astron. Soc.* 332 (2002), p. 9.

[241] M Pettini, D L King, L J Smith, et al. “Dust in high-redshift galaxies”. In: *Astrophys. J.* 478 (1997), pp. 536–541.

[242] Max Pettini and Ryan Cooke. “A new, precise measurement of the primordial abundance of deuterium”. In: *Mon. Not. R. Astron. Soc.* 425.4 (Oct. 2012), pp. 2477–2486.

[243] Max Pettini, Sara L Ellison, Jacqueline Bergeron, et al. “The abundances of nitrogen and oxygen in damped Lyman a systems”. In: *Astron. Astrophys.* 391.1 (Aug. 2002), pp. 21–34.

[244] Max Pettini, Sara L. Ellison, Charles C. Steidel, and David V. Bowen. “Metal Abundances at [FORMULA][F]z<1.5[/F][/FORMULA]: Fresh Clues to the Chemical Enrichment History of Damped [CLC]Ly[/CLC]a Systems”. In: *Astrophys. J.* 510.2 (Jan. 1999), pp. 576–589.

[245] Max Pettini, Sara L. Ellison, Charles C. Steidel, Alice E. Shapley, et al. “Si and Mn Abundances in Damped Lyα Systems with Low Dust Content”. In: *Astrophys. J.* 532.1 (Mar. 2000), pp. 65–76.

[246] Max Pettini, Linda J. Smith, Richard W. Hunstead, et al. “Metal enrichment, dust, and star formation in galaxies at high redshifts. 3: Zn and CR abundances for 17 damped Lyman-alpha systems”. In: *Astrophys. J.* 426 (May 1994), p. 79.

[247] Max Pettini, Linda J. Smith, David L. King, et al. “The Metallicity of High Redshift Galaxies: The Abundance of Zinc in 34 Damped Lyman Alpha Systems from z = 0.7 to 3.4”. In: *Astrophys. J.* 486 (1997), pp. 665–680.

[248] Max Pettini, Berkeley J. Zych, Michael T. Murphy, et al. “Deuterium abundance in the most metal-poor damped Lyman alpha system: converging on b,0 h 2”. In: *Mon. Not. R. Astron. Soc.* 391.4 (Dec. 2008), pp. 1499–1510.

[249] Max Pettini, Berkeley J. Zych, Charles C. Steidel, et al. “C, N, O abundances in the most metal-poor damped Lyman alpha systems”. In: *Mon. Not. R. Astron. Soc.* 385.4 (Apr. 2008), pp. 2011–2024.

[250] Andrew Pontzen, Fabio Governato, Max Pettini, et al. “Damped Lyman a systems in galaxy formation simulations”. In: *Mon. Not. R. Astron. Soc.* 390.October (2008), pp. 1349–1371.

[251] Attila Popping, R. Davé, Robert Braun, et al. “The simulated H I sky at low redshift”. In: *Astron. Astrophys.* 504.1 (Sept. 2009), pp. 15–32.

[252] J. X. Prochaska and A. M. Wolfe. “A Keck HIRES Investigation of the Metal Abundances and Kinematics of Three Damped Ly alpha Systems toward Q2206-199”. In: *Astrophys. J.* 474 (1997), p. 140.

[253] J. Xavier Prochaska and Arthur M. Wolfe. “On the (Non)Evolution of HI Disks over Cosmic Time”. In: *Astrophys. J.* 696 (2009), pp. 1543–1547.

[254] Jason X. Prochaska, Sandra Castro, and S. G. Djorgovski. “New Damped Lya Metallicities from Echellette Spectrograph and Imager Spectroscopy of Five Palomar Sky Survey Quasars”. In: *Astrophys. J. Suppl. Ser.* 148.2 (Oct. 2003), pp. 317–326.

[255] Jason X. Prochaska, Eric Gawiser, and Arthur M. Wolfe. “Galactic Chemical Abundances at z $>$ 3. I. First Results from the Echellette Spectrograph and Imager”. In: *Astrophys. J.* 552.1 (May 2001), pp. 99–105.

[256] Jason X Prochaska, Eric Gawiser, Arthur M Wolfe, et al. “The ESI/Keck II Damped Lya Abundance Database”. In: *Astrophys. J. Suppl. Ser.* 147.2 (Aug. 2003), pp. 227–264.

[257] Jason X. Prochaska, Richard B. C. Henry, John M. O’Meara, et al. “The UCSD HIRES/Keck I Damped Lyα Abundance Database. IV. Probing Galactic Enrichment Histories with Nitrogen”. In: *Publ. Astron. Soc. Pacific* 114.799 (Sept. 2002), pp. 933–954.

[258] Jason X. Prochaska, Stephane Herbert Fort, and Arthur M. Wolfe. “The SDSS Damped Lya Survey: Data Release 3”. In: *Astrophys. J.* 635.1 (2005), pp. 123–142.

[259] Jason X. Prochaska and Arthur M. Wolfe. “A Keck HIRES Investigation of the Metal Abundances and Kinematics of the Z = 2.46 Damped LY alpha System toward Q0201+365”. In: *Astrophys. J.* 470.1 (Oct. 1996), p. 403.

[260] Jason X. Prochaska and Arthur M. Wolfe. “On the Kinematics of the Damped Lyman-alpha Protogalaxies”. In: *Astrophys. J.* 487.1 (1997), pp. 73–95.

[261] Jason X. Prochaska and Arthur M. Wolfe. “Chemical Abundances of the Damped Lya Systems at”. In: *Astrophys. J. Suppl. Ser.* 121.2 (Apr. 1999), pp. 369–415.

[262] Jason X. Prochaska and Arthur M. Wolfe. “The UCSD HIRES/Keck I Damped Lya Abundance Database. II. The Implications”. In: *Astrophys. J.* 566.1 (Feb. 2002), pp. 68–92.

[263] Jason X. Prochaska, Arthur M. Wolfe, J. Christopher Howk, et al. “The UCSD/Keck Damped Lya Abundance Database: A Decade of High-Resolution Spectroscopy”. In: *Astrophys. J. Suppl. Ser.* 171.1 (2007), pp. 29–60.

[264] Gabriel E. Prochter, J. Xavier Prochaska, John M. O’Meara, et al. “The Keck+Magellan Survey for Lyman Limit Absorption II: A Case Study on Metallicity Variations”. In: *Astrophys. J.* (2010), p. 20.

[265] R Quast, D Reimers, and R Baade. “Astrophysics HE 0515 – 4414 : an unusual sub-damped Ly a system revisited”. In: *Astron. Astrophys.* 457 (2008), pp. 443–457.

[266] S. Quiret, B. Milliard, R. Grange, et al. “The FIREBall-2 UV sample grating efficiency at 200-208nm”. In: *SPIE*. Ed. by Tadayuki Takahashi, Jan-Willem A. den Herder, and Mark Bautz. July 2014, p. 914432.

[267] S Quiret, C Péroux, T Zafar, et al. “The ESO UVES advanced data products quasar sample – VI. Sub-damped Lyman a metallicity measurements and the circumgalactic medium”. In: *Mon. Not. R. Astron. Soc.* 458.4 (June 2016), pp. 4074–4121.

[268] Marc Rafelski, Marcel Neeleman, Michele Fumagalli, et al. “THE RAPID DECLINE IN METALLICITY OF DAMPED Lya SYSTEMS AT z $\sim$ 5”. In: *Astrophys. J.* 782.2 (Feb. 2014), p. L29.

[269] Marc Rafelski, Arthur M. Wolfe, J. Xavier Prochaska, et al. “METALLICITY EVOLUTION OF DAMPED Lya SYSTEMS OUT TO z $\sim$ 5”. In: *Astrophys. J.* 755.2 (Aug. 2012), p. 89.

[270] Olivera Rakic, Joop Schaye, Charles C. Steidel, et al. “NEUTRAL HYDROGEN OPTICAL DEPTH NEAR STAR-FORMING GALAXIES AT z = 2.4 IN THE KECK BARYONIC STRUCTURE SURVEY”. In: *Astrophys. J.* 751.2 (June 2012), p. 94.

[271] Sandhya M. Rao, Jason X. Prochaska, J. Christopher Howk, et al. “Elemental Abundances in Two High Column Density Damped Lyα Systems at z $<$ 1.5”. In: *Astron. J.* 129.1 (Jan. 2005), pp. 9–19.

[272] Sandhya M. Rao and David a. Turnshek. “Discovery of Damped Lya Systems at Redshifts Less than 1.65 and Results on Their Incidence and Cosmological Mass Density”. In: *Astrophys. J. Suppl. Ser.* 130.1 (Sept. 2000), pp. 1–35.

[273] Sandhya M Rao, David a Turnshek, and Daniel B Nestor. “Damped Lya Systems at $z < 1.65$: The Expanded Sloan Digital Sky Survey Hubble Space Telescope Sample”. In: *Astrophys. J.* 636 (2006), p. 610.

[274] Michael Rauch, Martin Haehnelt, Andrew Bunker, et al. “A Population of Faint Extended Line Emitters and the Host Galaxies of Optically Thick QSO Absorption Systems”. In: *Astrophys. J.* 681.2 (July 2008), pp. 856–880.

[275] Mj Rees and Jp Ostriker. “Cooling, dynamics and fragmentation of massive gas clouds-Clues to the masses and radii of galaxies and clusters”. In: *Mon. Not. R. Astron. Soc.* 179 (1977), pp. 541–559.

[276] Joseph Ribaudo, Nicolas Lehner, J. Christopher Howk, et al. “EVIDENCE FOR COLD ACCRETION: PRIMITIVE GAS FLOWING ONTO A GALAXY AT z $\sim$ 0.274”. In: *Astrophys. J.* 743.2 (Dec. 2011), p. 207.

[277] Philipp Richter, Tobias Westmeier, and Christian Bruens. “Low-column density gas clumps in the halo of the Milky Way”. In: 52.June 2001 (2005), p. 4.

[278] Adam G. Riess, Alexei V. Filippenko, Peter Challis, et al. “Observational Evidence from Supernovae for an Accelerating Universe and a Cosmological Constant”. In: *Astron. J.* 116.3 (Sept. 1998), pp. 1009–1038.

[279] Samantha a. Rix, Max Pettini, Charles C. Steidel, et al. “The Sightline to Q2343-BX415: Clues to Galaxy Formation in a Quasar Environment”. In: 2002 (2007), p. 27.

[280] Brant E Robertson, Richard S Ellis, James S Dunlop, et al. “Early star-forming galaxies and the reionization of the Universe.” In: *Nature* 468.7320 (Nov. 2010), pp. 49–55.

[281] J. Rosdahl and J. Blaizot. “Extended Lya emission from cold accretion streams”. In: *Mon. Not. R. Astron. Soc.* 423.1 (2012), pp. 344–366.

[282] J Rosdahl, J Blaizot, D Aubert, et al. “RAMSES-RT: radiation hydrodynamics in the cosmological context”. In: *Mon. Not. R. Astron. Soc.* 436.3 (Dec. 2013), pp. 2188–2231.

[283] Kate H R Rubin, J Xavier Prochaska, David C Koo, Andrew C Phillips, et al. “EVIDENCE FOR UBIQUITOUS COLLIMATED GALACTIC-SCALE OUTFLOWS ALONG THE STAR-FORMING SEQUENCE AT z $\sim$ 0.5”. In: *Astrophys. J.* 794.2 (2014), p. 156.

[284] Kate H. R. Rubin, Xavier J. Prochaska, David C. Koo, and Andrew C. Phillips. “THE DIRECT DETECTION OF COOL, METAL-ENRICHED GAS ACCRETION ONTO GALAXIES AT z $\sim$ 0.5”. In: *Astrophys. J.* 747.2 (Mar. 2012), p. L26.

[285] Gwen C. Rudie, Charles C. Steidel, Ryan F. Trainor, et al. “THE GASEOUS ENVIRONMENT OF HIGH- z GALAXIES: PRECISION MEASUREMENTS OF NEUTRAL HYDROGEN IN THE CIRCUMGALACTIC MEDIUM OF z $\sim$ 2-3 GALAXIES IN THE KECK BARYONIC STRUCTURE SURVEY”. In: *Astrophys. J.* 750.1 (May 2012), p. 67.

[286] Emma V. Ryan-Weber, Max Pettini, Piero Madau, et al. “A downturn in intergalactic C iv as redshift 6 is approached”. In: *Mon. Not. R. Astron. Soc.* 395.3 (2009), pp. 1476–1490.

[287] Yu-ji Saito, Masahide Takada-Hidai, Satoshi Honda, et al. “Chemical Evolution of Zinc in the Galaxy”. In: *Publ. Astron. Soc. Japan* 61.3 (June 2009), pp. 549–561.

[288] Munier Salem, Greg L. Bryan, and Lauren Corlies. “Role of cosmic rays in the circumgalactic medium”. In: *Mon. Not. R. Astron. Soc.* 456.1 (2016), pp. 582–601.

[289] Blair D. Savage and Kenneth R. Sembach. “INTERSTELLAR ABUNDANCES FROM ABSORPTION-LINE OBSERVATIONS WITH THE HUBBLE SPACE TELESCOPE”. In: *Annu. Rev. Astron. Astrophys.* 34.1 (1996), pp. 279–329.

[290] S. Savaglio, K. Glazebrook, D. Le Borgne, et al. “The Gemini Deep Deep Survey. VII. The Redshift Evolution of the Mass-Metallicity Relation”. In: *Astrophys. J.* 635.1 (Dec. 2005), pp. 260–279.

[291] Ilane Schroetter, Nicolas Bouché, Céline Péroux, et al. “THE VLT SINFONI Mg ii PROGRAM FOR LINE EMITTERS (SIMPLE). II. BACKGROUND QUASARS PROBING $Z \sim 1$ GALACTIC WINDS”. In: *Astrophys. J.* 804.2 (May 2015), p. 83.

[292] a. E. Shapley, C. C. Steidel, M. Pettini, et al. “Rest-Frame Ultraviolet Spectra of z$\sim$3 Lyman Break Galaxies”. In: *Astrophys. J.* 588 (2003), pp. 65–89.

[293] Sijing Shen, Piero Madau, Javiera Guedes, et al. “THE CIRCUMGALACTIC MEDIUM OF MASSIVE GALAXIES AT z $\sim$ 3: A TEST FOR STELLAR FEEDBACK, GALACTIC OUTFLOWS, AND COLD STREAMS”. In: *Astrophys. J.* 765.2 (Mar. 2013), p. 89.

[294] J. Michael Shull, Charles W. Danforth, and Evan M. Tilton. “TRACING THE COSMIC METAL EVOLUTION IN THE LOW-REDSHIFT INTERGALACTIC MEDIUM”. In: *Astrophys. J.* 796.1 (Nov. 2014), p. 49.

[295] J. Michael Shull, Joshua Moloney, Charles W. Danforth, et al. “the Metagalactic Ionizing Background: a Crisis in Uv Photon Production or Incorrect Galaxy Escape Fractions?” In: *Astrophys. J.* 811.1 (2015), p. 3.

[296] J. Michael Shull, Britton D. Smith, and Charles W. Danforth. “The Baryon census in a multiphase intergalactic medium: 30% of the baryons may still be missing”. In: *Astrophys. J.* 759.1 (Nov. 2012), p. 23.

[297] J. Silk. “On the fragmentation of cosmic gas clouds. I - The formation of galaxies and the first generation of stars”. In: *Astrophys. J.* 211 (Feb. 1977), p. 638.

[298] Robert a. Simcoe, Wallace L. W. Sargent, and Michael Rauch. “The Distribution of Metallicity in the Intergalactic Medium at z $\sim$ 2.5: O vi and C iv Absorption in the Spectra of Seven QSOs”. In: *Astrophys. J.* 606.1 (2004), pp. 92–115.

[299] D. Som, V. P. Kulkarni, J. Meiring, D. G. York, C. Péroux, P. Khare, et al. “Element abundances at high redshift: MIKE observations of sub-damped Lyman absorbers at $1.7 < z < 2.4$”. In: *Mon. Not. R. Astron. Soc.* 435.2 (Aug. 2013), pp. 1469–1485.

[300] Debopam Som, Varsha P. Kulkarni, Joseph Meiring, Donald G. York, Celine Péroux, James T. Lauroesch, et al. “HUBBLE SPACE TELESCOPE OBSERVATIONS OF SUB-DAMPED Ly a ABSORBERS AT z $<$ 0.5, AND IMPLICATIONS FOR GALAXY CHEMICAL EVOLUTION”. In: *Astrophys. J.* 806.1 (June 2015), p. 25.

[301] Antoinette Songaila and Lennox L. Cowie. “Metal Enrichment and Ionization Balance in the Lyman α Forest at $z = 3$”. In: *Astrophys. J.* 112 (1996), pp. 335–351.

[302] Antoinette Songaila and Lennox L. Cowie. “Approaching Reionization: The Evolution of the L[CLC]y[/CLC]a Forest from [CLC][ITAL]z[/ITAL][/CLC] = 4 to [CLC][ITAL]z[/ITAL][/CLC] = 6”. In: *Astron. J.* 123.5 (May 2002), pp. 2183–2196.

[303] Volker Springel, Carlos S Frenk, and Simon D M White. “The large-scale structure of the Universe.” In: *Nature* 440.7088 (Apr. 2006), pp. 1137–44.

[304] R. Srianand, N. Gupta, P. Petitjean, et al. “Search for cold gas in z $>$ 2 damped Lya systems: 21-cm and H2 absorption”. In: *Mon. Not. R. Astron. Soc.* 421 (Jan. 2012), no–no.

[305] R. Srianand and P. Petitjean. “A near-solar metallicity damped Lyman-alpha system toward the BAL quasar Tol 1037-2703”. In: *Eur. Sp. Agency, (Special Publ. ESA SP* 826.419 (2001), p. 12.

[306] R Srianand and Patrick Petitjean. “ASTRONOMY AND Molecules in the z abs = 2 . 8112 damped system toward PKS 0528-250”. In: *Astron. Astrophys.* 40 (1998), pp. 33–40.

[307] R. Srianand, Patrick Petitjean, and Cedric Ledoux. “The microwave background temperature at the redshift of 2.33771”. In: *Nature* 408 (2000), pp. 1–20.

[308] Raghunathan Srianand, Neeraj Gupta, and Patrick Petitjean. “Multiwavelength investigation of a near-solar metallicity sub-DLA at Z abs = 1.3647 towards PKS 0237-233”. In: *Mon. Not. R. Astron. Soc.* 375.2 (2007), pp. 584–594.

[309] Raghunathan Srianand, Patrick Petitjean, Cédric Ledoux, et al. *The VLT-UVES survey for molecular hydrogen in high-redshift damped Lyman a systems: Physical conditions in the neutral gas*. 2005.

[310] C C Steidel, M Dickinson, D M Meyer, et al. “Quasar absorbing galaxies at z less than or similar to 1: Deep imaging and spectroscopy in the field of 3C 336”. In: *Astrophys. J.* 480.2 (1997), pp. 568–+.

[311] Charles C Steidel, Kurt L Adelberger, Alice E Shapley, et al. “Lya Imaging of a Proto–Cluster Region at z=3.09”. In: *Astrophys. J.* 532.1 (2000), pp. 170–182.

[312] Charles C. Steidel, Milan Bogosavljević, Alice E. Shapley, et al. “DIFFUSE Lya EMITTING HALOS: A GENERIC PROPERTY OF HIGH-REDSHIFT STAR-FORMING GALAXIES”. In: *Astrophys. J.* 736.2 (Aug. 2011), p. 160.

[313] Charles C. Steidel, Dawn K. Erb, Alice E. Shapley, et al. “THE STRUCTURE AND KINEMATICS OF THE CIRCUMGALACTIC MEDIUM FROM FAR-ULTRAVIOLET SPECTRA OF z = 2-3 GALAXIES”. In: *Astrophys. J.* 717.1 (July 2010), pp. 289–322.

[314] Kyle R. Stewart, Tobias Kaufmann, James S. Bullock, et al. “OBSERVING THE END OF COLD FLOW ACCRETION USING HALO ABSORPTION SYSTEMS”. In: *Astrophys. J.* 735.1 (July 2011), p. L1.

[315] Greg Stinson, Anil Seth, Neal Katz, et al. “Star formation and feedback in smoothed particle hydrodynamic simulations - I. Isolated galaxies”. In: *Mon. Not. R. Astron. Soc.* 373.3 (2006), pp. 1074–1090.

[316] Lisa J. Storrie-Lombardi and Arthur M. Wolfe. “Surveys for $z > 3$ Damped Lyman alpha Absorption Systems”. In: *Astrophys. J.* 543.2 (2000), p. 46.

[317] Kirill Tchernyshyov, Margaret Meixner, Jonathan Seale, et al. “Elemental Depletions in the Magellanic Clouds and the Evolution of Depletions”. In: *Astrophys. J.* 811.2 (2015), pp. 1–21.

[318] R. Teyssier. “Cosmological hydrodynamics with adaptive mesh refinement”. In: *Astron. Astrophys.* 385.1 (Apr. 2002), pp. 337–364.

[319] Romain Teyssier, Andrew Pontzen, Yohan Dubois, et al. “Cusp-core transformations in dwarf galaxies: Observational predictions”. In: *Mon. Not. R. Astron. Soc.* 429.4 (2013), pp. 3068–3078.

[320] Thorlabs. *alpha-BBO Glan-Laser Polarizers*.

[321] Evan M. Tilton, Charles W. Danforth, J. Michael Shull, et al. “THE LOW-REDSHIFT INTERGALACTIC MEDIUM AS SEEN IN ARCHIVAL LEGACY HST /STIS AND FUSE DATA”. In: *Astrophys. J.* 759.2 (Nov. 2012), p. 112.

[322] F. X. Timmes, J. T. Lauroesch, and J. W. Truran. “Abundance Histories for QSO Absorption Line Systems”. In: (1995), p. 22.

[323] P. B. Tissera, D. G. Lambas M. B. Mosconi, and S. A. Cora. “Chemical Enrichment at High Redshifts: Understanding the Nature of Damped Lyα Systems in Hierarchical Models”. In: 20 (2001), pp. 527–532.

[324] Maxime Trebitsch, Anne Verhamme, Jérémy Blaizot, et al. “Lyman-a blobs: polarization arising from cold accretion”. In: *Astron. Astrophys.* 593 (Sept. 2016), A122.

[325] Christy A Tremonti, Timothy M Heckman, Guinevere Kauffmann, et al. “The Origin of the Mass–Metallicity Relation: Insights from 53,000 Star-Forming Galaxies in the SDSS”. In: *Astrophys. J.* 613.2 (Oct. 2004), p. 15.

[326] Todd M. Tripp, Edward B. Jenkins, David V. Bowen, et al. “Discovery of a Primitive Damped Lya Absorber near an X-Ray-bright Galaxy Group in the Virgo Cluster”. In: *Astrophys. J.* 619.2 (Feb. 2005), pp. 714–732.

[327] Todd M Tripp, Joseph D Meiring, J Xavier Prochaska, et al. “The hidden mass and large spatial extent of a post-starburst galaxy outflow.” In: *Science* 334.6058 (Nov. 2011), pp. 952–5.

[328] Todd M. Tripp, Kenneth R. Sembach, David V. Bowen, et al. “A High-Resolution Survey of Low-Redshift QSO Absorption Lines: Statistics and Physical Conditions of OVI Absorbers”. In: *Astrophys. J. Suppl. Ser.* 177.1 (July 2008), pp. 39–102.

[329] Jason Tumlinson, Christopher Thom, Jessica K Werk, et al. “The large, oxygen-rich halos of star-forming galaxies are a major reservoir of galactic metals.” In: *Science* 334.6058 (Nov. 2011), pp. 948–52.

[330] Monica L. Turner, Joop Schaye, Charles C. Steidel, et al. “Detection of hot, metal-enriched outflowing gas around $z \approx 2.3$ star-forming galaxies in the Keck Baryonic Structure Survey”. In: 17.October (Oct. 2014), p. 14.

[331] David A Turnshek, Eric M Monier, Sandhya M Rao, et al. “36 new, high-probability, damped Ly absorbers at redshift $0.42 < z < 0.70$”. In: *Mon. Not. R. Astron. Soc.* 449.2 (2015), pp. 1536–1544.

[332] David A. Turnshek, Sandhya M. Rao, Daniel B. Nestor, et al. “Double-damped Lya Absorption: A Possible Large Neutral Hydrogen Gas Filament near Redshift z = 1”. In: *Astrophys. J.* 609.2 (July 2004), pp. L53–L57.

[333] D. Tweed, J. Devriendt, J. Blaizot, et al. “Building merger trees from cosmological N -body simulations”. In: *Astron. Astrophys.* 506.2 (2009), pp. 647–660.

[334] A de la Varga, D Reimers, D Tytler, et al. “ASTRONOMY AND Damped Lyman α systems at z = 0 . 68 and z = 1 . 15 towards HE 1122 – 1649 and HE 0515 – 4414”. In: *Astron. Astrophys.* 363 (2000), pp. 69–83.

[335] A Verhamme, Y Dubois, J Blaizot, et al. “Lyman- a emission properties of simulated galaxies : interstellar medium structure and inclination effects”. In: 111 (2012), pp. 1–12.

[336] A. Verhamme, D. Schaerer, and A. Maselli. “3D Lya radiation transfer. I. Understanding Lya line profile morphologies”. In: *Astron. Astrophys.* 460 (2006), pp. 397–413.

[337] G Vladilo, C Abate, J Yin, et al. “Silicon depletion in damped Ly a systems”. In: *Astron. Astrophys.* 530 (June 2011), A33.

[338] G. Vladilo, M. Centurión, S. a. Levshakov, et al. “Extinction and metal column density of HI regions up to redshift z $\sim$2”. In: *Astron. Astrophys.* 454.1 (July 2006), pp. 151–164.

[339] Giovanni Vladilo. “Dust and Elemental Abundances in Damped Lya Absorbers”. In: *Astrophys. J.* 493.2 (Feb. 1998), pp. 583–594.

[340] Giovanni Vladilo, Miriam Centurion, Piercarlo Bonifacio, et al. “Ionization Properties and Elemental Abundances in Damped Lya Systems”. In: *Astrophys. J.* 557.2 (Aug. 2001), pp. 1007–1020.

[341] Freeke van de Voort and Joop Schaye. “Properties of gas in and around galaxy haloes”. In: *Mon. Not. R. Astron. Soc.* 423.4 (July 2012), pp. 2991–3010.

[342] Freeke van de Voort, Joop Schaye, Gabriel Altay, et al. “Cold accretion flows and the nature of high column density H i absorption at redshift 3”. In: *Mon. Not. R. Astron. Soc.* 421.4 (Apr. 2012), pp. 2809–2819.

[343] George Wallerstein. “Abundances in G. Dwarfs.VI. a Survey of Field Stars.” In: *Astrophys. J. Suppl. Ser.* 6 (Feb. 1962), p. 407.

[344] Benjamin J. Weiner, Alison L. Coil, Jason X. Prochaska, et al. “UBIQUITOUS OUTFLOWS IN DEEP2 SPECTRA OF STAR-FORMING GALAXIES AT z = 1.4”. In: *Astrophys. J.* 692.1 (Feb. 2009), pp. 187–211.

[345] Jessica K. Werk, J. Xavier Prochaska, Jason Tumlinson, et al. “THE COS-HALOS SURVEY: PHYSICAL CONDITIONS AND BARYONIC MASS IN THE LOW-REDSHIFT CIRCUMGALACTIC MEDIUM”. In: *Astrophys. J.* 792.1 (Aug. 2014), p. 8.

[346] Simon D. M. White and M. J. Rees. “Core condensation in heavy halos: a two-stage theory for galaxy fromation and clustering”. In: *Mon. Not. R. Astron. Soc.* 183 (1978), pp. 341–358.

[347] L. Wisotzki, R. Bacon, J. Blaizot, et al. “Extended Lyman a haloes around individual high-redshift galaxies revealed by MUSE”. In: *Astron. Astrophys.* 587 (Mar. 2016), A98.

[348] Aida Wofford, Claus Leitherer, and John Salzer. “Lya ESCAPE FROM z $\sim$ 0.03 STAR-FORMING GALAXIES: THE DOMINANT ROLE OF OUTFLOWS”. In: *Astrophys. J.* 765.2 (Mar. 2013), p. 118.

[349] Isak G. B. Wold, Amy J. Barger, and Lennox L. Cowie. “z $\sim$ 1 Lya EMITTERS. I. THE LUMINOSITY FUNCTION”. In: *Astrophys. J.* 783.2 (Mar. 2014), p. 119.

[350] Arthur M. Wolfe, Eric Gawiser, and Jason X. Prochaska. “Damped Lya Systems”. In: *Annu. Rev. Astron. Astrophys.* 43.1 (Sept. 2005), pp. 861–918.

[351] Arthur M Wolfe, Jason X Prochaska, Regina A Jorgenson, et al. “Bimodality in Damped Lya Systems”. In: *Astrophys. J.* 681.2 (July 2008), pp. 881–896.

[352] Christopher B. Wotta, Nicolas Lehner, J. Christopher Howk, et al. “Low-metallicity Absorbers Account for Half of the Dense Circumgalactic Gas at z $<$ 1”. In: (Aug. 2016).

[353] T Zafar, D Watson, J P U Fynbo, et al. “The extinction curves of star-forming regions from z = 0.1 to 6.7 using GRB afterglow spectroscopy”. In: *Astron. Astrophys.* 532 (Aug. 2011), A143.

[354] Tayyaba Zafar, Miriam Centurion, Celine Peroux, et al. “The ESO UVES advanced data products quasar sample - III. Evidence of bimodality in the [N/] distribution”. In: *Mon. Not. R. Astron. Soc.* 444.1 (Aug. 2014), pp. 744–756.

[355] Tayyaba Zafar, C. Péroux, Attila Popping, et al. “The ESO UVES advanced data products quasar sample- II. Cosmological evolution of the neutral gas mass density”. In: *Astron. Astrophys.* 556 (Aug. 2013), A141.

[356] Tayyaba Zafar, Attila Popping, and Céline Péroux. “The ESO UVES advanced data products quasar sample”. In: *Astron. Astrophys.* 556 (Aug. 2013), A140.

[357] Tayyaba Zafar, Giovanni Vladilo, Celine Peroux, et al. “The ESO UVES Advanced Data Products Quasar Sample - IV. On the deficiency of Argon in DLA systems”. In: *Mon. Not. R. Astron. Soc.* September (Sept. 2014), p. 14.

[358] H J Zahid, G I Dima, L J Kewley, et al. “A CENSUS OF OXYGEN IN STAR-FORMING GALAXIES: AN EMPIRICAL MODEL LINKING METALLICITIES, STAR FORMATION RATES, AND OUTFLOWS”. In: *Astrophys. J.* 757.1 (Sept. 2012), p. 54.

[359] Zheng Zheng, Renyue Cen, David Weinberg, et al. “EXTENDED Lya EMISSION AROUND STAR FORMING GALAXIES”. In: *Astrophys. J.* 739.2 (Oct. 2011), p. 62.

[360] Martin Zwaan, Fabian Walter, Emma Ryan-Weber, et al. “ARE THE KINEMATICS OF DLAs IN AGREEMENT WITH THEIR ARISING IN THE GAS DISKS OF GALAXIES?” In: *Astron. J.* 136.6 (Dec. 2008), pp. 2886–2896.

[361] Berkeley J. Zych, Michael T. Murphy, Paul C. Hewett, et al. “Dust depletion, chemical uniformity and environment of Ca ii H&K quasar absorbers”. In: *Mon. Not. R. Astron. Soc.* 392.4 (2009), pp. 1429–1450.